Imperial College London
Mechanical Engineering Department

Bubble characteristics during flow boiling at artificial and natural cavities

Dapeng Yang

Submitted in part fulfilment of the requirements for the degree
of
Doctor of Philosophy

October 2023

To my family, friends and teachers supporting me through the whole investigation.

Abstract

Flow boiling is an efficient heat transfer mechanism widely used in many applications. In the current work, a novel parametric experiment has been performed to investigate how the nucleation site geometry of artificial cavities, such as cavity depth, diameter and, for the case of two cavities tested, spacing, affect the ebullition dynamics during flow boiling. Understanding the effects of these parameters can help the design of improved flow boiling heat transfer surfaces.

The bubble dynamics at artificial cavities are compared to those at natural cavities to understand whether the underlying physical mechanisms for both sites remain the same. It was discovered that the bubble dynamics at artificial cavities develop differently to those at natural sites, an original finding. A different bubble growth and condensation mechanism is found at artificial cavities compared to natural cavities which might explain the observed disparities. The widely reported energy balance bubble growth mechanism at natural sites fails to predict the behaviour of bubbles at artificial sites. The current work found and further developed suitable models to predict the bubble dynamics at artificial cavities, something which has not been attempted before.

It was possible to fit the bubble growth profile at most single artificial cavities to a dimensionless power equation which uses the departure diameter and growth period. Two newly developed correlations provided the bubble ebullition frequency and its departure diameter. The departure diameter was accurately calculated from a novel force balance model originally suggested by Du, Zhao & Bo (2018) and further developed in the current work. As such, the bubble growth profile, departure diameter and frequency at an artificial cavity in flow boiling can be predicted based on the experimental boundary conditions, which is a new finding.

The application of the developed models to bubbles growing at a pair of cavities was also investigated. This parametric study showed that an optimum spacing and cavity depth exists which could be explored to achieve improved critical heat flux values or greater heat transfer at lower heat fluxes, which can assist the development of augmented flow boiling heat transfer surfaces.

Declaration of originality

The work reported in this thesis is an original work of Dapeng Yang except where appropriately referenced.

Copyright declaration

The copyright of this thesis rests with the author. Unless otherwise indicated, its contents are licensed under a Creative Commons Attribution-Non-Commercial 4.0 International Licence (CC BY-NC). Under this licence, you may copy and redistribute the material in any medium or format. You may also create and distribute modified versions of the work. This is on the condition that: you credit the author and do not use it, or any derivative works, for a commercial purpose. When reusing or sharing this work, ensure you make the licence terms clear to others by naming the licence and linking to the licence text. Where a work has been adapted, you should indicate that the work has been changed and describe those changes. Please seek permission from the copyright holder for uses of this work that are not included in this licence or permitted under UK Copyright Law.

Acknowledgements

As this PhD study approaches to an end, I would like to express my gratitude to many people for their assistance thought this project. This PhD experience not only involves the study of natural phenomena but also provides instruction in reasoning logic.

First of all, I would like to thank Prof. Yannis Hardalupas, my primary supervisor, very much. He is very patient, nice and kind. He rarely presses me on the experiment's progress. Rather, a polite reminder regarding the deadline was obtained. When I was struggling with decision-making, courage and relief were received. Furthermore, I had the freedom to explore fascinating study areas that initially appear unrelated to the primary research area. Such a relaxed, unhurried pace offered me a fantastic study experience.

I express my gratitude to Dr. Antonis Sergis, my co-supervisor, for sharing his invaluable knowledge and rich experience on the conditioning tunnel design, Graduate Teaching Assistants (GTA), risk assessment evaluation and so on. We also explore in depth certain experimental questions.

I would like to express my gratitude to all of our group members and college pals. Dr. Chaoxu Chen, many thanks. He assisted me with the MATLAB coding and the arrangement of the optical system. In addition, a lot of well-planned hiking tours by Chaoxu enriched my life in the UK. I would also like to thank Dr. Xihua for his share of life experiences in the UK, including recommendations on available accommodations before I came to the UK. Many thanks to Dr. Yushuai Liu for sharing his knowledge of flow dynamics and for interesting publications and books. We have patient conversations on philosophy from time to time. He also assisted me with the optical arrangement and rig design. For their help with this project and enjoyable moments during my free time, I would like to thank Drs. Tianyi Wang, Han Yuan, Yuqi Hu, Marcus Horwich, Lili Lu, Paul Andrade and Mustafa Iqbal, Xiyi Qiu, Hao Hao, Goswami Anjan and Khalad AlMuhaysh. I wish you well and hope that both your life and career are fulfilling.

I express my gratitude to the personnel for their kind assistance. Serena Dalrymple assisted me with purchase orders as well as the expense claim work. Asanka Munasinghe assisted me in assembling a PID controller and connecting electrical systems. Edward Benbow connected tubes, suggested valve suppliers, and helped solve problems identified during the experiments. He is incredibly helpful and kind. A safety officer named Efthymia Bekiri offered sage advice on the rig arrangements. Express sending and delivery assistance is provided by Mark Holloway and Kevin Palmer. I get assistance from Harminder Flora with cavity drilling and cleaning tasks. I appreciate his excellent work on the test section's design. The measurements of the surface condition and the use of a confocal microscope were

assisted by Pawel F. Orzlowski. I received training from Sharad Patel and Ruth D. Brooker on the use of micro-CT and SEM, respectively.

I want to thank the China Scholarship Council (CSC) and Imperial College London for supporting me financially.

Last but not least, I would like to express my sincere gratitude to my parents and grandparents for their nursing, love and education and to my future wife, Run Pan, for her patience and love.

Contents

Abstract III
Declaration of originality IV
Copyright declaration V
Acknowledgements VI
List of Figures XII
List of Tables XIX
Nomenclature XX
Latin symbols XX
Greek symbols XXII
Subscripts XXII
Abbreviations XXIII
Chapter 1 Introduction 1
1.1 What is boiling? 1
1.1.1 Classification 1
1.1.2 Boiling regimes 2
1.2 Motivation 4
1.3 Flow boiling unknowns and their challenges. 5
1.4 Present contribution 6
1.5 Thesis outline 8
Chapter 2 Experimental methodology 9
2.1 Experimental rig 9
2.2 Experimental procedure 13
2.3 Wall temperature estimation 15
2.4 Surface roughness characterisation 16
2.4.1 Measurement equipment 16
2.4.2 Surface roughness measurements 17
2.5 Imaging system: optical configuration and the frame rate setting 18
2.6 Image processing algorithm 19
2.7 Calibration of instrumentation and uncertainty estimation 20
2.7.1 Relative uncertainty estimation 20
2.7.2 Calibration of the high-speed camera 21
2.7.3 Calibration of the flowmeter 22
2.7.4 Calibration of the thermocouples 22
2.8 Calculation of equivalent bubble diameter and advancing and receding contact angle 23

2.8.1 Equivalent bubble diameter 23
2.8.2 Advancing and receding contact angles 24
2.9 Quantifying the equivalent bubble diameter estimation uncertainty 25
2.9.1 Contribution of bubble baseline fluctuations on equivalent bubble diameter uncertainty 25
2.9.2 Contribution of bubble shape deformation to equivalent bubble diameter estimation uncertainty 26
2.9.3 Contribution of nucleation surface levelness to equivalent bubble diameter estimation uncertainty 27
2.9.4 Contribution of applied image processing functions ('edge' and 'bwconvhull') to equivalent bubble diameter estimation uncertainty 27
2.9.5 The relative uncertainty of the equivalent bubble diameter 29
2.10 Summary 31
Chapter 3 Bubble behaviour at an artificial and a natural cavity during flow boiling 33
3.1 Review of cavity geometry effects on boiling dynamics 34
3.2 Geometries of artificial and natural bubble nucleation cavities and flow condition 40
3.2.1 Artificial cavity geometry 40
3.2.2 Natural cavity geometry 41
3.2.3 Relative surface positions of the artificial and natural cavities 41
3.3 Definition of bubble characteristics 42
3.3.1 The bubble growth period, waiting period, condensation period 42
3.3.2 Bubble departure, lift-off time, departure diameter and lift-off diameter 43
3.4 Bubble growth period of different bubble events 44
3.5 Bubble waiting time of different bubble events 45
3.6 Bubble lift-off diameter of different bubble events 46
3.7 Temporal evolution of bubble diameter 47
3.7.1 Review of existing bubble growth temporal evolution models during boiling 47
3.7.2 Bubble growth period diameter 51
3.7.3 Temporal evolution of bubble diameter during the condensation period 54
3.8 Temporal evolution of advancing and receding bubble contact points 56
3.8.1 Bubble advancing and receding points at natural cavity 57
3.8.2 Bubble advancing and receding points at artificial cavity 59
3.9 Diameter of bubble contact region on nucleation wall 61
3.10 Advancing and receding bubble contact angles 64
3.10.1 Natural cavity contact angles 65
3.10.2 Artificial cavity contact angles 67
3.11 Bubble inclination angle 68
3.11.1 Natural cavity bubble inclination angle 69
3.11.2 Artificial cavity bubble inclination angle 70
3.12 Bubble interfacial wave propagation speed 71

3.13 Bubble shape evolution 72
3.14 Nucleation wall deposition Patterns 73
3.14.1 Fan-shaped patterns on nucleation wall 74
3.14.2 Theoretical estimation of the required onset temperature of boiling at natural cavity type 2 85
3.14.3 Probability of active cavity types 88
3.15 Summary 89
Chapter 4 Influence of flow boiling conditions on the temporal evolution of bubble growth at an artificial cavity 93
4.1 Considered operating conditions for flow boiling experiments 93
4.2 Typical bubble images during growth for all operating conditions (cases of Table 4.1) 95
4.3 Effect of liquid velocity on bubble growth characteristics 96
4.4 Effect of wall superheats on bubble growth characteristics. 97
4.4.1 Boiling at negative wall superheat 98
4.5 Effect of water entry temperature and resulting local subcooling 100
4.6 Effect of nucleation wall orientation 101
4.7 Non-dimensional correlation of bubble growth and considered flow parameters 102
4.8 Summary 104
Chapter 5 Modelling bubble departure diameter and frequency at an artificial cavity 106
5.1 Existing models for departure diameter and frequency prediction 106
5.1.1 Definition of non-dimensional parameters 106
5.1.2 Existing modelling approaches for the bubble departure diameter 110
5.1.3 Existing modelling approaches for bubble departure frequency 120
5.2 Experimental observations 129
5.2.1 Measured bubble characteristics 130
5.2.2 Discussion of effects of operating conditions on bubble characteristics 132
5.3 Comparison between existing modelling approaches and current measurements 136
5.3.1 Bubble departure diameter 136
5.3.2 Bubble departure frequency 137
5.4 Empirical correlations approaches 138
5.4.1 Bubble departure diameter 138
5.4.2 Bubble departure frequency 140
5.5 Force balance modelling approaches 141
5.5.1 The criterion for bubble departure 141
5.5.2 Bubble force balance in the flow direction 142
5.5.3 Comparison between predicted departure diameter and measurements 147
5.6 Summary 148
Chapter 6 Bubble dynamics at single and pair of artificial cavities and effect of cavity geometry 150

6.1 Effect of single cavity depth 150
6.1.1 Bubble growth, waiting time and departure diameter 150
6.1.2 Continuous boiling in cavities 152
6.2 Effect of cavity diameter 154
6.3 Bubble behaviour at artificial cavity pairs during flow boiling 156
6.3.1 Effect of spacing between two cavities on bubble behaviour 156
6.3.2 Effect of operating conditions on cavity pair ebullition behaviour 166
6.4 Summary 169
Chapter 7 Conclusions and recommendations for future work 171
7.1 Conclusions 171
7.2 Future work 174
Chapter 8 Bibliography 177

List of Figures

Figure 1.1. Effects of the liquid temperature on boiling (white refers to the vapour, grey refers to the liquid) (Faghri, Zhang & Howell, 2010). 2
Figure 1.2. Pool boiling curve for saturated boiling (Faghri, Zhang & Howell, 2010). 3
Figure 2.1 Schematic of the complete rig (not to scale). 10
Figure 2.2 A photo of the complete setup. 10
Figure 2.3 Cross section of the flow conditioning channel, test section and diffuser. 12
Figure 2.4 Isometric view of the test section. 13
Figure 2.5 Temperature temporal evolution for all thermocouples in one case. 15
Figure 2.6 Positions of the thermocouples (represented by red and green dots) from the top view (a) and side view (b). 15
Figure 2.7 Image of the microscope OLS5000 used for the measurements of the surface roughness of the nucleation wall. 17
Figure 2.8 Four measurement lines on an image of the surface of a nucleation wall; the mean of the measured values along the four lines represents the measured surface roughness. 18
Figure 2.9 Imaging system. 18
Figure 2.10 Steps used for the image processing of the captured bubble images. 20
Figure 2.11 Example of (a) indistinct bubble edge in the raw image, (b) detected broken edge and (c) repaired edge when such raw image is considered. This is mainly used for bubbles initiated from natural nucleation sites, for which cases a limited number of images are available. 20
Figure 2.12 Flowmeter operation equation at water temperatures of 92, 82 and 72 °C. 22
Figure 2.13 Temperature readings against the reading of the RTD for all thermocouples. 23
Figure 2.14 Schematic drawing for the illustration of the equivalent bubble diameter estimation approach. 24
Figure 2.15 Contact angle definition. 25
Figure 2.16 Maximum observed bubble baseline variation as revealed from three images.... 26
Figure 2.17 Relative upper and lower bounds of uncertainty contributed by the varying baseline against the equivalent bubble diameter. 26
Figure 2.18 Equivalent bubble diameter difference from estimates from two events with a delay time of 2.72 ms between them at two heat fluxes during the lift-off from the nucleation surface. 27
Figure 2.19 Indication of the nucleation surface levelness, which is 0.72 °..... 27

Figure 2.20 Detected bubble edge (green line) during image processing superimposed on its raw image. 28
Figure 2.21 The missing bubble edge between the two green dots is repaired with a straight line, while the original edge is estimated as the convex curve. 29
Figure 3.1 Bubble neck captured during boiling studies (Siedel, Cioulachtjian & Bonjour, 2008). 36
Figure 3.2 Example geometries of (a) blind circle hole (Marto, Moulson & Maynard, 1968), (b) conical cavity (Marto, Moulson & Maynard, 1968), (c) bulb-shaped cavity (Baldwin, Bhavnani & Jaeger, 2000) and (d) straight unidirectional parallel tunnel with circular base (Das, Das & Saha, 2009). 36
Figure 3.3 Example geometries of (a) coral-rock structure, (b) star-like structure, (c) inner-fin structure (Kang & Wang, 2018). 37
Figure 3.4 Example geometries of (a) reentrant cavity (Kuo & Peles, 2007) and (b) interconnected reentrant cavities (Kuo & Peles, 2008). 38
Figure 3.5 Cross-section of (a) Ω-shaped and (b) rectangular channels (Deng et al., 2015)... 38
Figure 3.6 The mouth (a) and the bottom (b) image of the artificial cavity as captured by a SEM. 40
Figure 3.7 The chequered area (fenced by green lines) containing the natural site is depicted in (a); A crevice captured in the centre of the rectangular area is shown in (b). The relevant scale is indicated by the red arrow on each image. 41
Figure 3.8 The relative position between the artificial and the natural cavity on the nucleation wall. 42
Figure 3.9 Bubble images during the growth time at (a) artificial and (b) natural cavities for operating conditions. The green arrow shows the corresponding scale of the images. 43
Figure 3.10 Bubble images captured after the detachment from the wall at the natural site (a) and artificial site (b) for same operating conditions as Figure 3.9. The green arrow shows the corresponding scale of the images. 43
Figure 3.11 Bubble growth time at the natural (a) and artificial (b) cavity for different sequential individual bubble boiling events. Note that the units of the vertical axis of the two figures are different, which indicates the much longer growth period at the artificial cavity. 45
Figure 3.12 Bubble waiting time at the natural (a) and artificial (b) cavity for different sequential individual bubble boiling events. Note that the scale of the vertical axis of the two figures is different, which indicates the much longer waiting time at the natural site. 46

Figure 3.13 Bubble lift-off diameter at the natural (a) and artificial (b) cavity for different sequential individual bubble boiling events. Note that the difference at the scale of the vertical axis of the two figures, which indicates the high stability of the bubble size at the artificial site for different events. 47
Figure 3.14 Bubble diameter temporal evolution at the natural cavity for five typical bubble boiling events of the current study (black colour symbols). The green colour shows the predicted values based on models of Zuber (1961), Mikic, Rohsenow & Griffith (1970) and Zhou et al. (2020b). The red dots show the predicted values based on the model of Prodanovic, Fraser & Salcudean (2002). 52
Figure 3.15 Comparison between experimental data and predicted values by model type 5 of Prodanovic and Chen of the temporal evolution of bubble growth. The red line represents the best fit equation, which is shown in equation (3.12)..... 52
Figure 3.16 Temporal evolution of bubble diameter at the natural cavity after the bubble lift-off from the wall. Time zero coincides with the bubble lift-off. The red colour shows the predicted values based on the model of Prodanovic, Fraser & Salcudean (2002). 56
Figure 3.17 Temporal evolution of bubble diameter at the artificial cavity after the bubble lift-off from the wall. Time zero coincides with the bubble lift-off. The results are best fitted by the linear expression shown on the graph. 56
Figure 3.18 Illustration indicating the definition of the advancing and receding contact points. 57
Figure 3.19 Temporal evolution of the displacements of the advancing and receding contact points for bubble event 1 (which has a lift-off diameter of 729 μm) of Figure 3.14 at the natural cavity. 57
Figure 3.20 Temporal evolution of the relative positions of the advancing and receding contact points at times 0.2, 0.7, 1.2 and 1.7 ms for bubble event 1 of Figure 3.14 at the natural cavity. 57
Figure 3.21 Temporal evolution of the displacements of the advancing and receding contact points for bubble event (a) 2 (lift-off diameter of 450 μm), (b) 3 (lift-off diameter of 1100 μm), (c) 4 (lift-off diameter of 640 μm) and (d) 5 (lift-off diameter of 880 μm) of Figure 3.14 at the natural cavity..... 58
Figure 3.22 Temporal evolution of the displacements of the advancing and receding contact points at 0-270 ms (a) and 0-40.52 s (b) at the artificial cavity. 59
Figure 3.23 Image of the bubble shape and its position relative to the cavity cross-section when the advancing contact point gains a displacement of -50 μm towards the cavity mouth centre. 60

Figure 3.24 Conceptual diagram of a complete (a), disturbed (b), disrupted (c) liquid microlayer between a bubble and a surface with specific roughness (Sarker et al., 2017). 61
Figure 3.25 Illustration of the definition of the contact diameter of a bubble on a nucleation wall. 62
Figure 3.26 Temporal evolution of the contact diameter of a bubble on the nucleation wall for the five typical flow boiling events of Figure 3.14 at the natural site (a) and for the one typical flow boiling event of Figure 3.15 at the artificial site (b). 63
Figure 3.27 The ratio of the contact diameter to the bubble diameter as a function of time for the five boiling events of Figure 3.14 at the natural cavity (a) and for one typical boiling event of Figure 3.15 at the artificial site (b). 63
Figure 3.28 Definition of micro (θm) and apparent (θa or θr) bubble contact angles in pool boiling. 64
Figure 3.29 Temporal Evolution of advancing and receding contact angles for bubble event 1 (a), 5 (b), 3 (c), 4 (d) and 2 (e) with lift-off diameter of 729 μm, 880 μm, 1100 μm, 622 μm and 450 μm, respectively. 66
Figure 3.30 Temporal evolution of advancing contact angle (a) and receding contact angle (b) during the bubble growth period at the artificial cavity. 67
Figure 3.31 Values of advancing and receding contact angles and bubble shape temporal evolution at four times during the bubble growth period. 68
Figure 3.32 Inclination angle demonstration for artificial (a) and natural (b) cavity. 69
Figure 3.33 Temporal evolution of bubble inclination angle for the five typical boiling events of Figure 3.15. 70
Figure 3.34 Temporal evolution of bubble inclination angle during the bubble growth period (a) and the time range of the last 0.28 s before the departure time (b). 70
Figure 3.35 Temporal behaviour of boiling bubble on the cavity. Elongated neck (a), breakage of the neck (b), propagating wave along the interface (c) and the outline of the bubble temporal evolution (d). 72
Figure 3.36 Irregular bubble shape observations for 11 events of bubble lifting-off from the natural site. 73
Figure 3.37 Images of fan shaped surface patterns and type 1 natural cavities (shown with the black circular shape at the start of the fan shaped patterns) (a-d), cross-section of type 1 natural cavities (e-h) and fan shaped surface patterns for type 2 natural cavities (the shape and size of the natural cavities cannot be detected at the start of the fan shaped patterns) (i-l). 76
Figure 3.38 Possible multiple small nucleation sites (green dots) present in a small region, which initiate the asymmetrical fan shaped patterns on the surface. 77

Figure 3.39 Height distribution along the purple line crossing the fan-shaped pattern, which indicates the presence of deposited material. 78
Figure 3.40 Measurement point (green dot) at the fan-shaped pattern (a) and list of detected element content of the deposited material (b). 78
Figure 3.41 Images of the nucleation surface with the liquid film (a) and after the evaporation of the liquid film (b) and the magnified image of the white layer of deposit (c). .. 79
Figure 3.42 List of analysed elements and the measurement position (green dot) at the clean nucleation surface (a) and at the white deposit layer (b). 79
Figure 3.43 Images of fan-shaped patterns captured on the same nucleation surface. 80
Figure 3.44 Square image (dimensions of 22.2 mm) of the nucleation wall surface, which shows numerous recorded fan-shaped patterns after the completion of the flow boiling experiments. The two black dots (outlined with green circles) at the central area are artificial cavities with diameter and spacing of 0.2 and 0.6 mm, respectively. The yellow arrows indicate the axis of symmetry of the patterns that coincide with the main flow direction, while the red arrows indicate the axes of patterns that deviate from the flow direction. 82
Figure 3.45 Fan-shaped patterns detected at natural sites fitted by red arcs and angle definitions for natural cavities (a, b & c) and the artificial cavity (d). The green dots show the corresponding centre of the added arc section. 84
Figure 3.46 Angles of the 63 fan-shaped patterns detected on the nucleation wall surface. ... 85
Figure 3.47 Minimum onset temperature predicted by models one (a) and two (b) as a function of cavity size. 88
Figure 4.1 Typical bubble images during the growth period at incipience, median and departure times for all cases of Table 4.1. 96
Figure 4.2 Temporal evolution of the bubble diameter during the growth period for liquid flow velocity of 0.12, 0.17 and 0.21 m/s (cases 1, 2 and 3 of Table 4.1). 97
Figure 4.3 Temporal evolution of the bubble diameter during the growth period for wall superheat in the range of -3.7 to 14.13 °C (cases 3-9 of Table 4.1). 98
Figure 4.4 Temporal evolution of the bubble diameter during the growth period for entry water temperature in the range of 75, 84 and 94 °C (cases 11,10 and 3 of Table 4.1). 101
Figure 4.5 Temporal evolution of the bubble diameter during the growth period for conditions of upward and downward facing (cases 3 and 12 of Table 4.1)..... 102
Figure 4.6 Non-dimensional temporal evolution of bubble growth at velocity range of 0.12 to 0.21 m/s, wall superheat of 7.02-14.13 °C and water inlet temperature of 75 and 94 °C (cases 1-3 and 7-11 of Table 4.1). All these cases are upward facing. 104

Figure 4.7 Non-dimensional temporal evolution of bubble growth at wall superheat range of -3.7 to 1.7 °C and downward facing (cases 4-6 & 12 of Table 4.1). 104
Figure 4.8 Non-dimensional temporal evolution of bubble growth predicted by the model of equation (4.1) for all cases of Figure 4.6. 104
Figure 5.1 Bubble departure diameter and frequency (a); bubble growth and waiting time (b) as a function of the liquid flow velocity..... 132
Figure 5.2 Bubble departure diameter and frequency (a); bubble growth and waiting time (b) as a function of the wall heat flux. 133
Figure 5.3 Bubble departure diameter and frequency (a); bubble growth and waiting time (b) as a function of subcooling. 134
Figure 5.4 Bubble departure diameter and frequency (a); bubble growth and waiting time (b) as a function of nucleation surface orientation. 135
Figure 5.5 Schematic representations of an elongated (a) and flattened (b) liquid-vapour interface of the bubble embryo at the artificial cavity at different nucleation surface orientations..... 136
Figure 5.6 Comparison of the experimental bubble departure diameter of this study at the artificial cavity with the predicted diameter by selected existing models..... 137
Figure 5.7 Comparison of the experimental data and predicted data of bubble departure frequency from selected existing models. 138
Figure 5.8 Comparisons between the bubble departure diameter predicted by the new empirical model and the measurements. 139
Figure 5.9 Comparison between the bubble growth time predicted by the model and the measurements. Note that the inverse of the growth time quantifies the bubble departure frequency..... 141
Figure 5.10 Images showing a typical bubble at the departure time from an artificial nucleation site during flow boiling. $\Delta t=0$ represents the time that the neck connecting the bubble with the cavity at the advancing contact point breaks. 142
Figure 5.11 Schematic diagram of the behaviour of a growing bubble on a nucleation wall under flow boiling conditions at an artificial site..... 143
Figure 5.12 The 2D test channel geometry and the corresponding mesh of the model that was used to calculate the liquid velocity at the bubble mass centre..... 145
Figure 5.13 Grid independence test for the computational calculation of the liquid flow velocity at the location of the bubble mass centre. 146
Figure 5.14 Comparison between the predicted bubble departure diameter from equation (5.111) and the measured departure diameter for all cases of Table 4.1..... 148

Figure 5.15 Flow chart showing the interdependency of various parameters and experimental conditions that determine the processes during flow boiling at artificial nucleation sites. 149
Figure 6.1 Temporal evolution of bubble growth (a), bubble departure diameter and growth time (b) and bubble waiting time (c) for artificial cavities with a depth range of 0.2-0.95 mm and diameter of 0.2 mm (cases according to Table 6.1). 151
Figure 6.2 Temporal evolution of the liquid vapour interface at the artificial cavity mouth area. 153
Figure 6.3 Temporal evolution of bubble growth (a), bubble departure diameter and growth time (b) and bubble waiting time (c) for artificial cavities with a diameter range of 0.05-0.2 mm at constant aspect (depth/diameter) ratio 3. 155
Figure 6.4 Change of vapour volume flowrate (fD^3) as a function of artificial cavity diameter. 156
Figure 6.5 Average duration (a) and probability (b) of the presence of cases C1, C2, C3 and C4 as a function of cavity spacing during flow boiling at two artificial sites. 163
Figure 6.6 Vapour volume flowrate per cavity as a function of cavity spacing. 165
Figure 6.7 Schematic of cavity arrangements on a nucleation wall with definition of the cavity distance P (Gong & Cheng, 2016). 166
Figure 6.8 Temporal evolution of the diameter of the coalescent single diameter at two artificial sites during case C4 under flow boiling for operating condition cases 21 (a), 22 (b), 23 (c) and 24 (d) of Table 6.8. 168
Figure 6.9 Recorded images of the coalescent bubbles growing as one at the two artificial sites during case C4 under flow boiling for operating condition cases 21, 22, 23 and 24 of Table 6.8. The scale arrow in the first row is the same for all rows. ... 169

List of Tables

Table 1.1 Classification of boiling types. 2
Table 2.1 List of components of the experimental rig..... 11
Table 2.2 Specifications of the microscope OLS5000 used for the measurements of the surface roughness of the nucleation wall. 17
Table 2.3 Information of the high-speed camera and lens..... 19
Table 2.4 Equivalent bubble diameter overall uncertainty estimation 30
Table 4.1 Operating conditions of each experimental case during flow boiling at an artificial cavity with diameter and depth of 0.2 and 0.95 mm..... 95
Table 5.1 Measured bubble characteristics for the condition numbers and associated operating conditions of Table 4.1..... 131
Table 5.2 Comparison of predicted bubble departure diameter from the available models with current measurements. The mean absolute relative error is shown..... 137
Table 6.1 Matrix of operating flow boiling conditions for artificial cavities with depth range from 0.2 to 0.95 mm and constant cavity diameter 0.2 mm..... 151
Table 6.2 Matrix of operating flow boiling conditions for artificial cavities with a diameter range of 0.05 to 0.2 mm for constant aspect (depth/diameter) ratio 3. The case numbers start from 17, continuing the cases considered previously in Table 4.1 and Table 6.1. 154
Table 6.3 Images of the bottom and top surfaces of artificial cavities with spacings 0.4, 0.6, 0.8, 1 and 1.2 mm..... 158
Table 6.4 Typical bubble images at the start and end times of each of the four identified cases, which have been identified from the imaging study of bubble formation at two cavities during flow boiling. 159
Table 6.5 Temporal sequences of cases of bubble pair evolution from left to right side for spacings of 0.4-1.2 mm between the two artificial cavities during flow boiling. 160
Table 6.6 Probability of appearance of a bubble case after each of the four cases C1-C4 in the temporal sequence for spacings of 0.4-1.2 mm between the two artificial cavities during flow boiling 161
Table 6.7 Estimate of vapour volume flowrate per artificial cavity at the nucleation wall during flow boiling. 164
Table 6.8 Operating conditions for studies of the behaviour of the two bubbles generated at two artificial cavities during flow boiling. 167

Nomenclature

Latin symbols

A	Value of constant	
A_{con}	Area of a bubble in contact with the condensation layer	m^2
A_{evap}	Area of evaporative micro-layer	m^2
A_{sup}	Area of a bubble in contact with the superheated layer	m^2
a b, c, d and e	Value of constant	
B	Numerical constant	
Bo	Boiling number	
b	Numerical constant	
C, C_B, C_s and C_F	Value of a constant	
C_D	Drag force coefficient	
C_l	Shear lift coefficient	
C_p	Specific heat capacity	J/(kg•K)
D	Bubble diameter	m
D_d	Bubble departure diameter	m
D_d^*	Dimensionless departure diameter	m
D_{dry}	Diameter of the dry patch	m
D_H	Hydraulic diameter	m
D_{lo}	Lift-off diameter	m
D_{lo}^*	Dimensionless lift-off diameter	m
D_m	Bubble maximum diameter	m
D_w	Diameter of the contact area	m
d	Distance	m
$\dot{E}$	Energy rate	J
F_{drag}	Drag force	N
F_{dux}	Bubble growth force in the x direction	N
F_{sx}	Surface tension force in the x direction	N
f_d	Bubble departure frequency	Hz
f_d^*	Non-dimensional departure frequency	
G	Mass flux	$kg/(m^2•s)$
g	Gravitational acceleration,	m/s^2
H	Constant	m
h	Heat transfer coefficient	$W/(m^2•K)$
h_{cond}	Condensation heat transfer coefficient	$W/(m^2•K)$
h_{fg}	Latent heat of evapouration	kJ/kg
Ja	Jakob number (dimensionless)	
Ja_e	Effective Jakob number	
Ja_{sub}	Subcooled Jakob number	
Ja_T	Total Jakob number	
Ja_w	Superheated Jakob number	
k	Thermal conductivity	W/(m•K)
L	Physical length of one pixel	µm/pixel
L_o	Laplace length	

l_o	Bubble sliding distance	m
M	A product	
N	Constant	
N_A	Dimensionless active nucleation site density	
N_i	Number of pixels at row i	
N_{qG}	Dimensionless heat flux using bubble departure diameter	
N_{qnb}	Dimensionless nucleate boiling heat flux	
N_{qNB}	Dimensionless heat flux representing nucleate boiling heat transfer	
N_T	Dimensionless temperature	
n''	Nucleation site density	
ΔP	Pressure difference	Pa
Pr	Prandtl number	
P_v	Pressure inside the bubble	Pa
P_∞	Pressure in the liquid	Pa
q	Heat flux	W/m^2
q_B	Heat flux to the bubble from the liquid film	W/m^2
q_c	Heat flux from the condensation layer	W/m^2
q_{nb}	Nucleate boiling heat flux	W/m^2
q_{sl}	Heat flux from the superheated liquid layer,	W/m^2
q_{tf}	Heat flux from the liquid film	W/m^2
R	Bubble radius	m
$\dot{R}$	First order differentiation with respect to time.	m/s
$\ddot{R}$	Second-order differentiation with respect to time.	m/s^2
R^*	Dimensionless radius	
$R_{detachment}$	Bubble radius at the detachment	m
Re	Reynolds number	
Re_b	Bubble Reynolds number	
Re_l	Reynolds number based on the sliding distance	
r_c	Cavity radius	m
s	Area	m^2
T	Temperature	°C
$\overline{T_1}$	Average temperature at the depth of 1 mm	°C
$\overline{T_2}$	Average temperature at the depth of 10 mm	°C
T_n	Temperature of the thermocouple n	°C
T_o	Temperature of the superheated liquid	°C
ΔT	Temperature difference	°C
ΔT_e	Effective wall superheat	°C
ΔT_{ONB}	Required wall superheat for the initiation of nucleate boiling	°C
ΔT_{sub}	Subcooling	°C
ΔT_w	Wall superheat	°C
t	Time	s
t_b	Bubble lifetime	s
t_d	Time between the bubble departures	s
t_g	Growth time	s
t_w	Waiting time	s
t_g^*	Dimensionless growth period	s
t^*	Dimensionless time	
U	Velocity	m/s

U_b	Velocity of the bubble mass centre	m/s
ΔU	Relative velocity between the bubble mass centre and the surrounding liquid	m/s
V	Volume	m^3
x_1	Value of coordinate in the x direction	
y_1	Value of coordinate in the y direction	

Greek symbols

α	Advancing contact angles	°
β	Receding contact angles	°
γ	Circumferential contact angle	°
δ	Thermal boundary thickness	m
η	Thermal diffusivity	m^2/s
θ	Inclination angle	°
μ	Dynamic viscosity	$N•s/m^2$
ν	Kinematic viscosity	m^2/s
ρ	Density	kg/m^3
ρ^*	Density ratio	
$\Delta\rho$	Density difference	kg/m^3
σ	Surface tension force	N
τ_w	Wall shear stress	N/m^2
υ_{fg}	The specific volume difference between liquid and vapour	
φ	Vapour content	
ϕ	The polar angle around the bubble	°
ω	Static contact angle	°
ψ	Non-dimensional subcooling	

Subscripts

f	Liquid
g	Vapour
w	Wall
$bulk$	Bulk liquid
sat	Saturation
ss	Stainless steel

Abbreviations

ANN	Artificial Neural Network
CHF	Critical Heat Flux
CFD	Computational Fluid Dynamics
DAQ	Data Acquisition Systems
EDS	Energy Dispersive Spectrometer
FPS	Frames Per Second
HTC	Heat Transfer Coefficient
ONB	Onset of Nucleation Boiling
PEN	Pre-Existing Nucleus Theory
PID	Proportional-integral-derivative
RTD	Resistance Temperature Detector
RMSE	Root Mean Square Error
SEM	Scanning Electron Microscope
T/C	Thermocouples

Chapter 1 Introduction

This thesis focuses on the investigation of flow boiling at artificial and natural cavities. In this chapter, the definition of boiling and its regimes are introduced in section 1.1. The motivation is introduced in section 1.2. The challenges that need to be addressed by the current research are introduced in section 1.3. This Chapter provides a brief review of boiling without going into the details of the findings of the literature. It was decided that it is easier for the presentation of the research results to include specific literature reviews at the start of each chapter to address the specific topic of the chapter. In this way, the current findings could be linked more directly to the past research and assist the discussion. The contribution of the current research and the thesis outline are presented in sections 1.4 and 1.5.

1.1 What is boiling?

Boiling is a phase change process in which a liquid changes phase into a gas as it absorbs heat. During this process, vapour bubbles are formed either on the heating surface (heater) and/or in a superheated liquid layer adjacent to the heated surface (Kandlikar, 1999).

The most common description of the boiling initiation mechanism is as follows. Miniscule quantities of air or gas embryos are trapped inside physical cracks on the nucleation surface. The embryos grow by the addition of vapour that is generated due to the liquid evapouration process, while the effects of the condensation process close to the wall are relatively weak. Consequently, the embryos develop into bubbles that grow on the nucleation surface. As the bubble evolves, the condensation process is enhanced and gradually becomes dominant. As a result, the bubble size starts to reduce. Therefore, the bubble size increase or decrease is believed to be a competition between local evapouration and condensation close to the nucleation wall. While the forces applied to a growing bubble at the wall remain balanced, the bubble remains attached. When this balance is violated, the bubble may depart from the wall. This process is repeated at multiple locations on the nucleation surface, and the bubbles initiate and evolve at different times. There is also the potential for bubbles to interact on the wall.

1.1.1 Classification

Four types of boiling can be classified based on the bulk temperature and the liquid's motion, shown in Table 1.1.

Table 1.1 Classification of boiling types.

Classification	Boiling Types	
Based on bulk liquid temperature	Subcooled boiling	Saturated boiling
Based on the motion of liquid	Pool boiling	Flow boiling

Subcooled boiling refers to boiling when the bulk liquid temperature is below the saturated liquid temperature. In this case, vapour bubbles experience condensation when moving in the bulk liquid and may collapse before reaching the free surface; see Figure 1.1 (a). Saturated boiling refers to boiling when the bulk liquid temperature is equal to the saturation temperature of the liquid; see Figure 1.1 (b). In this mode, the bubbles do not experience condensation effects. Both cases are associated with a stationary liquid, which is termed pool boiling, which occurs in the absence of bulk liquid flow. Natural convection currents impart motion to the bulk liquid during this boiling mode. As such, in pool boiling, the effect of buoyancy on bubble motion is significant.

Flow boiling refers to boiling in the presence of forced bulk liquid flow by external means. In flow boiling, the liquid is forced along a solid heater surface. Flow forced convection plays a significant role in flow boiling; nevertheless, the dynamics of the liquid flow around bubbles and their effects on local heat flux have not been established as well as those in pool boiling. This is because of the difficulties in obtaining such measurements. For example, there is a need to have a forced flow boiling device with optical access to allow for high-speed optical measurements. In addition, if many bubbles are generated simultaneously on the nucleation surface, it is difficult to observe their behaviour, and the process is even more complex if the bubbles interact with each other. The current study's experiments will focus on subcooled flow boiling conditions.

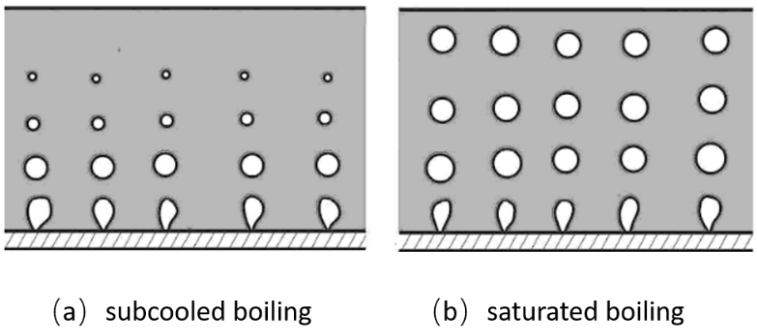


Figure 1.1. Effects of the liquid temperature on boiling (white refers to the vapour, grey refers to the liquid) (Faghri, Zhang & Howell, 2010).

1.1.2 Boiling regimes

Several boiling regimes have been proposed for pool and flow boiling. A typical saturated pool boiling curve, the Nukiyama curve, for water at atmospheric pressure with temperature

control is shown in Figure 1.2. The horizontal axis refers to the superheat, defined as T_w-$T_{sat,}$ where T_w is the heater surface temperature, T_{sat} is the liquid saturation temperature at a specific pressure, and the vertical axis refers to the heat transfer rate through the solid heater surface. With the increase of the superheat, four regions, separated by the dashed lines, are identified in Figure 1.2, namely Region I (Natural convection boiling), Region II (Nucleate boiling), Region III (Transition boiling), and Region IV (Film boiling). These regions were proposed by previous researchers such as Nukiyama (1934) and Farber & Scorah (1948).

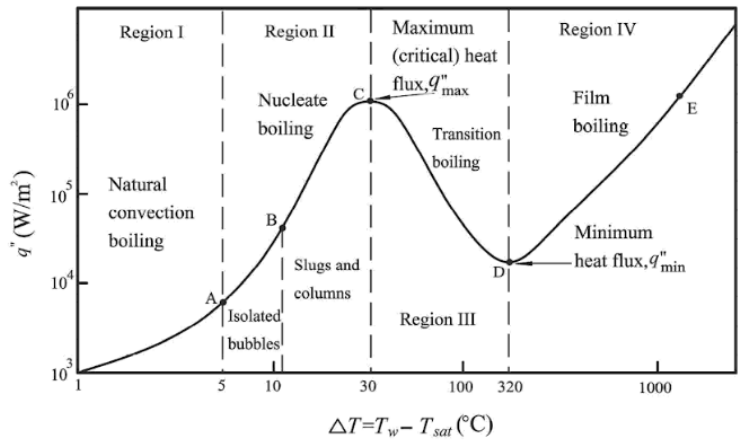


Figure 1.2. Pool boiling curve for saturated boiling (Faghri, Zhang & Howell, 2010).

In Region I, the superheat temperature is lower than 5 °C. However, no bubbles are formed. The liquid is heated by natural convection, where the heat transfer rate is nearly linearly proportional to the superheat (Tong, 2018). When the superheat temperature exceeds 5 °C, the systems enter Region II (nucleate boiling). Bubbles tend to form at different cavities or scratches on the heated surface. These cavities, where the bubbles are formed, are called nucleation sites. An increased heat transfer rate is observed in this region because the bubbles transfer energy away from the surface via latent heat due to the phase change from liquid to vapour. The convective heat transfer also increases by the departing bubbles' agitation of the surrounding liquid. The heat transfer rate is high in this region, even though a small superheat temperature is present. In addition, the heat transfer rate grows non-linearly with superheat temperature.

In Region II, when a bubble detaches from the nucleation site, the surrounding liquid can freely occupy the volume occupied by the departing bubble. However, with the increase of the superheat temperature, more bubbles are formed on the heater surface, and the departing bubbles may obstruct the path of the incoming liquid. Consequently, the vapour bubbles may form an insulating vapour layer on the heater surface (vapour has smaller thermal conductivity than liquid), reducing the heat transfer rate. The maximum heat transfer rate nucleates boiling can achieve is critical heat flux. Point C of the curve refers to the critical heat flux point. The critical heat flux can be achieved in pool and flow boiling (Tong, 2018).

Increasing the critical heat flux or reducing the wall superheat at the critical heat flux is valuable for protecting the physical integrity of the heat transfer surface and operational safety.

In Region III, the heater surface is alternately covered by a vapour blanket or a liquid layer, resulting in a fluctuating surface temperature. This region is called the transition region, as boiling becomes unstable. If the same heat flux input is maintained at the heater surface, the temperature of the heater surface will increase rapidly, and the heat transfer rate will steadily decrease to a minimum point D of the curve. In Region IV, the heater surface is steadily covered by a vapour film. In this region, the heat transfer rate increases from its minimum value (point D) due to thermal radiation from the heater surface as the surface temperature increases. The heater surface material can be damaged if the surface temperature exceeds material tolerances (burnout). Hence, the heater surface temperature is limited by the material of the heater surface (Tong, 2018).

The above four regions may also exist in flow boiling, but the mechanisms of heat transfer and bubble dynamics become more complicated. The only difference between flow and pool boiling lies in the influence of the flowing liquid (Tong, 2018). The buoyancy effect on bubble behaviour is significant in a pool boiling system, while the flow forced-convection effect is significant in flow boiling. For instance, the flow shear may contribute to the removal of bubbles from the nucleation sites and thus reduce the average bubble sizes with an increasing bubble departure frequency.

1.2 Motivation

Nucleate boiling is most desirable in industrial applications due to the relatively high heat transfer rates achieved with low heater surface temperatures (Faghri, Zhang & Howell, 2010). It provides an efficient method of heat removal from heated surfaces and is common in electronic cooling applications as well as large-scale nuclear reactors (Thorncroft, Klausner & Mei, 1998; Kandlikar, Steinke & Balasubramanian, 2002; Hibiki & Ishii, 2009; Brooks, 2014; Klausner et al., 1993). Understanding the physical mechanisms of nucleate boiling at the microscopic scales of the heater surface is of great importance for performance improvement of boiling heat transfer systems (Brooks & Hibiki, 2015).

The computational approach of nuclear systems relies on Computational Fluid Dynamics (CFD) simulations. The experimental studies are helpful for the development of new CFD modelling approaches and for the improvement of the performance of existing models. The boiling heat flux is required in these models. The boiling heat flux suggested by Kurul & Podowski (1990) consists of three parts: (i) the latent heat of evapouration to form the bubbles, (ii) heat expended in the re-formation of the thermal boundary layer following

bubble departure, or the so-called quenching heat flux and (iii) heat transferred to the liquid phase outside the zone of influence of the bubbles by convection. The latent heat flux is expressed by equation (1.1).

$$q = \frac{\pi}{6} D_b^3 \rho_g h_{fg} f_d n'' \tag{1.1}$$

where D_d, ρ_g, h_{fg}, f_d and n'' refers to the bubble departure diameter, vapour density, latent heat, the frequency of bubble departure, and the nucleation site density, respectively. The cubic dependence on bubble diameter in equation (1.1) suggests that the bubble departure diameter greatly affects the latent heat flux. In addition, accurate bubble departure diameter data and models are essential for ensuring accurate CFD simulations of boiling.

1.3 Flow boiling unknowns and their challenges.

Flow boiling is a complex phenomenon affected by many factors, which can be found in the literature, such as in Dadhich & Prajapati (2019) and Mohanty & Das (2017). Detailed reviews will be provided in the relevant chapters. This thesis is trying to improve the understanding missing from the literature behind some issues and possibly assist the design of nucleation surfaces to deliver improved performance during boiling heat transfer.

The first unknown is how the geometry of the nucleation cavity affects boiling performance. It is known that nucleation cavity geometry can affect boiling dynamics. Examples can be found in Kang & Wang (2018) and Baldwin, Bhavnani & Jaeger (2000). A detailed review of the findings is reported in section 3.1. However, the way the nucleation sites affect bubble formation is unclear despite the extensive literature focusing on boiling at natural cavities. Most of these boiling studies are focused on natural cavities whose geometries are unknown. Therefore, the effect of natural cavity geometry on boiling is still not understood and needs further investigation.

The second unknown that requires further investigation is the interaction between bubbles on the nucleation surface. For intensive boiling, interactions between neighbouring bubbles exist and affect bubble characteristics through hydrodynamic and thermal interactions (Shoji et al., 2002) since the growth of a single bubble is affected by surrounding bubbles. Although more information may be available for pool boiling, the interaction between bubbles during flow boiling requires further effort to deliver the necessary understanding.

The third unknown is the physical description of the mechanism responsible for boiling initiation. The most popular mechanism described in the literature is the pre-existing gas embryo in a cavity, which is trapped air inside a naturally occurring physical crack on the nucleation surface. This mechanism is reported by Dinh et al. (2003) and is based on the presence of a physical crack and its geometry. However, experimental observations of the

shape and size of physical cracks cannot be found in the literature. In addition, this mechanism cannot explain all observations. Thus, other mechanisms are hypothesised to explain the process, including a mechanism based on nanobubbles on the surface (Tyrrell & Attard, 2001; Lou, Ouyang & Zhang, 2000). However, nanobubbles have not been experimentally observed on surfaces. Therefore, the observation of physical cracks on the surface is necessary before the proposed gas embryo mechanism can be supported better. The same applies to the observation of nanobubbles. However, there is no available method that can locate natural cavity positions and, therefore, the ability to characterise the geometry of natural cavities and link the geometry of the natural cavities with the generated bubbles is missing.

The fourth unknown is the effects of cavity spacing, diameter, depth and operating conditions on bubble characteristics. Limited literature found that artificial cavities have advantages in reducing local pressure fluctuations and the initiation temperature of boiling and formation of bubbles (Kuo & Peles, 2008, 2007), which could lead to more beneficial heat transfer processes and applications. In addition, the literature suggests that artificial cavities may increase the critical heat flux, and an example can be found in Baldwin, Bhavnani & Jaeger (2000). However, there is limited understanding of the mechanism behind such observations/suggestions. Therefore, the ability to design and manufacture heat transfer surfaces with artificial cavities is missing, and a new understanding of flow boiling at single artificial cavities is required. In addition, the optimum design of nucleation surfaces for boiling heat transfer requires an understanding of the effects of cavity depth, diameter, operating conditions and bubble interactions on the surface. Such studies are missing from the literature, and this thesis will also study the behaviour of artificial cavities during flow boiling.

1.4 Present contribution

The previous section summarised the main issues that require a new understanding of boiling heat transfer and demonstrated that the available information in the literature for flow boiling is mostly limited to natural sites for which it has not been possible to establish their geometry. However, there is evidence that cavity geometry affects the bubble characteristics. In addition, the interaction of bubbles on the nucleation surface of practical applications is a significant factor that can influence heat transfer.

The existing limitations in understanding and the complexity of the underlying physics led to a study of the boiling process based on one or two artificial cavities on a nucleation surface. This approach allowed the study of the generated bubbles at the microscale. The experimentation was performed at a specially designed experimental facility where the

operating conditions are controlled for well-defined artificial and naturally occurring nucleation sites. A comparison between the bubble characteristics from known geometry artificial sites and natural cavities is provided. The research of this thesis provided novel contributions in four areas, as summarised below.

Firstly, the effects of cavity geometry on bubble characteristics and boiling heat transfer are investigated, and results at artificial and natural cavities at the same operating conditions are compared. An achievement of this thesis is the development of a method that allows the identification of the exact location of natural cavities. This allows the characterisation of natural cavity geometries and the development of a correlation between natural cavity geometry and bubble characteristics. In addition, two types of natural cavities are identified, and their influence on bubble nucleation is established.

Secondly, the effects of operating conditions on bubble characteristics are investigated, and the results quantify how the bubble characteristics change under various conditions. A dimensionless equation is proposed to fit bubble growth profiles for most cases investigated. The previously proposed correlations predicting the bubble departure diameter and frequency based on dimensionless parameters representing the various experimental conditions are assessed with the current results. In addition, a new model, based on the balance of forces on a boiling bubble attached to the wall, is proposed that predicts the bubble departure diameter well. The bubble departure diameter, frequency and profile can be predicted by input experimental conditions only into the above correlations.

Thirdly, the effects of cavity depth, diameter, interaction of bubbles from multiple cavity spacings and effects of experimental conditions at a fixed spacing are investigated. The way that the two bubbles evolve and interact is a novel contribution of this thesis and is important for the assessment of the heat transfer characteristics of practical nucleation surfaces. The results for multiple cavities evaluate possible approaches to design novel heat transfer surfaces with numerous artificial cavities. Such designs may expand the safe operational range of such surfaces by increasing their critical heat flux.

Fourthly, the thesis contributes to the improved understanding of the mechanism that initiates bubbles at nucleation cavities, either artificial or natural sites. It provides, for the first time, experimental evidence supporting the suggested gas embryo mechanism found in the literature. In addition, it provides new insights into the bubble growth mechanism during flow boiling.

These contributions are expanded in the rest of the thesis. The following section provides an outline of the thesis.

1.5 Thesis outline

The thesis consists of 7 chapters in total. Apart from the current chapter, the rest of the thesis is structured as follows.

Chapter 2 presents the experimental arrangement that has been used for the flow boiling studies of the current thesis. All the preparatory work to ensure the appropriate operation of the rig is detailed. This includes the rig design, calibration of instruments, experimental procedures, wall temperature estimation, optical configuration, and image processing algorithms for different quantities, including the bubble diameter estimation. Finally, an uncertainty analysis of all contributing factors to the measurement of bubble diameter is presented.

Chapter 3 shows a qualitative comparison of the behaviour of bubbles that are generated at artificial and natural sites on the nucleation surface during flow boiling under an identical operating condition. In addition to that, patterns formed downstream of cavities, and two types of natural cavities found are reported.

Chapter 4 reports the temporal evolution of bubble growth for different experimental conditions. The available information in the literature on bubble characteristics is summarised. Existing models in the literature for bubble characteristics are presented and compared to the experimental data of this thesis. A well-defined dimensionless equation is proposed that fits the data of this study well.

Chapter 5 defines dimensionless parameters, including dimensionless bubble diameter and frequency, and correlates the results for the different operational conditions of Chapter 4 using these parameters. In addition, a bubble force balance model is developed for the bubble departure diameter, which demonstrates good ability to describe the measurements.

Chapter 6 presents the effects of the diameter and depth of single artificial cavities on bubble characteristics. Since bubble interactions are inevitable on nucleation surfaces during boiling, this chapter extends the study to multiple artificial sites and understands bubble interactions on surfaces. The cavity spacing on bubble interaction is considered. The heat transfer ability from the surface to the bubbles is estimated for different cavity spacings to identify the most efficient geometry. In addition to these, the effect of operational conditions on the bubble characteristics generated from two artificial sites at a fixed spacing is reported.

Chapter 7 completes the thesis, presents the main findings of the research, and provides recommendations for future work.

Chapter 2 Experimental methodology

This chapter introduces the design of the experimental water flow boiling facility, which includes a channel flow that delivers a conditioned fluid flow to a test section, a heated wall where boiling is initiated, instrumentation for wall temperature measurements, control of the water flowrate, wall temperature and heat flux. It also describes the temperature estimation method, associated uncertainties and the calibration of instruments, including the liquid flowmeter and thermocouples. It introduces the imaging system that includes a high-speed camera and associated optics for the time-dependent recording of the bubble formation and growth during boiling. The experimental procedure for characterising the bubbles is explained, including the custom-made image processing algorithm for identifying the bubble boundaries. Therefore, the methodology for the quantification of the equivalent bubble diameter and the advancing and receding bubble contact angles on the wall is detailed, and the associated uncertainties are estimated.

2.1 Experimental rig

The research requires investigating boiling at stable boundary conditions, i.e., where the water flowrate, water temperature, wall temperature and heat flux are kept stable throughout. To achieve this aim, a novel experimental rig is designed (the schematic of the complete rig is shown in Figure 2.1). A photo of the complete rig with indicated equipment is shown in the Figure 2.2.

In Figure 2.1, the deionised water, as the working fluid, is stored in an overhead tank (gravitational tank), from where it flows to the test section through branch 1 (represented by a red line) and then returns to the overhead (gravitational) tank placed at a height of 2.5 m through branch 3 (represented by a blue line). The level tube (length of 20 cm), positioned upright, maintains the level of water (and hence hydrostatic pressure) in the overhead tank by continuously draining excess water delivered from the collection tank back to the collection tank through branch 2 (represented by a green line).

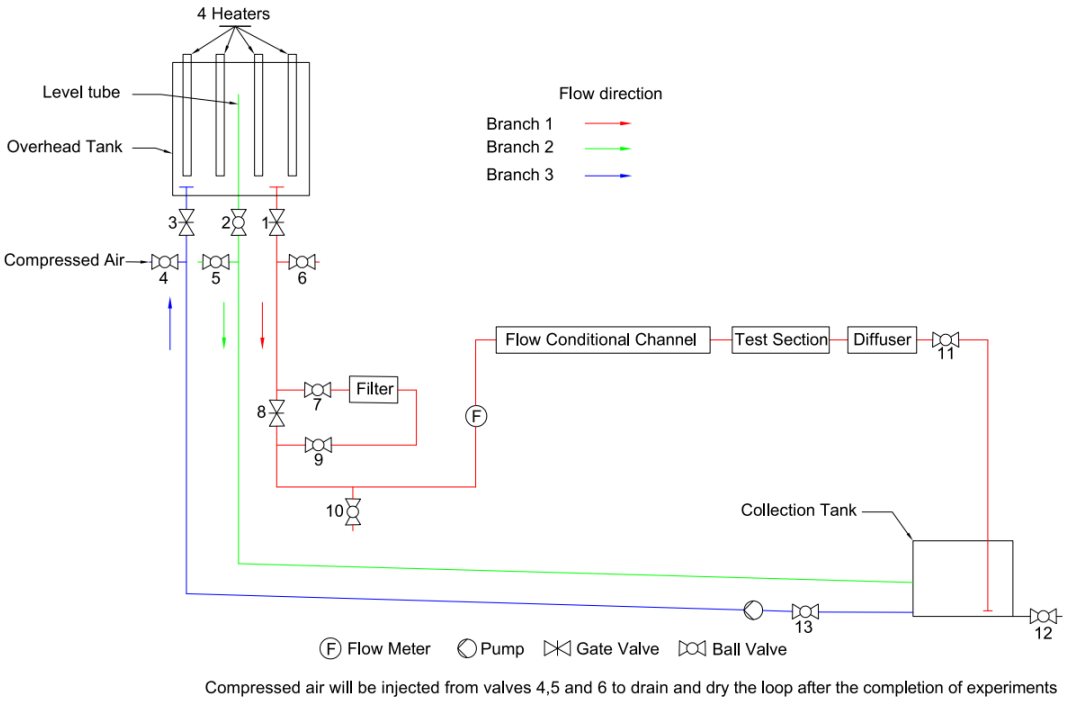


Figure 2.1 Schematic of the complete rig (not to scale).

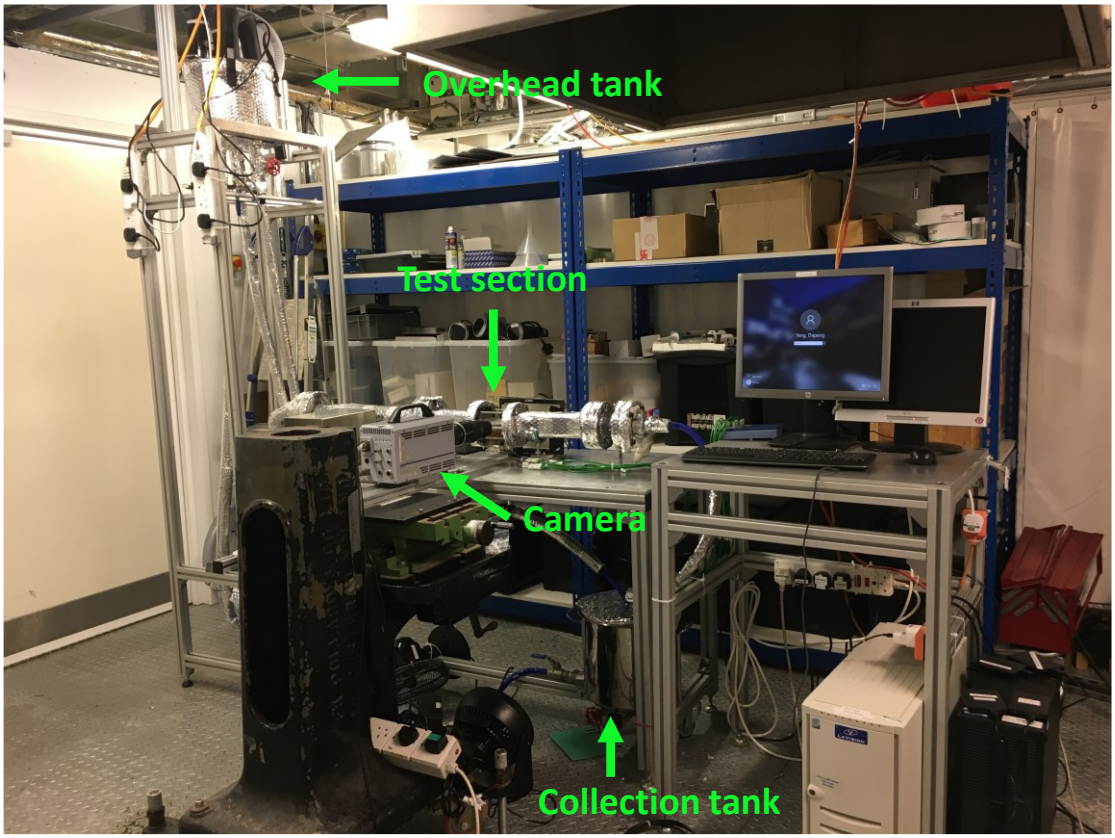


Figure 2.2 A photo of the complete setup.

In the overhead tank, four heaters keep the water temperature to a desired value. To reduce heat losses along the tubing system, branch 1 and a major part of branches 2 and 3 are insulated with calcium-magnesium silicate thermal insulation sheets and bubble foil

insulation. The remaining parts are not insulated intentionally to facilitate more agile thermal control of the hot branches in the absence of an active heat rejection system. In branch 1, a filter with a 5-micrometre cartridge is utilized to remove impurities. After experimentation, compressed air is injected into the rig through valves 4, 5, and 6 to drain the remaining water and dry the rig, hence avoiding potential organic growth formations. To minimize corrosion of the functional elements in contact with water, the materials utilized in the whole rig are stainless steel, silicon rubber, anodised aluminium, and high-temperature resins (named 'FLHTAM02').

Table 2.1 provides a detailed list of all the components of the experimental rig. The specifications of the components listed are determined by experimental conditions.

Table 2.1 List of components of the experimental rig

Items	Model or Supplier	Specification
Mini water pump	JT-660B-24	Input:12 V-24 V 500-1000 LPH -40 ℃ ~100 ℃
Variable area flowmeter	1750S	1.5-15 LPM 100 ℃
Thermal immersion circulator (heater)	Sous vide cooker	Temperature range: 25-95 ℃ Temperature variance: ± 0.1 ℃ Power:1000 W
Heat reflective foil (insulation)	Superfoil	Reflect 95 % of heat back
Overhead tank	Buckingham	Stainless steel 15 litres (29 x 29 x25 cm)
Collection tank	Geezy	Stainless steel 21 Litres

The maximum operating water temperature in the rig is 95 °C. Thus, the selected components were chosen to tolerate up to 100 °C. The maximum flowrate range is determined by the height of the overhead tank (i.e., the pressure head) and the flow resistance (i.e., pressure losses due to the flow of water in the system). The system is open to the atmosphere at the collection tank. The insulation foil is wrapped at the outside of tubes and instruments to reduce heat loss. Thermal immersion circulators with built-in proportional-integral-derivative (PID) controllers and in-tank water circulation pumps have been chosen due to their stable performance in temperature maintain. The size of the tank is limited by the physical space. The volume of the collection tank is larger than the overheat tank to ensure adequate capacity for storing all of the water in the system during experimentation downtime.

Figure 2.3 shows the cross-section of the flow conditioning channel, test section and diffuser. The water flows through a flow conditioning section, which then feeds it to the transparent test section, followed by the final diffuser flow section.

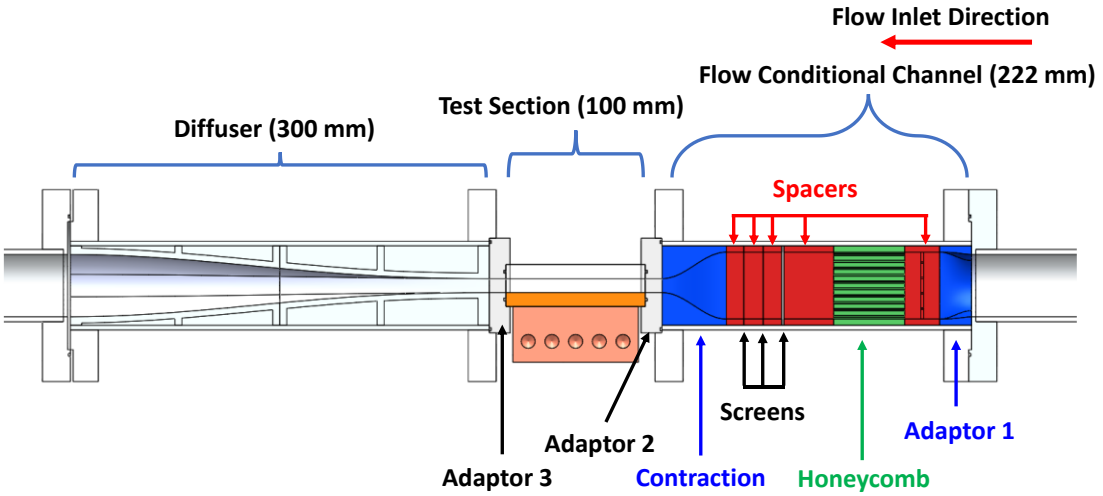


Figure 2.3 Cross section of the flow conditioning channel, test section and diffuser.

The flow conditioning section consists of a circular to rectangular cross-section flow adaptor, honeycomb, spacers (red parts), screens, and a contraction part; see Figure 2.3. The design of the conditioning channel and its dimensions are based on the design guidelines provided in published literature for wind tunnel designs (Mehta & Bradshaw, 1979; Cattafesta, Bahr & Mathew, 2010; Morel, 1975). The honeycomb section downstream of the flow adaptor has a representative dimension of 57 x 57 mm with a length of 51 mm that is long enough to remove the remaining swirling or lateral flow velocity components of the liquid flow. The screens were made of a wire mesh, each with individual cell sizes of 0.12 x 0.12 mm^2, 1 x 1 mm^2 and 3 x 3 mm^2, which provided enough uniform blockage to the incoming flow to remove longitudinal non-uniformities across the channel flow. The contraction accelerates the conditioned liquid flow to suppress the boundary layers close to the channel walls and ensure that a uniform velocity profile is generated at the exit of the contraction. The cross-sectional area ratio of the entrance to the exit of the contraction is 7.68, which is according to the guidelines found in the literature. The area ratio combined with the appropriately design shape of the contraction ensures that the accelerated flow through the contraction exits with a 'top-hat' uniform flow at the entrance of the test section. The diffuser, test section and the conditioning channel shown in Figure 2.3 are at the orientation of upward facing. The orientation is changed to downward facing in some cases in this project.

The test section consists of an optical U-shaped quartz glass cover, a stainless-steel substrate and a copper block holding five cartridge heaters in blind holes, see Figure 2.4.

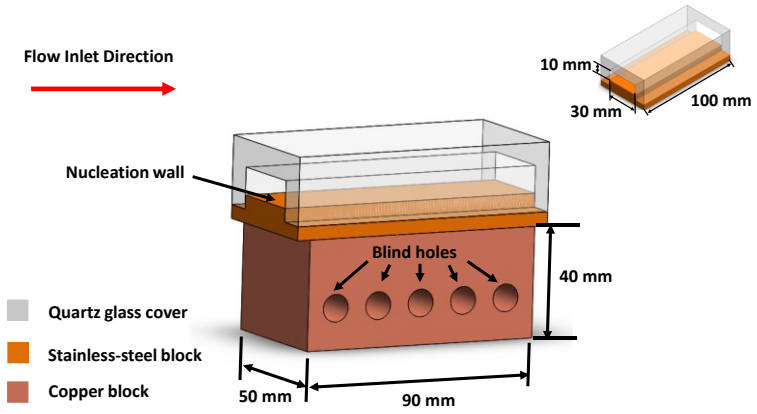


Figure 2.4 Isometric view of the test section.

The flow channel consists of the glass cover and the heated substrate with a cross-section of 30 x 10 mm and a length of 100 mm. This maintains the boundary layer of the flow laminar over the entire length of the channel under the flow conditions tested, and therefore, the liquid flow interacting with the bubbles was well defined.

Due to its high thermal conductivity, the copper ensures uniformity of temperature across its interface with the stainless-steel block containing the cartridge heaters. The copper and stainless-steel blocks are mounted together. Thermal paste is used in the interface between the copper and stainless-steel block to reduce interfacial thermal resistance effects. The outer surfaces of the metallic blocks (those not in contact with the flow) are thermally insulated.

Downstream of the test section, a diffuser is placed to recover the static pressure in the test section and to avoid any turbulent flow effects to vary the downstream pressure that might affect the upstream flow through the test section. The length of the diffuser was 300.39 mm, and the cross-sectional area ratio of the entrance to the exit was 0.148. These dimensions were selected according to the guidelines from the literature.

2.2 Experimental procedure

The bubble characteristics at specially designed artificial nucleation sites and natural sites are studied based on time-dependent captured bubble images at a controlled “steady” state, which is achieved by following procedural steps. Before the image recording, the following actions are taken.

- STEP 1: deionized water is transferred to the collection tank (see Figure 2.1).
- STEP 2: Then, the pump transfers water into the overhead tank. Once the water in the overhead tank reaches the desired level, it passes through the test section by flowing through branch 1 (see Figure 2.1).
- STEP 3: After a flow is established, all heaters in the overheat tank are switched on to raise the water temperature to a desirable value. In the meantime, the temperature readings of all thermocouples start to be recorded.

- STEP 4: When the desired water temperature is reached, the five cartridge-heaters underneath the test section are operated to raise the temperature of the nucleation wall. Around 2.5 hours are required to achieve a steady desired temperature at the nucleation wall. The recorded data at the stable state are utilized for heat flux and wall temperature estimation.

It is found that a slight overpressure rather than under pressure of the test section prevents the air leakage from entering the test section through micro-imperfections/movements due to thermal expansion at the sealing points of the quartz U-shaped section onto the heated substrate (a part that frequently needs to be accessed to allow cleaning and switching of the nucleation side area). The overpressure is negligible, with the test section operating near atmospheric pressure for the experiment. The sealing points are away from the area of interest, and the strategy followed does not affect the remaining boundary conditions of the experiment. Even though the sealing points are away from the observed area, the presence of static air bubbles at these locations obstructs the line of sight of the camera and the observed area, which is of critical importance.

The bubble images are recorded when the temperature profiles of all thermocouples are stable for at least 15 mins. Figure 2.5 shows the temperature evolution of all thermocouples for a typical run whilst following the procedures detailed. The locations of all thermocouples are shown in Figure 2.6. It is found that the water temperature (measured by thermocouple 1 named T/C 1 gradually increases to around 94 °C. At the time of 1.56 h after the initialisation of the start-up sequence of the experiment, the heater underneath the nucleation wall is operated, and thus, the temperature at a depth of 1 mm and 10 mm measured from the substrate surface facing the water jumps. The temperatures of T/C 3&4 and T/C 5&6 remain at ~110 °C and ~120 °C respectively thereafter.

After the completion of the bubble image recording, all heaters are switched off while the pump is kept running for several hours to cool the rig down. The water in the rig is drained, and compressed air is circulated through the rig to dry it and hence avoid potential organic growths between non-continuous experimental excursions.

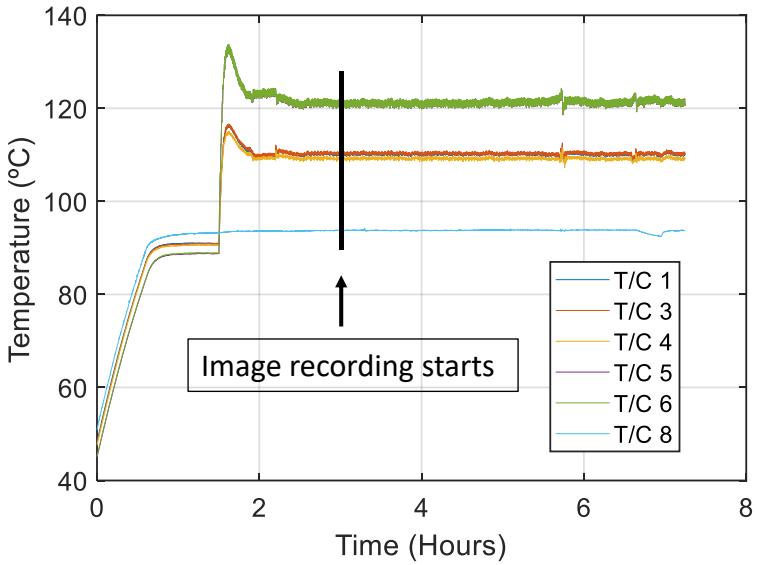


Figure 2.5 Temperature temporal evolution for all thermocouples in one case.

2.3 Wall temperature estimation

The average nucleation wall temperature is estimated by extrapolating the one-dimensional heat transfer equation from temperature measurements at two depths underneath the nucleation surface. Respectively, four and two thermocouples measure the temperature at a depth of 1 mm and 10 mm beneath the nucleation surface. The positions of the thermocouples located at the depth of 1 mm and 10 mm are marked in Figure 2.6 with red and green circle dots, respectively. The wall temperature is controlled by a PID controller regulating the heat generation from the five cartridge heaters. T_n represents the average reading over 10,000 seconds for thermocouple n.

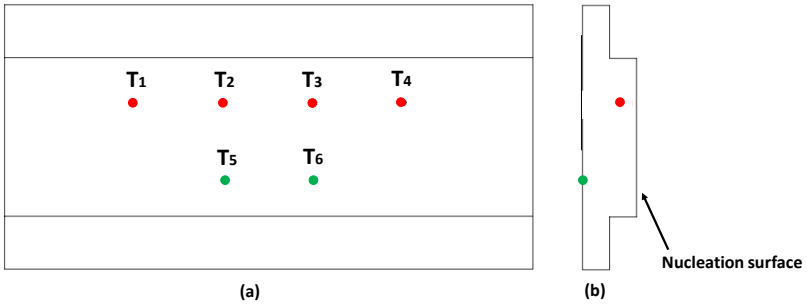


Figure 2.6 Positions of the thermocouples (represented by red and green dots) from the top view (a) and side view (b).

The wall temperature and heat flux are calculated based on the temperature readings of these thermocouples in conjunction with the evaluation of the one-dimensional steady-state Fourier conduction equation. $\overline{T_1}$ and $\overline{T_{10}}$ represent the average temperature at depths 1 and 10 mm, respectively, which are calculated through Equations (2.1) and (2.2). T_2 is connected to the PID controller to adjust the input heat flux. Thus, its reading is not utilized for the estimation of the average value.

$$\overline{T_1} = \frac{T_1 + T_3 + T_4}{3} \tag{2.1}$$

$$\overline{T_{10}} = \frac{T_5 + T_6}{2} \tag{2.2}$$

$$T_w = \overline{T_1} - (\overline{T_{10}} - \overline{T_1})/H \tag{2.3}$$

$$q = k_s * (\overline{T_{10}} - \overline{T_1})/H \tag{2.4}$$

Wall temperature (T_w) and heat flux (q) are calculated from equations (2.3) and (2.4), respectively, where H = 9 mm, represents the distance between the two depths of the thermocouple planes and k_s refers to the thermal conductivity of the stainless steel 316L, which is 15 W/(mK).

The water temperature at the outlet of the test section is measured by embedding a thermocouple inside adaptor 3; see Figure 2.3. The effects of heat input from the substrate heaters on the water temperature close to the channel top wall are negligible. This is proved by Figure 2.5, which shows that the temperature readings of T/C 1 have no obvious change when the substrate heaters are operated.

2.4 Surface roughness characterisation

The roughness value affects the boiling heat flux (Bui & Dhir, 1985); thus, the same polish procedures of the surface are kept. The exact value of the surface roughness is measured with the equipment introduced in section 2.4.1, and the values are reported in section 2.4.2.

The nucleation wall is polished with sandpaper in the following sequence: P600, P1200, P2500 and a diamond suspension (size of 3 and 1 μm) in sequence. The surface roughness was quantified by a Laser Microscope OLS5000 at a magnification of 50X. The mean roughness value ranges from 6 nm to 49.5 nm. Therefore, this surface acted as the boiling nucleation wall with a small number of remaining surface imperfections that acted as natural nucleation sites for boiling.

2.4.1 Measurement equipment

The surface roughness of the nucleation wall substrate is measured by an OLS5000 3D Laser Confocal Microscope, whose image and specification are shown in Figure 2.7 and Table 2.2. The resolution of the images is ~200 nm and 6 nm in lateral and vertical directions, respectively.



Figure 2.7 Image of the microscope OLS5000 used for the measurements of the surface roughness of the nucleation wall.

Table 2.2 Specifications of the microscope OLS5000 used for the measurements of the surface roughness of the nucleation wall.

Model		OLS5000-SAF
Height measurement	Accuracy	0.15+L/100 μm (L: measuring length[μm])
	Resolution	200 nm
Width measurement	Accuracy	Measurement value ± 1.5 %
	Resolution	6 nm

2.4.2 Surface roughness measurements

The height profile along four lines on a random square area (258 μm in dimension) of an image of each nucleation surface is measured. Figure 2.8 shows an example pattern of four measured lines on an image of a nucleation surface. The value of the surface roughness (Ra) along each line is measured, and the mean value along all lines is calculated to obtain the Ra of each nucleation surface. The mean Ra ranges from 6 nm to 49.5 nm for all nucleation walls used in this research, which is generally considered low.

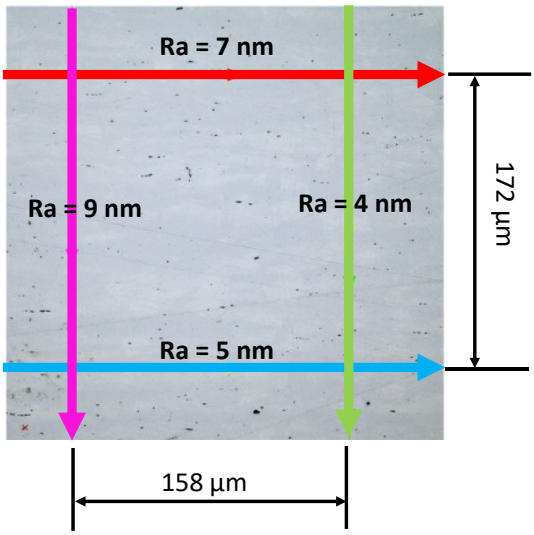


Figure 2.8 Four measurement lines on an image of the surface of a nucleation wall; the mean of the measured values along the four lines represents the measured surface roughness.

2.5 Imaging system: optical configuration and the frame rate setting

The bubble characteristics are recorded by an imaging system, which includes a high-speed camera and an illumination source. A sketch of the imaging system is shown in Figure 2.9. A high-speed camera is placed normally to the flow direction to record images of the boiling bubbles as they are initiated on a nucleation site through the side wall of the test section. A backlight source is on the opposite side of the test section. In this way, time-dependent shadow images of the bubble growth on a nucleation site inside the test section can be captured by the camera. The light source and the combination of the lens are shown in Table 2.3. Various lenses are combined to fit the bubble in the middle of the field of view with a clear edge. The spatial resolution of the imaging system is introduced in section 2.7.2.

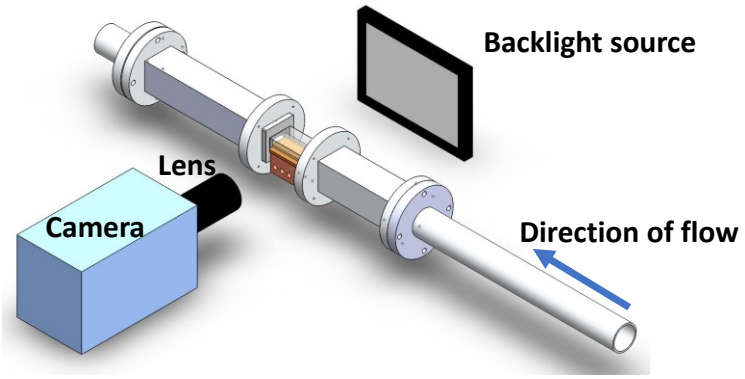


Figure 2.9 Imaging system.

Table 2.3 Information of the high-speed camera and lens

Equipment name	Model
Camera	FASTCAM SA 1.1 675K-M1
Backlight source	YN300 III
Lens in an installation order (from the camera sensor and outwards)	N-Afs 2X Teleplus MC7 + Micro-Nikkor 105 mm 1:4 215839 + AC508-180-A+AC508-300-A

To capture complete ebullition cycles, various imaging frequencies, in units of Frames Per Second (FPS), are selected according to the time scale of the physical phenomena, available camera memory and temporal resolution. For example, at the artificial cavity, 50 and 1000 FPS are selected for the growth and lift-off moment because the growth time is in the range of 20 to 493 s and a high spatial resolution of 1024 x 512 pixels is required to capture a relatively large physical field of view during the lift-off moment. However, at natural sites, the complete ebullition cycles are of the order of hundreds of milliseconds. Thus, a high image recording rate, for example, 5400 FPS, is selected. In this study, the artificial cavity refers to a blind drilled hole on the heating substrate, and the natural site represents natural cracks on the surface. Detailed information on the artificial and natural site geometries is introduced in section 3.2.

2.6 Image processing algorithm

Following the descriptions of the previous sections, the appropriate imaging system is setup, and the optimised bubble images are acquired during the measurements. These images must be processed to quantify the bubble characteristics. Therefore, the image processing approach is described in this section.

The captured raw images are saved in a ‘tiff’ file format, and the light intensity is recorded with 2^{16} steps. The images are processed by MATLAB R2022a according to the following steps. Figure 2.10 shows an example of processed images at each processing step.

A raw bubble image, shown in Figure 2.10 (a), is imported. The bubble edge is detected by function ‘edge’ using the ‘canny’ approach (Canny, 1986), and the outcome is shown in Figure 2.10 (b). This method detects the edge according to the local maxima of the gradient of intensity on the image. The detected edge is cropped at a line representing the nucleation surface, see Figure 2.10 (c), and the enclosed area is filled, see Figure 2.10 (d). After that, denoising is applied. The final bubble shape is obtained in Figure 2.10 (e), and it is used for the calculations of all characteristics, such as the equivalent bubble diameter and inclination angle.

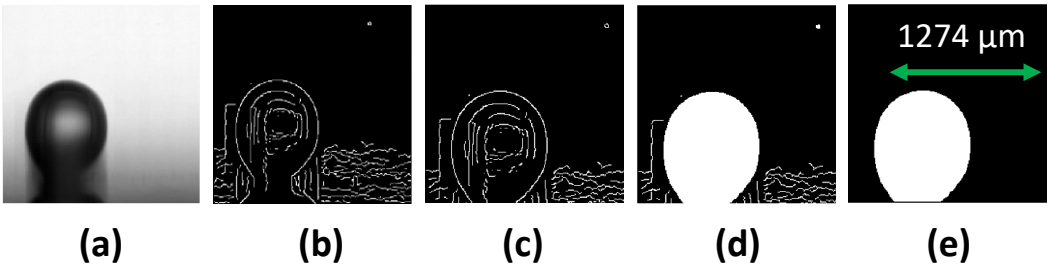


Figure 2.10 Steps used for the image processing of the captured bubble images.

Challenges exist in detecting the bubble edge at the base area where an indistinct edge is captured by the imaging system; see Figure 2.11 (a). A broken edge is the output after the processing; see Figure 2.11 (b). For these images, the function 'bwconvhull' is utilized to close off the broken edge with a straight line, see Figure 2.11 (c). This function is only applied for bubbles lifting off from a natural site. For bubbles initiated from the artificial cavity, images with indistinct edges are discarded since enough alternative images are available to provide appropriate statistics.

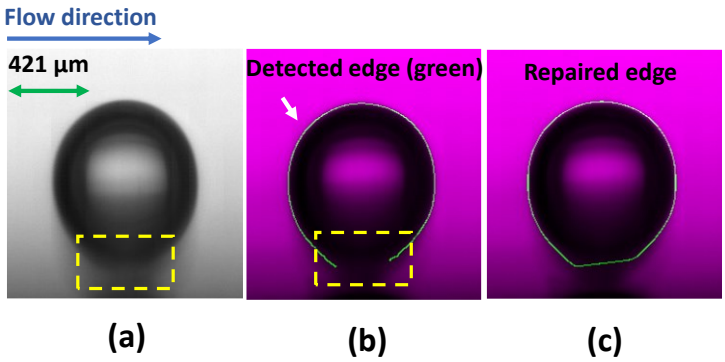


Figure 2.11 Example of (a) indistinct bubble edge in the raw image, (b) detected broken edge and (c) repaired edge when such raw image is considered. This is mainly used for bubbles initiated from natural nucleation sites, for which cases a limited number of images are available.

2.7 Calibration of instrumentation and uncertainty estimation

The wall temperature, liquid flow rate and the spatial resolution of the imaging system are important experimental parameters that affect the reported results. The relative uncertainty of these parameters propagates to parameters such as the heat flux, bubble size, and forces applied to the boiling bubbles. As such, there is a need to have confidence in the instrumentation. Therefore, calibration is performed to establish the capability of the flowmeter, thermocouples and high-speed camera. The uncertainty propagation equations (Moffat, 1988) are introduced in section 2.7.1.

2.7.1 Relative uncertainty estimation

If a product M can be expressed by the calculation of independent elements of X_1 and X_2, see equation (2.5). This approach was proposed by Moffat (1988) and accepted in literature

(Ho, Wong & Leong, 2016; Zhou et al., 2020b; Yoo, Estrada-Perez & Hassan, 2014; Das, Das & Saha, 2009) based on assumptions that repeated measurements of each element follows a gaussian distribution. Then, the overall relative uncertainty of the product M, $\frac{\delta M}{M}$, can be calculated based on the relative uncertainty of X_1, $\frac{\delta X_1}{X_1}$ and X_2, $\frac{\delta X_2}{X_2}$ through equation (2.6). This method is also applied to the overall uncertainty estimation in section 2.9. This approach is utilized to estimate the relative uncertainty of the physical resolution, flow rate and the bubble diameter.

$$M = X_1^a X_2^b \tag{2.5}$$

$$\frac{\delta M}{M} = \left\{ \left(a \frac{\delta X_1}{X_1} \right)^2 + \left(b \frac{\delta X_2}{X_2} \right)^2 \right\}^{1/2} \tag{2.6}$$

An example of the utilization of this equation is mentioned in section 2.7.2, where the relative uncertainty of the physical resolution is obtained.

2.7.2 Calibration of the high-speed camera

The physical length of one pixel of the focal plane represents the spatial resolution of the imaging system. Its value is determined by the combination of the camera sensor and the specific optical system used (this is described in Table 2.3).

The spatial resolution (L) is estimated by dividing the mean physical length imaged by the number of pixels of the camera sensor (1024 pixels) using equation (2.7). The process is repeated five times, and an average spatial resolution is determined.

$$L = \frac{mean\ physical\ length}{1024} \tag{2.7}$$

The calibration procedure is as follows. The camera and a digital calliper are fixed on the same horizontal surface. Then, the camera focuses on one reference point on the calliper and zero the calliper. Then, the calliper moves the reference from the bottom to the top of the field of view, whose height is 1024 pixels. The reading of the distance shown on the calliper is recorded. The above procedures are repeated five times, and values of 6.79, 6.79, 6.77, 6.75 and 6.72 mm are obtained. The spatial resolution of 6.61 μm/pixel is calculated according to equation (2.7). The results were repeatable. The spatial resolution was increased to 5.549 μm/pixel for the results presented in chapters 7 and 8 because a different high-speed camera was used.

The overall relative uncertainty of the spatial resolution in equation (2.7) is estimated according to equation (2.6). The relative uncertainty of the denominator in the equation (2.7)

is estimated as ± 0.4 % due to small vibrations of the camera or/and rig (spanning a maximum of 4 pixels) during the calibration process, and the relative uncertainty of ± 0.3 % is estimated for the numerator in the equation (2.7). The relative uncertainty of the mean physical length in equation (2.7) is estimated by dividing the resolution (± 0.02 mm) by the mean value of a physical length mean value of 6.764 mm. Finally, the relative uncertainty of spatial resolution in equation (2.7) is estimated as ± 0.5 %. The propagated uncertainty on the bubble diameter is ± 0.5 % as well because the diameter is equal to the multiplication of the physical resolution and a constant.

2.7.3 Calibration of the flowmeter

In this experimentation, an analogue variable-area flowmeter utilising a float is utilized to indicate the water flow rate. The flowmeter operation calibration equation at experimentation temperatures of 92, 82 and 72 °C is obtained. The indicated average flow rate at a certain float position is calculated based on a certain amount of water volume collected in a tank for a fixed time. The water volume is measured when the water is cooled down with graduated beakers. The calibrated flow rate against the flowmeter float position in mm is plotted in Figure 2.12. The maximum relative uncertainty of the flow rate is estimated as ± 2 %.

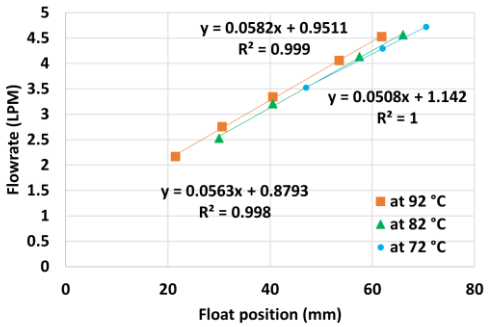


Figure 2.12 Flowmeter operation equation at water temperatures of 92, 82 and 72 °C.

2.7.4 Calibration of the thermocouples

As mentioned in section 2.3 above, 6 K-type thermocouples (T/C) are utilized for temperature measurements. They are calibrated with a Resistance Temperature Detector (RTD) under model 3754-PT100 supplied by Digitron, which has an accuracy of ± 0.2 % of the outputted reading values displayed on a screen with one decimal place.

The tips of all TCs and RTD are placed at the same position inside a water bath and allowed to reach thermal equilibrium. As a result, the calibration temperature is limited to 100 °C and the range of 20 to 95 °C is selected as the calibration range. The maximum temperature measured in the experimentation is at the depth of 10 mm beneath the nucleation wall, which is 150 °C. The correlation fitted at the range of 20 to 95 °C is applied to estimate the temperature 95 to 150 °C. Each point in Figure 2.13 represents an average of 400 data

points, and best-fit equations for each T/C are shown. Accurate linear correlations are obtained. Thus, the estimation of temperature at the working temperature exceeding 95 °C is believed to be available.

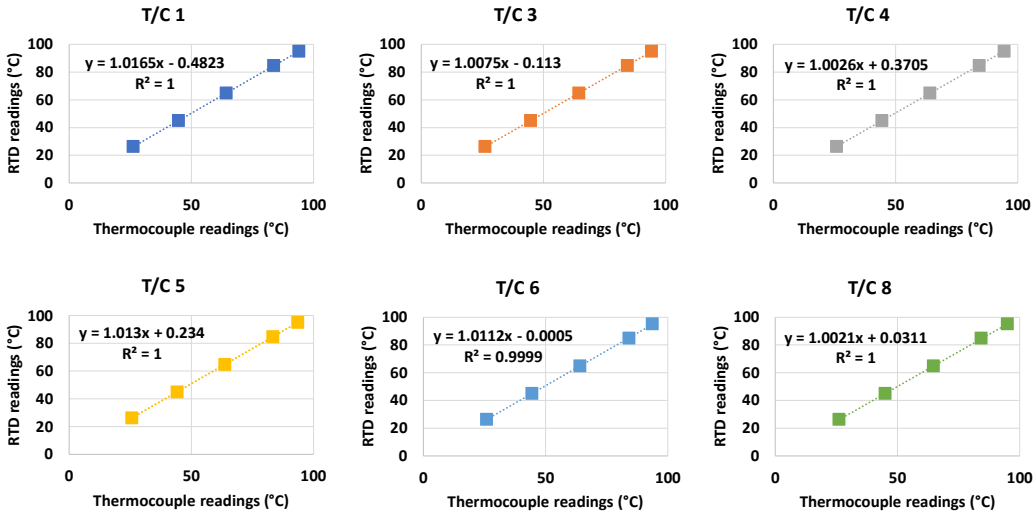


Figure 2.13 Temperature readings against the reading of the RTD for all thermocouples.

2.8 Calculation of equivalent bubble diameter and advancing and receding contact angle

In this section, the estimation method of the equivalent bubble diameter, a significant observed parameter to fulfil the tasks of this study, is described. The advancing and receding contact angles are estimated based on a novel method developed for this purpose.

2.8.1 Equivalent bubble diameter

The recorded images have a narrow depth of field. Hence, a near 2-dimensional image was obtained (the bubble evolution information in the third dimension cannot be detected). The bubble shape is usually found to be non-spherical (i.e., the bubble shape is usually non-symmetric about any horizontal plane of the images obtained). Three-dimensional (e.g., volumetric) quantities are required to perform the analysis. To obtain the best estimate of the volume of the bubble, it is assumed that rotational symmetry exists along an axis formed by the loci of points marking the midpoints of horizontal elemental slices of the bubble boundaries (see Figure 2.14). The volume is estimated by considering elemental cylindrical volumes of 1 pixel in height and summing them to estimate the volume of the entire bubble. This approach is also employed by Siedel, Cioulachtjian & Bonjour (2008) and Narayan, Singh & Srivastava (2020). Once the bubble volume is determined, then an equivalent bubble diameter can be estimated.

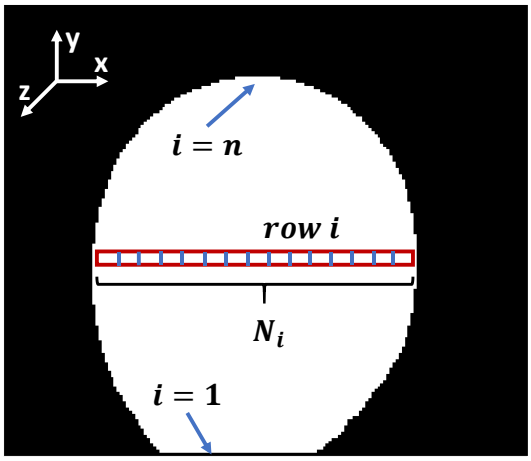


Figure 2.14 Schematic for the illustration of the equivalent bubble diameter estimation approach.

The processed image is a bitmap (see Figure 2.14) where the bubble area is represented by n rows of pixels in white (i.e., a mathematical matrix representing the pixels where the numerical value inside is equal to 1). The volume of each cylinder is calculated by equation (2.8):

$$V_i = \frac{\pi}{4} \cdot (N_i L)^2 \cdot L \tag{2.8}$$

where V_i refers to a cylinder volume at row i. N_i represents the number of pixels at row i, and L signifies the physical length of one pixel. The total volume of a bubble is estimated by

$$V = \sum_{i=1}^{n} V_i \tag{2.9}$$

summing all the volumes of these cylinders in equation (2.9). The equivalent bubble diameter of a sphere is then calculated in equation (2.10) by using the equivalent volume:

$$D = \sqrt[3]{\frac{6V}{\pi}} \tag{2.10}$$

2.8.2 Advancing and receding contact angles

The advancing and receding contact angles of the bubble on the nucleation surface are associated with the contact angles of the bubble along the liquid flow direction, respectively, which distorts the bubble. They are extracted by estimating the slope of a best-fit line for five points at the bubble base region (see red and green dots in the example magnified image of Figure 2.15). The estimated advancing and receding contact angles in this example are 45 and 33 °, respectively. The uncertainty of both angles is ± 5 °.

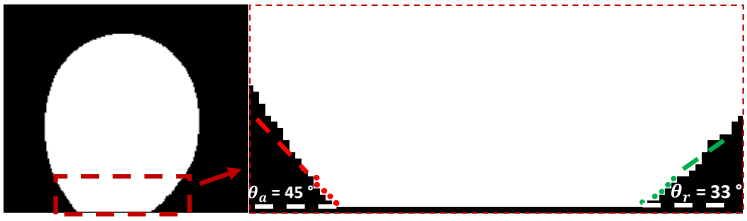


Figure 2.15 Contact angle definition.

2.9 Quantifying the equivalent bubble diameter estimation uncertainty

The accuracy of the estimated bubble diameter is affected by several factors. In this experiment, a varying bubble baseline is observed, which is the main cause affecting the diameter accuracy. In addition to this, the accuracy of the edge detection and repair functions, shape deformation, diameter estimation method and surface levelness and physical resolution can also play a role in the equivalent bubble diameter uncertainty. This section estimates the resulting uncertainties because of all these parameters.

2.9.1 Contribution of bubble baseline fluctuations on equivalent bubble diameter uncertainty

It is found that the observed bubble baseline position varies during the growth period, and its maximum amplitude of fluctuations is ~152 μm, see Figure 2.16. Such large variation is not observed for low heat flux conditions (e.g., lower than 4,100 W/m^2). The nucleation wall mechanical vibrations may result in a displacement of the image under 20μm. Therefore, it is suspected that the increased fluctuations observed for high heat fluxes are due to light ray refraction by the relatively high thermal gradients near the bubble base. Considering such a case, the middle line (see the yellow line in Figure 2.16) is selected as the baseline of the bubble for all images, which is away from the true baseline by ± 76 μm. The selection of baseline results in a systematic error, which is considered in the equivalent bubble diameter uncertainty estimation.

The upper and lower bounds of the relative uncertainty of the calculated bubble diameter are plotted in Figure 2.17. It can be found that the relative uncertainty reduces as the bubble diameter increases. The maximum uncertainty of - 8.3 % is obtained for the equivalent diameter of 395 μm, and then it quickly reduces to ± 2.2 % at a diameter of 744 μm. In Figure 3.15, the bubble diameter exceeds 744 μm quickly, and for 95 % of the bubble growth period, the bubble diameters are larger than the 744 μm. Thus, it is believed that most of the time, this contribution to the relative uncertainty of the equivalent bubble diameter is within ± 2.2 %.

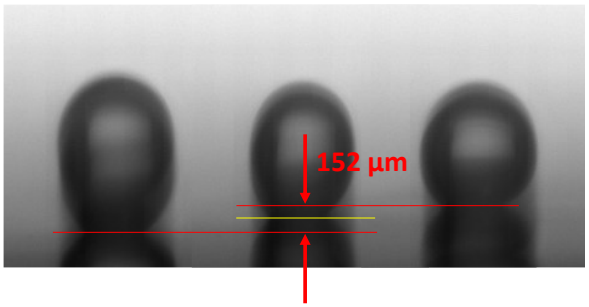


Figure 2.16 Maximum observed bubble baseline variation as revealed from three images.

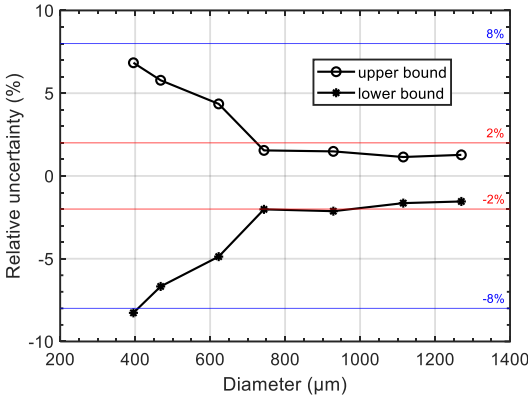


Figure 2.17 Relative upper and lower bounds of uncertainty contributed by the varying baseline against the equivalent bubble diameter.

2.9.2 Contribution of bubble shape deformation to equivalent bubble diameter estimation uncertainty

Due to the bubble inclination caused by the liquid flow over the nucleation surface, the bubble shape is deformed, and an asymmetrical shape develops, especially at the bubble lift-off moment. The diameter estimation method, mentioned in section 2.8.1, assumed a symmetrical shape. As a result, the formation of the asymmetrical shape may result in some errors in the equivalent bubble diameter estimation.

The bubble inclination at the artificial cavity gradually increases with bubble size reaching a maximum at the departure moment. The resulted asymmetrical shape could generate errors because the diameter estimation method assumes a spherical bubble shape based on the estimated volume from the 2D images. The bubble diameter overestimation for the minimum heat flux of 2,956 W/m^2 and maximum heat flux of 29,476 W/m^2 are estimated. This error is estimated by comparing the size of bubbles in two successive frames just before and after the lift-off moment at an interval of 2.72 ms. At lift-off, the bubble shape becomes close to a perfect sphere; hence, the diameter estimation algorithm employed is more accurate. Figure 2.18 shows that the maximum overestimation of the bubble diameter due to the asymmetry is 1.6 %, occurring at the minimum heat flux of 2,956 W/m^2.

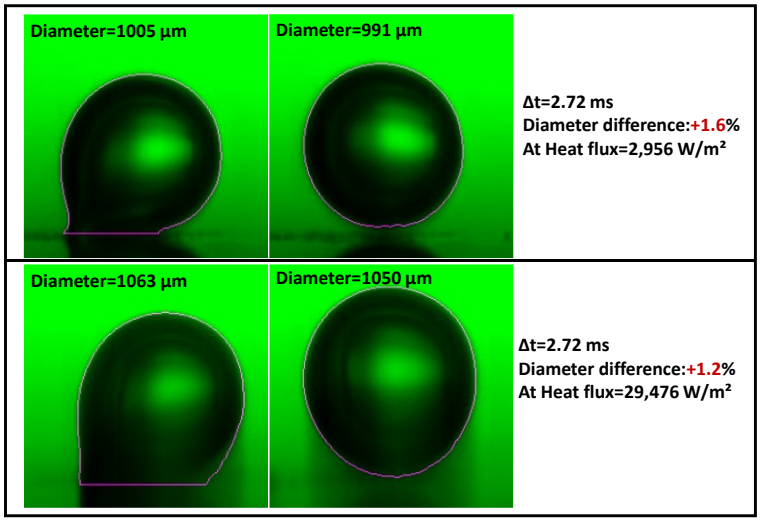


Figure 2.18 Equivalent bubble diameter difference from estimates from two events with a delay time of 2.72 ms between them at two heat fluxes during the lift-off from the nucleation surface.

2.9.3 Contribution of nucleation surface levelness to equivalent bubble diameter estimation uncertainty

The nucleation surface (represented by a yellow dashed line in Figure 2.19) has a slight inclination to the horizontal line with an angle of around 0.72 °, resulting in a projected height difference of one pixel per 500 µm of horizontal length. Therefore, the error generated by this inclination is ignored.

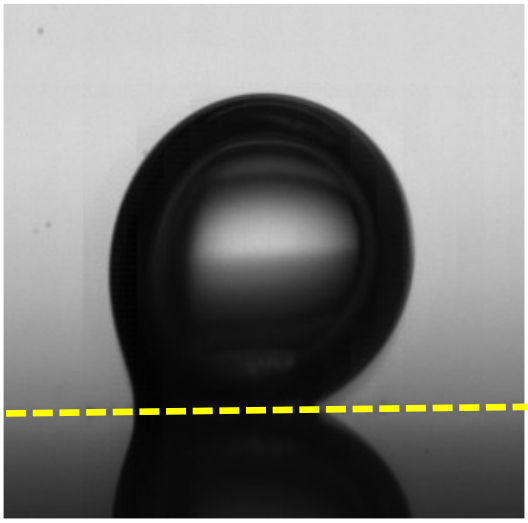


Figure 2.19 Indication of the nucleation surface levelness, which is 0.72 °.

2.9.4 Contribution of applied image processing functions ('edge' and 'bwconvhull') to equivalent bubble diameter estimation uncertainty

As mentioned in section 2.6, the function 'edge' with the method 'canny' (Canny, 1986) is utilized as the basic edge detection routine. Figure 2.20 shows that the detected edge (green line) is superimposed on the raw image as an example. The uncertainty contributed by the utilization of these functions is estimated to be ± 1 %.

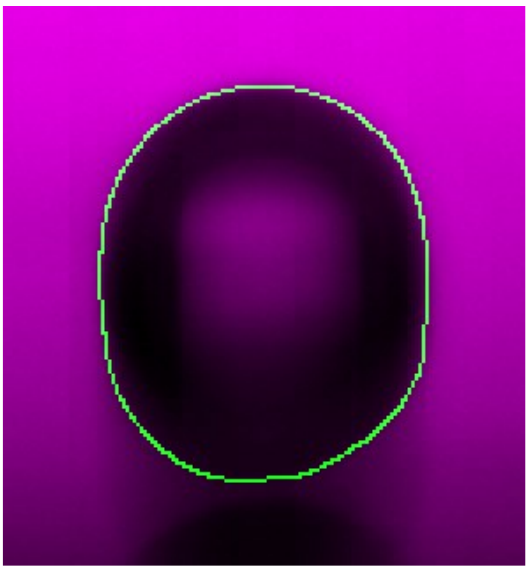


Figure 2.20 Detected bubble edge (green line) during image processing superimposed on its raw image.

The function 'bwconvhull' is used to repair broken bubble edges from the edge detection routine after the bubble lift-off moment from the natural site. Figure 2.21 is used to illustrate the resulting uncertainty from the utilization of this function. The imposed uncertainty can result in an enlargement of the bubble size because a larger convex hull area must be fitted to contain the detected broken edge. In addition to this, the missing part (convex curve between the two green dots) is replaced by a straight line during the image processing, which can underestimate the bubble diameter. The overestimation is estimated by determining the bubble size increase after applying this function on two bubbles (diameter of 1010 and 444.3 μm) with closed edges. The obtained maximum overestimation is 0.76 %. The underestimation is estimated by quantifying the size reduction when replacing the convex curve with a straight line. Figure 2.21 demonstrates the resulting bubble shape when a broken edge between green dots is closed off by a straight line. The effect leads to a 0.18 % underestimation in equivalent bubble diameter. In summary, the uncertainty on lift-off diameter contributed by utilisation of the function of 'bwconvhull' is between +0.76 % and -0.18 %. As such, the relative uncertainty is rounded up to ± 1 %.

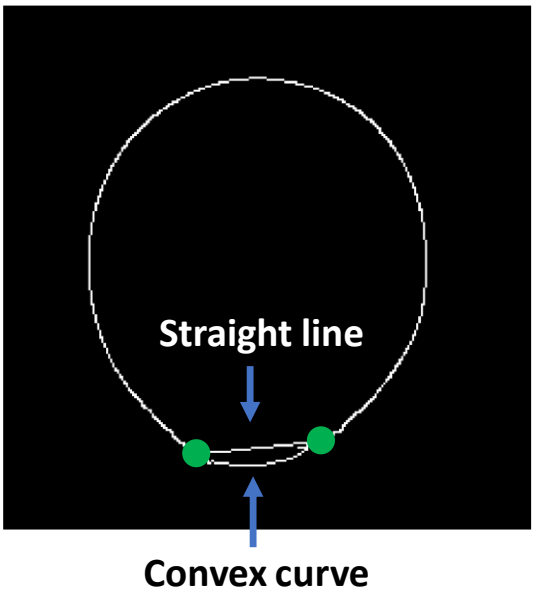


Figure 2.21 The missing bubble edge between the two green dots is repaired with a straight line, while the original edge is estimated as the convex curve.

2.9.5 The relative uncertainty of the equivalent bubble diameter

The bubble diameter uncertainty contributions from all the considered factors above are tabulated in Table 2.4. The overall relative uncertainty of the equivalent bubble diameter is estimated based on the method proposed by Moffat (1988), which is described in section 2.7.2. The maximum relative uncertainty is, therefore, found to be -3.18 % to +3.56 %.

Table 2.4 Equivalent bubble diameter overall uncertainty estimation

			Factors contributing to the uncertainty of bubble diameter					
			Observed bubble base variation	Shape deformation	Physical resolution	Applied functions (function name)	Estimation method	Final Uncertainty
Bubble diameter	Growth period	artificial cavity	± 2.2 %	+ 1.6 % (max)	± 0.5 %	± 1 % (‘edge’)	± 2 %	-3.18 % to +3.56 %
		natural cavity	NA	NA	± 0.5 %	± 1 % (‘edge’)	± 2 %	± 2.29 %
	After the lift-off moment	artificial cavity	NA	NA	± 0.5 %	± 1 % (‘edge’)	± 2 %	± 2.29 %
		natural cavity	NA	NA	± 0.5 %	± 1 % (‘edge’) and ± 1 % (‘bwconvhull’)	± 2 %	± 2.5 %

2.10 Summary

This chapter introduced the preparation effort required for the experimentation, including the experimental rig design, image processing system for bubble characterisation, temperature measurements and temperature estimation methods and relative uncertainty estimation approach. In addition, it described the calibration of the relevant instruments, the experimental procedure, the image processing algorithm for the estimation of the equivalent bubble diameter and its advancing and receding contact angle on the nucleation surface, the corresponding uncertainty estimation and so on. The key points of this chapter are summarized as follows.

1. The novel experimental rig is designed to provide well-defined and controlled operating conditions. The nucleation surface is well polished to avoid the initiation of bubbles in addition to the bubble of interest. Across the test section, a uniform flow velocity profile is achieved by a specially designed flow conditioning channel.
2. The wall temperature is estimated by extrapolating the one-dimensional conduction equation using the measured temperature underneath the nucleation wall at depths of 1 mm and 10 mm.
3. An optical configuration is arranged for the bubble image capturing. A variable image acquisition frequency (FPS), 50 and 5400, is applied accordingly due to the large temporal evolution difference in the observed bubble boiling physics. The images recorded are processed with the software MATLAB R2022a, and functions such as ‘edge’ and ‘bwconvhull’ are utilized for bubble edge detection and closure, respectively. Parameters are extracted based on a well-processed bubble image.
4. The widely accepted uncertainty estimation and propagation model (Moffat, 1988) is used to evaluate the associated uncertainties of considered quantities. A maximum uncertainty of ± 2 % and ± 0.5 % for the flow rate and spatial resolution is obtained, respectively. The thermocouples are calibrated with an RTD with an accuracy of ± 0.2 % of readings, and very well-fitted correlations are obtained.
5. The bubble diameter is a critical parameter. The relative uncertainty contributed factors are estimated, and the final uncertainties estimated are -3.18 % to +3.56 %.

The advancing and receding contact angles are necessary parameters for the surface tension force estimation. They are extracted by estimating the slope of a best-fit line for five points at the bubble base area, and their uncertainty is estimated as ± 5 °. All results presented in subsequent sections are within the calculated accuracies described or otherwise stated.

Chapter 3 Bubble behaviour at an artificial and a natural cavity during flow boiling

This chapter presents the temporal evolution of the bubble characteristics initiated at artificial and natural cavities under the same flow boiling conditions. Boiling at natural cavities is commonly studied in the literature. However, boiling studies at artificial cavities during flow boiling are rare. This is demonstrated in the literature review in section 3.1 below. Thus, a comparison of the bubble characteristics initiated from artificial cavities with known geometry and natural cavities during flow boiling may assist the physical understanding of the boiling processes at the microscale.

The structure of the chapter is as follows. Section 3.1 provides a critical review of past boiling studies. Section 3.2 describes the geometry of the artificial and natural cavities in sections 3.2.1 and 3.2.2, respectively. Section 3.2.3 reports the relative position of two cavities.

The parameters used for the comparison between the artificial and natural cavity bubbles are growth time, waiting time between the formation of a detectable bubble, and lift-off diameter, which are the three critically important parameters describing the bubble characteristics. The results are presented in sections 3.4, 3.5 and 3.6. In addition to that, the diameter profile at the growth time and condensation time are reported in section 3.7, which are determined by net heat transfer calculations. The contact diameter, advancing and receding contact angles and the inclination angle are three necessary parameters in the calculation of applied forces on bubbles. The contact diameter is affected by the advancing and receding contact points; thus, both points are investigated in section 3.8. The above parameters are studied for the comparison between bubbles in the natural and artificial cavities. The speed of the liquid/vapour interface and the bubble shape evolution are reported in section 3.12 and 3.13. Section 3.14 reported the patterns observed downstream of the cavity, and relevant analysis is given.

The observations reported in this chapter are operated with the experimental facility of Chapter 2 under one single flow condition where the flow velocity, water inlet temperature, heat flux, and wall temperature are 0.21 m/s, 94 °C, 20,000 W/m^2 and 109.5 °C.

3.1 Review of cavity geometry effects on boiling dynamics

Boiling is a very efficient mode of heat transfer and, therefore, has attracted a lot of interest. It is relevant to many applications, such as heat sink cooling (Deng et al., 2015), hot-water heating systems (Kang & Wang, 2018), nuclear-boiling water reactors (Yuan et al., 2018) and engine cooling systems (Zhou et al., 2020b) because the formation of bubbles on nucleation surfaces due to the phase change of the liquid can transfer high heat fluxes at low superheats. However, a lot of factors affect bubble behaviour.

The parameters that influence the boiling process include surface roughness (Bui & Dhir, 1985), surface wettability (Liaw & Dhir, 1989), surface orientation (Kaneyasu et al., 1984), surface or liquid contamination (Fang et al., 2015) , surface corrosion (Ross, 1967), system pressure (Yuan et al., 2011), gravity (Merte Jr, 1988), magnitude and state of input heat flux, i.e., transient (Sakurai & Shiotsu, 1977a, 1977b) and steady (Vlachou & Karapantsios, 2018) state, dissolved gas fraction in the liquid (Henry, Kim & McQuillen, 2006), liquid flow shear rate (Groß et al., 2018), liquid flow channel geometry, i.e., diameter for circular cross-section (Saitoh, Daiguji & Hihara, 2005), width and height for rectangular cross-section (Vlachou et al., 2017), nucleation cavity geometry, for artificial (Siedel, Cioulachtjian & Bonjour, 2008) and natural (Singh, Mikic & Rohsenow, 1976) cavities and nucleation cavity size (Kubo, Takamatsu & Honda, 1999).

All these studies attempted to establish empirical correlations that describe the process. Until now, no correlation can account for all factors involved satisfactorily due to the complex interaction of the different parameters during the underlying boiling phenomena. Therefore, the predicted behaviour of the boiling process from the developed models may sometimes deviate from experimental data. Most of these models do not consider the detailed behaviour of the boiling process at the scale of the individual bubble formation. Therefore, the mechanisms of boiling are still not well understood, and more efforts are required to

understand the way that the bubble formation at the microscales associated with the nucleation sites affects the macroscale behaviour of the boiling process.

This study focuses on the influence of nucleation cavity geometry and size on bubble formation during flow boiling. Therefore, a brief review of representative studies related to the effects of nucleation sites is provided. However, the review includes both pool boiling and flow boiling studies in conventional (large dimension) channels and mini-channels due to the limited number of available studies on the effects of cavity geometry and size during flow boiling. The channel type is classified according to the method proposed by Kandlikar & Grande (2003), where conventional channels and mini-channels are identified as those that have a channel hydraulic diameter larger than 3 mm and between 3 mm and 200 μm, respectively.

During pool boiling, the effects of cavities with different geometries and sizes are widely tested. Howell & Siegel (1966) performed saturated pool boiling experiments to explore the thermal performance of drilled cylindrical cavities with a diameter range of around 97 to 1049 μm and depths varying from 254 to 762 μm. Their findings are summarised here. At the early stage of bubble evolution, the surface tension force on the bubble surface (i) does not depend on the contact angle of the liquid-vapour interface, (ii) is affected by the diameter of the drilled cavities possibly because liquid microlayers that are found below the bubbles at natural nucleation sites do not exist at artificial sites. At the later stages of bubble growth, due to the increase of buoyancy force, the bubble shape becomes gradually elongated, and the vapour connected with the cavity forms a neck (see Figure 3.1). The neck becomes progressively narrow, and finally, a bubble breaks, leaving a vapour nucleus inside the cavity. It is observed that for cavities with a small diameter, the neck width is somewhat wider than the cavity diameter, while for larger cavities, the neck width is the same as the cavity diameter. The equilibrium shape profile predicted by Bashforth & Adams (1883) matches reasonably well with all bubble portions except for the bubble base, which is constrained by the artificial cavity. In addition, depending on the artificial cavity size and geometry, the predicted bubble departure size by Fritz & Ende (1936) was found not to be always correct.

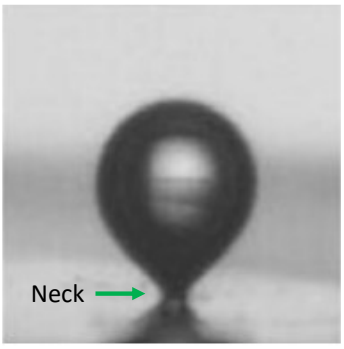


Figure 3.1 Bubble neck captured during boiling studies (Siedel, Cioulachtjian & Bonjour, 2008).

Marto, Moulson & Maynard (1968) investigated the heat transfer performance of two blind circle holes (approximate diameter of 109 and 381 μm) see Figure 3.2 (a) and a conical cavity (approximate diameter of 559 μm) see Figure 3.2 (b) in pool boiling for nitrogen. The boundaries of cavities in Figure 3.2 (a-c) are outlined with red lines for clarity. The cavities are drilled on 'mirror polished' surfaces and repolished prior to tests. Experimental results showed that the heat transfer coefficient increases with the cavity mouth size. The average wall temperature at the incipience is approximately the same, and the local wall superheat at the incipience is not clear.

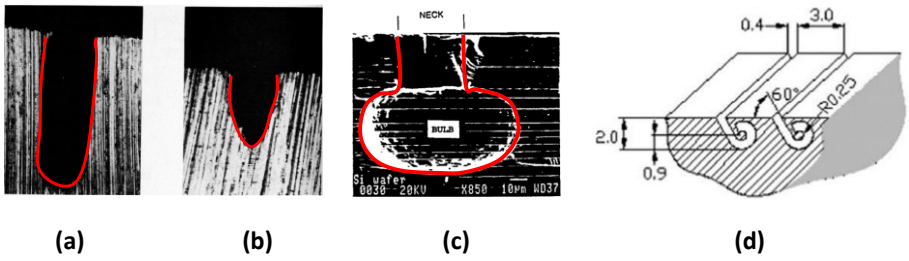


Figure 3.2 Example geometries of (a) blind circle hole (Marto, Moulson & Maynard, 1968), (b) conical cavity (Marto, Moulson & Maynard, 1968), (c) bulb-shaped cavity (Baldwin, Bhavnani & Jaeger, 2000) and (d) straight unidirectional parallel tunnel with circular base (Das, Das & Saha, 2009).

The thermal performance of bulb-shaped, see Figure 3.2 (c) and inverted pyramidal cavities are investigated by Baldwin, Bhavnani & Jaeger (2000) in pool boiling. The pyramidal cavities lead to increased critical heat flux and lower wall superheat, and lower heat flux is required to incipient a bubble. It is proposed that the sharp internal corners at the base of the pyramidal cavity are effective for trapping vapour embryos. Vapour pockets can be sustained even at high subcooling levels. The pyramidal cavity is also superior in eliminating wall temperature overshoot compared to a bulb-shaped cavity.

Das, Das & Saha (2009) tested heat transfer performance of surfaces with parallel or orthogonally intersecting tunnels, see Figure 3.2 (d) with different tunnel inclination angles and tunnel base geometries in pool boiling. It is concluded that all surfaces perform an augmentation in heat transfer compared to plain surfaces. The augmented heat transfer is contributed by not only the boiling surface area increase generated by tunnel geometry but also the release of bubbles. It is found that the surface inclination angle significantly affects the boiling characteristics.

Kang & Wang (2018) tested the effects of microstructures with three geometries (see Figure 3.3) on pool boiling heat transfer. They showed that appropriately designed microstructure patterns could weaken the heat flux, although the boiling surface area is increased because vapour could be entrapped by these microstructures, resulting in a lower thermal conductivity at the boiling surface. Rainey, You & Lee (2003) found that the CHF increases with the increase of the fin length (area). However, it reduces as the length of the fin increases beyond 4 mm due to the reduced fin tip temperature. Wei & Honda (2003) found the same boiling curves at a pin length range of 60-200 μm except for the region near the CHF point.

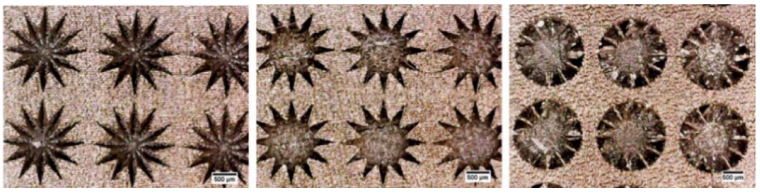


Figure 3.3 Example geometries of (a) coral-rock structure, (b) star-like structure, (c) inner-fin structure (Kang & Wang, 2018).

In mini-channels, Kuo & Peles (2007) investigated re-entrant cavities, see Figure 3.4 (a) in channels (with a hydraulic diameter of 223.4 μm), and experimental results are compared to plain walls. It is concluded that re-entrant cavities lead to better bubble reproducibility and uniformity than the plain wall because a significant low wall superheat is required to trigger boiling. The reproducibility and uniformity assist in enhancing the critical heat flux, which is increased by 11 to 55 %. The required heat flux for initiating the bubble nucleate is around 70 % lower than that of a plain surface with a peak-to-peak roughness of 0.3 μm. In addition, the

ability to suppress flow boiling oscillations and instabilities is examined by Kuo & Peles (2008), and the heat transfer performance of the coolant HFE-7000 in micro channels with re-entrant cavities, see Figure 3.4 (b) are investigated by Kuo & Peles (2009).

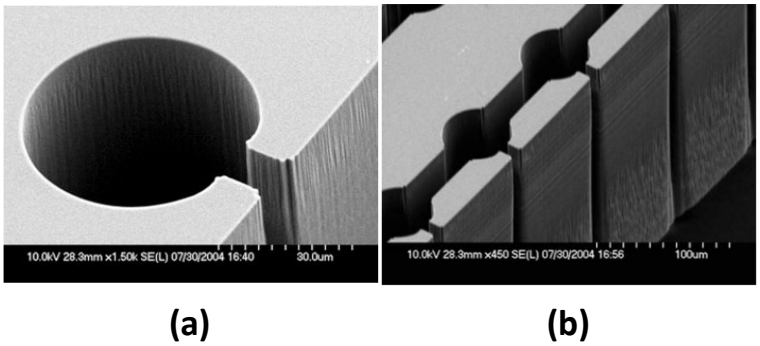


Figure 3.4 Example geometries of (a) reentrant cavity (Kuo & Peles, 2007) and (b) interconnected reentrant cavities (Kuo & Peles, 2008).

Deng et al. (2015) explore the effects of the channel shape (see Figure 3.5) on heat transfer during flow boiling. The tests were conducted in unique Ω-shaped channels (hydraulic diameter of 781 μm) and rectangular channels (hydraulic diameter of 776 μm). Experimental results show that heat transfer coefficient augmentation of Ω-shaped channels reaches 25-70 %. It is explained that the Ω-shaped channel has a circular inside where the distribution of liquid films is more uniform, which maintains stable evaporation and hinders the occurrence of local dry-out. Besides, the narrow slot on the channel top confines the bubbly flow. Consequently, the heat transfer is enhanced. The pressure drop generated in Ω-shaped channels is approximately 40 % and 70 % lower for water and ethanol tests, respectively. It is explained that the Ω-shape significantly decreases local flow turbulence due to its internal circular shape, which eliminates the sudden transition of corners between the bottom and side walls. Consequently, the interfacial shear stress is reduced.

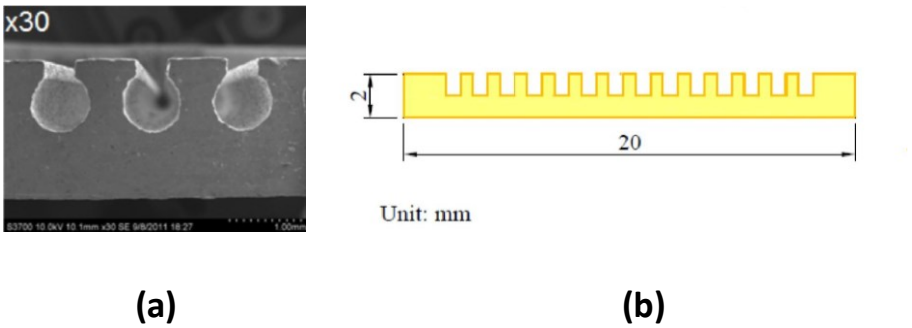


Figure 3.5 Cross-section of (a) Ω-shaped and (b) rectangular channels (Deng et al., 2015).

Flow boiling experiments in conventional channels are mainly related to natural sites, whose geometry and size are not well known, on smooth surfaces such as stainless steel surfaces (Goel et al., 2018; Ooi et al., 2018; Levin & Khan, 2018; Sugrue, Buongiorno & McKrell, 2014), copper surfaces (Vlachou et al., 2017; Vlachou & Karapantsios, 2018; Prodanovic, Fraser & Salcudean, 2002; Yang, Guo & Liu, 2016; Basu, 2003), Cr20Ni80 alloy surface (Yuan et al., 2011, 2018), silicon surfaces (Zhang et al., 2018a), Indium-Tin-Oxide (ITO) coated surface (Richenderfer et al., 2018; Amidu, Jung & Kim, 2018), micro-structurally enhanced surfaces (Zhang et al., 2018b; Sommers & Yerkes, 2013; Lie et al., 2007). Artificial cavities on polyimide film are fabricated (Yoo, Estrada-Perez & Hassan, 2016a, 2016b, 2018) with a needle but they did not report the geometry of the cavity. In conclusion, studies of the effects of artificial cavities with known geometry and size during flow boiling in conventional channels are rare.

The findings from the above-reported studies of flow boiling are summarized as follows:

- An artificial nucleation cavity can generate lower wall superheat and wall heat flux at the bubble incipience. The liquid microlayer between the bubble and the surface, present at natural sites, may not exist at artificial sites.
- The boiling heat transfer can be weakened or enhanced depending on the geometry and size of the artificial cavity.
- The existence of re-entrant cavities can enhance the reproducibility and uniformity of bubble generation and suppress flow boiling oscillations.

In summary, the bubble nucleation cavity geometry and size do affect flow boiling characteristics in conventional channels but have received little attention. Therefore, the current study uses single artificial cavities to understand their influence on the process of bubble formation and characteristics and compare them to behaviour at natural cavities under the same operating conditions. It is noted that the artificial and natural cavities cannot be at the same surface location as the natural cavity is naturally occurring. The natural cavity is active at the same time as the artificial cavity; however, both cavities and the ebullition cycle they undergo are considered independent. This is because they are separated by 14 mm along the flow direction, which avoids bubble interaction, but at the same time, they are close

enough to assume that the properties of the bulk liquid field around them are identical (e.g., flow velocity, shape, and temperature). This approach eliminates the effects of multiple interacting bubbles and allows the quantification of the effect of the cavity itself on the individual bubble behaviour. This chapter provides a qualitative analysis of bubble behaviour at an artificial and natural cavity for one flow boundary condition.

3.2 Geometries of artificial and natural bubble nucleation cavities and flow condition

Before moving to the results, the geometry of the artificial cavity and the natural cavity, as well as their relative positions on the nucleation wall, are introduced.

3.2.1 Artificial cavity geometry

An artificial cavity geometry is used in this chapter to provide a qualitative description of bubble behaviour and define the relevant parameters that are quantified following image processing. The cavity is formed by micro-drilling with a drill diameter of 200 µm. The utilised drills were from Drill Service (Horley) Ltd with a point angle of 118 °. A brass holder was manufactured to ensure drilling perpendicular to the wall. The cavity mouth and bottom (pit) images, captured by a Scanning Electron Microscope (SEM), are shown in Figure 3.6 (a) and (b), respectively. The measured cavity diameter is around 209 µm, which matches expectations.

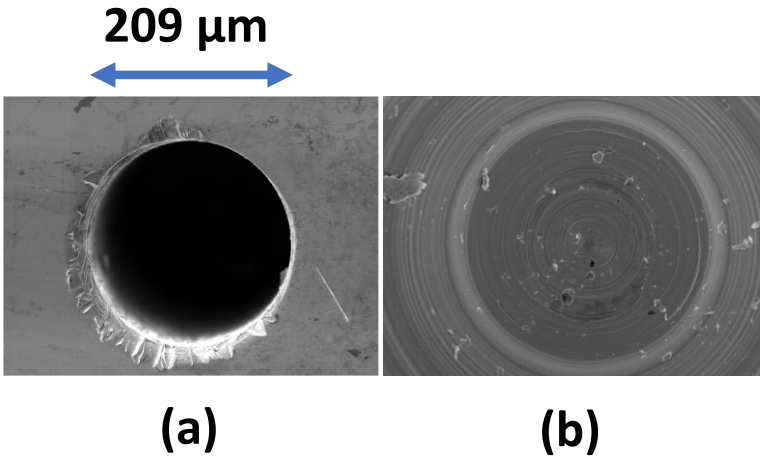


Figure 3.6 The mouth (a) and the bottom (b) image of the artificial cavity as captured by a SEM.

3.2.2 Natural cavity geometry

In literature, crevices (Mu et al., 2017) are thought of as natural boiling sites on nucleation walls under boiling. The natural boiling site in this study is identified by the observed generation of bubbles. Since the surface roughness is very low, the number of natural nucleation sites is low, and, therefore, it is possible to identify their exact surface location on the surface. Therefore, the nucleation site is located inside the red rectangle of Figure 3.7 (a). Further magnification of this region using SEM indicates the presence of a crevice in Figure 3.7 (b) with an approximate length of 60 µm, maximum width of 11 µm and an unknown depth.

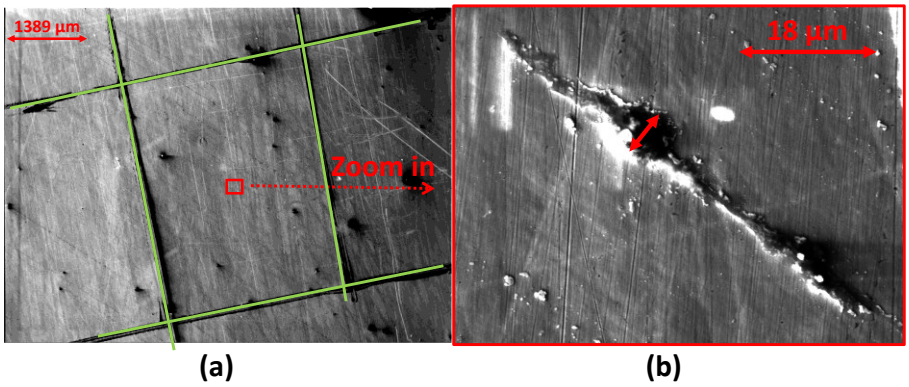


Figure 3.7 The chequered area (fenced by green lines) containing the natural site is depicted in (a); A crevice captured in the centre of the rectangular area is shown in (b). The relevant scale is indicated by the red arrow on each image.

3.2.3 Relative surface positions of the artificial and natural cavities

The considered artificial cavity in the reported experimentation of this chapter is a blind hole drilled on the polished stainless-steel surface with a diameter of 200 µm and 950 ±10 µm depth. Figure 3.8 shows the relative positions of the natural and artificial cavities on the nucleation wall of the experimental facility described in Chapter 2. The figure shows that the artificial cavity is located on the centreline of the nucleation surface 35 mm from the leading edge of the plate. The natural cavity is 49 mm from the leading edge and 4.5 mm in the lateral direction away from the centreline. Therefore, the natural cavity is located 14 mm downstream of the artificial cavity and at a lateral distance of 4.5 mm.

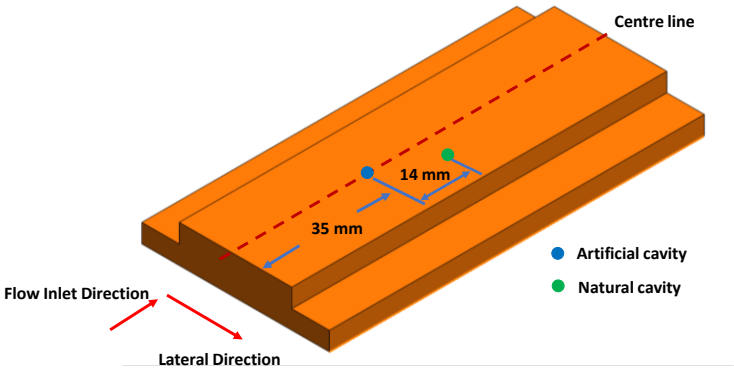


Figure 3.8 The relative position between the artificial and the natural cavity on the nucleation wall.

3.3 Definition of bubble characteristics

This section defines the different bubble characteristics, and their behaviour are reported in the following sections. Results would be presented in the rest of the thesis in terms of individual boiling events. Each boiling event is a record of individual bubble formation, growth, lift-off from the wall and condensation in the surrounding liquid and does not include the waiting time before the start of the next boiling event.

3.3.1 The bubble growth period, waiting period, condensation period

The time between the incipience of a bubble and its departure from the surface is the bubble growth period. Figure 3.9 (a) and (b) shows typical bubble images at different times during the growth period at the artificial and natural cavities for the selected flow condition. After the bubble departure or lift-off, time is required for the initiation of a new bubble, which is defined as the waiting time. The condensation period starts from the bubble detachment from the wall. Figure 3.10 shows example bubble images captured after the detachment from the wall at the natural and artificial cavities. The bubble size is reduced faster in Figure 3.10 (a) for the natural site than that for the artificial site in Figure 3.10 (b) as the bubble moves away from the wall.

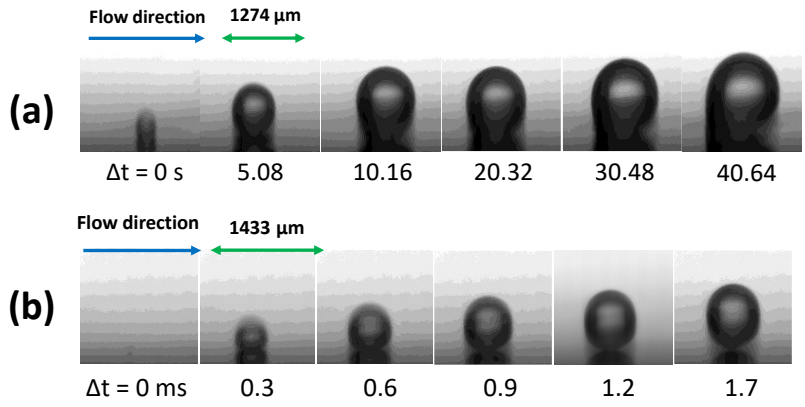


Figure 3.9 Bubble images during the growth time at (a) artificial and (b) natural cavities for operating conditions. The green arrow shows the corresponding scale of the images.

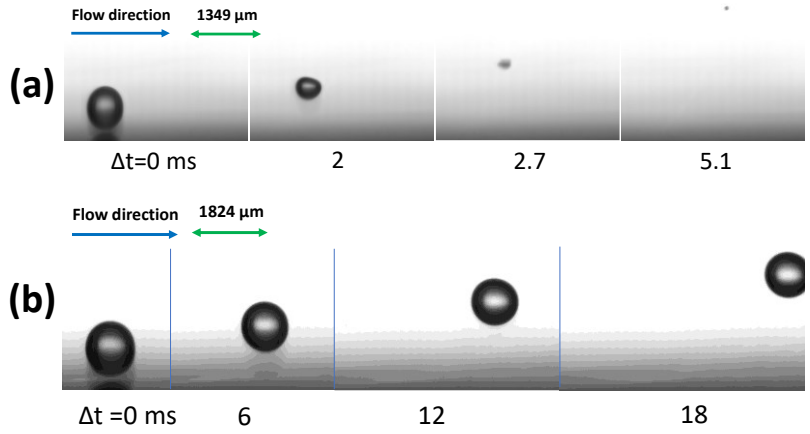


Figure 3.10 Bubble images captured after the detachment from the wall at the natural site (a) and artificial site (b) for same operating conditions as Figure 3.9. The green arrow shows the corresponding scale of the images.

3.3.2 Bubble departure, lift-off time, departure diameter and lift-off diameter

There are two bubble behaviours reported in the literature: (1) a bubble nucleates at a site and, after growing for some time, it departs from the site and starts sliding on the wall for a distance before lifting off from the nucleation wall. For this case, the departure time is defined as the moment when the bubble departs from the nucleation site (i.e. when it starts to slide). The lift-off time is the moment when the bubble detaches from the wall after sliding relative to the initiation of the bubble. (2) If a nucleated bubble lifts off from its nucleation site directly without sliding, the 'departure' and 'lift-off' times coincide. In this experimentation, the departure time of the bubble can be regarded as equal to the lift-off time due to the small sliding distance of 1 mm. Thus, the bubbles at the artificial cavity and the natural site follow

behaviour 2. Finally, the bubble diameter at the lift-off time and departure time are defined as the lift-off diameter and departure diameter respectively.

3.4 Bubble growth period of different bubble events

Figure 3.11 (a&b) presents the measured bubble growth time for sequential individual boiling bubble events at both cavities, respectively, for the flow condition of Chapter 3. At the natural cavity, ~120 bubble events are recorded. Due to the relatively stable performance on the bubble characteristics, 20 bubble events are recorded at the artificial cavity. The impact of the reduced number of samples recorded for the artificial cavity was evaluated to assess the confidence level of the observations. It was found that the measured difference between the averaged quantities for a sample size of 20 and an enlarged sample size of 49 events to be insignificant (~2 %), which demonstrated that the observed bubble behaviour had low uncertainty. The average artificial site ebullition cycle time is around 23,290 larger than that for the natural site. The results show that the mean growth period at the natural and artificial cavity is 1.76 ms and 41 s with a relative standard deviation of 32 % and 7 %, respectively. The increased level of fluctuations, indicated by the high relative standard deviation, at the natural site (Klausner, Mei & Zeng, 1997; Martínez-Cuenca et al., 2015) is reported in the literature. The reported time scale of the growth period for bubbles at natural sites is of the order of 1ms (Goel et al., 2018; Dhir, Abarajith & Li, 2007; Mukherjee & Dhir, 2004; Unal, 1976) which agrees with the current observation. The large bubble growth time at the artificial cavity is due to the large bubble departure diameter and the slow growth rate, which will be demonstrated further later. It is also noted the limited fluctuation of the growth period for the artificial site despite the much longer mean growth time.

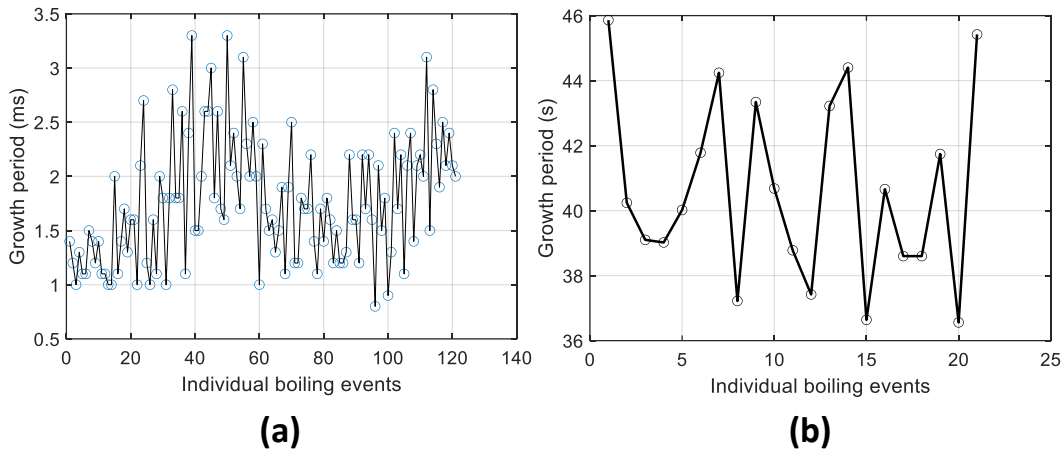


Figure 3.11 Bubble growth time at the natural (a) and artificial (b) cavity for different sequential individual bubble boiling events. Note that the units of the vertical axis of the two figures are different, which indicates the much longer growth period at the artificial cavity.

3.5 Bubble waiting time of different bubble events

The bubble waiting time refers to the speed of accumulating enough energy at the nucleation site to initiate a new bubble. Tong (2018) suggests that this period refers to the required time for a new thermal boundary layer to be re-established at the nucleation wall and the wall temperature to reach the value required for the incipience of a new bubble. The bubble waiting times at the natural site and artificial cavity are presented in Figure 3.12 (a & b), respectively. The average waiting time for individual bubble events at the natural cavity is 213.8 ms, which is much longer than that (1.20 ms) at the artificial cavity. The waiting time at the artificial site is short, possibly due to the local high temperature (Basu, Warrier & Dhir, 2005). The relative standard deviation of bubble waiting times at the natural and artificial sites are 35 % and 14 %, respectively, showing again that the bubble behaviour at the artificial site is more repeatable, while the relatively high standard deviation at the natural site confirms that the boiling process at the natural site is more stochastic.

Han & Griffith (1965) suggested that the waiting time, t_w, is the heating time needed for a thermal layer thickness equivalent to 3/2 times the cavity radius to be established, which is expressed by equation (3.1) following assumptions of potential flow theory and a uniform wall temperature.

$$t_w = \frac{9}{4\pi\eta_f}\left\{\frac{(T_w - T_{bulk})r_c}{T_w - T_{sat}\left[1 + \left(2\sigma/r_c\rho_g h_{fg}\right)\right]}\right\}^2 \tag{3.1}$$

here η_f, T_w, T_{bulk}, r_c, T_{sat}, σ, ρ_g and h_{fg} refer to the thermal diffusivity of fluid, wall temperature, the temperature of bulk fluid, the radius of the cavity, saturation temperature of the liquid at the system pressure, the surface tension of the liquid, density of vapour and latent heat of evaporation of liquid, respectively.

Equation (3.1) calculates a bubble waiting time of around 121 ms for bubbles at the current artificial cavity for the selected flow condition, which is 100 times larger than the measured value. In equation (3.1), the estimated waiting time increases with the increase of cavity radius (at $r_c > 7\ \mu m$), which is opposite from the observation in the experiment where the bubble waiting time is shorter at the large size artificial cavity and larger at the small size natural site. Therefore, the validity of equation (3.1) is doubtful.

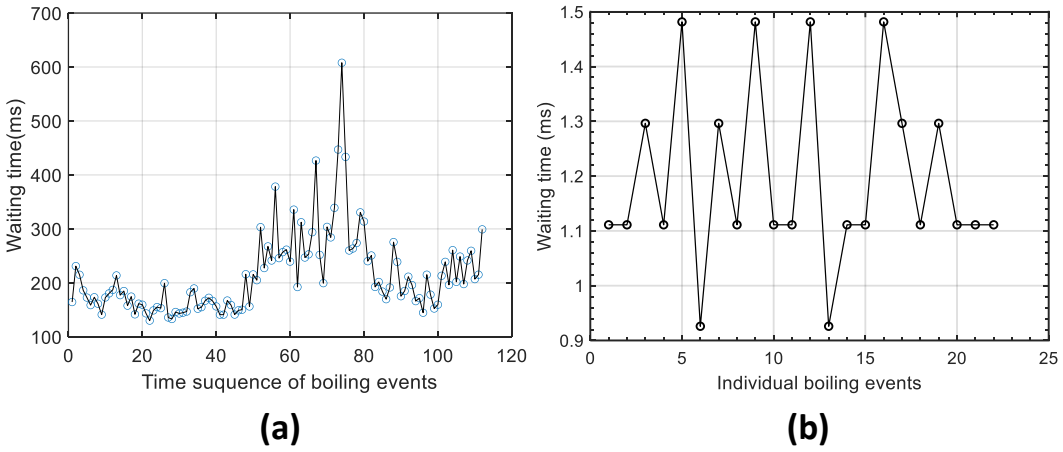


Figure 3.12 Bubble waiting time at the natural (a) and artificial (b) cavity for different sequential individual bubble boiling events. Note that the scale of the vertical axis of the two figures is different, which indicates the much longer waiting time at the natural site.

3.6 Bubble lift-off diameter of different bubble events

The bubble lift-off diameter at the natural and artificial cavities is presented in Figure 3.13 (a & b), respectively. It varies between 369 and 1102 μm at the natural site with mean value and relative standard deviation of 672 μm and 22 %, respectively. However, a much lower relative standard deviation of 3 % is obtained at the artificial cavity and a larger mean diameter of 1218 μm. Similarly, a high relative standard deviation of 51 % (Kaiho, Okawa &

Enoki, 2017) is found for the fluctuations of the bubble lift-off diameter at natural cavities. Klausner, Mei & Zeng (1997) think that the stochastic behaviour of the bubble lift-off diameter is caused by the Gaussian distributions of the fluctuations of wall superheat and velocity at the bubble natural nucleation site and bubble mass centre. The higher bubble departure diameter at the artificial cavity is caused by the required higher drag force for bubble lift-off, which is demonstrated in section 5.5. The increased importance of the bubble drag force at the artificial cavity for the lift-off mechanism may also be responsible for the observed low level of fluctuations.

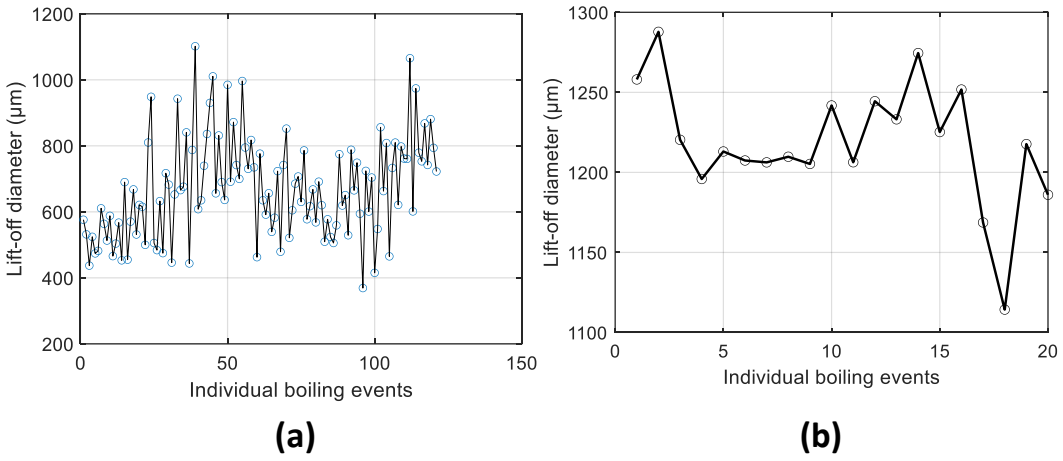


Figure 3.13 Bubble lift-off diameter at the natural (a) and artificial (b) cavity for different sequential individual bubble boiling events. Note that the difference at the scale of the vertical axis of the two figures, which indicates the high stability of the bubble size at the artificial site for different events.

3.7 Temporal evolution of bubble diameter

In this section, the bubble diameter temporal evolution during the growth period and condensation period is reported, where the condensation and growth period were defined in section 3.3.1. The existing models predicting the bubble growth profile are reported in section 3.7.1 and the measurements are used to evaluate their abilities in the rest of the section.

3.7.1 Review of existing bubble growth temporal evolution models during boiling

The previously proposed models for bubble growth during boiling are introduced, which have been developed for natural cavities. These models are obtained either through mathematical derivation with some assumptions or through empirical correlations from

boiling measurements at natural cavities. An extensive review of bubble growth models can be found in Yang et al. (2022).

Model type 1: heat conduction energy balance

Bosnjaković (1930) proposed a theory for a growing bubble in a uniformly superheated liquid. The bubble growth (through an interface evaporation process) is maintained by the energy conducted from the superheated liquid and the resulted temperature drop in a thin boundary layer surrounds the bubble. The relation between the bubble growth rate, the temperature drop, and the heat transfer coefficient is obtained by equation (3.2) from an energy balance.

$$h(T_o - T_s) = h_{fg}\rho_g \frac{dR}{dt} \tag{3.2}$$

where $h, T_{sup}, T_{sat}, h_{fg}, \rho_c, R$ and t refer to the heat transfer coefficient, the temperature of the superheated liquid, saturation temperature, latent heat of evaporation, vapour density, bubble radius and time, respectively.

Zuber (1961) extended the theory of Bosnjaković (1930) to include the effects of a nonuniform (superheated) temperature field. The heat transfer into the bubble is driven by conduction through the thermal boundary layer. Equation (3.3) describes (R_b) as:

$$R_b = \frac{2b}{\sqrt{\pi}} Ja \sqrt{\eta_f t} \tag{3.3}$$

where R_b, b, Ja, η_f and t represent bubble radius, a numerical constant (ranging from 1-1.73), Jakob number (dimensionless) defined as the ratio of the sensible heat to the heat absorbed for evaporation, liquid thermal diffusivity, and time, respectively.

Model type 2: kinetic energy balance

Mikic, Rohsenow & Griffith (1970) derived the bubble growth profile on a heated surface. Equation (3.4) is derived assuming that the total kinetic energy of the liquid equals the approximate net work done by the liquid-vapour interface.

$$R(t) = \frac{2}{3}\frac{B^2}{A}\left[(t^+ + 1)^{3/2} - (t^+)^{3/2} - 1\right]$$
$$t^+ = \frac{A^2 t}{B^2} \tag{3.4}$$

where A and B are constants related to the wall superheat, ΔT_{sat}, and are given by Equations (3.5) and (3.6) respectively.

$$A = \left[\frac{\pi}{7}\frac{h_{fg}\rho_g \Delta T_w}{\rho_f T_{sat}}\right]^{1/2} \tag{3.5}$$

$$B = \left[\frac{12}{\pi}\eta_f\right]^{1/2}\frac{\Delta T_w C_{pf}\rho_f}{h_{fg}\rho_g} \tag{3.6}$$

where h_{fg}, ρ_g, ρ_f, T_{sat}, η_f, and C_{pf} refer to the latent heat of evaporation, vapour density, liquid density, saturation temperature, thermal diffusivity of liquid and specific heat of liquid respectively.

Model type 3: energy balance of conduction, evaporation, and condensation

Raj, Pathak & Khan (2017) assumed that the heat transfer rate contributed from the evaporative microlayer, superheated layer, and condensation layer determines the bubble growth rate and the net (stored) energy of these three factors is expressed as the bubble mass rate times the latent heat. The energy balance equation is shown in equation (3.7), which was adopted by Zhou et al. (2020b).

$$\begin{aligned}\rho_g h_{fg}\frac{d\left(\frac{4\pi R^3}{3}\right)}{dt} &= \left\{Pr^{-0.5} \times \left[\rho_f C_{pf}(T_o - T_{sat}) \times \eta_f^{0.5} A_{evap}\right]\right\} \\ &+ \sqrt{\frac{3}{\pi}}\frac{k_f(T_o - T_{bulk})}{\eta_f^{0.5}} t^{-0.5} \times A_o \\ &- \left[h_{con}(T_{sat} - T_{bulk})\right] \times A_{con}\end{aligned} \tag{3.7}$$

where $h_{cond} = \frac{k_l}{2R}(2 + 0.6Re_b^{0.5}Pr^{0.3})$ is recommended by Ranz, W. E. and Marshall (1952) and ρ_g, h_{fg}, R, t, Pr, ρ_f, C_{pf}, T_o, T_{sat}, A_{evap}, k_f, T_{bulk}, η, A_o and A_{con} refer to vapour density, latent heat, bubble radius, time, Prandtl number, specific heat, wall temperature, saturation temperature, the area of evaporative micro-layer, the thermal conductivity of the liquid, the temperature of bulk liquid, thermal diffusivity of liquid, the area of a vapour bubble in contact with superheated layer, the area of a vapour bubble in contact with condensation layer respectively.

Model type 4: energy balance of conduction and condensation

Yun et al. (2012) extended the bubble growth model of Zuber (1961) by adding a term to include the effect of condensation. Equation (3.8) shows the temporal evolution of the bubble radius *R(t)*.

$$R(t) = \frac{3.12}{\sqrt{\pi}} Ja_w \sqrt{\eta_f t} - \frac{1.56k_f\left(2 + 0.6Re_b^{0.5}Pr^{0.3}\right)\left(T_{sat} - T_f\right)}{2h_{fg}D_d\rho_g} t \qquad (3.8)$$

where Ja_w, η_f, t, k_f, Re_b , Pr, T_{sat}, T_f, h_{fg}, D_d, and ρ_g refer to wall Jakob number, liquid thermal diffusivity, time, thermal conductivity of liquid, bubble Reynolds number, saturation temperature, liquid temperature, latent heat, bubble departure diameter and vapour density, respectively. The different types of Jakob number reported in this thesis are summarized in section 5.1.1.

Model type 5: Experimental data fitting

Chen et al. (2010) fitted measured bubble diameter evolution data to describe the process as two stages using non-dimensional quantities. The presence of two stages in the bubble growth is also reported by Mikic, Rohsenow & Griffith (1970). The derived correlations include a linear equation (3.9) for t^*<0.3 to fit the inertia-controlled stage and a power law equation (3.10) for t^*≥0.3 to fit the heat diffusion-controlled stage.

$$R^* = 2.787t^* \quad for\, t^* < 0.3 \qquad (3.9)$$

$$R^* = t^{*0.25} \quad for t^* \geq 0.3 \tag{3.10}$$

where the non-dimensional parameters are related to time $t^* = \frac{t}{t_{growth\ time}}$ and bubble radius $R^* = \frac{R(t)}{R_{detachmetn}}$. The parameters of t, $t_{growth\ time}$, R, and $R_{detachmetn}$ refer to the time, growth time, bubble radius and the bubble radius at the detachment, respectively.

Prodanovic, Fraser & Salcudean (2002) correlates the bubble growth rate in terms of the bubble maximum diameter and bubble lifetime in equation (3.11). The form suggested by Akiyama & Tachibana (1974) is adopted, and new empirical constants are obtained.

$$\frac{D}{D_m} = 1 - 2^{2.5} \left| \frac{1}{2} - (\frac{t}{t_b})^{0.7} \right|^{2.5} \tag{3.11}$$

where D, D_m, t and t_b represents to the bubble diameter, bubble maximum diameter, time and the bubble lifetime.

Summary

These 5 model types have been derived for boiling at natural cavities, and their ability to describe the boiling process at artificial cavities has not been assessed due to the lack of experimental studies. The time scale of models 1-4 is in ms, while the timescale of model 5 is based on dimensionless time.

3.7.2 Bubble growth period diameter

The measured bubble diameter temporal evolution of five typical boiling events at the natural cavity and one typical event at the artificial cavity in the current study are presented in Figure 3.14 and Figure 3.15, respectively. The selected five boiling events were chosen to indicate typical cases which have lift-off diameter between the minimum and maximum values of Figure 3.13 (a) while the image quality of the captured bubble edges is high. Time zero in these figures represents the bubble incipience time, and the maximum time of each event corresponds to the bubble lift-off time. In Figure 3.14, the current experimental data are plotted in black colour, and the predicted bubble profile by models of Zuber (1961), Mikic, Rohsenow & Griffith (1970) and Zhou et al. (2020b) are plotted in green colour, respectively.

In addition, the bubble growth profile predicted by the model of Prodanovic, Fraser & Salcudean (2002) is presented in red colour.

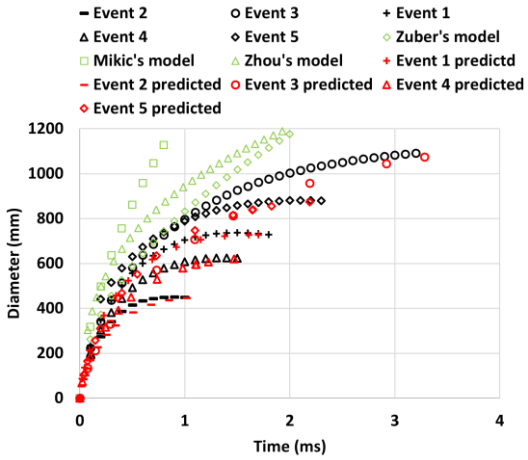


Figure 3.14 Bubble diameter temporal evolution at the natural cavity for five typical bubble boiling events of the current study (black colour symbols). The green colour shows the predicted values based on models of Zuber (1961), Mikic, Rohsenow & Griffith (1970) and Zhou et al. (2020b). The red dots show the predicted values based on the model of Prodanovic, Fraser & Salcudean (2002).

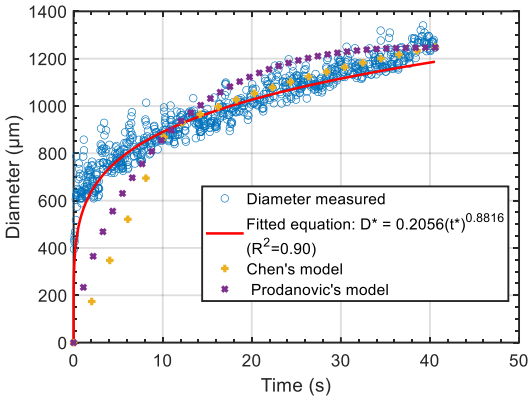


Figure 3.15 Comparison between experimental data and predicted values by model type 5 of Prodanovic and Chen of the temporal evolution of bubble growth. The red line represents the best fit equation, which is shown in equation (3.12).

In Figure 3.14, the experimental bubble diameter of all events, except for event 3, reaches a maximum value before the lift-off time. It is observed that the bubble diameter increase rate reduces with time. The observed small bubble size reduction before the lift-off time is thought to be due to condensation becoming dominant in the net heat transfer rate at the late stage of the evolution before lift-off. Similar bubble size reduction has been observed in literatures (Prodanovic, Fraser & Salcudean, 2002; Sinha, Mahimkar & Srivastava, 2019) as well. Figure 3.14 shows a large variation of the bubble growth profile between each bubble event, even for the same flow condition. This results from the stochastic nature of boiling at the natural site.

Numerous researchers have developed bubble growth profile models, and five types of models were reported in section 3.7.1. The results predicted by models of Zuber (1961), Mikic, Rohsenow & Griffith (1970), Zhou et al. (2020b) and Prodanovic, Fraser & Salcudean (2002) have been included in Figure 3.14. In Figure 3.14, the data predicted by Zuber (1961) and Zhou et al. (2020b) show a better agreement with the current experimental data compared to those predicted by Mikic, Rohsenow & Griffith (1970). However, the over-prediction of bubble maximum diameter by the two models is clearly shown, which is also reported by

Prodanovic, Fraser & Salcudean (2002). The model suggested by Prodanovic, Fraser & Salcudean (2002) leads to acceptable predictions for bubble growth profile with a maximum deviation of – 29.5 %, although this is mainly an empirical correlation based on measured data.

In Figure 3.15, the bubble diameter for the artificial cavity for one event grows up to around 600 μm in 240 ms and then increases at a slower rate up to around 1300 μm with fluctuations. These fluctuations can lead to bubble diameter changes of around 164 μm in 20 ms. An example estimation of the energy required for a bubble diameter to change size from 800 to 1000 μm is 3.38e-04 J, and such energy must be delivered in 18 ms at an area of 1 mm² based on the average input heat flux of 20 kW/m². Such bubble size fluctuations (increase or decrease) over short periods (20 ms) are observed during the whole growth period, which is thought to be due to competition between evaporation and condensation.

It is found that all models introduced in section 3.7.1 except the model of Prodanovic, Fraser & Salcudean (2002) and Chen et al. (2010) are not available for predicting the diameter at artificial cavities because the associated time scale of these models is ms. The models of Prodanovic, Fraser & Salcudean (2002) and Chen et al. (2010) are built based on a dimensionless bubble growth time and departure time. They show an underestimation of the bubble diameter at time < 10 s. After that, a relatively good prediction is observed for the diameter predicted by Chen et al. (2010). Therefore, based on these findings, dimensionless definitions are accepted, and the correlation approach is utilized. As a result, the data in Figure 3.15 is plotted with a dimensionless power equation with exponent and proportion coefficient of 0.8816 and 0.2056, respectively. Equation (3.12) shows a relatively good data-fitting performance with an R^2 of 0.90. The values of the two coefficients would change as the experimental conditions vary. A generalised equation that covers most considered cases at one single cavity is reported in Chapter 4.

$$D^* = 0.2056 * t^{*0.8816} \tag{3.12}$$

The parameters of equation (3.12) are the dimensionless diameter (D^*) and time (t^*) and are defined as $\frac{D}{D_m}$ and $\frac{t}{t_g}$, respectively. The D_m and t_d refer to the maximum bubble diameter and bubble growth time, respectively.

3.7.3 Temporal evolution of bubble diameter during the condensation period

Figure 3.16 and Figure 3.17 present the temporal evolution of the bubble diameter during the condensation period, which starts after they detached from the wall, at the natural and artificial cavity, respectively. Time zero coincides with the bubble lift-off from the wall for each bubble event.

In Figure 3.16, the bubble diameter of events 1, 2, 4 and 5 reduces with time. This is generally reported in the literature as the vapour is condensed. Figure 3.16 also shows that the predicted evolution of the bubble diameter after the lift-off by the model of Prodanovic, Fraser & Salcudean (2002) (plotted in red colour) is in good agreement with the experimental results. In addition, Mukherjee, Basu & Mondal (2022) reported a steady decline in the bubble cross-section after the lift-off and the rate of reduction enhanced with time in their simulations, which is also consistent with the cross-section evolution of the experimental data of Figure 3.16. However, the bubble diameter for event 3 increases until a time of 2.2 ms and such an increase in diameter after the detachment is interesting. After the detachment, the near wall microlayer does not exist, and more than 79 % of the bubble surface area has emerged into the subcooled liquid. Generally, the bubble growth occurs due to the energy transfer from the microlayer, superheated layer and condensation layer (Zhou et al., 2020b). The bubble growth is affected by the net heat energy input from the three sources (namely, the evaporation from the microlayer, evaporation from the superheated layer and the condensation). However, it is possible that a superheated layer exists around the bubble, which contributes to the bubble growth as well. The last mechanism has not been demonstrated in the literature, and more research is needed to understand the behaviour. In addition, it is noted that the bubble diameter temporal evolution of event 3 is not completely recorded, since the bubble flows out of the field of view before it condenses fully.

For all events of Figure 3.16, apart from event 3, the bubble diameter reduces by more than 87 % in a period of 5.5 ms at the natural cavity. However, at the artificial site, Figure 3.17 shows that the bubble diameter reduced by only 10 % in a period of 20 ms. The bubble diameter temporal evolution in Figure 3.17 is fitted well by a linear equation from around 1206 to 1082 μm. The bubble diameter reduces linearly in Figure 3.17 for the artificial site, while a faster high-order polynomial bubble diameter decline rate occurs at the natural cavity. Therefore, the condensation rate for bubbles at the artificial cavity is much slower. This difference is possibly due to two reasons. One reason is that the temperature of the vapour within detached bubbles from the artificial cavity could be higher because the bubble remains on the wall for a long time, around 40 seconds, and a thicker thermal boundary layer surrounds the bubble interface. This high vapour temperature and thick thermal boundary layer might lead to a slower temperature reduction relative to bubbles from natural sites that could delay condensation. The second reason may be the presence of an increased amount of non-condensable gas in the bubble at the artificial cavity rather than the natural site that slows down vapour condensation. It is noted that some non-condensable gas may remain in the water despite the exposure to high temperature.

More interestingly, all bubble events in Figure 3.16 at the natural site, except from event 3, tend to have a constant bubble size after some time, and this size increases with the bubble lift-off size. It is found that the mean ratio of the resulting constant bubble size divided by the corresponding bubble lift-off size is 0.11, with a relative standard deviation of 6 %, estimated from 112 individual boiling events. Such a small relative standard deviation may indicate that the bubble size at the final state relates to the bubble lift-off size. Such behaviour of bubble constant size after condensation was also observed by Cao et al. (2016). This observation may be caused by the remaining non-condensable gas in the liquid, which leads to the observed final size of the bubbles after vapour condensation.

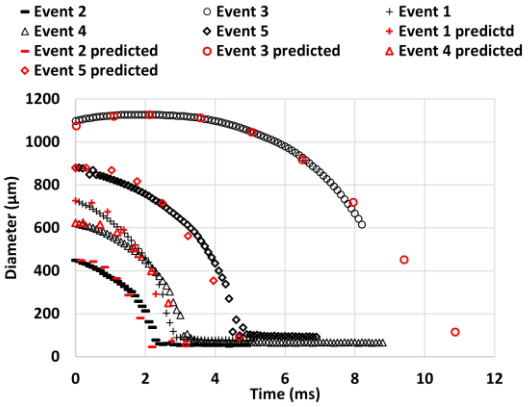


Figure 3.16 Temporal evolution of bubble diameter at the natural cavity after the bubble lift-off from the wall. Time zero coincides with the bubble lift-off. The red colour shows the predicted values based on the model of Prodanovic, Fraser & Salcudean (2002).

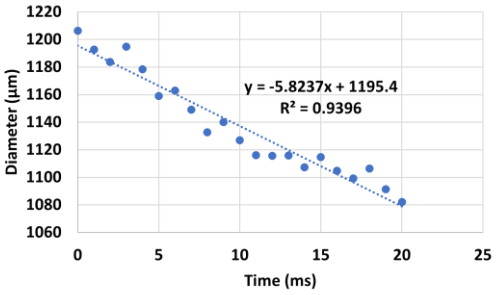


Figure 3.17 Temporal evolution of bubble diameter at the artificial cavity after the bubble lift-off from the wall. Time zero coincides with the bubble lift-off. The results are best fitted by the linear expression shown on the graph.

3.8 Temporal evolution of advancing and receding bubble contact points

This section evaluates the temporal evolution of the position and relative distance between advancing and receding bubble contact points on the nucleation wall. The distance between the advancing and receding contact points represents the contact diameter of the bubble on the wall, which is important for the analysis of the forces acting on a bubble. Figure 3.18 demonstrates the advancing and receding contact points for a typical bubble outline at a time 0.2 ms after its incipience. They are defined as intersections of the bubble outline and the nucleation wall with respect to the flow direction. To quantify their position, the cavity centre is defined as the reference point, and the temporal evolution of the displacement of both contact points relative to the cavity centre is investigated. The flow direction serves as the positive direction. If a contact point is located upstream of the cavity centre, the displacement is negative, and this represents the advancing contact point. In contrast, a positive displacement is obtained when the contact point is located downstream of the cavity centre, and this represents the receding contact point.

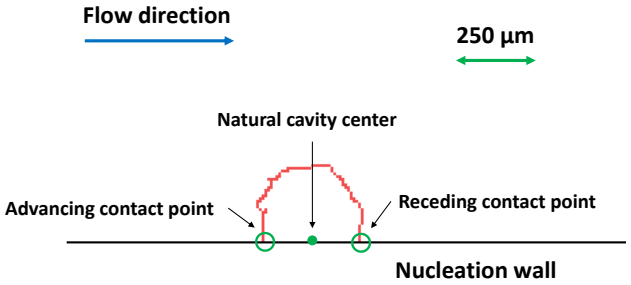


Figure 3.18 Illustration indicating the definition of the advancing and receding contact points.

3.8.1 Bubble advancing and receding points at natural cavity

Figure 3.19 presents the temporal evolution of the displacement of both contact points for event 1 at the natural cavity during flow boiling, where time zero represents the incipience time and time 2.0 ms represents the lift-off instance. The relative positions of both points at times 0.2, 0.7, 1.2 and 1.7 ms for this event are shown in Figure 3.20. The displacement evolution of the other four events will be reported in the later part of this section.

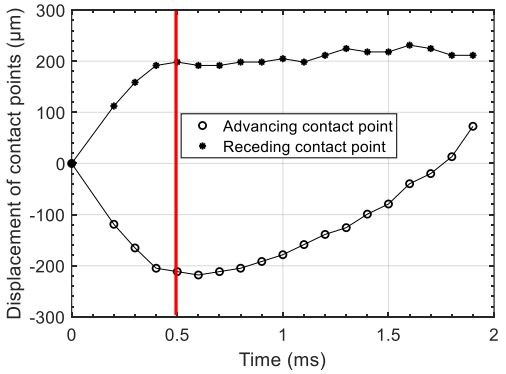


Figure 3.19 Temporal evolution of the displacements of the advancing and receding contact points for bubble event 1 (which has a lift-off diameter of 729 µm) of Figure 3.14 at the natural cavity.

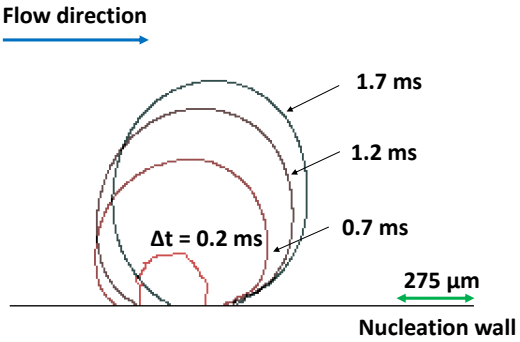


Figure 3.20 Temporal evolution of the relative positions of the advancing and receding contact points at times 0.2, 0.7, 1.2 and 1.7 ms for bubble event 1 of Figure 3.14 at the natural cavity.

Up to time 0.5 ms, the magnitude of the displacements of both points increases to around 200 µm. The maximum difference between the displacements of the two points is around 7 % within this time. Such a small difference indicates that the position of both points can be regarded as symmetric around the cavity centre (i.e., symmetrical motion).

At the time range of 0.6-1.9 ms, an asymmetrical bubble motion is observed relative to the cavity centre. The advancing contact point gradually shifts towards the cavity centre and moves downstream of the cavity centre, with its displacement varying from -218 µm to

around +73 µm. The absolute distance change of its location is 291 µm. During this time, the receding contact point moves very little, and its displacement increases from 192 µm to 212 µm, a change of only around 20 µm. Considering the uncertainty of ± 13.22 µm (2 pixels), the receding contact point could be regarded as stationary. As a result, during this period, an asymmetrical bubble movement is observed.

Similar symmetrical and asymmetrical motions are observed for both contact points, as shown in Figure 3.21 (a, b, c and d) for bubble events 2, 3, 4 and 5, respectively of Figure 3.14 at the natural cavity. The switch between symmetrical and asymmetrical bubble motion occurs at the same time of around 0.5-0.6 ms for all events. The observation of the motion of the advancing contact point is possibly not a dynamic movement but due to the shrinkage as a consequence of the enhanced condensation at the advancing contact point.

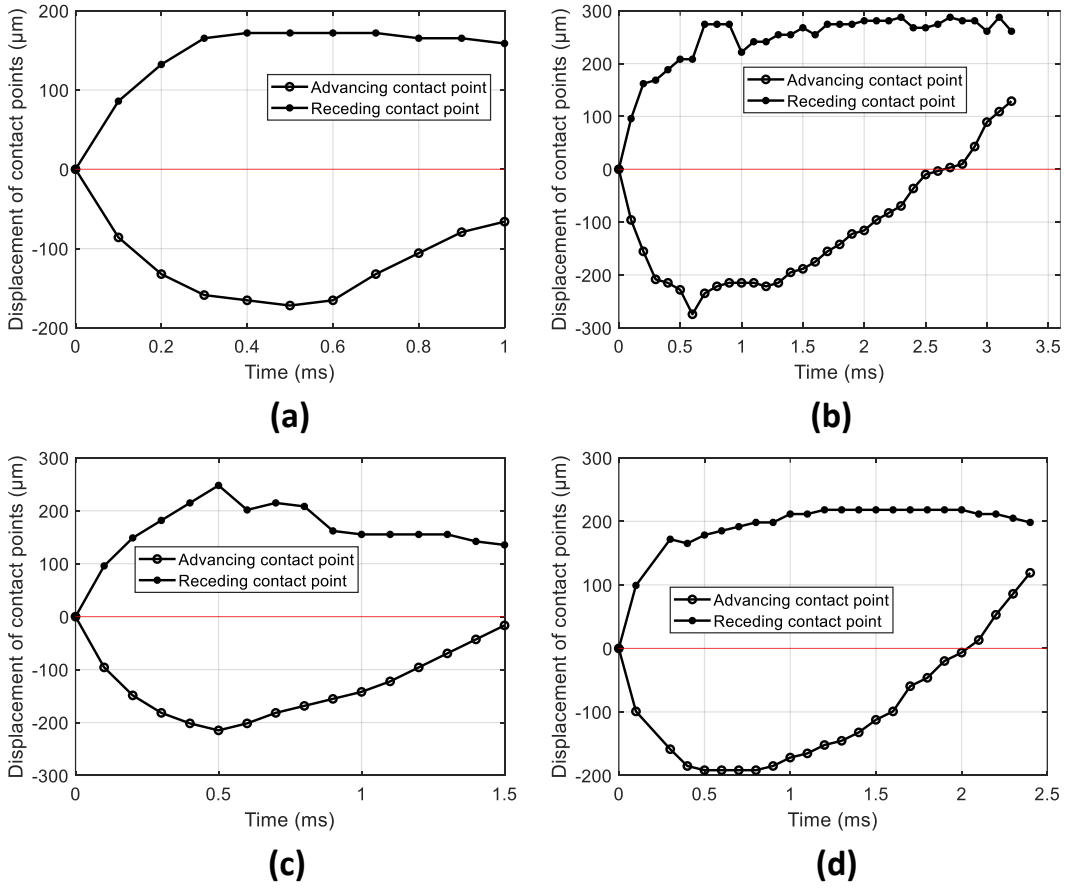


Figure 3.21 Temporal evolution of the displacements of the advancing and receding contact points for bubble event (a) 2 (lift-off diameter of 450 µm), (b) 3 (lift-off diameter of 1100 µm), (c) 4 (lift-off diameter of 640 µm) and (d) 5 (lift-off diameter of 880 µm) of Figure 3.14 at the natural cavity.

3.8.2 Bubble advancing and receding points at artificial cavity

The temporal evolution of the positions of the advancing and receding contact points at the artificial cavity for one bubble event is presented in Figure 3.22 (a & b).

Figure 3.22 (a) shows the displacement of both points relative to the cavity mouth centre up to the time of around 200 ms. In this figure, the displacements start from ±100 µm, positions around the cavity mouth edge since the artificial cavity radius is 100 µm. Figure 3.22 (a) shows a symmetrical bubble movement during this time window at the early stage of the event.

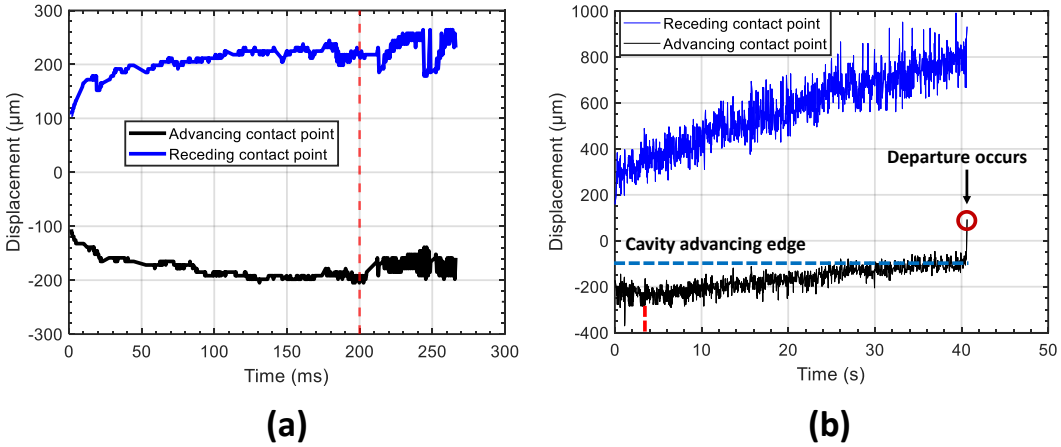


Figure 3.22 Temporal evolution of the displacements of the advancing and receding contact points at 0-270 ms (a) and 0-40.52 s (b) at the artificial cavity.

Figure 3.22 (b) shows the temporal evolution of the displacements of the advancing and receding contact points during the whole bubble growth period. At times lower than 3.5 s, the displacement of the advancing contact point changes from -100 to -250 µm, and after that, it evolves to -50 µm. At times larger than 34 s, the displacement magnitude of the advancing contact point starts to be smaller than 100 µm, which indicates that the point starts to cross the cavity advancing edge and is located within the cavity mouth area. Figure 3.23 helps to demonstrate this statement. The observed temporal fluctuations of the displacement indicate that the advancing contact point shifts back and forth over the cavity advancing edge at times larger than 34 s. At the bubble departure time (time of 40.52 s for this event), the displacement is 92.5 µm, which means that the advancing contact point shifts downstream of the mouth centre of the cavity by a distance of 92.5 µm. Noting that the radius of the cavity

mouth is 100 μm, this means that the advancing bubble contact point almost attaches to the receding edge of the cavity mouth at the departure moment.

At times up to 200 ms, both contact points move symmetrically in Figure 3.22 (a). After this time, an asymmetrical motion of the two bubble contact points is observed. At times lower than 3.5 s, the advancing contact point moves away from the cavity centre. At times larger than 3.5 s, the advancing contact point moves towards the cavity centre. When the advancing contact point moves towards the cavity centre, the main difference between the behaviour at the natural site and artificial cavity is that the advancing contact point at the natural cavity moves beyond the cavity position, while it is stopped before the cavity mouth centre at the artificial cavity until the bubble departure time. Another obvious difference is that the receding contact point continues to move far away from the cavity centre at the artificial cavity because of the increased bubble size and inclination angle.

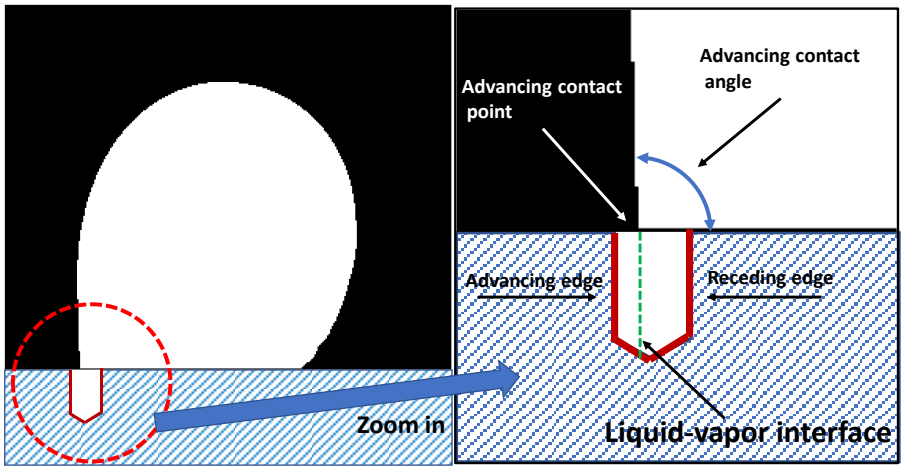


Figure 3.23 Image of the bubble shape and its position relative to the cavity cross-section when the advancing contact point gains a displacement of -50 μm towards the cavity mouth centre.

Figure 3.23 shows the relative position of the advancing contact point, advancing edge and receding edge at the displacement of -50 μm in Figure 3.22 (b). Currently, the advancing contact angle is around 90 ° in Figure 3.23, and the advancing contact point is located within the cavity mouth. Based on these facts, it is conjectured that the liquid-vapour interface (green dashed line) inside the cavity might be normal to the nucleation wall. In this case, the cavity interior could be split into two parts by the liquid-vapour interface, and as a result, a certain amount of liquid could flow into the upstream part of the cavity interior, which could lead to

further liquid evaporation. In order to clarify the inferred physics of this process, a transparent cavity is required that could be pursued in the future.

The mean deviation of the displacement between two successive data of the receding and advancing contact points in Figure 3.22 is 60 μm and 24 μm, respectively. These fluctuations may influence the heat transfer between the bubble and the wall through a mechanism that is described below. Sriraman (2008) suggested that nano-fins with heights greater than 100 nm on a wall can disturb or disrupt the liquid microlayer between a bubble and the wall. Sarker et al. (2017) reported that, depending on the value of the height of the liquid microlayer relative to the surface roughness profile, the surface roughness can disturb the liquid microlayer for Rt = 0.821 μm increasing the microlayer heat transfer area or disrupt the microlayer for Rt = 3.65 μm. Rt refers to the vertical distance between the maximum profile peak height and the maximum profile valley depth. The conceptual diagram of disturbed and disrupted microlayer below a bubble is shown in Figure 3.24 (b and c), which suggests a mechanism that could cause liquid to be stored inside the rough surface space. The average Rt of the bubble contact area in the current experiment was measured as 2.33 μm, which is higher than 0.821 μm. Consequently, it is proposed that the liquid microlayer underneath the bubble is disrupted. Moreover, the advancing and receding contact points shift back and forth on the surface frequently, which can lead to the microlayer underneath the bubble being refreshed (Sriraman, 2008; Sarker et al., 2017). This assumption needs further investigation in the future.

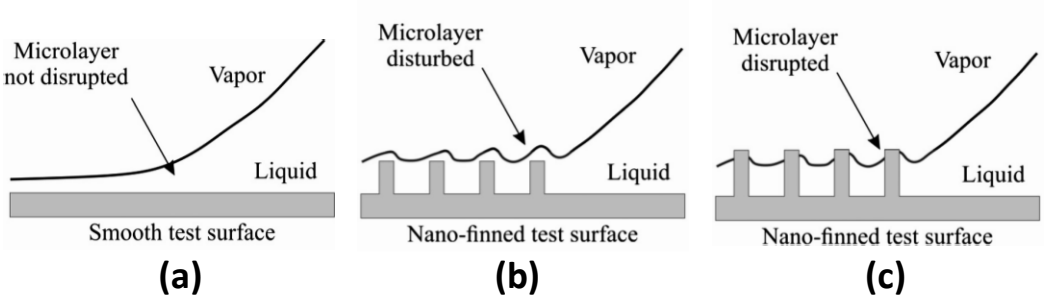


Figure 3.24 Conceptual diagram of a complete (a), disturbed (b), disrupted (c) liquid microlayer between a bubble and a surface with specific roughness (Sarker et al., 2017).

3.9 Diameter of bubble contact region on nucleation wall

The contact region of a bubble attached to the wall is assumed to be a circle, and the distance between the advancing and receding contact points is defined as the contact diameter,

which is demonstrated in Figure 3.25. This definition is also accepted by Zhou et al. (2020b) and Sugrue & Buongiorno (2016). The contact diameter is required for the calculation of the surface tension force on a bubble.

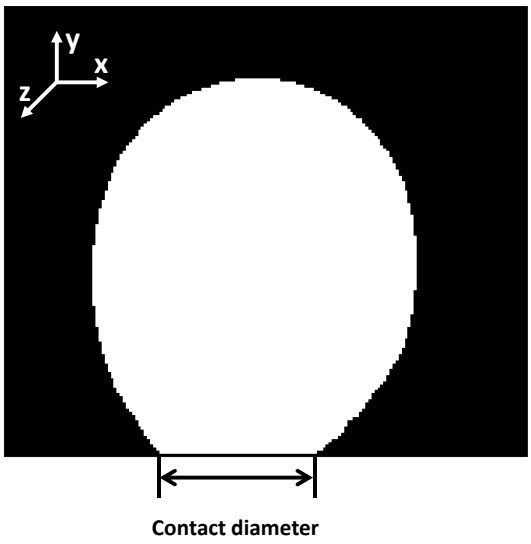


Figure 3.25 Illustration of the definition of the contact diameter of a bubble on a nucleation wall.

The temporal evolution of the contact diameter of the five typical boiling events at the natural site and one event at the artificial cavity are presented in Figure 3.26 (a & b), respectively. At the natural cavity, the contact diameter increases linearly with time up to around 0.5-0.7ms, and after its maximum, it reduces because the advancing contact point shifts towards the receding contact point. The contact diameter is reported to be zero at the lift-off time in Situ et al. (2005). The bubble contact diameter at the artificial cavity generally increases linearly with time from 509 μm at time 260 ms to around 900 μm at time 40s, although with temporal fluctuations. It increases with the bubble diameter. The values of the ratio of the contact diameter to the bubble diameter at the natural site and artificial site are presented in Figure 3.27 (a & b), respectively. The ratio gradually reduces from around 1 to zero at the lift-off time at the natural site, while the ratio at the artificial cavity is reduced from 1 to around 0.7 at the departure time.

The temporal fluctuations of the contact diameter between two successive data (time interval of 29.6 ms on average) is 68 μm. Such fluctuations are due to the varying bubble diameter and corresponding inclination angle.

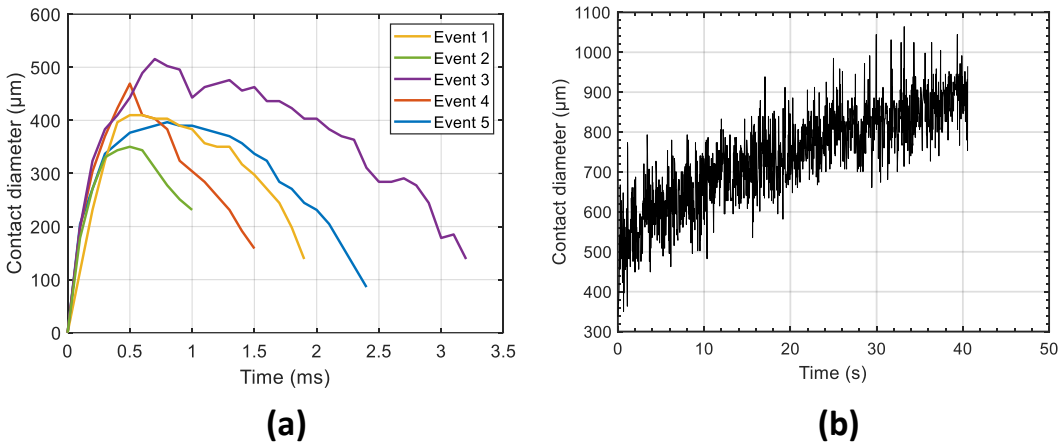


Figure 3.26 Temporal evolution of the contact diameter of a bubble on the nucleation wall for the five typical flow boiling events of Figure 3.14 at the natural site (a) and for the one typical flow boiling event of Figure 3.15 at the artificial site (b).

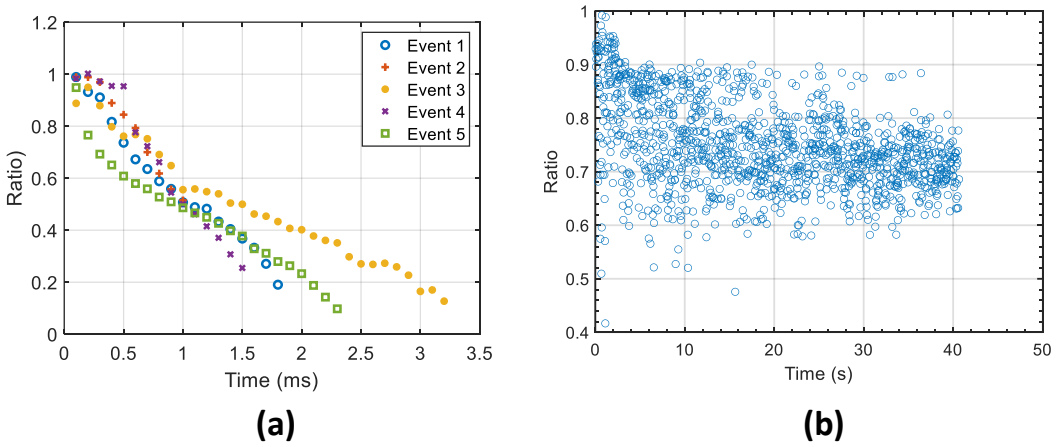


Figure 3.27 The ratio of the contact diameter to the bubble diameter as a function of time for the five boiling events of Figure 3.14 at the natural cavity (a) and for one typical boiling event of Figure 3.15 at the artificial site (b).

As mentioned above, the existence of a liquid microlayer in flow boiling has not been proved experimentally, and more importantly, it is not possible to be identified from captured images. The contact diameter at the natural site could be overestimated by the current imaging method, especially close to the incipience, because it is reported by Jung & Kim (2014) that the microlayer is eliminated in pool boiling when the bubble is close to the lift-off time. Similarly, such overestimation could happen for the contact diameter at the artificial cavity at the same time.

The comparison of the bubble contact diameter at the natural and the artificial cavity shows that the bubble contact diameter gains a maximum and then starts to reduce to zero at the lift-off time at the natural cavity. However, the contact diameter at the artificial cavity gradually increases, which contributes to an increase in the surface tension force, which resists the bubble's departure from the wall. The increase in the contact diameter is thought to be one of the reasons why the bubble growth period at the artificial cavity is much longer than that at the natural site.

3.10 Advancing and receding bubble contact angles

The contact angle is an important parameter that is required for the surface tension force calculation (Zhou et al., 2020b; Klausner et al., 1993). The nucleated bubble at the artificial cavity shows unique advancing and receding contact angle temporal evolution compared to that at the natural cavity. Therefore, the definition of the relevant bubble contact angles is important for the evaluation of bubble behaviour in flow boiling, and we will use those available from pool boiling. Two types of contact angles are reported in pool boiling because of the existence of the liquid microlayer below a bubble. One is called micro contact angle (θ_m) (Gao et al., 2013) or triple line contact angle (Hänsch & Walker, 2019) as it appears in the micro-region between the liquid-vapour interface. The second type is called apparent contact angle (Hänsch & Walker, 2019) or traditional contact angle (Gao et al., 2013), as it appears in the macro-region. These micro and apparent contact angles are denoted as θ_m and θ_a or θ_r respectively in Figure 3.28.

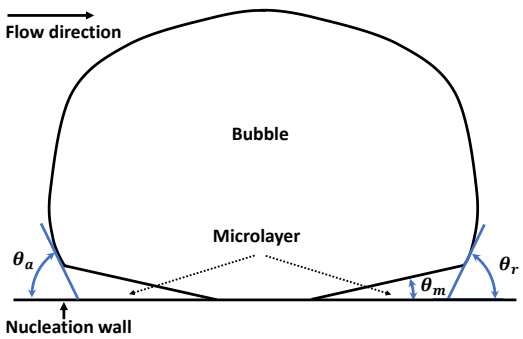


Figure 3.28 Definition of micro (θ_m) and apparent (θ_a or θ_r) bubble contact angles in pool boiling.

In flow boiling, experimental data on the liquid microlayer are not available (Owoeye & Schubring, 2016). The existence of a liquid microlayer in flow boiling has not been demonstrated, and, more importantly, the limited physical resolution of an advanced imaging system (6.61 μm/pixel) does not allow to distinguish the microlayer whose maximum thickness is expected to be around 4 μm as reported by Gao et al. (2013) and Jung & Kim (2014) in pool boiling.

All measured contact angles of this study in flow boiling refer to the apparent contact angles of Figure 3.28 in pool boiling. The effects of temporal evolution of microlayer (Jung & Kim, 2014) is negelected. These apparent contact angles are named as advancing contact angle (θ_a) and receding contact angle (θ_r) relative to the flow direction (Raj, Pathak & Khan, 2017). The estimation method of these angles is demonstrated in section 2.8.2.

3.10.1 Natural cavity contact angles

The temporal evolution of the advancing and receding contact angles of five typical boiling events at the natural cavity are presented in Figure 3.29. The contact angle measurement accuracy is reduced for small bubble sizes close to the incipience time and throughout the bubble growth process due to the refraction of light through the high thermal gradients near the bubble base. It is difficult to quantify accurately an error for each data point, but the maximum estimated error is evaluated as ± 15 ° due to the small bubble size and the high thermal gradients near the wall.

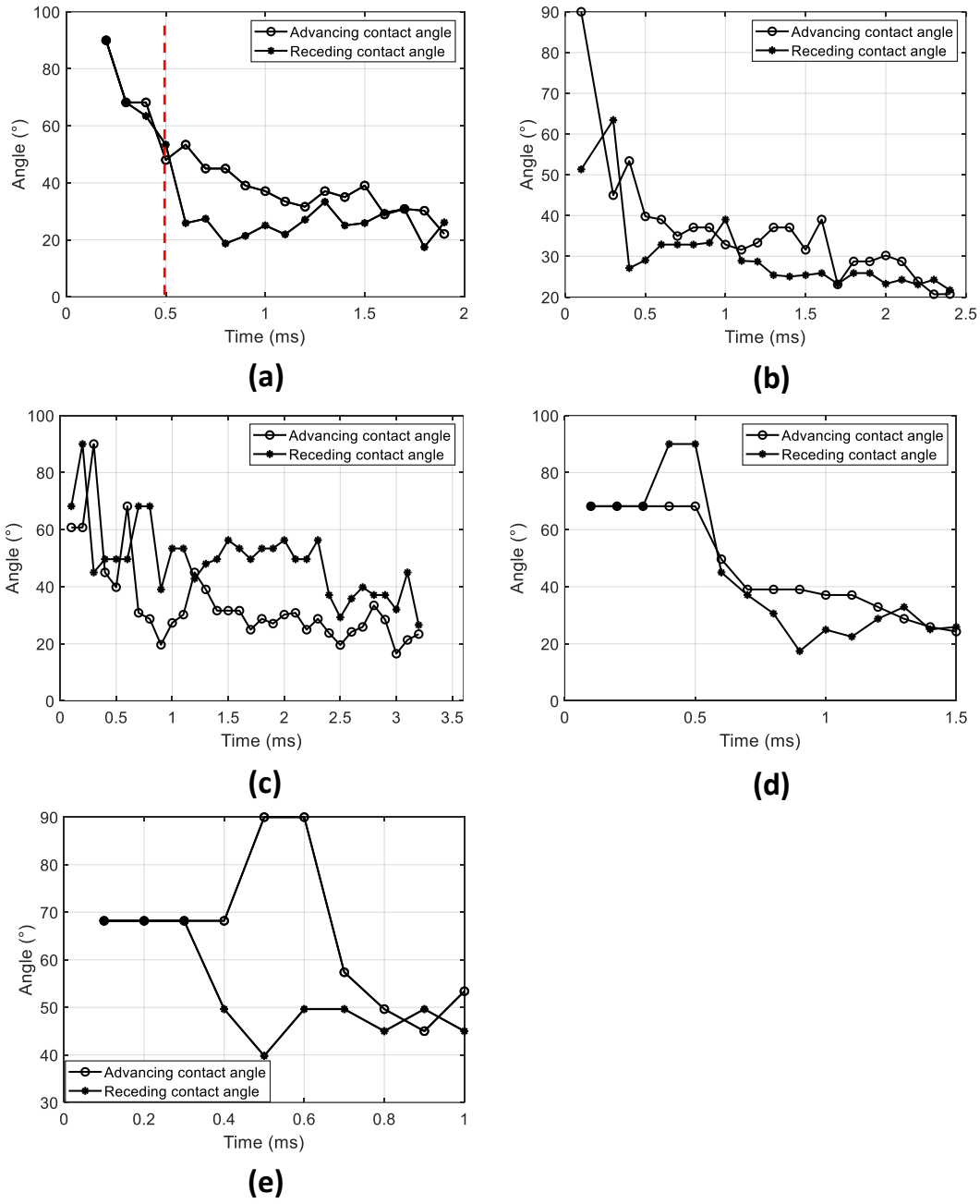


Figure 3.29 Temporal Evolution of advancing and receding contact angles for bubble event 1 (a), 5 (b), 3 (c), 4 (d) and 2 (e) with lift-off diameter of 729 µm, 880 µm, 1100 µm, 622 µm and 450 µm, respectively.

In these figures, at time 0.1 ms, both contact angles are in the range of 50-90 °. However, it seems that both angles for most bubble events tend to be the same due to the symmetrical bubble motion close to the incipience time. The angles tend to reduce after the incipience and have an approximate range of 20-30 ° just before the lift-off time except from event 2 in Figure 3.29 because of the bubble's indistinct edges near the base. The advancing contact angle is larger than the receding contact angle for all events except from event 3 in Figure

3.29 at time > 0.5 ms, where the advancing contact point starts to shift towards the receding contact point.

3.10.2 Artificial cavity contact angles

The temporal evolution of the advancing and receding contact angles during the bubble growth period is presented in Figure 3.30 (a & b), respectively, where time zero (defined with uncertainty of ±0.02 s) represents the estimated incipience time. The wide range of the temporal fluctuations of the angle is obvious on the figures and occurs because of the interactions between the flow and the bubble. That is why the trend in the two figures is not that clear. Data points in the two figures are connected with lines, and the density of lines represents the concentration range to some extent. In Figure 3.30 (a), the advancing contact angle is mainly distributed in three ranges: 70-90 ° (fenced by green lines), 60-70 ° (fenced by red lines) and 70-90 ° (fenced by yellow lines).

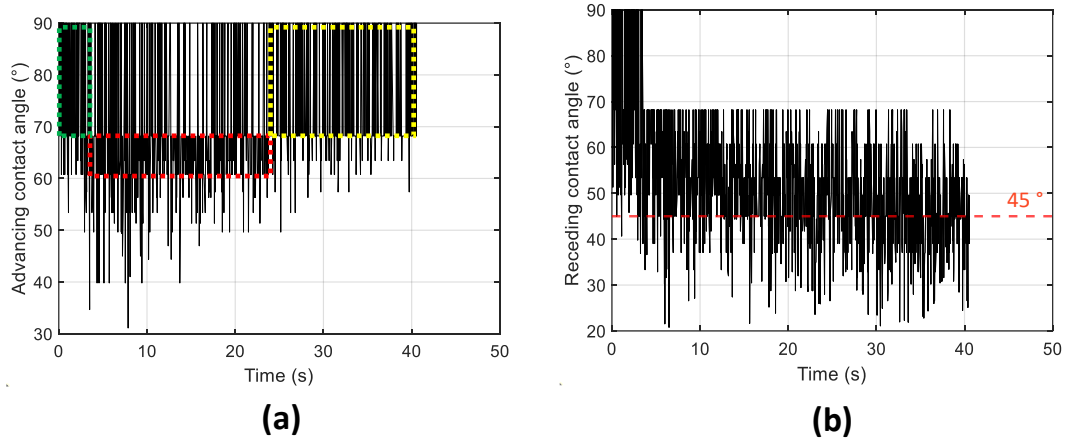


Figure 3.30 Temporal evolution of advancing contact angle (a) and receding contact angle (b) during the bubble growth period at the artificial cavity.

For times shorter than 3 s in Figure 3.30 (b), both angles are within 70-90 °. Later, the receding contact angle gradually decreases to around 45 ° at the departure time with an apparent fluctuation range between 20 and 70 °. It is obvious that both angles show a large scatter, maximum of around 60 °. Fluctuations of the contact angle of 50 ° are frequently observed for the receding contact angle at times > 3 s. Such fluctuations are resulted by the interactions between the flow and the bubble.

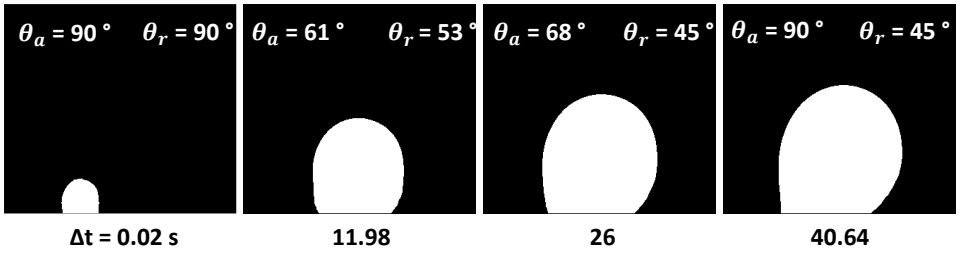


Figure 3.31 Values of advancing and receding contact angles and bubble shape temporal evolution at four times during the bubble growth period.

Figure 3.31 shows example images of the evolution of the bubble shape and both contact angles, which are plotted in Figure 3.30 (a & b) during the bubble growth period. The advancing contact angle reduces from 90 ° to 61 ° from time 0.02 s to 11.98 s, and after that time, it increases to around 90 ° at time 40.64 s. The general tendency of the receding contact angle is to reduce with time. Both contact angles adjust according to the bubble shape deformation, which is determined by the applied forces on the bubble. This information will be used later to evaluate the forces that the bubbles experience.

3.11 Bubble inclination angle

In Figure 3.9 (a), as a bubble grows, it is found that the bubble inclines in the flow direction. Such inclination is possibly the result of the drag force and inviscid interaction between the uniform flow and the flow induced by the expansion of the bubble (Klausner et al., 1993; Zeng et al., 1993). The inclination angle is required for the force estimation model on a bubble (Chen, Pan & Ren, 2012). Measurements of the inclination angle are not available in the literature. This section presents the measured inclination angle of five typical boiling events at the natural cavity and one single boiling event at the artificial cavity.

The inclination angle estimation method is explained here. As discovered in section 3.7.2, the advancing contact point position at the artificial cavity gradually approaches the cavity centre as the bubble size increases and remains at the upstream part of the cavity, even at times close to the bubble departure from the wall. As a result, the bubble inclination is gradually enhanced due to the relatively fixed position of the advancing contact point. In contrast, the advancing contact point at the natural site gradually moves across the cavity centre and approaches the receding contact point, which results in a moving contact area

centre along the wall and a gradually reducing bubble inclination. The sliding of the cavity centre on the wall is also reported by Golobic et al. (2009). Considering these facts, the inclination angle of bubbles at the artificial cavity is defined as an angle between the normal line at the cavity mouth centre and the line crossing this centre and the bubble mass centre, see Figure 3.32 (a). At the natural cavity, it refers to the angle between the normal line at the evolving contact area centre and another line crossing this centre and the bubble mass centre, see Figure 3.32 (b).

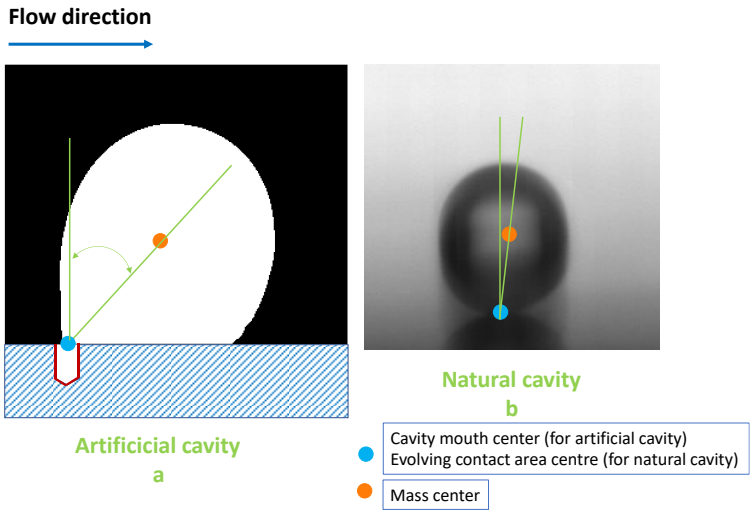


Figure 3.32 Inclination angle demonstration for artificial (a) and natural (b) cavity.

3.11.1 Natural cavity bubble inclination angle

The temporal evolution of the bubble inclination angle of the five typical events of Figure 3.14 at the natural cavity is presented in Figure 3.33. The maximum angle varies from 7.3-11.4 ° in the time range of 0.4-1 ms and mainly at around 0.6 ms. After this time, the bubble inclination angle starts to reduce. The time 0.6 ms coincides well with the turning moment of the advancing contact point, discussed in section 3.8, where the advancing contact point starts to shift towards the receding contact point.

This indicates that the reduction of the inclination angle is due to the gradual motion of the advancing contact point towards the receding contact point. At the extreme of the lift-off time, the bubble inclination angle tends to zero. An inclination angle of zero at the lift-off time is considered by Zeng et al. (1993). For bubble departure that is followed by sliding on the heater wall, an inclination angle of 10 ° is assumed at the departure time (Klausner et al.,

1993; Zhou et al., 2020b; Chen, Pan & Ren, 2012), which is confirmed by the measurements of maximum inclination angle indicated in Figure 3.33.

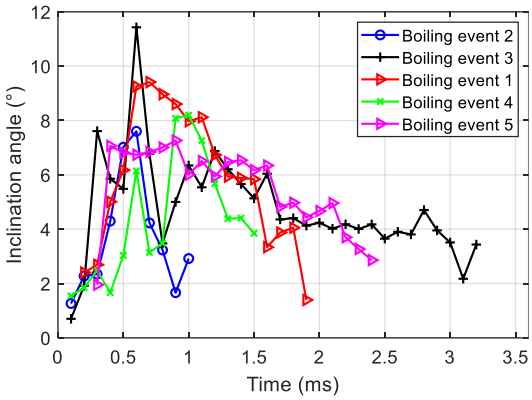


Figure 3.33 Temporal evolution of bubble inclination angle for the five typical boiling events of Figure 3.15.

3.11.2 Artificial cavity bubble inclination angle

Figure 3.34 (a) presents the temporal evolution of the inclination angle during the bubble growth period, where time zero represents the incipience time. The inclination angle gradually increases from zero to around 40 ° with several fluctuations. At the departure time, it jumps to around 49 ° from 40 °. This jump is clearly depicted in Figure 3.34 (b), which shows the inclination angle temporal evolution during the last 0.28 s before the departure time. In Figure 3.34 (b), the uncertainty of the measured inclination angle at time ranges 0-0.2s and 0.2-0.28 s is within +1.69 and -1.3 ° and +2.43 and -0.6 °, respectively.

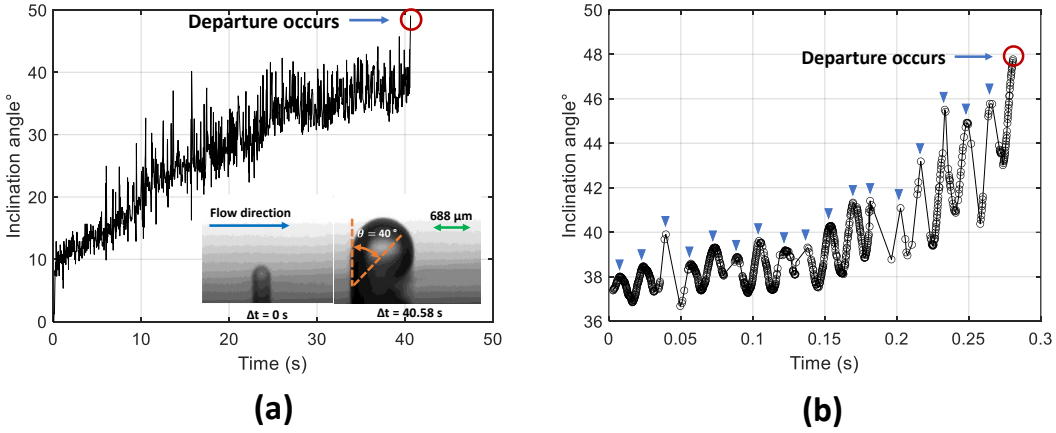


Figure 3.34 Temporal evolution of bubble inclination angle during the bubble growth period (a) and the time range of the last 0.28 s before the departure time (b).

In Figure 3.34 (a), the magnitude of temporal fluctuations of the inclination angle between two successive times (time interval around 0.02 s) increases to around 2.58 ° at times

> 10 s from 1.64 ° at times < 10 s. This indicates that the temporal fluctuations are enhanced after the time of 10 s. This enhancement is possibly the result of the increased bubble size and the corresponding drag force. During the growth period, the maximum magnitude of fluctuations of the inclination angle is around 22 ° between times of 15.74 and 15.76 s.

Figure 3.34 (b) shows that the inclination angle increases periodically to 48 ° from around 38 °. The angle difference between neighbouring peaks increases from 1.6 ° to 5 °. The average time between neighbouring peaks (indicated by inverted triangles) is around 0.0161s with a normalized standard deviation of 12.3 %. The formation of such periodic fluctuations of the inclination angle may indicate that a periodic shedding of vortices occurs behind the bubble as the liquid flows downstream. These periodic fluctuations are not observed in Figure 3.34 (a) Possibly, the low image frame rate is not high enough to reveal such periodic fluctuations. The literature does not provide any information on vortex shedding taking place behind a growing bubble during flow boiling. Future flow simulations and time-dependent flow measurements may verify the current suggestion. Such periodic shedding at the natural site is not observed because of the small growth time. During the average bubble growth time, the distance that the liquid moved is around 143 μm, which is around 21 % of the bubble average lift-off diameter. This indicates that the liquid flow has not moved completely around the bubble during the bubble growth time, and as a result, it is reasonable to expect that there is no vortex shedding downstream of the bubble at the natural site.

3.12 Bubble interfacial wave propagation speed

For bubbles growing at the artificial cavity, it is observed that, close to the departure time, the bubble inclines towards the flow direction with a neck (represented by two yellow dashed lines in Figure 3.35 (a) connected to the cavity mouth (represented by red lines in Figure 3.35 (a). As the bubble is slowly dragged away from the cavity, the neck is elongated, narrowed, and finally breaks. This breakage results in a shock initiating a wave propagating along the bubble interface from the breakage point to the end point. Figure 3.35 (c) shows approximately the wave front position on the bubble interface at a time 2.59 ms after the initiation. As the wave arrives at the end point, the whole body of the bubble gains an initial velocity and starts to slide on the wall for a distance and then lifts off from the wall.

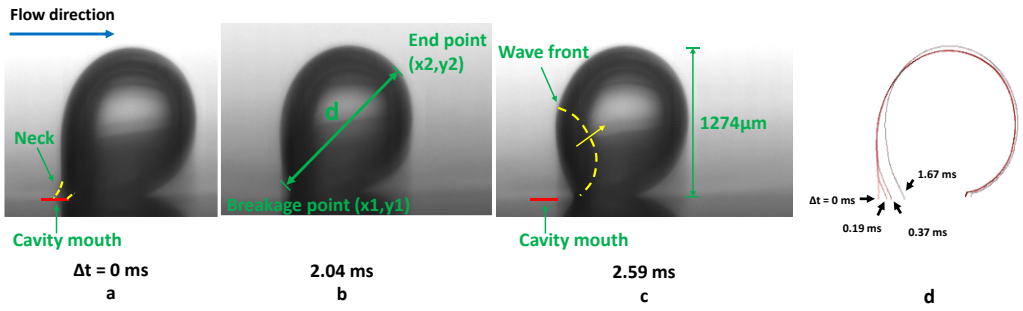


Figure 3.35 Temporal behaviour of boiling bubble on the cavity. Elongated neck (a), breakage of the neck (b), propagating wave along the interface (c) and the outline of the bubble temporal evolution (d).

The wave is observed to propagate along the bubble interface, and its average propagation speed is estimated. The propagation distance is estimated as the half-length of a circle perimeter with diameter d, which is the length between the neck breakage point and the propagation end, shown in Figure 3.35 (b). The wave propagation speed (U) is calculated from equation (3.13) and (3.14).

$$U = \pi * d/(2 * \Delta t) \tag{3.13}$$

$$d = L * \sqrt{(x_1 + x_2)^2 + (y_1 + y_2)^2} \tag{3.14}$$

The mean propagation speed from the current experiment is 125.5 cm/s with a standard deviation of 8.0 cm/s for a sample size of 22. A bubble wave front velocity of 63cm/s is reported by Siedel, Cioulachtjian & Bonjour (2008) due to the breakage of the liquid film between two bubbles, which is about half of that found in the current results. Possibly, the generated shock accelerates the propagation speed.

3.13 Bubble shape evolution

The shape of a bubble that lifts-off from the natural site varies after a certain time (from 1.5 to 8.3 ms), while this is not observed for bubbles lifting-off from the artificial cavity at a time of 20 ms. Figure 3.36 shows the shape evolution for 11 events (S1-S11), where Δt = 0 represents the start time when irregular bubble shapes are observed. The irregular shapes usually exist for 1 ms. The bubble shape is more spherical before and after this period. After this period, the bubble size reaches a stable value, as seen by images fenced by the green line in Figure 3.36.

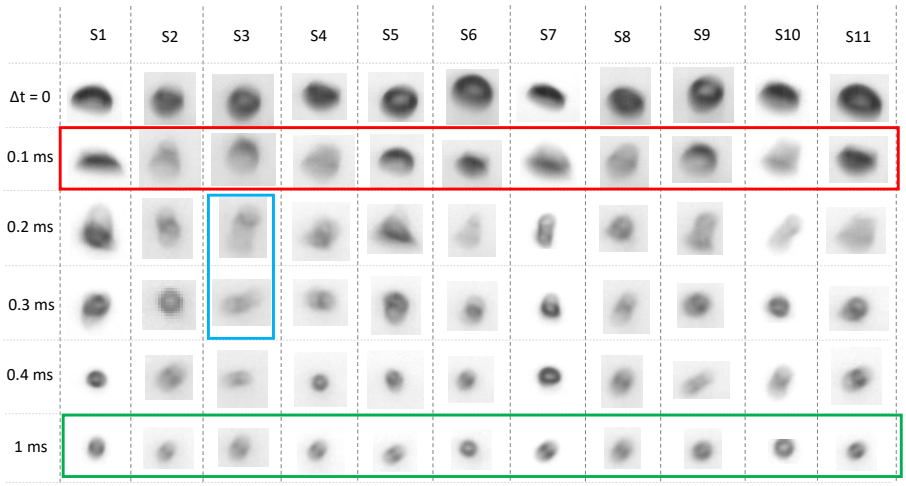


Figure 3.36 Irregular bubble shape observations for 11 events of bubble lifting-off from the natural site.

The images fenced by the red line have a somewhat pyramid-like shape. During this 1 ms, tails are observed in the images, such as the two identified by the blue line. The integrating time for one image is 0.1 ms, and the formation of the tail either is artificially generated by the relatively fast displacement of the bubble or the tail does exist and accompanies the bubble's main body. Finally, the green line indicates bubbles with a shape that becomes spherical at late times.

This difference in bubble shapes between bubbles lifted from artificial and natural sites indicates that condensation mechanisms are different. The non-condensable gas possibly plays a role. In addition to that, the temperature of the bubble lifted from the artificial cavity is higher, and a thick thermal layer surrounds the outer layer of the bubble, which slows down the condensation rate. Additional research is required for the investigation of this bubble behaviour.

3.14 Nucleation wall deposition Patterns

A fan-shaped pattern is found on the surface of the nucleation wall around the artificial cavity after performing experiments, while the surface of the nucleation wall was perfectly clean at the start of the experiment. Such patterns are also widely found on the surface around natural sites when the wall superheat is increased to 20 °C. The patterns' height, element type, dimensions, and angle are reported in section 3.14.1. Tracking the deposit patterns on the wall enables localising two types of natural cavities in the current work for the first time. The theoretical estimation of the required boiling initiation temperature at one type of natural site

is reported in section 3.14.2. Section 3.14.3 reports the probabilistic distribution of natural site types on the nucleation wall.

3.14.1 Fan-shaped patterns on nucleation wall

The fan-shaped patterns on the surface of the nucleation wall in the region of the artificial sites were observed first. Then, similar patterns were identified at other parts of the wall, which were close to the region of the natural nucleation sites. The literature has not reported the existence of such patterns on nucleation surfaces. It is noted that it is difficult to identify such patterns on commonly used walls since many natural nucleation patterns are present. However, in the current study, since artificial sites were considered and the surface was very smooth, it was possible to identify these patterns. The origin of these patterns is not clear.

This section attempts to understand the origin of these patterns and presents measurements of the surface material height distribution along the fan-shaped patterns on the nucleation surface and the material elements present on the surface. In addition, a qualitative analysis of the pattern radius, direction and angle is provided. The results show that the fan-shaped patterns are due to a deposition layer, which includes some elements that are present in the working liquid.

(a) Experimental observations of fan-shaped patterns

A few natural cavities remain on the nucleation wall despite the low surface roughness, which led to the nucleation of bubbles from them during flow boiling. The bubble dynamics from these cavities behave in a similar way to those reported for natural cavities in flow boiling studies from the literature. Therefore, it is interesting to identify the types of natural nucleation sites on the surface. Examination of the surface with a confocal microscope (model: 3D Measuring Laser Microscope OLS5000) identified two types of natural cavities (Ra = 0.0495 μm). The natural cavities that act as active boiling sites are identified by fan-shaped patterns that are formed on the surface during boiling. The origin of these fan-shaped patterns will be examined later. The two types of natural cavities that have been identified are as follows.

'Type 1' natural cavities: These are physical cracks or indentations on the polished surface. Typical images of such cavities are shown in Figure 3.37 (a-d) and are represented by the black circular areas. Their diameter varies from 7 to 25 μm, and their depth varies between 3 and 26 μm. The depth profiles of the cavities of Figure 3.37 (a-d) were also measured and are presented in three-dimensional graphs in Figure 3.37 (e-h). The measured interior geometry of the cavities of Figure 3.37 (a & d), Figure 3.37 (b), and Figure 3.37 (c) are cylindrical, conical and irregularly shaped, respectively. It is the first time in the literature that the interior and exterior geometry and the accurate location of active natural sites on the wall are reported. The cavity geometry information is hypothesised via schematic drafts in literature (Hsu, 1962; Chi-Yeh & Griffith, 1965b; Kandlikar et al., 2006)**.** This finding supports the bubble initiation mechanism, suggesting that physical cracks or indentations served as natural boiling sites.

'Type 2' natural cavities. These are boiling sites where obvious natural indentations or cracks are not observed. The existence of the fan-shaped patterns indicates active nucleation sites. One explanation is that this type of cavity is natural cracks or surface defects that have a size smaller than 0.25 μm, which was the resolution of the used confocal microscope. Another explanation is that distinct physical surface features are not required for boiling initiation. However, it is expected that the surface materials will always have some irregularities/non-uniformities at these small scales. As such, an open question remains related to the bubble initiation mechanism and the possible minimum size of surface imperfections that can initiate bubbles during boiling. The current study suggests that if there is such a surface imperfection size threshold for bubble initiation, this must be smaller than 0.25 μm.

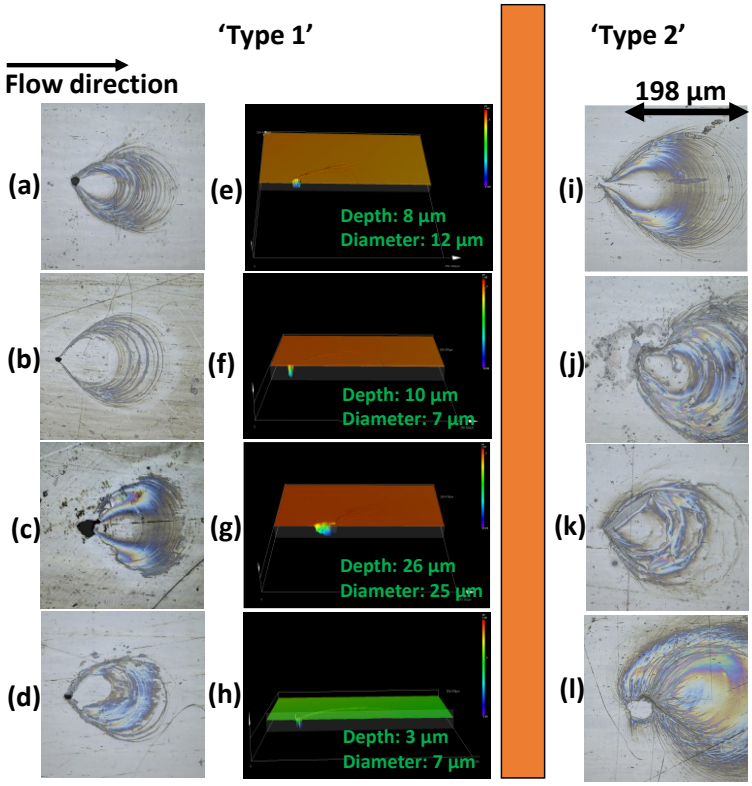


Figure 3.37 Images of fan shaped surface patterns and type 1 natural cavities (shown with the black circular shape at the start of the fan shaped patterns) (a-d), cross-section of type 1 natural cavities (e-h) and fan shaped surface patterns for type 2 natural cavities (the shape and size of the natural cavities cannot be detected at the start of the fan shaped patterns) (i-l).

The measured cavity images and the associated fan shaped patterns allow the assessment of pattern symmetry of cavities type 1 and 2. The symmetry is assessed relative to the flow direction. It is observed that the fan patterns are always symmetrical for cavities type 1, see Figure 3.37 (a-d). However, asymmetrical fan shaped patterns are present at cavities type 2, see Figure 3.37 (j) and (l).

It is thought that the symmetrical fan shaped surface patterns observed at type 1 cavities are the result of single fixed-location physical cavities that act as nucleation sites. The existence of asymmetrical fan patterns of type 2 cavities requires some explanation. It is possible that the asymmetrical pattern is the result of several very small nucleation sites close to each other in a small surface area, and the probabilities of activation of each site are not equal. As a result, the remaining fan shaped patterns are asymmetric. This hypothesis is demonstrated in Figure 3.38, where the green dots represent potential small nucleation sites. Since the current study of boiling at artificial cavities focused on symmetrical cylindrical

geometries only, it may be useful in the future to manufacture asymmetrical artificial cavities and evaluate if the resulting fan shaped surface patterns are asymmetrical.

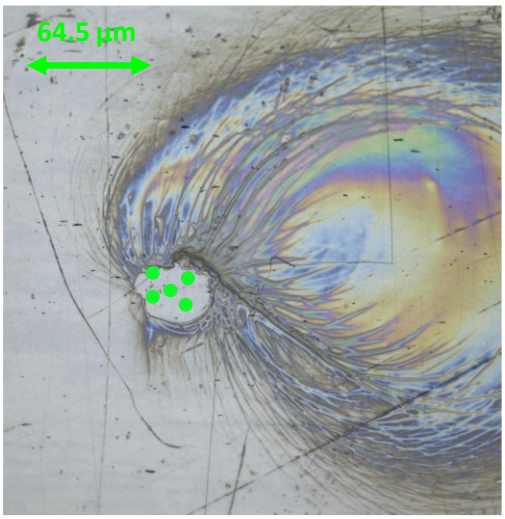


Figure 3.38 Possible multiple small nucleation sites (green dots) present in a small region, which initiate the asymmetrical fan shaped patterns on the surface.

(b) Surface material height distribution across fan-shaped patterns

The height distribution across the fan-shaped patterns of Figure 3.37 (i) is evaluated to understand the origin of these patterns. The height distribution is presented in Figure 3.39 along the purple line superimposed on the image of the fan-shaped patterns, which is measured by the confocal microscope. The height of the surface profile increases at the existence of the pattern (arrow 1), and height reduces to zero at the end of the pattern (arrow 2), which indicates that the pattern distribution coincides accurately with the pattern area. The height goes below zero due to the relatively small surface height. The height distribution shows that peaks (height of 0.4 µm) exist across the pattern area, which indicates that the pattern is associated with a deposition layer. It is also observed that the thickness of the layer varies along the purple line.

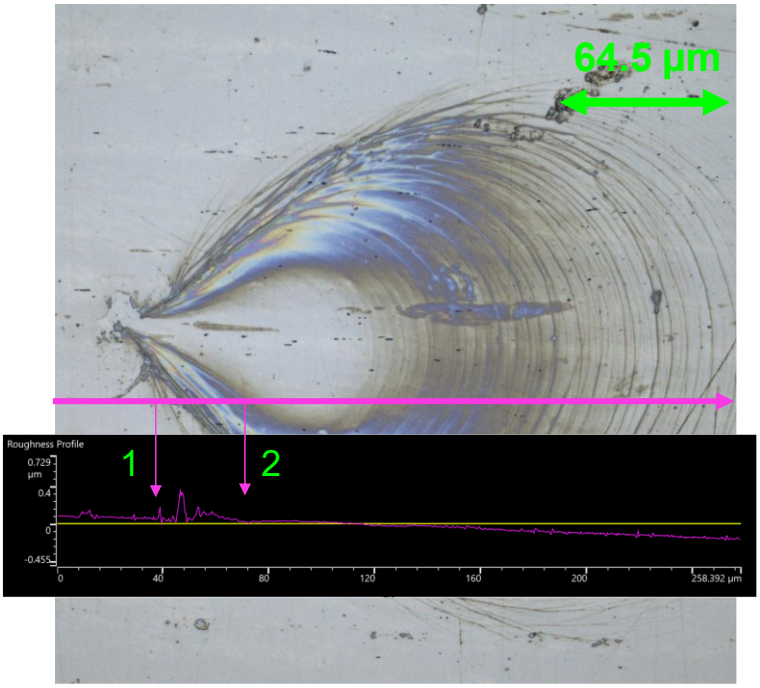
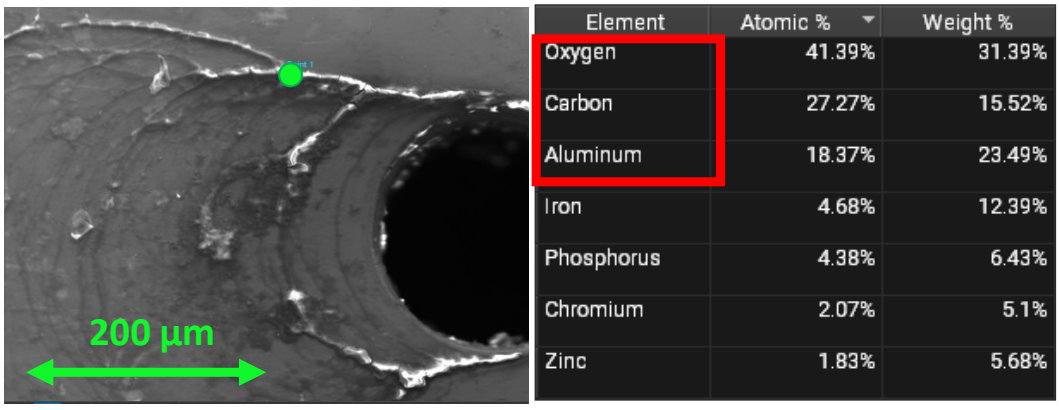


Figure 3.39 Height distribution along the purple line crossing the fan-shaped pattern, which indicates the presence of deposited material.

(c) Material elements present on the surface close to the fan-shaped patterns



Element	Atomic %	Weight %
Oxygen	41.39%	31.39%
Carbon	27.27%	15.52%
Aluminum	18.37%	23.49%
Iron	4.68%	12.39%
Phosphorus	4.38%	6.43%
Chromium	2.07%	5.1%
Zinc	1.83%	5.68%

Figure 3.40 Measurement point (green dot) at the fan-shaped pattern (a) and list of detected element content of the deposited material (b).

The surface material element composition close to the fan-shaped pattern was measured by Energy-dispersive X-ray Spectroscopy (EDS). The measurement point represented by a green dot is shown in Figure 3.40 (a), which is within the fan-shaped pattern. The list of the detected element types and corresponding weight (%) at the measuring point is shown in

Figure 3.40 (b). It is shown that the top three elements are oxygen, carbon, and aluminium, with weight contribution to the deposit of 31 %, 16 % and 23 %, respectively.

Interestingly, these three elements were also detected in the working liquid. To detect the dissolved elements in the water, a liquid film remaining on the nucleation surface is evaporated by keeping the surface at a temperature of 45 °C for one hour. Images of the nucleation surface before and after the evaporation of the water are shown in Figure 3.41 (a) and (b), respectively. After the evaporation, a white layer is found on the surface, and the magnified image of the white layer is shown in Figure 3.41 (c).

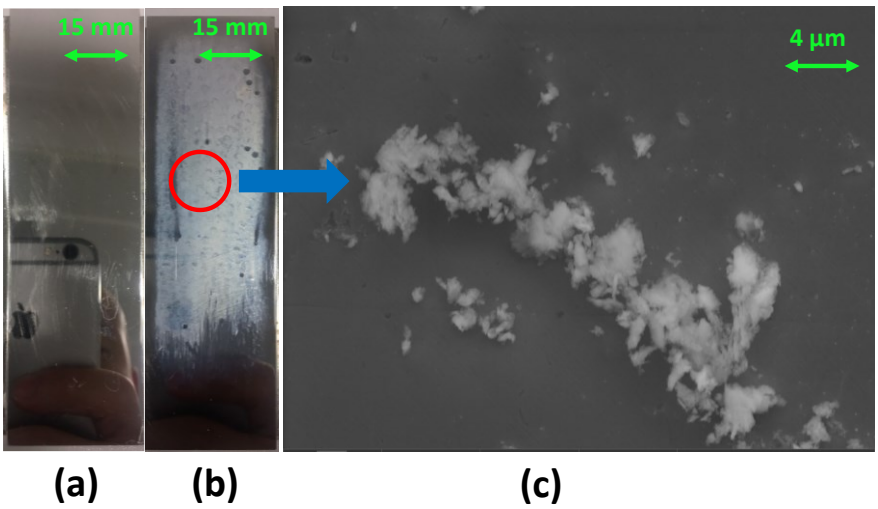


Figure 3.41 Images of the nucleation surface with the liquid film (a) and after the evaporation of the liquid film (b) and the magnified image of the white layer of deposit (c).

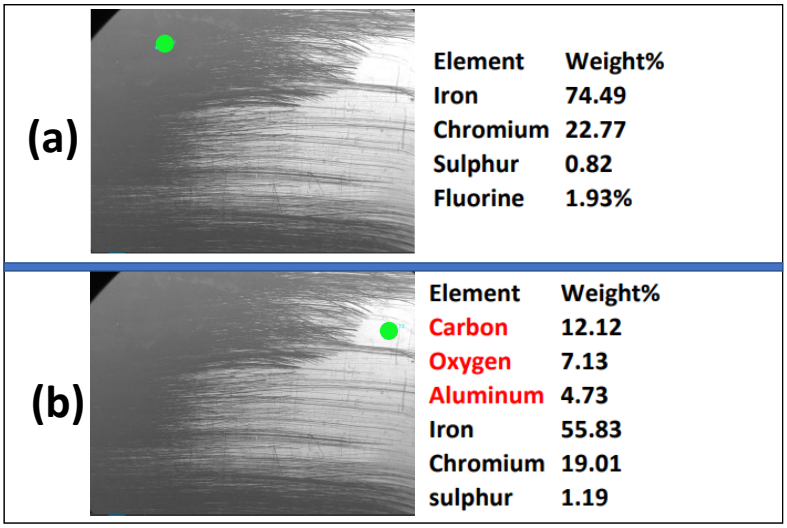


Figure 3.42 List of analysed elements and the measurement position (green dot) at the clean nucleation surface (a) and at the white deposit layer (b).

The material element content of the deposited white layer is measured. The measurement positions (represented by green dots) at the white layer and clean nucleation surface are marked in Figure 3.42 (a) and (b), and the detected elements are shown in the list beside the images. The top two elements detected at the nucleation surface are iron and chromium in weight per cent of 75 % and 22 %, respectively, which is consistent with the element composition of stainless steel 316L. Thus, the accuracy of the measurement technique is demonstrated.

The results have shown that the top three elements detected in the fan-shaped pattern are also detected in the deposited layer on a surface after evaporating the working liquid; see the top three elements in Figure 3.42 (b). This indicates that the fan-shaped patterns are formed from a deposit extracted from the liquid. The detected aluminium and oxygen element in the liquid is probably extracted from the aluminium tube of the experimental facility by deionized water. The carbon-based deposits might be a result of something else present in the rig or contaminants.

(d) Fan-shaped dimensions and axes of symmetry

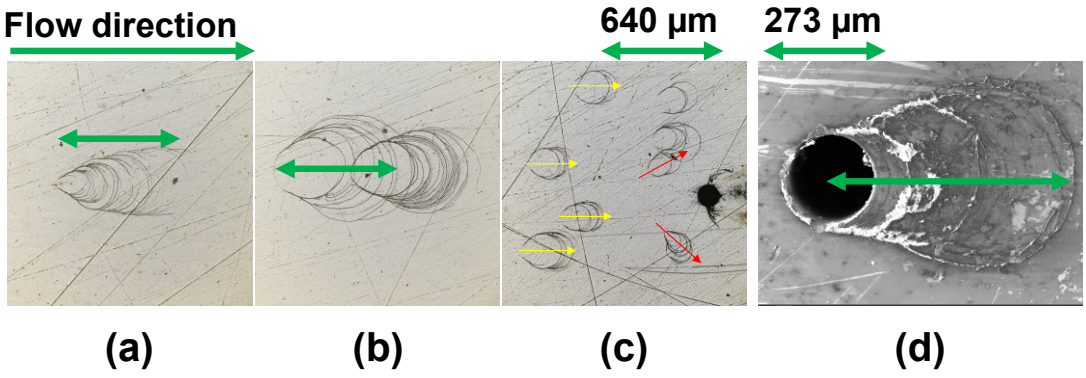


Figure 3.43 Images of fan-shaped patterns captured on the same nucleation surface.

Figure 3.43 (a, b & c) and (d) shows the images of fan-shaped patterns captured at natural sites and the artificial cavity (diameter of 200 µm), respectively. The bubble size at these natural sites is unknown, although the previously presented results provide information on the bubble dimensions. The maximum dimension of the fan-shaped patterns in Figure 3.43 (a), (b) and (d) is measured in the flow direction, and the two-way arrows on these figures represent a length of 640, 640 and 546 µm, respectively. However, the maximum dimension

captured in Figure 3.43 (c) is 210 μm, which is smaller than those in Figure 3.43 (a), (b) and (d). All patterns shown in Figure 3.43 (a, b & c) are captured on the same nucleation surface with the same length scale. It is interesting to note that an overlapping pattern area is observed in Figure 3.43 (b). It is not clear if the two patterns are generated at the same time or if one is formed independently from the other at different times. In addition, the pattern size at the downstream region is smaller, which might be because of the influence of an upstream bubble modifying the size of the second bubble and, therefore, its pattern size.

The one-way red and yellow arrows in Figure 3.44 (c) indicate the axis of symmetry of the patterns. The yellow arrows coincide with the main flow direction. However, the direction changes for the red arrows for natural sites close to the artificial cavity, a black circle dot in the figure. This alteration of direction can be better observed when imaging a larger area of the nucleation wall with dimensions of 22.2 x 22.2 cm (Figure 3.44) close to the artificial cavity. In this figure, 63 patterns are present at natural cavities, as well as those associated with the two artificial cavities with diameter and spacing of 0.2 and 0.6 mm respectively, which can be seen as black dots outlined by green circles at the central region. In general, most of the patterns have an axis of symmetry in the same direction (yellow arrows), which coincides with the flow direction. There are only three patterns that perform differently, and their axes deviate from the flow direction and are indicated by red arrows. It is thought that the axes of these patterns are affected by the local flow direction. This is supported further by the fact that the red arrows are close to the two artificial cavities. Those that are upstream of the artificial cavities may deviate from the main flow direction because the generation of bubbles at the artificial cavity makes the liquid flow direction to change at local areas. The third red arrow downstream of the artificial cavities may also suggest that the bubbles at the artificial cavities generate a wake in the liquid flow that leads to a reversal of the local flow direction.

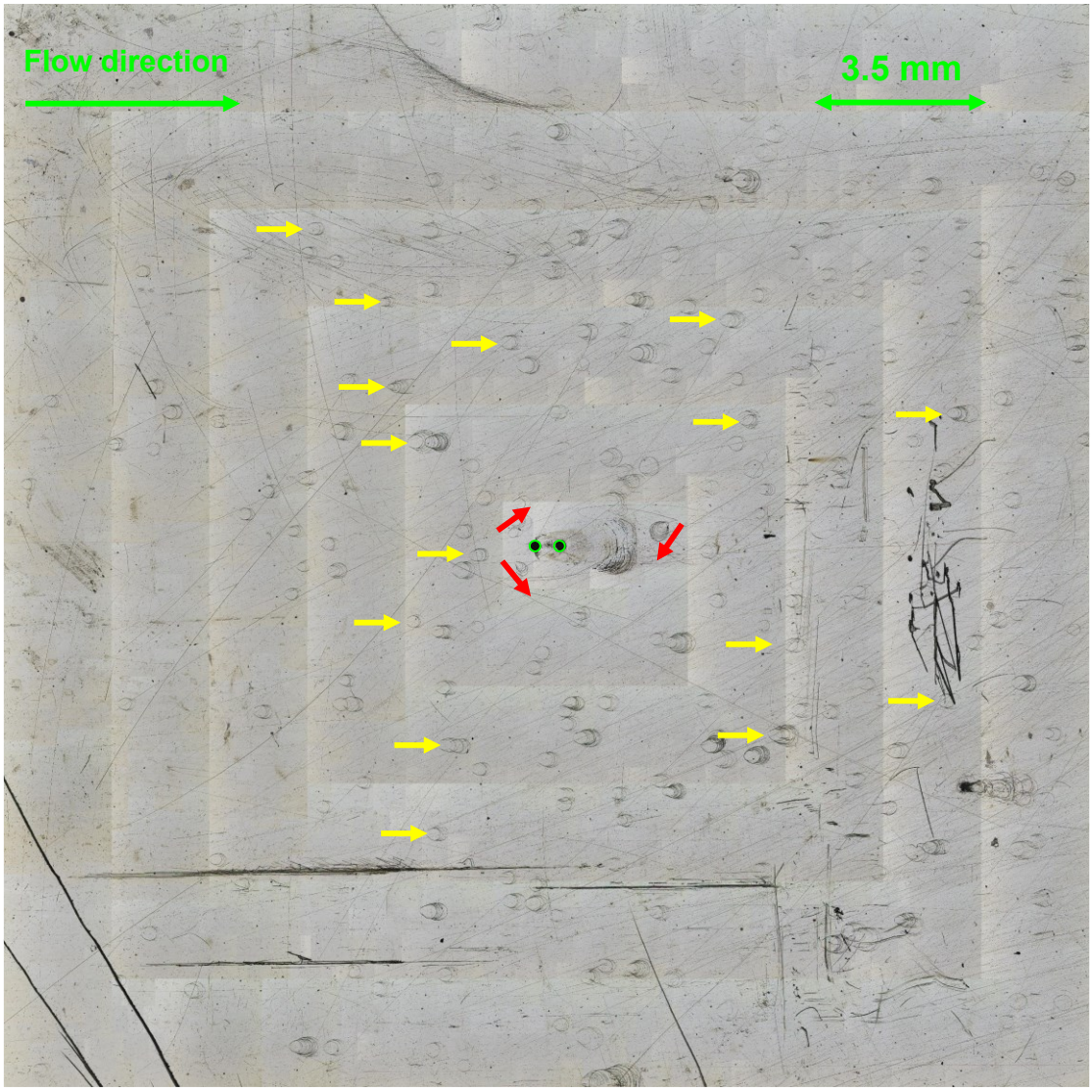


Figure 3.44 Square image (dimensions of 22.2 mm) of the nucleation wall surface, which shows numerous recorded fan-shaped patterns after the completion of the flow boiling experiments. The two black dots (outlined with green circles) at the central area are artificial cavities with diameter and spacing of 0.2 and 0.6 mm, respectively. The yellow arrows indicate the axis of symmetry of the patterns that coincide with the main flow direction, while the red arrows indicate the axes of patterns that deviate from the flow direction.

(e) Fan-shaped pattern angle

The fan-shaped patterns can be fitted by arcs at various distances from the cavity site and with the centre of a corresponding imaginary circle located on the axis of symmetry; see the three patterns of Figure 3.45. It seems that the arcs are in a fan-shaped area with an angle that is defined by the two yellow dashed lines. The arc centres in Figure 3.45 (a), (b) and (c) are located at the green dots. It is found that as the size of the arc increases, the position of the arcs moves along the flow direction with a maximum distance of 134 μm from the position of

the cavity to the second green dot along the flow direction. In Figure 3.45, the maximum movement distance of the contact area centre from the initial nucleation site centre to the position of the contact area at the lift-off moment is 140 μm. These two values are very close. This consistent behaviour suggests that the green dots in Figure 3.45 represent the evolutional bubble contact area centre, which has been quantified earlier in this chapter. As a result, the patterns possibly refer to the evaporated liquid at the contact line of the bubble that grow at the nucleation sites.

Based on the above hypothesis, a mechanism responsible for the formation of the fan-shaped patterns is hypothesised. Based on the finding in section 3.14.1, the working liquid contains suspended elements of aluminium, oxide, and carbon. The formation of the pattern is possibly due to the evaporation of liquid underneath the bubble, causing the suspended elements to deposit. The pattern forms downstream of the nucleation site because the receding contact point is located at a position for a relatively long time without movement, which provides enough time for the liquid underneath the bubble to evaporate. The position evolution of the receding contact point can be found in Figure 3.19. It is reported that the microlayer underneath the bubble is gradually eliminated due to the evaporation (Hänsch & Walker, 2019; Jung & Kim, 2014). As a result, the dry spot area gradually increases, and the contact line gradually shrinks toward the downstream of the cavity due to the evaporation of the microlayer during the bubble growth on the wall. This possibly is the reason that several lines are observed in each pattern. Therefore, it is possible that the formation of the fan-shaped patterns is assisted by the high wall temperature at the dry area below the bubble and the liquid evaporation.

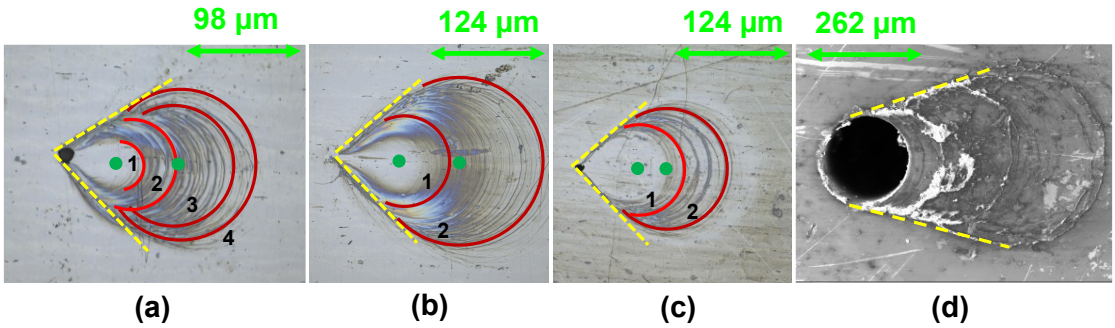


Figure 3.45 Fan-shaped patterns detected at natural sites fitted by red arcs and angle definitions for natural cavities (a, b & c) and the artificial cavity (d). The green dots show the corresponding centre of the added arc section.

The angles of the 63 patterns developed at the natural sites of Figure 3.44 are measured and presented in Figure 3.46. The average value is 73 ° with a standard deviation of 9 °. The average angles of all type 1 and type 2 natural cavities are 76 ° and 73 °, respectively, which is very similar and suggests that the effect of natural cavity size on the angle is negligible. This happens probably because the size of the natural cavities is small. In contrast, the angle at the artificial cavities is 34 °, which is quite different from those at natural sites and caused by the increased size of the cavity mouth diameter. Figure 3.45 (d) shows an example of patterns observed at the artificial cavity. Since the artificial cavities lead to larger bubble sizes during lift-off, this possibly also affects the angle and the size of the corresponding fan-shaped patterns.



Figure 3.46 Angles of the 63 fan-shaped patterns detected on the nucleation wall surface.

3.14.2 Theoretical estimation of the required onset temperature of boiling at natural cavity type 2

In section 3.14, it is speculated that type 2 cavities could be naturally occurring cracks that have a size smaller than 0.25 μm. In this section, the required onset wall temperature for a cavity of this size is estimated based on existing correlations. The operation of type 1 natural cavities as nucleation sites can be explained by the Pre-Existing Nucleus Theory (PEN) reported by (Dinh et al., 2003), stating that air is trapped inside the cavity, which serves as the embryo for boiling. A detailed explanation of this can be found in Qi & Klausner (2005). Two popular models based on the PET theory to estimate the required wall superheat

for bubble initiation come from the work of Griffith & Wallis (1960) and Hsu (1962) and are utilized here.

(a) Model one

Griffith & Wallis (1960) proposed a model which is accepted by Euh et al. (2010) and Song et al. (2021). In this model, the bubble interface gradually expands after the initiation, and, thus, the interface tip gradually shifts from the cavity interior to the outside. The radius of the bubble curvature, which is assumed to be equal to the cavity mouth radius, is defined as a critical radius. To initiate the growth of a bubble, this critical radius determines the required onset wall superheat. The pressure difference across the bubble interface at this time can be expressed by the surface tension and the cavity radius.

$$\Delta P = \frac{2\sigma}{r_c} \tag{3.15}$$

where ΔP, σ and r_c refer to the pressure difference across the bubble interface, surface tension force and cavity radius, respectively. It is assumed that, currently, the bubble is at an equilibrium state where the vapor inside the bubble is at the saturation temperature corresponding to its pressure. The liquid temperature is equal to a superheat temperature.

The excess temperature of the liquid can be related to the pressure difference across the interface through the Clausius-Clapeyron equation, see equation (3.15):

$$\frac{dP}{dT} = \frac{h_{fg}}{T\,\upsilon_{fg}} \tag{3.16}$$

Thus, equation (3.16) is rewritten as:

$$\frac{\Delta P}{(T_w - T_{sat})} = \frac{h_{fg}}{T_s\,\upsilon_{fg}} \tag{3.17}$$

where T_w, T_{sat}, h_{fg} and υ_{fg} refer to the wall temperature, saturation temperature, the latent heat of evaporation and the specific volume difference between liquid and vapour.

Substituting equation (3.15) into equation (3.17), the required wall superheat (ΔT_{ONB}) for the initiation of nucleate boiling can be expressed by equation (3.18):

$$\Delta T_{ONB} = T_w - T_{sat} = \frac{2\sigma T_{sat} \upsilon_{fg}}{r_c h_{fg}} \tag{3.18}$$

(b) Model two

Hsu (1962) derived a model to predict the active cavity size range at a given wall superheat. It is strongly dependent on the finite thickness of the thermal layer. The effect of the temperature profile and contact angle of the nucleation surface are not included. Yang, Guo & Liu (2016) reported that subsequent researchers incorporated the effects of various parameters based on Hsu's model, and such a model is used by Zhang, Zhang & Xu (2018) and Chu & Yu (2009).

This theory states that the bubble nucleus would grow only if the minimum temperature surrounding the bubble (i.e., the temperature at the tip of the bubble) is at least equal to the saturation temperature of the vapour inside the bubble. The mathematical expression of Hsu's model is given in equation (3.19)

$$R_{min} = \frac{\delta}{2C_1}\left[1 - \frac{T_{sat} - T_{bulk}}{T_w - T_{bulk}} - \sqrt{(1 - \frac{T_{sat} - T_{bulk}}{T_w - T_{bulk}})^2 - \frac{4AC_2}{\delta(T_w - T_{bulk})}}\right] \tag{3.19}$$

where δ, T_{sat}, T_w and T_{bulk} refer to the thermal boundary thickness, saturation temperature, wall temperature and bulk liquid temperature, respectively.

(c) Results from prediction models

The onset temperature as a function of the cavity diameter, predicted by models one and two, is presented in Figure 3.47 (a) and (b). It is found that the minimum wall superheat required to initiate boiling at a cavity with a diameter of 0.25 μm is 260 K and 54 K based on models one and two, respectively. However, the maximum wall superheat in this study is 20 K.

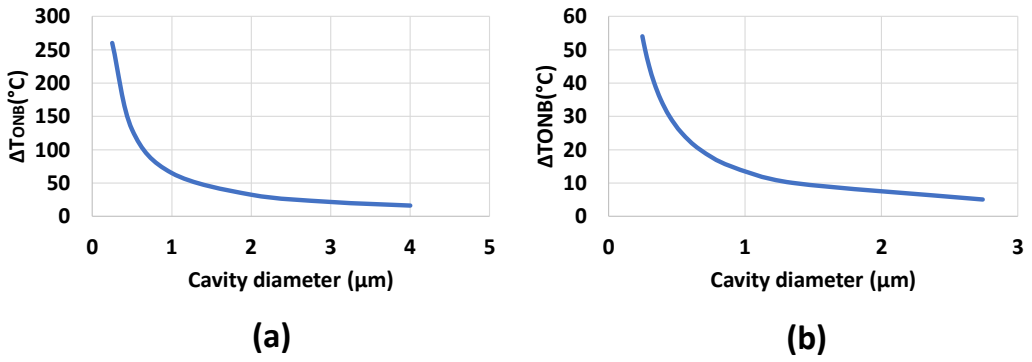


Figure 3.47 Minimum onset temperature predicted by models one (a) and two (b) as a function of cavity size.

Similar temperature overestimation is reported on nano smooth surfaces (Dinh et al., 2003; Theofanous et al., 2002; Nam & Ju, 2008; Bon, Guan & Klausner, 2011). Possibly, this similarity is due to the surface roughness (6 and 49.5 nm) of this study, which is in the nanoscale. The internal geometry of the cavity has been considered the main reason for the discrepancy between experimental observations and predicted wall superheats (Baldwin, Bhavnani & Jaeger, 2000). Another possibility is that some factors are not included, for example, the surface tension. In addition, it may be that the existing initiation theory is not suitable for the current study. It has also been reported that nanobubbles existed on the surface (Tyrrell & Attard, 2001; Lou, Ouyang & Zhang, 2000), which could grow on the surface even in the absence of micro cavities. Tyrrell & Attard (2001) suggested that nucleation does not occur on preferential sites like surface defects due to the existence of nanobubbles. However, there is no doubt that the wall superheat of the current study is correctly measured. Therefore, there may be an important physical process that is missing from existing computational models, and more experimental research is needed to identify the detailed physics of bubble initiation during boiling.

3.14.3 Probability of active cavity types

Finally, additional information that can be derived from the patterns is the probability of the types of active cavities on the nucleation wall. Figure 3.44 shows that 61 out of the 63 natural sites are type 2, and only 2 out of 63 are type 1. Therefore, it appears that type 2 cavities (which are smaller than 0.25 mm - the resolution of the microscope) play an important role in the initiation of flow boiling. Therefore, this suggests that the most popular

bubble initiation mechanism, the pre-existing embryo, may not be the main mechanism for boiling from low-roughness nucleation surfaces, such as the one used in the current study.

3.15 Summary

Studies of flow boiling at artificial cavities are limited. This chapter provides a comparison of bubble characteristics at artificial and natural cavities for the same operating condition (case 7 of Table 4.1). By comparing the different characteristics in terms of various parameters, the role of the artificial cavity on the dynamic bubble characteristics is revealed. The findings are summarized as follows. It is noted that the measured advancing and receding contact angle and the inclination angle will be used in section 5.5 for the estimation of the forces applied on a bubble.

1. The bubble growth time, waiting time and lift-off diameter are critical parameters for the evaluation of flow boiling performance. Their features are summarised in terms of the absolute value and the relative standard deviation.

   (a) Absolute Values

   The average bubble growth time is more than three orders of magnitude longer at the artificial cavity than at the natural nucleation cavity. This is possibly caused by the larger size of the artificial cavity mouth, which is suspected to generate a stronger surface tension force that keeps the bubble attached on the wall. This will be explored further in section 5.5.

   The waiting time is more than two orders of magnitude shorter at the artificial cavity than at the natural cavity. This behaviour is due to the remaining vapour inside the cavity, which serves as a nucleation embryo. The lift-off bubble diameter is around two times larger at the artificial cavity than at the natural cavity. The increased diameter at the artificial cavity is possibly due to the larger drag force. Section 5.5 evaluates this hypothesis.

   (b) Relative standard deviation

   The relative standard deviation of the fluctuations of bubble growth time, waiting time and lift-off diameter at the natural site is much larger than that at the artificial cavity. This indicates that boiling at the natural site is stochastic, in agreement with the literature. The

low relative standard deviation of the fluctuations of bubble characteristics at the artificial cavity shows stable boiling process. This is possibly attributed to the increased surface tension force at the large cavity diameter, which helps to keep the bubble attached to the wall for a long time. This feature is also in agreement with limited available literature. The stable performance of the boiling process is helpful to reduce the pressure fluctuations during the boiling.

2. The temporal evolution of the bubble diameter during the growth period and condensation period measured. The bubble growth rate at the artificial cavity is much smaller than that at the natural sites. The growth of the bubble at the natural sites is explained by the contributions of the evaporation from the microlayer, superheated layer and condensation layer. However, the contributed bubble diameter by the three sources does not match the measured temporal evolution of the bubble diameter. Thus, the growth rate at the artificial sites is different from that at the natural sites. It is hypothesised that the non-condensable gas, present in the liquid, plays a role on bubble growth in addition to the three sources mentioned above. Similar conclusions are obtained for the bubble condensation mechanism based on observations of the temporal evolution of the diameter during the condensation period. The bubble size at the artificial cavity only reduces by 10 % in 20 ms, as opposed to the reduction of the bubble diameter at the natural site which is reduced faster by 87 % in 5.5 ms.

   There are no available models in the literature for predicting the temporal evolution at the artificial cavity. A dimensionless equation model is proposed based on the comparison between predicted data of several modelling approaches and the experimental data, which shows a good fit to the experimental data at the artificial cavity.

3. Symmetrical and asymmetrical motion for advancing and receding contact points was observed at the natural and artificial cavities. Symmetrical motion is observed at the initial stage of the bubble growth period, followed by asymmetrical motion later. The asymmetrical motion of the two points at the natural site is the result of the shift of the advancing contact point on the wall towards the stationary receding contact point. The

artificial cavity assists the resistance of the motion of the bubble advancing contact point towards the flow direction. However, such resistance is not observed at the natural cavity.

4. At the natural site, the bubble contact diameter gradually increased to a maximum value before reducing gradually to zero at the lift-off time. At the artificial cavity, the contact diameter continuously increases during the growth period with temporal fluctuations, and it is around 0.7 times the bubble departure diameter at the departure time.
5. The advancing and receding bubble contact angles reduced after the incipience to an angle range of 20-30 ° at the lift-off moment at the natural sites. The receding contact angle gradually reduced after incipience from 90 ° to 45 ° at the bubble departure time at the artificial cavity.
6. At the natural site, the bubble inclination angle gradually increased after its incipience, and it rights itself at the lift-off moment. This behaviour coincides well with the temporal evolution of the advancing contact point. At the artificial cavity, the inclination angle gradually increased with time from 0 ° to around 40 ° and at the departure time increased to around 49 °. Periodic fluctuations of inclination angle with an average period of around 0.0161 s are observed, which may be due to the periodic shedding of liquid flow vortices downstream of the bubble.
7. The bubble departure at the artificial cavity is triggered by the breakage of the neck that connects the bubble with the cavity. Such breakage generated a shock, which initiated an interfacial wave along the bubble interface propagating with a measured speed of around 125.5 cm/s. This behaviour was not observed at the natural site.
8. The bubble shape is spherical at the lift-off time at the artificial sites. However, a range of irregular bubble shapes are observed when bubble lift-off occurs at the natural site. These irregular bubble shapes survive for around 1 ms after lift-off and can be pyramid-like or bubbles with tails before they become spherical.
9. Nucleation wall deposit patterns with a fan shape are observed downstream of the cavity. The measured maximum height distribution of one patter is 0.4 μm. The deposits forming these patterns include the elements of aluminium, oxide, and carbon, which are found in the working liquid as well. Therefore, the patterns are formed possibly due to the

evaporation of the liquid microlayer and the dissolved elements are deposited. The direction of the symmetry axis of the patterns is aligned with the flow direction at areas away from the artificial sites. However, the symmetry direction is modified close to the area of the artificial cavities, probably due to the modification of the local liquid flow direction by the presence of the bubble.

10. Two types of natural cavities were found. Type 1 are physical cracks or indentations on the polished surface. Type 2 are nucleation sites where physical cracks are not observed down to the 0.25 μm resolution of the microscope. Most of the active natural boiling sites are type 2. The presence of type 2 natural cavities challenges the validity of the commonly used Pre-Existing Nuclei theory, which requires further investigation.

Based on the reported findings on the bubble departure diameter and frequency at the artificial and natural cavities, it is concluded that the heat transfer performance of a single artificial cavity is lower than that of a natural site due to the extremely low frequency of the artificial site.

Chapter 4 Influence of flow boiling conditions on the temporal evolution of bubble growth at an artificial cavity

Chapter 3 presented the findings of the temporal evolution of bubble behaviour for one flow condition during flow boiling at the natural and artificial cavities and evaluated the variability of the bubble characteristics for different bubble events under the same flow condition. The evaluation of the effect of flow conditions on bubble formation at natural cavities is widely described in the literature. However, only a few studies of bubble behaviour at single artificial cavities are available. In addition, there are few studies that compare the bubble characteristics at natural and artificial sites. Therefore, an extensive evaluation of the effects of operating conditions, including heat flux, wall superheat, water inlet temperature, liquid flow velocity and orientation, on bubble behaviour at artificial cavities during flow boiling is performed and this chapter presents the results.

The chapter is structured as follows. Section 4.1 reports the matrix of the considered operating conditions, and typical bubble images for these conditions are shown in section 4.2. The effects of the liquid flow velocity, heat flux, wall temperature and orientation on the temporal evolution of bubble growth at artificial sites during flow boiling are discussed in sections 4.3-4.7, respectively. The chapter ends with a summary of the main findings.

4.1 Considered operating conditions for flow boiling experiments

The parameters that have been investigated are liquid velocity, wall superheat, water inlet temperature and rig orientation. The range of considered conditions is tabulated in Table 4.1. The table shows that the liquid velocity varied from 0.117 to 0.214 m/s, the wall superheat changed from -3.7 to 14.13 °C, and the water inlet temperature varied from 74.6 to 94 °C.

The maximum liquid velocity is determined by the overhead tank height and the pressure drop along the liquid flow circuit. It is observed that the bubble shape is unstable, oscillating forward and backwards in the flow when the velocity is below 0.117 m/s. The maximum water inlet temperature is limited by the maximum working temperature (95 °C) of the heaters

in the overhead tank and the heat loss along the liquid supply lines. The lower bound of the temperature is determined by the ability to identify the bubble edge near the nucleation surface. As the water temperature reduces, the thermal gradients near the nucleation wall increase for a given wall temperature. This induces blurring of the captured bubble edge on the wall due to light ray refraction, and hence, the difficulty in edge detection increases. This results in an overall reduction of the measurement accuracy. The minimum superheat that can lead to bubble formation is observed at -3.7 °C, which means that the temperature is below the saturation temperature; this is a surprising result and will be explained later.

It is noted that when the liquid velocity, wall superheat, water inlet temperature and rig orientation are fixed, the corresponding heat flux varies passively. This is because the heating system under the nucleation wall is designed to maintain the nucleation wall temperature constant. The artificial cavity is the same as that of Chapter 3, and its diameter and depth are 0.2 and 0.95 mm, respectively. Table 4.1 shows 12 considered experimental test cases. Case 3 is used as a reference to allow for the parametric study because its wall superheat is in the middle range. The table also shows which cases are used to evaluate the effects of different parameters.

Table 4.1 Operating conditions of each experimental case during flow boiling at an artificial cavity with diameter and depth of 0.2 and 0.95 mm

Factors investigated	Case number	Velocity (m/s)	Heat flux (W/m^2)	Water inlet temperature (°C)	Wall superheat (°C)	Rig Orientation
Inlet velocity	1	0.117	1.43E+04	93.75±0.25	7.0±0.07	facing upward
	2	0.166	1.56E+04			
	3	0.214	1.65E+04			
Wall superheat	4	0.214	3.09E+03	93.9±0.2	-3.70	
	5		5.04E+03		-1.95	
	6		9.66E+03		1.71	
	3		1.65E+04		7.02	
	7		2.00E+04		9.49	
	8		2.43E+04		11.67	
	9		2.84E+04		14.13	
Water inlet temperature	3	0.214	1.65E+04	94.0	6.67±0.35	
	10	0.215	2.89E+04	84.3		
	11	0.221	4.34E+04	74.6		
Orientation	3	0.214	1.65E+04	94.0	7.02	
	12		1.81E+04	92.1	6.77	facing downward

4.2 Typical bubble images during growth for all operating conditions (cases of Table 4.1)

Typical images of bubbles at the incipience time, median time, and departure time from the artificial cavity for all cases of Table 4.1 are shown in Figure 4.1 in terms of various water inlet velocities, water temperatures, wall superheats and orientation. The case numbers are indicated by the red boxes on the side of the images. The images of cases 4-6 are smaller because they are recorded with a smaller resolution.

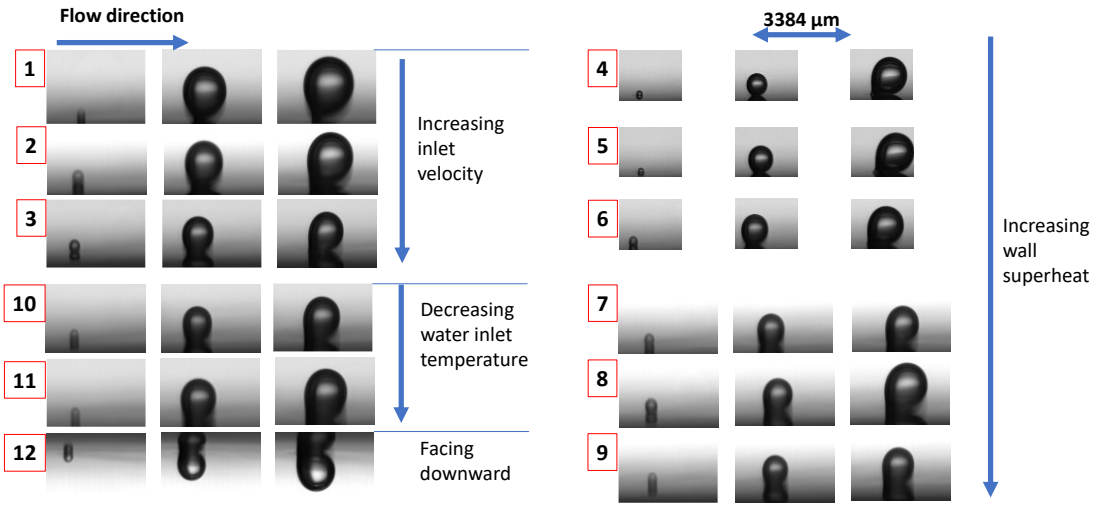


Figure 4.1 Typical bubble images during the growth period at incipience, median and departure times for all cases of Table 4.1.

It is observed that the bubble size and inclination angle increase from the incipience to the departure time. A smaller bubble departure diameter is observed at conditions of higher inlet liquid velocity and smaller water inlet temperature. However, the bubble departure size is kept almost unchanged for different wall superheats for cases 4-9. A detailed discussion of the effects of the experimental conditions is reported below.

4.3 Effect of liquid velocity on bubble growth characteristics

Figure 4.2 presents the temporal evolution of the bubble diameter during the growth period at velocities of 0.12, 0.17 and 0.21 m/s (cases 1, 2 and 3 of Table 4.1). If we use a bubble diameter of 1300 µm to compare the three cases, the figure shows that it takes around 103, 61 and 48 s for a bubble to reach the selected size for velocities 0.12, 0.17 and 0.21 m/s, respectively. Therefore, an increase in the liquid velocity leads to an increased bubble growth rate.

As the liquid velocity increases from 0.12 to 0.21 m/s, the temporal fluctuations of bubble diameter increase. The fluctuations are quantified by the Root Mean Square Error (RMSE), which represents how concentrated the data is around the line of best fit (9th-degree polynomial). The fluctuations are thought to be due to competition between evaporation and condensation. As the velocity increases, to keep a constant wall superheat, the input heat flux is increased to compete with the enhanced condensation resulting by the increased velocity.

Thus, the value of RMSE increases about two times due to the enhanced competition between the two processes.

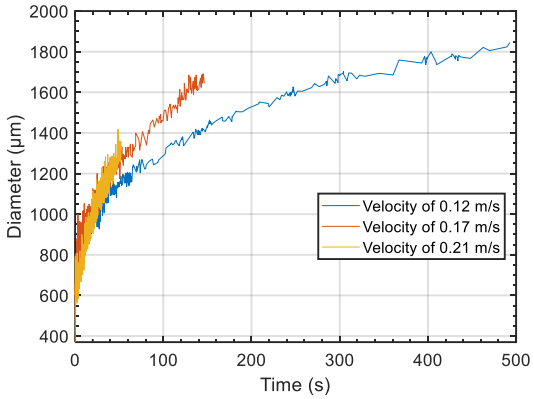


Figure 4.2 Temporal evolution of the bubble diameter during the growth period for liquid flow velocity of 0.12, 0.17 and 0.21 m/s (cases 1, 2 and 3 of Table 4.1).

4.4 Effect of wall superheats on bubble growth characteristics.

Figure 4.3 presents the temporal evolution of the bubble diameter during the growth phase for different wall superheats in the range of -3.70 to 14.13 °C (cases 3-9 of Table 4.1). During these experiments, the heat flux is increased from 3.09E+03 to 2.84E+04 W/m^2 because a higher heat flux is required for a higher wall superheat. It is interesting that the figure shows that the bubble departure diameter for all cases is almost the same; the difference between departure bubble diameter for all cases is within 10.5 %. This difference in departure bubble diameter is relatively small, given the large corresponding changes in heat flux, which suggests that the influence of heat flux on bubble departure diameter is small.

Figure 4.3, however, shows that an increase in wall superheat strongly increases the bubble growth rate. This influence has also been observed at natural sites (Kandlikar, Mizo & Cartwright, 1995). They reported that under some conditions, the bubble growth rate could increase by ten times for a 0.5 °C increase of wall superheat. Their observations are also in agreement with the increase of the temporal fluctuations of bubble diameter with the wall superheat, which is also quantified by the increase of the RMSE from 4 to 61 as the wall superheat increases from -3.70 to 14.13 °C. The physics behind the large sensitivity of the bubble diameter on the wall superheat will be discussed later. However, the observation of

boiling under negative superheat, i.e., -3.7 °C, requires special attention, and this is discussed in the following sub-section.

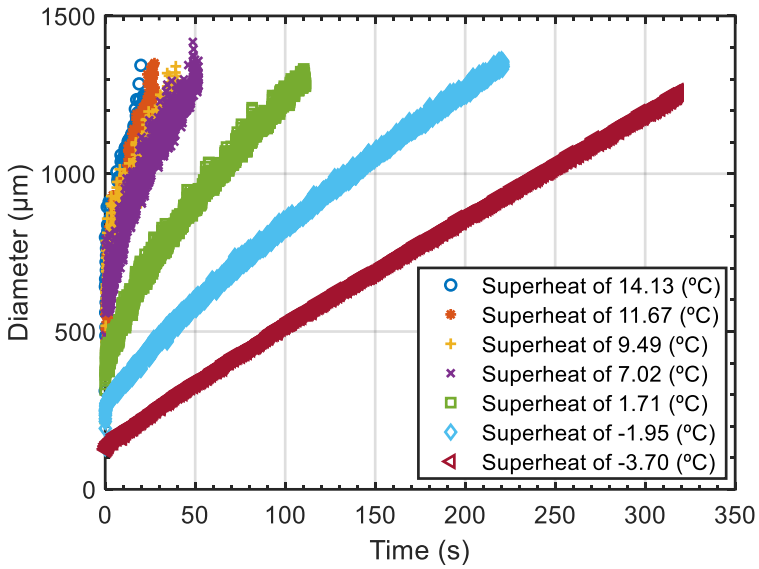


Figure 4.3 Temporal evolution of the bubble diameter during the growth period for wall superheat in the range of -3.7 to 14.13 °C (cases 3-9 of Table 4.1).

4.4.1 Boiling at negative wall superheat

It is surprising to find that bubbles can grow on the nucleation wall for small negative wall superheats (-3.7 and -1.95 °C). The bubbles are initiated when the wall temperature is below the water saturation temperature. It is difficult to explain why bubbles grow at negative wall superheat, and therefore, extra attention is given to consider the origin of the observation.

There are four possible suggestions for the origin of the bubbles. The first considers the existence of a systematic temperature recording error. The second considers the absence of phase change (i.e., boiling); hence, the accumulation of remaining dissolved air in the water might be partially responsible for the bubble growth observed. This could allow the bubble to grow for wall temperatures below the water temperature. The third, most controversial suggestion could be that boiling initiates below the saturation temperature of water, something that requires careful consideration. The fourth suggestion to explain the phenomenon is the presence of temporal and spatial temperature non-uniformities on the nucleation wall.

The first suggestion is examining the possibility of an erroneous temperature reading by the network of thermocouple sensors and, as a consequence, the actual wall superheat being,

in fact, positive. However, all thermocouples were repeatedly tested and are correlated with an RTD, which has a reading accuracy of ± 0.2 %. Such high accuracy, combined with the fact that wall temperatures are measured by several independent thermocouples, the negative wall superheats resulted by the error of the thermocouple readings are eliminated.

Moving on to the second suggestion, examining the possibility of accumulation of dissolved gas in the bulk flow that gives rise to a bubble incipience. Previous studies at natural nucleation sites have also found similar bubble formation at negative superheat. For example, bubble nucleation at wall temperature below the saturation temperature on a smooth surface is reported by Takata, Hidaka & Uraguchi (2006) and Shen et al. (2015). This was repeatedly observed for a range of experiments and was not explained. O'connor, You & Chang (1996) reported that the incipience at negative wall superheats occurs if the dissolved gas concentration is higher than 0.004 moles air/moles liquid. The concentration of air in this study was much lower, 8.68E-07 moles air/moles liquid, and therefore, the accumulation of dissolved gas in the observed bubble could not explain the initiation based on the argument of O'connor, You & Chang (1996).

The third suggestion is related to the possibility of initiation of boiling below the saturation temperature of the bulk liquid. This suggestion implies that the local saturation temperature of water at the cavity is reduced by 3.7 °C. However, in the experimentation, the pressure at the test section is always slightly higher than the ambient pressure, which eliminates this possibility as well.

The final suggestion of spatial-temporal temperature non-uniformities on the nucleation side is examined. Temperature non-uniformities could lead to the possible formation of a local dry spot below the bubble, which then leads to a local increase in the wall temperature above the average value measured by the thermocouples. In pool boiling, Jung & Kim (2014) and Sato & Niceno (2015) reported that the liquid microlayer underneath a bubble in pool boiling is completely depleted after 10 ms and 13 ms, as indicated by experimentation and simulation, respectively. After this time, the bubble contact area with the wall is considered a dry spot. The duration of the existence of the liquid microlayer in this experimentation is regarded of the same time scale as those reported in Jung & Kim (2014)

and Sato & Niceno (2015). Golobic et al. (2009) reports a temperature reduction of 14 °C at the nucleation site from 116 °C due to bubble initiation and growth in pool boiling. They also found that for about 6 ms before the bubble detachment, the dry spot temperature increased. CHF conditions below the bubble were reported by Kim, Song & Kim (2016) in pool boiling, who observed local overheat and expanding bubble contact area at the dry spot area. In the current study associated with flow boiling, a bubble is present at the wall surface close to the artificial nucleation site for much longer times than observed at natural nucleation sites, which is in the range of 20-493 s. This time is long enough to allow the bubble contact area on the nucleation wall to increase and lead to CHF conditions that can cause positive local superheat. This is also in agreement with the observed deposit patterns on the nucleation wall close to the artificial sites reported in Chapter 3. Thus, it is proposed that the local temperature at the dry-spot area below the bubble is higher than the saturation water temperature due to the low thermal conductivity of the vapour and long timescale, which can contribute to the slow bubble growth for average negative wall superheat.

4.5 Effect of water entry temperature and resulting local subcooling

The temporal evolution of the bubble growth at inlet water temperatures of 75, 84 and 94 °C (cases 11, 10 and 3 of Table 4.1) is presented in Figure 4.4. To keep the wall temperature constant, as the water inlet temperature reduces from 95 to 75 °C, the heat flux increases from 1.65 to 4.34 E+04 W/m^2. Based on the findings in section 4.4, the increase in heat flux results in a higher bubble growth rate. However, Zhou et al. (2020b) reported that, for natural sites, the reduction of water temperature results in a smaller departure diameter, which may be explained by the enhanced condensation. The RMSE of the temporal fluctuations increases from 21 to 42 because of the enhanced competition between the enhanced condensation and the evaporation when the water temperature reduces from 95 to 75 °C. As the water temperature increases, the bubble departure diameter reduces from 1619 to 1279 μm.

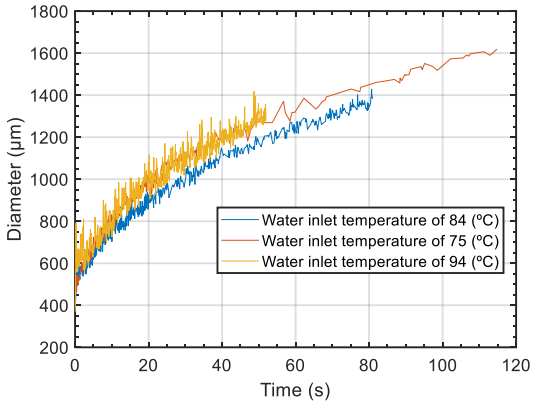


Figure 4.4 Temporal evolution of the bubble diameter during the growth period for entry water temperature in the range of 75, 84 and 94 °C (cases 11,10 and 3 of Table 4.1).

4.6 Effect of nucleation wall orientation

Figure 4.5 presents the temporal evolution of the bubble diameter for an upward and downward-facing rig orientation (cases 3 and 12 of Table 4.1), which means that the artificial site and the nucleation wall are at opposite sides of the channel flow rig. The bubble growth rate at the upward orientation is faster, as indicated by the time that it takes for the bubble diameter to reach 1300 μm, which is 50 s and 70 s for the upward and downward orientation, respectively. The higher growth rate is difficult to explain because heat flux at the downward facing case is around 10 % higher than that at the upward facing case. The findings in section 4.4 indicate that a higher growth rate is obtained for a higher heat flux. Possible reason is that the condensation is stronger at the downward facing. However, the specific reason responsible for stronger condensation is not clear. It is also found that the bubble has a larger departure diameter at the downward-facing condition. This is possibly related to the buoyancy force, which assists the bubble to detach from the wall at the upward-facing condition. In contrast, this force contributes to attaching the bubble to the wall at the downward-facing condition.

The RSME of the temporal bubble diameter fluctuations at the upward facing case is 42, while it is reduced to 30 at the downward-facing case, which indicates that the competition between evaporation and condensation at the downward facing case is reduced.

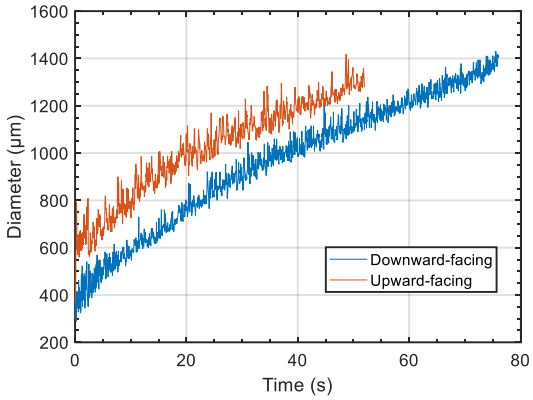


Figure 4.5 Temporal evolution of the bubble diameter during the growth period for conditions of upward and downward facing (cases 3 and 12 of Table 4.1).

4.7 Non-dimensional correlation of bubble growth and considered flow parameters

Bubble growth models are available in the literature only at natural sites. The widely reported bubble growth contributors at these sites are the evaporation of the microlayer, superheated layer, and condensation. Possibly, these three components contribute to bubble growth at the artificial cavity as well. However, the different bubble growth profiles at the artificial and natural sites indicate that possibly some other factors affect the bubble growth at the artificial site. For example, the non-condensable gas or the local high temperature at the dry spot can be contributors. The role of these two factors is not clear. Thus, the models built based on the three mentioned components for natural nucleation sites are not accepted. More importantly, these models are based on a timescale of ms, which is physically not relevant for the large growth period of 21-492 s at the artificial cavity. Therefore, only the nondimensional data fitting model, which was presented in section 3.7.2, may have a better chance to predict the bubble growth since it is not affected by the dimensional time.

As explained in Chapter 3, the model of Prodanovic, Fraser & Salcudean (2002) and Chen et al. (2010) normalizes the diameter and time by the departure diameter and the growth time, respectively. The nondimensional bubble growth profiles for all cases of Table 4.1 are plotted in Figure 4.6 and Figure 4.7, respectively, due to two different trends found for cases 1-3 & 7-11 and cases 4-6 & 12. The different bubble growth profiles of the two figures are reported for the first time for flow boiling at artificial sites.

In Figure 4.6, cases 1-3 and 7-11 show the same dimensionless growth profile. The maximum growth rate is observed at the initial period, and then it reduces. The maximum

growth rate at the initiation time indicates that evaporation is dominant in the initial stage of bubble growth. When the bubble size increases, the condensation rate is increased, which hampers the growth rate. Almost a constant growth rate persists afterwards. The temporal fluctuations of the bubble diameter during the growth time are possibly a result of competition between evaporation and condensation. The dimensionless growth profile for cases 4-6 and 12 varies with the wall superheat. A linear growth profile is observed for case 4. As the wall superheat heat increases, the growth rate gradually increases, and the previously linear profiles gradually become non-linear. It shows that the bubble growth profiles of Figure 4.7 gradually approach the growth profiles of Figure 4.6. The behaviour of profiles in Figure 4.7 are different from those in Figure 4.6, which indicates that the underlying mechanisms are different and require further investigation.

As a result, a data-fitting approach is proposed to correlate all data of Figure 4.6. Figure 4.8 replots the data of Figure 4.6, and all data are fitted by the dimensionless equation (4.1) with an R^2 value of 0.92.

$$D^* = 0.94{t^*}^{0.2} \tag{4.1}$$

Equation (4.1) fits well the bubble growth profiles at a velocity range of 0.12 to 0.21 m/s, wall superheat of 7.02-14.13 °C, and water inlet temperatures of 75 and 94 °C. This equation required a known bubble growth period and departure diameter, and they can be obtained by the proposed correlations in the following Chapter 5.

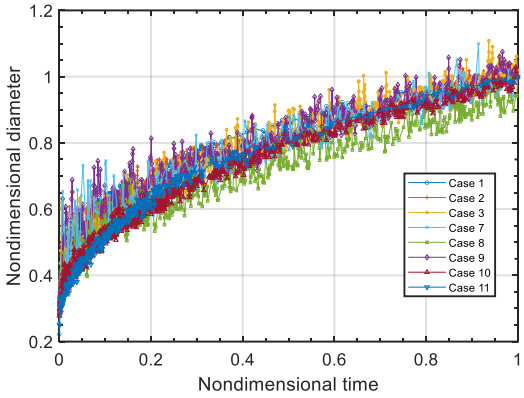


Figure 4.6 Non-dimensional temporal evolution of bubble growth at velocity range of 0.12 to 0.21 m/s, wall superheat of 7.02-14.13 °C and water inlet temperature of 75 and 94 °C (cases 1-3 and 7-11 of Table 4.1). All these cases are upward facing.

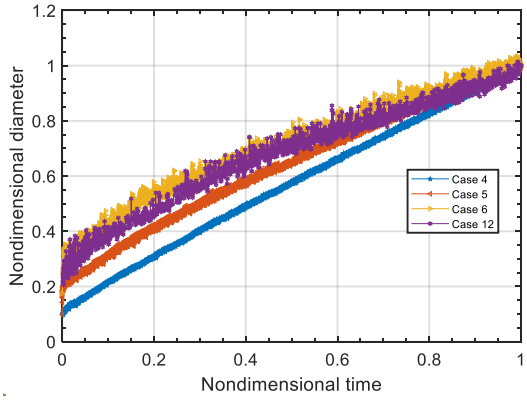


Figure 4.7 Non-dimensional temporal evolution of bubble growth at wall superheat range of -3.7 to 1.7 °C and downward facing (cases 4-6 & 12 of Table 4.1).

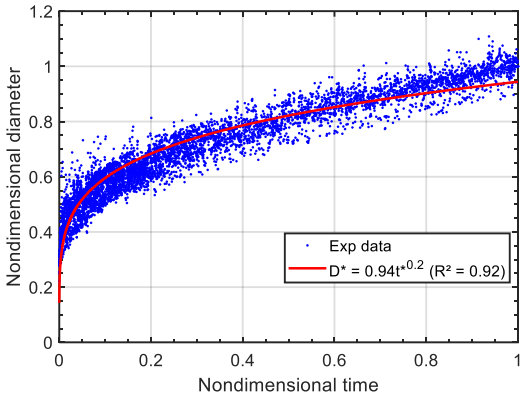


Figure 4.8 Non-dimensional temporal evolution of bubble growth predicted by the model of equation (4.1) for all cases of Figure 4.6.

4.8 Summary

A novel investigation of the effects of experimental conditions on flow boiling bubble dynamics at a single artificial cavity was reported. The effects of experimental bulk fluid velocity, wall superheat, subcooling and the orientation of the nucleation wall on the bubble growth profile at a single artificial cavity were presented in this chapter. The main findings are as follows.

1. Effects of liquid velocity and wall superheat.

   It is observed that as the bulk liquid flow velocity increases from 0.12 to 0.21 m/s, the bubble growth rate and departure diameter increase while the growth time decreases. As the wall superheat increases from -3.7 to 14.13 °C, the heat flux is increased from 3.09E+03 to 2.84E+04 W/m^2 to maintain the superheat temperature. The difference between departure bubble diameters for all cases at this heat flux range is within 10.5 %,

which is considered consistent. The slope of the bubble growth curve increases with the increase of the wall superheat. Boiling at negative wall superheats is observed repeatedly, which is possibly a result of local high wall temperatures at the dry-spot region below the bubble and the non-condensable gas.

2. Effects of water inlet temperature and wall orientation.

   When the water temperature increases from 75 to 95 °C, the departure diameter of the bubble reduces from 1,619 to 1,279 μm. A longer growth period and a larger departure diameter are observed at the downward-facing case compared with that at the upward-facing case. This is possibly due to the contribution of buoyancy force.

3. Non-dimensional correlation of bubble growth and considered flow parameters.

   The bubble growth profiles at the single artificial cavity for a velocity range of 0.12 to 0.21 m/s, wall superheat of 7.02-14.13 °C and water inlet temperature of 75 and 94 °C are fitted by a non-dimensional exponential type of equation. This equation delivered a good fit of the bubble growth profiles for all the above cases. This equation requires knowledge of the departure diameter and the growth time for each case, which can be obtained by correlations reported later in Chapter 5.

Chapter 5 Modelling bubble departure diameter and frequency at an artificial cavity

Successful prediction of bubble departure diameter and frequency is critically important, for example, in predicting the nucleate boiling heat flux.

This chapter considers the measured effects of the examined experimental conditions, reported in Chapter 4, on the bubble departure diameter and frequency and evaluates the ability of proposed models to predict the measured bubble behaviour. Sections 5.1.1 and 5.1.2 introduce the existing models for the prediction of departure diameter and frequency, respectively. The experimental matrix of Chapter 4 and the measured departure diameter and frequency for each case are reported in section 5.2.1. Section 5.2.2 considers the effects of velocity, heat flux, subcooling and surface orientation on departure diameter, growth time, waiting time and frequency. The predicted data from commonly used models in the literature is compared to the measurements of the current study in section 5.3. Section 5.4 proposes new empirical correlations for the departure diameter and frequency based on the experimental data of the current study. In addition to the empirical correlations, a force model predicting the departure diameter is proposed in section 5.5. The summary of this chapter is reported in section 5.6.

5.1 Existing models for departure diameter and frequency prediction

Numerous studies are available in the literature focusing on the prediction of bubble departure diameter and frequency. All of them are considering bubbles nucleating at natural sites. The existing models are introduced in sections 5.1.2 and 5.1.3, respectively. Before moving to models, the relevant dimensionless parameters are defined in section 5.1.1.

5.1.1 Definition of non-dimensional parameters

Dimensionless parameters utilized in proposed models predicting the departure diameter and frequency are defined in this section.

(a) Non-dimensional bubble departure diameter

The bubble departure diameter is nondimensionalized in three ways by using different parameters.

Situ et al. (2005) normalized the departure diameter with the bubble Reynolds number (Re_b), see equation (5.1).

$$D_{lo}^{*} = \sqrt{C_l} Re_b = \sqrt{C_l}\left(\frac{\Delta U D_{lo}}{v_f}\right) \tag{5.1}$$

where D_{lo}^{*}, C_l, ΔU, D_{lo}, v_f represent the dimensionless lift-off diameter, shear lift coefficient, relative velocity between the bubble centre of mass and the liquid phase, lift-off diameter, and kinematic viscosity.

Du, Zhao & Bo (2018) and Zhou et al. (2020b) normalized the departure diameter with a characteristic length $L_c = \frac{\rho_f v_f^2}{\sigma}$ which was identified by the force balance equation, see equation (5.2). This definition was accepted by Prodanovic, Fraser & Salcudean (2002) as well.

$$D^{*} = D/L_c \tag{5.2}$$

The most common definition normalizes the diameter with the Laplace length $Lo = \sqrt{\frac{\sigma}{g\Delta\rho}}$, which describes the balance of surface tension and buoyancy forces. It is a convenient and appropriate choice for the bubble length scale, which is accepted in the literature (Basu, Warrier & Dhir, 2005; Brooks, 2014; Brooks & Hibiki, 2015; Yang, Guo & Liu, 2016). This definition is shown in equation (5.3), and it is the approach used by the current study for diameter normalization.

$$D^{*} = D/L_o \tag{5.3}$$

(b) Absolute and non-dimensional bubble departure frequency

Before defining the dimensionless frequency, the bubble departure frequency is defined first. When a bubble nucleates at a nucleation site, a time interval t_g exists between the bubble inception and the bubble detachment. This time interval t_g is defined as the growth

period. When the bubble detaches from the nucleation site, cold liquid replenishes the void under the departing bubble. The liquid layer temperature at the original site hence decreases. A time interval t_w is thereafter required to heat up the new liquid layer to the superheat condition and activate the next bubble. t_w refers to the time interval between a bubble detachment and the nucleation of the next bubble for pool and flow boiling, which is defined as a waiting period. Han (1962) reports that t_w is the time required to heat the new thermal boundary layer thickness to 1.5 times the cavity radius. A waiting time is required mainly to accumulate energy and generate a successive nucleus (Sun et al., 2018). The bubble departure frequency is defined in equation (5.4) as the inverse of the sum of the growth and waiting times t_g and t_w.

$$f_d = \frac{1}{t_g + t_w} \tag{5.4}$$

The only definition of the dimensionless bubble departure frequency is defined as equation (5.5) in literature (Basu, Warrier & Dhir, 2005; Situ et al., 2008; Euh et al., 2010; Brooks & Hibiki, 2015; Zhou et al., 2020b)

$$f_d^* = \frac{f_d D_d^2}{\eta_f} \tag{5.5}$$

(c) Jakob number

This number refers to the ratio of sensible heat to latent heat absorbed (or released) during the phase change process. Three types of Jakob numbers are found in the literature covering the effects of superheat, water subcooling and the effects of both in relation to the bubble. The basic format of the Jakob number is shown in equation (5.6).

$$Ja \equiv \frac{C_{pf} \Delta T_w}{h_{fg}} \tag{5.6}$$

where ΔT_w refers to the wall superheat, subcooling and total temperature difference between the wall and the bulk liquid for the Superheat Jakob number (Zhou et al., 2020b; Du,

Zhao & Bo, 2018), Subcooled Jakob number (Zhou et al., 2020b) and Total Jakob number (Brooks, 2014; Brooks et al., 2015) respectively.

Other researchers multiplied the density ratio ($\frac{\rho_f}{\rho_g}$) with the basic Jakob number of equation (5.6), and the new definition is shown in equation (5.7). The Superheat Jakob number (Basu et al., 2005; Prodanovic et al., 2002; Yang et al., 2016), Subcooled Jakob number (Basu et al., 2005; Yang et al., 2016) and total Jakob number are defined based on equation (5.7).

$$Ja_{sup} = \frac{\rho_f C_{pf} \Delta T_w}{\rho_g h_{fg}} \tag{5.7}$$

In this study, the definition of the Jakob number in equation (5.6) is accepted because the system pressure is constant. The density ratio is not necessarily required.

(d) Prandtl number

The Prandtl number (Pr) is defined as the ratio of momentum diffusivity to the thermal diffusivity in equation (5.8).

$$Pr = \frac{viscous\ diffusivity}{thermal\ diffusivity} = \frac{C_p \mu}{k} \tag{5.8}$$

Where μ and k refer to dynamic viscosity and thermal conductivity, respectively.

It considers the effect of the properties of different fluids. When the Prandtl number is large, the heat diffuses quickly compared to the velocity. This means that the thermal boundary layer is thicker than the velocity boundary layer, and as a result, the departing bubbles have more room to grow in the superheated layer. It is used by Brooks & Hibiki (2015) and Zhou et al. (2020b) to correlate the fluid properties of different fluids.

(e) Density ratio

The density ratio (ρ^*) is defined as the ratio of the gas density (ρ_g) to the liquid density (ρ_f) in equation (5.9).

$$\rho^* = \frac{\rho_g}{\rho_f} \tag{5.9}$$

where ρ represents the substance density. The density ratio accounts for the effects of system pressure. The applicability of the bubble departure diameter model to high operating pressures is likely to depend on the correct determination of the density ratio behaviour (Brooks & Hibiki, 2015; Zhou et al., 2020b).

(f) Boiling number

The boiling number (Bo) is the ratio of the vapour velocity away from the heated surface to the flow velocity parallel to the surface, U. The vapour velocity is evaluated based on heat transfer by latent heat transport. It represents the stirring effect of the bubbles on the flow and is presented in equation (5.10).

$$Bo = \frac{q}{h_{fg}G} \tag{5.10}$$

where q and G represent wall heat flux and mass flux, respectively. The Boiling number accounts for the effect of changes in the wall heat flux as well as changes in the mass flux. It is reported in the literature (Prodanovic, Fraser & Salcudean, 2002; Basu, 2003; Abdelmessih, Hooper & Nangia, 1972) that the departure diameter is reduced by the increase of the liquid mass flux, which increases the drag force on the nucleating bubble, causing a sweeping removal from the site before the bubble reaches sizes found in flows of smaller mass flux. In addition, Klausner et al. (1993) and Abdelmessih, Hooper & Nangia (1972) found that the bubble departure diameter increases with the heat flux. Thus, an increase in the heat flux and a decrease in the mass flux lead to higher Boiling numbers, and, as a consequence, the bubble departure diameter is increased (Brooks & Hibiki, 2015).

5.1.2 Existing modelling approaches for the bubble departure diameter

The bubble departure diameter was defined earlier in the thesis as the diameter of a bubble at the time of departure from a cavity. It is a critically important parameter attracting many efforts to predict it. Predictive models for the departure diameter proposed in the

literature are reported here. Three basic approaches exist, namely, the force balance approach, the empirical correlation approach, and the energy balance approach. Five types of approaches exist in the literature that describe such phenomena, but they are limited to natural cavities. These combined elements from each approach are discussed in the current section.

(a) Force balance approach

This approach is based on the balance of forces on bubbles in one direction, for example, parallel to the flow direction, which is accepted in the literature (Fritz, 1935; Kocamustafaogullari & Ishii, 1983; Levy, 1967; Rong Situ et al., 2005). When the forces deviate from a balance, the bubble departure occurs.

Fritz (1935) predicted bubble departure diameter by considering the static equilibrium between the buoyant and adhesive forces only. The departure diameter is given by equation (5.11):

$$D_d = 0.022 \cdot \omega \sqrt{\frac{\sigma}{g(\rho_f - \rho_g)}} \tag{5.11}$$

where ω, σ, ρ_f and ρ_g refer to contact angle (in degrees), surface tension force, liquid density, and vapour density, respectively.

Levy (1967) derived a model based on the balance of buoyant force, surface tension force and a frictional force in the vertical upward flow direction. The departure diameter for this model is given by equation (5.12):

$$D = \left(\frac{4C_s\sigma}{C_B\frac{g}{g_c}(\rho_f - \rho_v) + C_F\frac{\tau_w}{D_H}}\right)^{0.5} \tag{5.12}$$

where D, C_s, σ, C_B, g, g_c, ρ_f, ρ_v, C_F, τ_w and D_H refer to the bubble diameter, proportionality constant, surface tension force, the proportionality constant, gravitational constant, conversion ratio from lb-force to lb-mass, liquid density, vapour density, proportionality constant, wall shear stress, and hydraulic diameter.

Kocamustafaogullari & Ishii (1983) included the effect of system pressure by using the density ratio of liquid and vapour in the model of Fritz to obtain equation (5.13).

$$D_d = 0.0012 \cdot (\frac{\Delta\rho}{\rho_g})^{0.9} \cdot D_{Fritz} \tag{5.13}$$

where $\Delta\rho$ and ρ_g refer to the density difference between liquid and vapour and vapour density. D_{Fritz} is the diameter computed by equation (5.11).

Harada, Nagakura & Okawa (2010) neglected the frictional force in the model of Levy (1967), considering the balance of buoyancy and surface forces only, and the bubble departure diameter is obtained by equation (5.14).

$$D_d = (\frac{6C_s\sigma}{C_B\rho_f g})^{0.5} \tag{5.14}$$

where C_s and C_B are proportionality factors. ρ_f, g and σ represents the liquid density, gravitational acceleration, and surface tension.

The bubble departure (or lift-off) diameter at subcooled flow boiling experiments in vertical upward annular channel was studied by Situ et al. (2005). The non-dimensional lift-off diameter is derived based on the growth model of Zuber (1961) and the force balance equation at the lift-off time. The dimensionless form of the lift-off diameter (D_{lo}^*) was formulated as a function of Prandtl number (Pr) and effective Jakob number, which is related to the effective wall superheat. These non-dimensional diameter is defined in equation (5.15).

$$D_{lo}^* = \frac{4\sqrt{22/3}\,b^2}{\pi} Ja_e^2 Pr_f^{-1} \tag{5.15}$$

where b represents a constant. The effective Jakob number, Ja_e and effective wall superheat, ΔT_e, are defined in equations (5.16) and (5.17):

$$Ja_e = \frac{\rho_f C_{pf} \Delta T_e}{\rho_g h_{fg}} \tag{5.16}$$

$$\Delta T_e = S(T_w - T_{sat}) \tag{5.17}$$

where S is the suppression factor, the definition of the Prandtl number is introduced in section 5.1.1.

(b) Empirical correlation approach

For this approach, parameters significantly affecting departure diameter are extracted from literature (Basu et al., 2005; Prodanovic et al., 2002; Yang et al., 2016) using theoretical and experimental results and are correlated by fitting appropriate curves. The derivation of such models has not originated from defined physical processes or meanings. Instead, a combination of assumed relevant parameters (i.e., non-dimensional numbers) have been mathematically fitted to experimental datasets.

Prodanovic, Fraser & Salcudean (2002) studied the departure diameter in subcooled upward flow boiling of water at a vertical, annular test section. The dimensionless departure diameter D_d^+ and all relevant variables, superheat Jakob number (Ja_w), non-dimensional subcooling (ψ), density ratio (ρ^*), boiling number (Bo), are accepted according to suggestions in the literature. Equation (5.18) provides the relevant correlation based on experimental data.

$$D_d^* = \frac{D_d \sigma}{\rho_f \eta_f^2} = A Ja_w^b \psi^c (\frac{\rho_f}{\rho_g})^d Bo^e \tag{5.18}$$

where constants A, b, c, d, and e are equal to 440.98, -0.708, -1.112, 1.747 and 0.124, respectively. Definitions of superheat Jakob number (Ja_w), non-dimensional subcooling (ψ), density ratio (ρ^*) and boiling number (Bo) are shown in equations (5.19), (5.20), (5.21), (5.22) and (5.23), respectively:

$$Ja_w = \frac{\rho_f Cp_f (T_w - T_{sat})}{\rho_g h_{fg}} \tag{5.19}$$

$$\psi = \frac{T_w - T_{bulk}}{T_w - T_{sat}} \tag{5.20}$$

$$\rho^* = \frac{\rho_f}{\rho_g} \tag{5.21}$$

$$Bo = \frac{q}{h_{fg} G} \tag{5.22}$$

where ρ_f, C_{pf}, T_w, T_{sat}, ρ_g, h_{fg}, T_{bulk}, q and G refer to the liquid density, the specific heat capacity of liquid, wall temperature, saturation temperature, vapour density, latent heat, bulk liquid temperature, heat flux and mass flux, respectively.

Basu, Warrier & Dhir (2005) found that the departure diameter increases with the increase of wall superheat and contact angle (ω) and decreases with the increase of subcooling and liquid flow velocity. The increase in velocity assists bubble detachment from the surface, and thus, a smaller departure diameter is obtained. The effects of superheat, subcooling, liquid velocity and contact angles are represented by the following parameters, namely Jakob numbers Ja_{sup}, Ja_{sub} , Reynolds number Re_l and sin (ω). The first three parameters are defined in equations (5.24), (5.25) and (5.26) respectively. Based on their experimental data and data from the literature, the dimensionless bubble departure diameter normalized with the Laplace length (Lo) is correlated in equation (5.23).

$$\frac{D_d}{Lo} = 1.3(sin\omega)^{0.4}[0.13\,exp(-1.75\times10^{-4}Re_l) + 0.005]Ja_{sup}^{0.45}exp\,(-0.0065Ja_{sub}) \tag{5.23}$$

$$Ja_{sup} = \frac{\rho_f C_{pf}\Delta T_w}{\rho_g h_{fg}} \tag{5.24}$$

$$Ja_{sub} = \frac{\rho_f C_{pf}\Delta T_{sub}}{\rho_g h_{fg}} \tag{5.25}$$

$$Re_l = \frac{\rho_f U_f l_o}{\mu_f} \tag{5.26}$$

where D_d, ρ_f, C_{pf}, ΔT_w, ΔT_{sub}, ρ_g, h_{fg}, U_f, l_o and μ_f refer to bubble departure diameter, liquid density, specific heat capacity of liquid, wall superheat, subcooling, vapour density, latent heat, liquid velocity, bubble sliding distance and dynamic viscosity, respectively. The Laplace length is defined as equation (5.27):

$$Lo \equiv \sqrt{\frac{\sigma}{g\Delta\rho}} \tag{5.27}$$

Yang et al. (2016) studied the bubble departure diameter in subcooled flow boiling at an upward, narrow rectangular channel experimentally. They found that the departure diameter is affected by wall superheat, subcooling and liquid mass flux. Their effects are represented by dimensionless parameters of superheat Jakob number (Ja_{sup}), subcooled Jakob number (Ja_{sub}) and liquid Reynolds number (Re_l), respectively. The procedures of Basu, Warrier & Dhir (2005) are followed, and an empirical correlation is developed where the departure diameter is nondimensionalized by the Laplace length (Lo) in equation (5.28).

$$\frac{D_d}{Lo} = 0.0058 Ja_{sup}^{1.45} exp\,(-0.015 Ja_{sub}) exp\,(-0.0001 Re_l) \tag{5.28}$$

The liquid Reynolds number is defined based on the hydraulic diameter of the channel as equation (5.29):

$$Re_l = \frac{\rho_f U_f D_h}{\mu_f} \tag{5.29}$$

(c) Energy balance approach

By considering the balance between the heat transfer into the bubble and the energy loss from the bubble by condensation, the bubble diameter temporal evolution is derived (Ünal, 1976; Dong & Zhang, 2021), e.g. The maximum diameter is calculated when the first-order time derivative of the diameter equals zero.

Ünal (1976) balanced energy input to the bubble through the liquid film between the bubble and wall, the condensation at the curved surface, and the remaining latent heat. The resulting energy balance model is given in equation (5.30):

$$\frac{q_B \pi D^2}{4}\left(1 - \frac{D_{dry}^2}{D^2}\right) = h_c \Delta T_{sub} \frac{\pi D^2}{2} + \frac{\pi}{6} \rho_f h_{fg} \frac{dD^3}{dt} \tag{5.30}$$

where h_c and q_B represent the condensation heat transfer coefficient and the heat flux to the bubble from the liquid film. D and D_{dry} are the diameter of bubble and the dry patch. The detachment diameter is assumed to be equal to the maximum bubble size, where $\dot{D} = 0$.

Dong & Zhang (2021) assumed that the growth of a bubble is affected by three heat sources: heat flux contributed from the thin liquid film, the superheated layer and the condensation layer. The resulting energy balance model is shown in equation (5.31).

$$\rho_g h_{fg} \frac{d}{dt}\left(\frac{\pi D^3}{6}\right) = q_{sl}A_{sl} + q_{tf}A_{tf} - q_c A_c \tag{5.31}$$

where q_{sl}, q_{tf} and q_c refers to the heat flux from the superheated liquid layer, liquid film, and condensation layer, respectively. The temporal evolution of the bubble diameter is expressed in equation (5.32), and the maximum diameter is obtained at $\dot{D} = 0$ and expressed in equation (5.33). The definitions of A and B can be found in (Dong & Zhang, 2021).

$$D(t) = \frac{2A\sqrt{t}(1 + Bt/3)}{1 + Bt} \tag{5.32}$$

$$D_{max} = \frac{1.20724A}{\sqrt{B}} \tag{5.33}$$

(d) Combined force balance and empirical correlation approach

Some researchers combined two modelling approaches. The parameters affecting bubble departure diameter were identified from the force balance approach, and these parameters were used to generate a correlation using the measured diameter (Du, Zhao & Bo, 2018).

The forces experienced by bubbles growing on a horizontal surface in flow boiling were analysed by Du, Zhao & Bo (2018), and a balance equation was obtained. Consideration of the resulting equation indicated that four dimensionless parameters were important, namely density ratio (ρ^*), Jakob number (Ja), Prandtl number (Pr), and bubble Reynolds number (Re_b), which were adopted as the main parameters affecting the bubble departure diameter. Their definitions are shown in equations (5.35), (5.36), (5.37) and (5.38), respectively. The characteristic length (L_c) is adopted to non-dimensional the bubble departure diameter and is given in equation (5.39). Therefore, the correlation for the dimensionless departure diameter model based on the available experimental data is given in equation (5.34).

$$\frac{D_d}{L_c} = 10^{7.196}\rho^{*-0.319}Ja^{0.123}Pr^{-1.939}Re_b^{-0.751} \tag{5.34}$$

where

$$\rho^* = \frac{\rho_f}{\rho_g} \tag{5.35}$$

$$Ja = \frac{C_{pf}(T_w - T_{sat})}{h_{fg}} \tag{5.36}$$

$$Pr = \frac{\mu_f C_{pf}}{k_f} \tag{5.37}$$

$$Re_b = \frac{GD}{\mu_f} \tag{5.38}$$

$$L_c = \frac{\rho_f v_f^2}{\sigma} \tag{5.39}$$

(e) Energy balance and empirical correlation approach

Brooks (2014a) found that dimensionless parameters influence the dimensionless bubble departure diameter using a Nusselt number expression. The bubble departure diameter was nondimensionalised by the Laplace length *Lo*, describing the balance of surface and buoyancy forces. The nondimensional departure diameter was then given by the function of equation (5.40).

$$D_d^* \equiv f(Ja_T, \frac{\rho_g}{\rho_f}, \frac{D_h}{Lo}, Re, Bo, Pr) \tag{5.40}$$

where Ja_T, $\frac{\rho_g}{\rho_f}$, $\frac{D_h}{Lo}$, Re, Bo and Pr refer to the total Jakob number, density ratio of vapour to liquid, dimensionless hydraulic diameter, Reynolds number, Boiling number and Prandtl number, respectively.

The dependence of mass flux on the diameter is given by the boiling number, Bo. Thus, the dependence on the Reynolds number is weakened because the flow dependence is captured by the Boiling number. Based on the small experimental database, the range of considered Prandtl numbers was limited, and thus, its dependence was absorbed into the constant. The final empirical correlation is equation (5.41):

$$D_d^* \equiv \frac{D_d}{Lo} = 3.96 \times 10^{-5} Ja_T^{-0.9} (\frac{\rho_g}{\rho_f})^{-1.3} Bo^{0.47} \tag{5.41}$$

The total Jakob number Ja_T is defined in equation (5.42) and represents the ratio of the total available sensible energy to the latent energy.

$$Ja_T \equiv \frac{C_{pf}(T_w - T_f)}{h_{fg}} \tag{5.42}$$

The boiling number Bo was defined in section 5.1.1.

Brooks & Hibiki (2015) obtained a dimensionless bubble departure diameter model containing several dimensionless parameters based on a Nusselt number expression, see equation (5.43). It was found that the dimensionless departure diameter D_d^*, normalized by Laplace length (Lo), was a strong function of the total Jakob number (Ja_T), Density ratio (ρ^*), Boiling number (Bo), and Prandtl number (Pr). Adjustable constants in the departure diameter correlation of equation (5.44) were obtained by fitting the experimental data. The total Jakob number and Laplace length number are defined in equations (5.45) and (5.46), respectively.

$$Nu = CRe^m Pr^n \tag{5.43}$$

$$D_d^* \equiv \frac{D_d}{Lo} = C \cdot Ja_T^{-0.49} \cdot \rho^{*-0.78} \cdot Bo^{0.44} \cdot Pr_{sat}^{1.72}) \tag{5.44}$$

$$Ja_T \equiv \frac{C_{pf}(T_w - T_f)}{h_{fg}} \tag{5.45}$$

$$Lo \equiv \sqrt{\frac{\sigma}{g\Delta\rho}} \tag{5.46}$$

For conventional channels, $C = 0.00211$.

(f) <u>Force balance, heat transfer balance and empirical correlation approach</u>

Zhou et al. (2020b) derived an expression for the dimensionless departure diameter by balancing forces experienced by bubbles growing on a nucleation wall in the horizontal flow direction, see equation (5.47).

$$D_d^* = \frac{D_d}{\frac{\rho_f v_f^2}{\sigma_f}} = \frac{4(\pi^2 - (\alpha-\beta)^2)}{0.4027 \times 5(\alpha-\beta)(\sin\alpha + \sin\beta)} \times \{4Re_b + 6Re_b\}^{-1/n} \left\{ 4Re_b + 6Re_b \left[\left(\frac{12}{Re_b}\right)^n + 0.796^n \right]^{-1/n} - \frac{R^2\left(R\ddot{R} + \frac{3}{2}\dot{R}^2\right)\sin\theta}{v_f^2} \right\} \quad (5.47)$$

where $\dot{R}$ refers to the bubble growth rate, which is derived by balancing the heat transferred into and out of the bubble, which includes the heat transferred from the evaporation layer, superheated layer and condensation layer. Equation (5.48) provides the bubble growth rate based on the energy balance model.

$$\dot{R} = \frac{1}{C} Pr^{-0.5} Ja_w \eta_f^{0.5} t^{-0.5} + \sqrt{\frac{3}{\pi}} Ja_T \eta_f^{0.5} t^{-0.5} min\left(\frac{y_{sat}}{2R}, 1\right) - \frac{\eta_f}{2R} Ja_{sub}\left(2 + 0.6 Re_b^{0.5} Pr^{0.3}\right) max\left(\frac{H - y_{sat}}{2R}, 0\right) \quad (5.48)$$

By analysing equations (5.47) and (5.48), it is found that the non-dimensionless departure diameter is a function of 5 dimensionless parameters and a function of the contact angles α and β, see equation (5.49)

$$D_d^* = f\left(Pr, \rho^*, Ja_{N,w}, Ja_{N,sub}, Re_b\right) \cdot g(\alpha, \beta) \quad (5.49)$$

Thereby, the dimensionless correlation of departure diameter is developed as equation (5.50) by using the linear regression method to establish the appropriate exponents in the correlation.

$$D_d^* = 10^{2.4086}\rho^{*-0.6613}Ja_{N,w}^{0.1557}Ja_{N,sub}^{-0.01592}Re_{Lo}^{-0.6647}Pr^{-1.8477}\sin\theta^{0.4} \quad (5.50)$$

(g) Final comments on modelling approaches for bubble departure diameter

The presented models for bubble departure diameter are all linked to boiling on natural cavities, which were shown in Chapter 3 to be associated with very short timescales relative to those of artificial cavities. Therefore, the applicability of the presented models to artificial cavities may be limited.

The introduced energy balance-related approaches are associated with time scales of ms, which are too short relative to those of bubble growth at the artificial cavity. Therefore, only the force balance model and the empirical correlation approaches, which are not limited to short timescales, may be acceptable for boiling at artificial cavities.

5.1.3 Existing modelling approaches for bubble departure frequency

The typical bubble departure frequency models in the literature are obtained for pool boiling and flow boiling. So, the models are presented below for pool and flow boiling separately.

(a) Models for pool boiling

Jakob (1949) found that vapour bubbles are detached from a heated surface at equal intervals and have identical sizes for a given nucleation site, and the product of bubble departure diameter times the frequency remains approximately constant for water during pool boiling, see equation (5.51).

$$f_d \cdot D_d = constant \quad (5.51)$$

Cole (1960) proposed the bubble frequency model of equation (5.52) based on the following assumption. At critical heat flux conditions, successive bubbles touch and coalesce. It is assumed that the required time for a detached bubble to move over a distance of one bubble departure diameter equals the sum of the growth time and the waiting time of the next bubble.

$$f_d \cdot D_d = U_b \tag{5.52}$$

By equating the buoyancy force to the drag force on a freely rising vapour bubble, the velocity (U_b) is obtained in equation (5.53).

$$U_b = \left[\frac{4g(\rho_f - \rho_g)D_d}{3\rho_f C_D}\right]^{1/2} \tag{5.53}$$

By combining equations (5.52) and (5.53), the relationship between bubble departure frequency and diameter is shown in equation (5.54).

$$f_d D_d^{1/2} = \left[\frac{4g(\rho_f - \rho_g)}{3\rho_f C_D}\right]^{1/2} \tag{5.54}$$

Zuber (1963) studied conditions where bubbles grow rapidly and follow each other with a similar diameter closely. In a complete cycle (including the waiting and growth time), the absolute distance travelled by a bubble after the departure equals twice the bubble departure diameter. This is because it is reported that while the bubble remains attached to the wall, its mass centre rises with the same velocity as that observed during the rise after the detachment by Jakob & Linke (1935). This observation is expressed by equation (5.55).

$$N = f_d D_d = \frac{U_b}{2} \tag{5.55}$$

The bubble rise velocity is then given by equation (5.56)

$$U_b = 1.18\left[\frac{\sigma g(\rho_f - \rho_g)}{\rho_f^2}\right]^{1/4} \tag{5.56}$$

Hatton & Hall (1966) deduced the bubble growth time and assumed that the waiting time is negligible compared to the growth time. By correlating pool boiling measurements of water, the bubble departure frequency f_d and the square power of the bubble departure diameter D_d were expressed as equation (5.57).

$$\frac{f_d D_d^2}{\eta_f} = 284.7 \tag{5.57}$$

where η_f is liquid thermal diffusivity.

Ivey (1967) separated the experimental data into three regions and fitted the data of each region individually. The corresponding fitted equations for the three regions are shown by equations (5.58), (5.59) and (5.60).

- The hydrodynamic region, at medium and high heat fluxes, for which the major forces acting on the bubble are buoyancy and drag.

$$f_d \cdot D_d^{0.5} = 0.9g^{0.5} \tag{5.58}$$

- Transition region, at the lowest heat flux, for which buoyancy, drag and surface tension forces are comparable:

$$f_d \cdot D_d^{0.75} = 0.44g^{0.5} \tag{5.59}$$

- The thermodynamic region, at the higher heat fluxes, is controlled by bubble growth conditions:

$$f_d \cdot D_d^2 = constant \tag{5.60}$$

Malenkov (1971) also related the detachment frequency to the diameter via the speed of motion of the bubbles, see equation (5.61). The difference between this model and that found by Jakob (1949) is that, in this case, the bubble detachment frequency and diameter were considered certain characteristics of a wave process arising in the liquid at the start of bubble growth, which is an inherent relation.

$$f_d D_d = \frac{1}{\pi} \cdot \frac{U_b}{1-\varphi} \tag{5.61}$$

where φ and U_b represent the vapour content and the bubble rise velocity, respectively. See equations (5.62) and (5.63).

$$\varphi = \frac{q}{q + \hbar_{fg}\rho_g U_b} \tag{5.62}$$

$$U_b = \left[\frac{gD_d(\rho_f - \rho_g)}{2(\rho_f + \rho_g)} + 2\frac{g\sigma}{D_d(\rho_f + \rho_g)}\right]^{1/2} \tag{5.63}$$

Chen, Chen, Zou, Yao, & Gong (2017) estimated the bubble growth time in equation (5.65) by integrating the bubble growth rate of equation (5.64).

$$\frac{dR}{dt} = \beta^* \frac{\lambda \Delta T_w}{R \rho_g h_{fg}} = \frac{\beta^* Ja \cdot \eta_f}{R} \tag{5.64}$$

$$t_G = \frac{R^2}{2\beta^* Ja \cdot \eta_f} \tag{5.65}$$

The waiting time in equation (5.66) is obtained from the thermal layer thickness, which is derived by Chi-Yeh & Griffith (1965).

$$\delta = \sqrt{\pi \eta_l t_w} \tag{5.66}$$

The bubble frequency expression of equation (5.67) is obtained from equations (5.65) and (5.66), and the empirical constants are obtained by data fitting.

$$\frac{f_d D_d^2}{Ja \cdot \eta_l} = \frac{31.26}{0.2297 + Ja} \tag{5.67}$$

During bubble growth, the wall temperature reduces, and it gradually recovers after bubble departure. It is reported that two heat transfer processes work to recover the wall temperature, namely heat transferred through rewetting of surrounding superheated liquid by convection and through the solid substrate by conduction from the heat source. Zhang et al. (2021) proposed a unified relationship between bubble frequency and diameter for conditions when the wall temperature recovery is dominated by the superheated liquid rewetting shown in equations (5.68), (5.69) and (5.70).

$$f_d{}^* D_d{}^* = 1 \tag{5.68}$$

$$f^* = \frac{f}{\left(C_w^2 \left(\frac{k_l}{k_s} \right)^2 (\nu_l \alpha \eta_l)^{-0.5} \alpha_s \right) g^{0.5}} \tag{5.69}$$

$$D_d^* = D_d^{0.5} \tag{5.70}$$

Hamzekhani et al. (2022) used an artificial neural network (ANN) method to predict the bubble departure frequency based on experimental data. The results showed that the RMSE of the neural network is lower than those of the other models.

(b) Models for flow boiling

Podowski et al. (1997) proposed an analytical solution for the bubble waiting time of equation (5.71) and growth time of equation (5.72) for forced convection subcooled boiling. The waiting time was derived by balancing the transient heat transfer in the heated wall and from the wall to the liquid.

$$t_w = \left[\frac{1}{2C_1}\left(-C_3 + \sqrt{C_3^2 - 4C_1C_2}\right)\right]^2 \tag{5.71}$$

During the growth period, the local heat flux from the wall to the bubble is assumed to be entirely used for evaporation and contributes to bubble growth. The growth time of equation (5.72) is derived according to the energy balance assumption.

$$t_g = \left\{\frac{1}{2A_1}\left[-A_2 + \sqrt{A_2^2 - 4A_1A_3}\right]\right\}^2 \tag{5.72}$$

where definitions of parameters C_1, C_2, C_3, C_4, A_1, A_2, A_3 are reported in the original paper.

Basu, Warrier & Dhir (2005) experimentally studied the subcooled flow boiling and developed a mechanistic model. The non-dimensional growth time ($\frac{D_d^2}{\eta_l Ja_{sup} t_g}$) was chosen based on the consideration that the bubble growth is contributed by the heat transferred from the superheated liquid layer during the growth time. The growth time showed a relation with the wall superheating and subcooling. It was found that the growth time increased with the increase of subcooling and a decrease in wall superheat, which slowed down the growth rate and, thus, the time required for bubbles to grow to a given size. The effects of the superheat and subcooling are represented by the dimensionless parameters of Ja_{sup} and Ja_{sub}, expressed by equations (5.74) and (5.75). Based on limited experimental data on growth time, the correlation for the bubble growth time model is given in equation (5.73).

$$\frac{D_d^2}{\eta_l Ja_{sup} t_g} = 45exp\,(-0.02Ja_{sub}) \tag{5.73}$$

where

$$Ja_{sup} = \frac{\rho_f C_{pf}(T_w - T_{sat})}{\rho_g h_{fg}} \tag{5.74}$$

$$Ja_{sub} = \frac{\rho_f C_{pf}(T_{sat} - T_{bulk})}{\rho_g h_{fg}} \tag{5.75}$$

and ρ_f, C_{pf}, T_w, T_{sat}, ρ_g, h_{fg} and T_{bulk} refer to the liquid density, specific heat, wall temperature, saturation temperature, vapour density, latent heat and bulk temperature, respectively.

The experimental data showed that the waiting time decreased with an increase in wall superheat. The dependence of the waiting time on water subcooling was not clear. Thus, the waiting time is given by equation (5.76).

$$t_w = 139.1(\Delta T_w^{-4.1}) \tag{5.76}$$

where ΔT_w is the wall superheat.

Situ et al. (2008) studied the bubble departure frequency at the partial boiling region, which is close to the point of onset of nucleation boiling (ONB). It is suggested by Ivey (1967) that in a thermal dynamic region, the bubble diameter is of the same order of magnitude as the thermal boundary layer thickness δ, which was expressed by equation (5.77).

$$\delta = 1.6(\pi \eta_f t_d)^{0.5} \tag{5.77}$$

where t_d and η_f refer to the period of single bubble and thermal diffusivity, respectively.

Thus, the dimensionless bubble departure frequency is deduced by replacing δ and t_b with D_d and $1/f$, respectively, see equation (5.78).

$$f_d^* = \frac{f_d D_d^2}{\eta_f} \tag{5.78}$$

It was found that the liquid mass flux, wall superheat and heat flux affect the bubble growth and waiting times, which are represented by the Jakob number and liquid Reynolds number and dimensionless heat flux, respectively, see equations (5.79), (5.80) and (5.81).

$$Ja_w = \rho_f C_{pf}(T_w - T_{sat})/(\rho_g h_{fg}) \tag{5.79}$$

$$Re_f = \rho_f U_f D_H/\mu_f \tag{5.80}$$

$$N_{qG} = \frac{q_w D_d}{\eta_f \rho_g h_{fg}} \tag{5.81}$$

Data analysis suggests that the dimensionless bubble departure frequency is a weak function of Jakob number and Reynolds number and is related to heat flux, which is chosen as nucleate boiling heat flux calculated by Chen (1966). Thus, a dimensionless heat flux representing nucleate boiling heat transfer is defined in equation (5.82).

$$N_{qNB} = \frac{q_{qNB} D_d}{\eta_f \rho_g h_{fg}} \tag{5.82}$$

An empirical correlation can be derived by using the least square method to fit experimental data and is presented in equation (5.83).

$$f_d^* = \frac{f_d D_d^2}{\eta_f} = 10.7 N_{qNB}^{0.634} \tag{5.83}$$

Euh et al. (2010) measured the bubble departure frequency in a vertical annulus test section. The experiments were operated at pressures and heat flux ranges from 167 to 346 kPa and 61 to 238 kW/m^2, respectively. It was found that the model of Situ et al. (2008) demonstrated a small deviation from the experimental data. Thus, this model is accepted with modified empirical constants in equation (5.84).

$$\frac{f_d D_d^2}{h_f} = 1.6 N_{qNB}^{1.3} \tag{5.84}$$

The time, t_d, between bubble departures given by Rohsenow (1952) is accepted by Brooks (2014), which is expressed in equation (5.85).

$$t_d \propto \left(\frac{\rho_g h_{fg} D_d^3}{q_w D_d^2}\right) \tag{5.85}$$

The numerator on the right side refers to the energy required for the formation of a bubble at the departure size, while the denominator refers to the energy provided in the area projected by the bubble departure diameter and the wall heat flux. The dimensionless bubble frequency is obtained in equation (5.86) by rearranging equation (5.85).

$$N_f = f_d \frac{\rho_g h_{fg} D_d}{q_w} \tag{5.86}$$

The wall heat flux, q_w, is replaced by the nucleation boiling heat flux on the wall, which is expressed in equation (1.1). This equation expresses the average energy to all nucleating bubbles and, therefore, includes a dependence on the active nucleation site density. The right-hand side estimates the energy required for the bubbles departing from all sites on the wall. The n'' in equation (1.1) refers to the active nucleation site density calculated with the model of Hibiki & Ishii (2003).

As a result, the dimensionless bubble frequency of equation (5.87) is expressed in relation to the dimensionless active nucleation site density by substituting equation (1.1) into (5.86). The constants C_f and a are adjusted to correlate with available experimental data and are found to be 0.667 and -0.117, respectively, and q_{NB} is calculated with the model of Liu & Winterton (1991).

$$N_f = f \frac{\rho_g h_{fg} D_d}{q_{NB}} = C_f N_A^a \tag{5.87}$$

where the dimensionless active nucleation site density is given in equation (5.88):

$$N_A = N_n D_d^2 \tag{5.88}$$

Brooks & Hibiki (2015) accepts the non-dimensional bubble frequency proposed by Situ et al. (2008), where the dimensionless frequency is related to the bubble departure diameter, see equation (5.89). The dimensional departure diameter of equation (5.44) serves as an important indication of relevant dimensionless groups. Therefore, important dimensionless groups for modelling departure frequency are derived by considering the Nusselt number of equation (5.43). Hence, the non-dimensional bubble departure frequency is given as a strong

function of Jakob number, density ratio, Prandtl number, and dimensionless temperature in equation (5.89).

$$f_d^* \equiv \frac{f_d D_d^2}{\eta_f} = 5.5 \cdot Ja_W^{0.82} \cdot N_T^{-1.46} \cdot \rho^{*-0.93} \cdot Pr_{sat}^{2.36} \tag{5.89}$$

Yang et al. (2016) investigated the subcooled flow boiling in a narrow rectangular channel and developed empirical correlations for the prediction of frequency, see equation (5.90). It was found that the waiting time occupied more than 90 % of the ebullition cycle. Thus, the frequencies were primarily determined by the waiting time. Han (1962) reports that the waiting time refers to the time required for the thermal boundary layer to regrow to 1.5 times the cavity radius. Since the heating near the wall is driven by the wall superheat, it is expected that the frequency in this study is related to the wall temperature, regardless of other parameters. The validation range of this correlation is shown in equation (5.91). The mean deviation between the experimental data and the predicted data is 18 %.

$$f_d = 0.032\Delta T_w^{3.08} \tag{5.90}$$

$$For\ \Delta T_w < 12℃ \tag{5.91}$$

Zhou et al. (2020a) studied the effects of subcooling (5-15 K), wall superheat (6.7–20.7 K), flow velocity (0.5-2.0 m/s), and system pressure (121–312 kPa) on the bubble departure frequency for subcooled flow boiling with water. It is reported that wall superheat and system pressure shows a strong relation to the frequency, while the effects of liquid subcooling and flow velocity have little influence. The model of equation (5.92) is built based on the model of (Situ et al., 2008) due to its relatively good performance in the prediction of the experimental data. The relationship between the dimensionless frequency and dimensionless heat flux of equation (5.92) is obtained by fitting the experimental data of Basu, Warrier & Dhir (2005) and the above study.

$$f_d^* = \frac{f_d D_d^2}{\eta_f} = 0.218 N_{qnb}^{1.1424} \tag{5.92}$$

The bubble departure diameter is calculated by the equation (5.44), and the dimensionless heat flux, which represents nucleate boiling heat flux, is expressed by equation (5.93).

$$N_{qnb} = \frac{q_{nb} D_d}{\eta_f \rho_g h_{fg}} \tag{5.93}$$

He et al. (2022) predicted bubble departure frequency by applying a machine learning-based approach. One model reported a mean absolute relative error of 11.57 % in predicting the dataset of Basu (2003) and Zhou et al. (2020a). This study showed that the machine learning-based approach is a reliable tool for bubble departure frequency prediction. A similar model can be found in Yang, Guo & Liu (2016) as well, where the frequency is related to the wall superheat only without other parameters included.

(c) Final comments on modelling approaches for bubble departure frequency

For pool boiling, it is found that the bubble departure frequency is usually correlated with bubble departure diameter with a correlation form of $fD^m = C$. However, this is not used for the current study of flow boiling.

For flow boiling, the physical process of boiling is different from pool boiling, and an additional group of dimensionless parameters must be considered. For flow boiling, the modelling of the dimensionless frequency as ($\frac{f_d D_d^2}{\eta_f}$), is supported by Euh et al. (2010), Zhou et al., (2020a) and Brooks & Hibiki (2015), where the waiting time dominated the bubble departure frequency. Yang et al. (2016) and Basu, Warrier & Dhir (2005) correlate the bubble departure frequency and waiting time with the wall superheat only. In this thesis, the bubble departure frequency is determined by the growth period and, thus, the dimensionless growth period ($\frac{D_d^2}{\eta_f Ja_{sup} t_g}$), suggested by Basu, Warrier & Dhir (2005), is selected.

5.2 Experimental observations

The measured bubble departure diameter, waiting time and growth time at the artificial cavity for the operating conditions of the cases of Table 4.1 are reported in section 5.2.1. The presentation of the measurements is followed by discussions in section 5.2.2.

5.2.1 Measured bubble characteristics

Table 5.1 presents the measured bubble departure diameter, waiting time and growth time and calculated bubble frequency for all considered flow conditions at the artificial cavity. The conditions of inlet liquid velocity, heat flux, subcooling, wall superheat, and orientation are the same as those presented in Table 4.1.

Note that the reported bubble departure diameter and growth time occur during the same boiling event. However, the waiting time is obtained by averaging 9 to 21 boiling events. Since the bubble growth time is of the order of seconds, the process was recorded at a rate of 50 fps. However, the waiting time is of the order of ms. Therefore, the required imaging frame rate is much higher and varied from 1000 to 6250 during these experiments. Given the large timescale difference between the growth time and the waiting time, the waiting time can be neglected in the calculation of the bubble frequency.

Table 5.1 Measured bubble characteristics for the condition numbers and associated operating conditions of Table 4.1

Condition number	Velocity (m/s)	Heat flux (W/m2)	Subcooling (°C)	Wall superheat (°C)	Orientation	Departure diameter (μm)	Growth time (s)	Waiting time (s)	Frequency (Hz)
1	0.117	1.43E+04				1844.788	492.9	0.00136	0.002029
2	0.166	1.56E+04	6.25±0.25	7.0±0.07		1644.284	146.5	0.00213	0.006826
3	0.214	1.65E+04				1279.033	51.96	0.00292	0.019244
4		3.09E+03		-3.7		1259.059	318.8	0.041	0.003144
5		5.04E+03		-1.95		1350.136	221.14	0.0099	0.004545
6		9.66E+03		1.71		1286.31	111.22	0.0089	0.008928
3	0.214	1.65E+04	6.1±0.2	7.02	facing upward	1279.033	51.96	0.00292	0.01923
7		2.00E+04		9.49		1246.728	40.58	0.00119	0.024999
8		2.43E+04		11.67		1350.107	27.38	0.00099	0.036629
9		2.84E+04		14.13		1221.976	21.7	0.0006	0.046082
3	0.214	1.65E+04	6			1279.033	51.96	0.00292	0.019244
10	0.215	2.89E+04	15.7	6.67±0.35		1388.937	81.02	0.00471	0.012342
11	0.221	4.34E+04	25.4			1619.109	114.8	0.00494	0.00871
3	0.214	1.65E+04	6	7.02		1279.033	51.96	0.00292	0.019244
12		1.81E+04	7.9	6.77	facing downward	1410.218	76.1	0.00371	0.01314

5.2.2 Discussion of effects of operating conditions on bubble characteristics

The effects of liquid velocity, wall superheat, subcooling and rig orientation on bubble departure diameter, frequency, growth period and waiting time are reported and discussed in this section. New correlations are built based on the correlation approach to predict the bubble departure diameter and frequency.

(a) Effect of liquid velocity

The effect of liquid velocity on bubble departure diameter and frequency is presented in Figure 5.1 (a). For this investigation, the wall superheat, water temperature and orientation are kept unchanged while the velocity is varied. As a result, the heat flux varies accordingly. For a liquid velocity decrease of around 55 %, from 0.214 to 0.117 m/s, the departure diameter increases by 44 %, from 1279 to 1844 µm, while the frequency reduces by 89 %, from 0.019244 to 0.002029 Hz. These large changes indicate that the liquid velocity has a significant influence on the bubble departure diameter and frequency.

The increase in liquid flow velocity results in an increase in drag force applied to the bubbles, which contributes to the bubble departure from the surface. Thus, the bubbles tend to depart at a smaller diameter for a larger velocity. As the flow velocity increases, the bubble growth rate increases, see Figure 4.2, due to the increase of the heat flux, and therefore, the growth time of the bubble is shorter. Figure 5.1 (b) shows that the growth time reduces from 493 to 52 s. Interestingly, the waiting time shows an increase in Figure 5.1 (b) from 1.4 to 2.9 ms. Goel et al. (2018) reported that the waiting period significantly increases for higher liquid velocity due to increased disruption in the boundary layer. However, the magnitude of the waiting time remains much shorter than the growth time to influence the frequency of bubble departure.

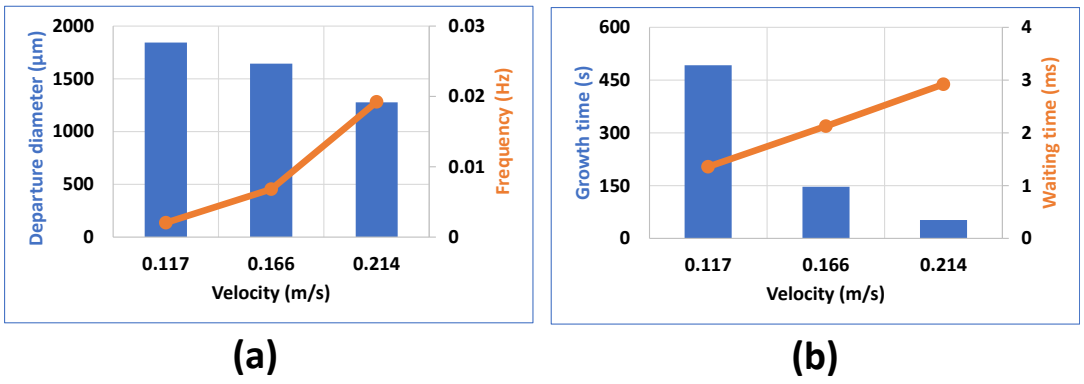


Figure 5.1 Bubble departure diameter and frequency (a); bubble growth and waiting time (b) as a function of the liquid flow velocity.

(b) Effect of wall heat flux

The effect of wall heat flux on bubble departure diameter, frequency, growth time and waiting time is presented in Figure 5.2 (a) and (b), respectively. For this investigation, the water inlet velocity, inlet temperature, and orientation are fixed, while the wall superheat or heat flux varies. It is noted that the wall superheat increases with the heat flux.

As the wall heat flux increases from 3.1 to 28.4 kW/m^2, an increase of 8 times, the departure diameter increases from 1221 to 1350 µm, which is only around a 10.5 % change between the maximum and minimum diameter measured at this heat flux range. However, the frequency increases by 1365 %, from 0.003144 to 0.046082 Hz. This indicates that the wall superheat or heat flux strongly influences the bubble frequency but not the bubble departure diameter. For these conditions, the liquid velocity is kept constant. Thus, it is suggested that the departure diameter is strongly affected by the liquid velocity because of the drag force, which is supported by the force model at the time of bubble departure, which is developed in section 5.5, where the departure is determined by the competition between the drag and the surface tension forces.

Figure 5.2 (a) and (b) show that both the growth and waiting times reduce with the increase of the wall heat flux. Since the growth rate is increased with the heat flux while the bubble departure diameter is only slightly affected, the growth time is reduced.

The literature also reports a reduction in the waiting time with the increase in heat flux (Goel et al., 2018; Yin et al., 2000). It is proposed that an increased thermal gradient is formed at the wall due to the high heat flux, resulting in a quick recuperation of the new liquid layer, which leads to the required superheat for the nucleation of the next bubble. Yang, Guo & Liu (2016) reports that since the heating near the wall is driven by the wall superheat; it is expected that the frequency (primarily determined by the waiting time) in their study is related to the wall temperature in equation (5.90), regardless of other parameters, which shows that when the wall superheat increases, the waiting time reduces. Basu, Warrier & Dhir (2005) correlates the waiting time with wall superheat as well; see equation (5.76).

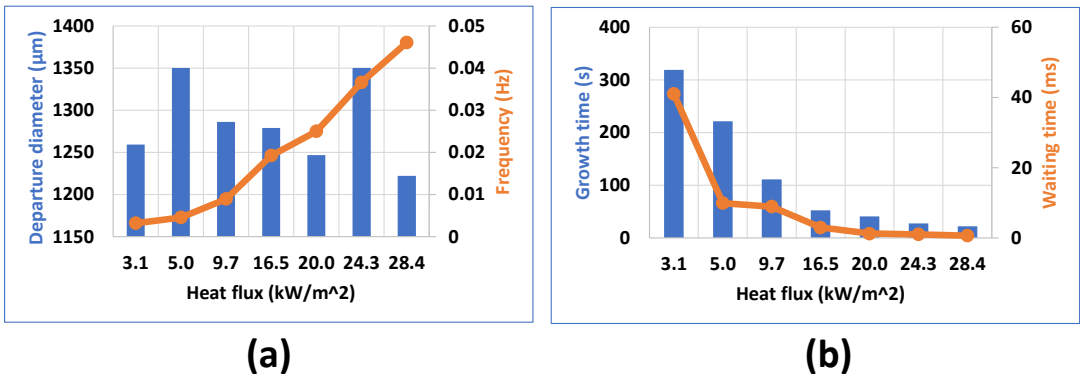


Figure 5.2 Bubble departure diameter and frequency (a); bubble growth and waiting time (b) as a function of the wall heat flux.

(c) Effect of subcooling

The effect of subcooling on bubble departure diameter, frequency, growth and waiting time are presented in Figure 5.3 (a) and (b). Figure 5.3 (a) shows that for a subcooling increase from 6 to 25.4 °C, a factor of 4, the departure diameter increases by around 27 %, from 1279 to 1619 µm, while the frequency reduces from 0.019244 to 0.00871 Hz, a 45 % decrease. Such a trend in the frequency was also observed in the literature (Brooks et al., 2015; Euh et al., 2010; Yin et al., 2000). However, the increase in bubble departure diameter at a larger subcooling is inconsistent with observations at the natural sites, which show a smaller departure diameter at a higher subcooling. It is not clear what mechanism is responsible for this difference at the artificial site. In most models for natural sites, the effect of subcooling is represented by the subcooling Jakob number, as shown in section 5.1.2, but the current findings suggest that some additional parameter is omitted at artificial sites.

The increase in subcooling reduces the bubble growth rate, which increases the growth time to achieve a certain bubble size, which is determined by the force balance equation in section 5.5. The growth time increases from 52 to 115 s, around 55 %, as shown in Figure 5.3 (b). The waiting time also increased from 2.9 ms to 4.9 ms, which most probably happened because more time is required for the wall superheat to return at larger subcooling. Euh et al. (2010) and Goel et al. (2018) also report that the waiting time increases with the increase of subcooling.

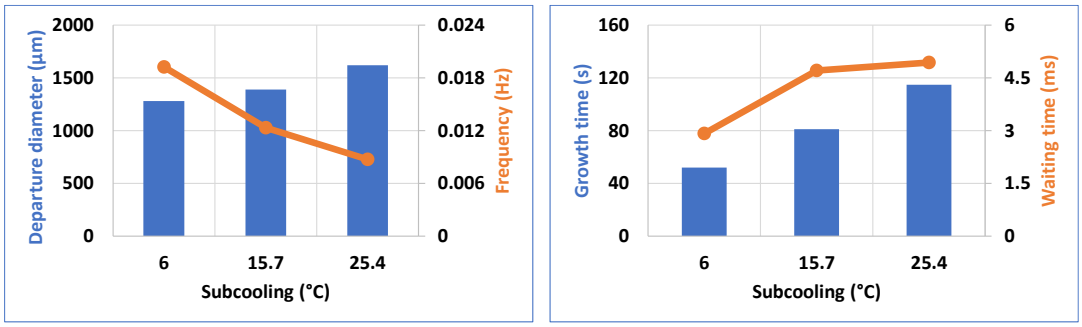


Figure 5.3 Bubble departure diameter and frequency (a); bubble growth and waiting time (b) as a function of subcooling.

Bubble behaviour in subcooled flow boiling in a vertical annulus was studied by Zeitonu & Shoukr, (1996). It was found that the bubble mean diameter increases as the subcooling decreases, probably because the condensation at the liquid-vapour interface is enhanced for reduced subcooling. The bubble departure diameter decreases for lower subcooling and increased velocity (Kandlikar, Mizo & Cartwright, 1995). In general, a smaller bubble size is obtained for lower subcooling in Roy et al. (1994).

(d) Effect of nucleation surface orientation

The effect of surface orientation (upward-facing and downward-facing) on bubble departure diameter, frequency, growth and waiting times is shown in Figure 5.4 (a) and (b), respectively.

As the facing direction of the nucleation surface changes from upward to downward, the departure diameter increases from 1279 to 1410 µm, around 10 %, while the frequency is reduced by 31.7 %, from 0.019244 to 0.01344 Hz. Contrary to the upward-facing condition, where the buoyancy force acts against the forces keeping the bubble on the nucleation wall, at the downward-facing condition, this acts in a beneficial way to delay bubble departure; this, hence, allows for an increased bubble departure diameter. The reduction of growth rate at the downward-facing condition is reported in Section 4.6, which leads to an increase in the absolute growth time. Figure 5.4 (b) shows that the growth time increases from 52 s to 76 s, around 30 %.

The waiting time increased from 2.9 ms to 3.7 ms, around 25 %, which is possibly explained by the shape of the bubble embryo, which is flattened at the downward condition while it is elongated at the upward condition. Figure 5.5 shows schematic representations of an elongated and flattened interface represented by green and blue curves, respectively. Therefore, the bubble embryo can be observed earlier at the upward condition, leading to a shorter waiting time.

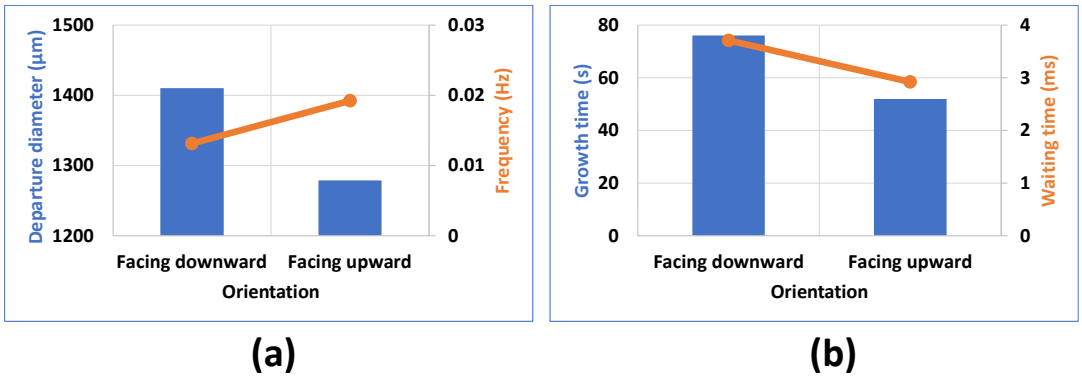


Figure 5.4 Bubble departure diameter and frequency (a); bubble growth and waiting time (b) as a function of nucleation surface orientation.

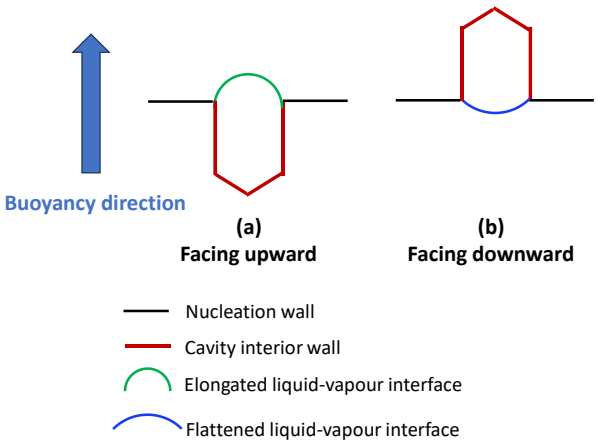


Figure 5.5 Schematic representations of an elongated (a) and flattened (b) liquid-vapour interface of the bubble embryo at the artificial cavity at different nucleation surface orientations.

There is only one operating condition investigated for the evaluation of the effect of surface orientation, and, therefore, the effect of the surface orientation is not included through a dedicated influencing parameter in correlation models. Based on the limited experiments, the surface orientation range is small and thus, any dependence on surface orientation affects the value of constants of any correlation model in the discussion of the next section.

5.3 Comparison between existing modelling approaches and current measurements

The predicted bubble departure diameter and frequency by existing models are compared to the measurements of this study in this section.

5.3.1 Bubble departure diameter

Models, which can be regarded as representatives of departure diameter behaviour, are selected from the literature because of their relatively high accuracy and the large data set used for the development of the corresponding correlations. All these correlations fit the measured bubble departure diameter at natural sites, while the bubble diameter at an artificial cavity has not been studied.

Figure 5.3 presents the data predicted by the five typical equations (5.44), (5.28), (5.34), (5.47) and (5.18) presented earlier in the chapter against the measured bubble departure diameter. The predicted diameter is consistently smaller than the current measurements. The mean absolute relative error of these models is tabulated in Table 5.2, demonstrating the high value of the mean absolute relative error of all models except for the model of Prodanovic, Fraser and Salcudean (2002), which shows a fair agreement with the experimental data with a mean absolute relative error of 16 %. Therefore, there are additional physical processes present for a bubble growing at artificial than natural cavities, which are not captured by these models. A new model proposed for the bubble diameter of this study at the artificial cavity is presented later.

Table 5.2 Comparison of predicted bubble departure diameter from the available models with current measurements. The mean absolute relative error is shown.

	(Brooks & Hibiki, 2015)	(Yang, Guo & Liu, 2016)	(Prodanovic, Fraser & Salcudean, 2002)	(Zhou et al., 2020b)	(Du, Zhao & Bo, 2018)
Mean absolute relative error	77 %	72 %	17 %	52 %	80 %

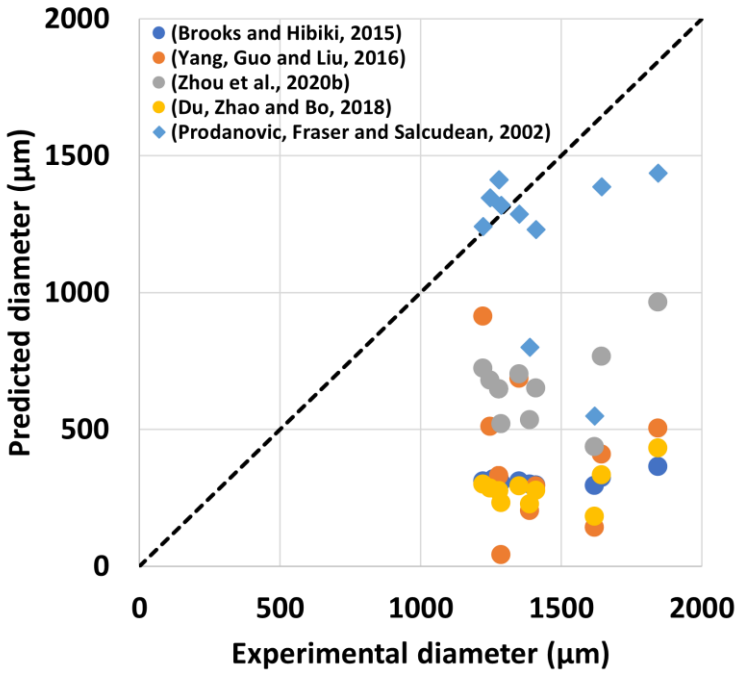


Figure 5.6 Comparison of the experimental bubble departure diameter of this study at the artificial cavity with the predicted diameter by selected existing models.

5.3.2 Bubble departure frequency

Typical bubble frequency predictive models are selected for the comparisons with the measured results. The comparisons of predicted bubble frequency by equations (5.73), (5.89) and (5.92) (Basu, Warrier & Dhir, 2005; Brooks & Hibiki, 2015; Zhou et al., 2020b) with experimental data are shown in Figure 5.7. The predicted frequency is much higher than the measurements for all the conditions of Table 4.1, and the resulting ratio of predicted to measured frequency varies from 7.2 to 6015 with an average of 1297. This large deviation occurs due to the predicted timescales of growth time of the order of ms at natural sites, while the timescale is at least several tens of seconds for the cases of this study at artificial sites. This indicates that existing models for bubble departure frequency prediction at the natural sites are not valid at the artificial cavity.

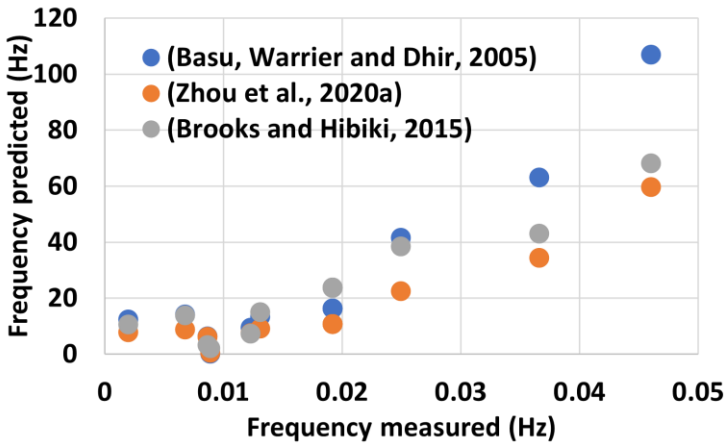


Figure 5.7 Comparison of the experimental data and predicted data of bubble departure frequency from selected existing models.

5.4 Empirical correlations approaches

In this section, the dimensionless bubble departure diameter and the frequency are correlated with dimensionless parameters representing the experimental conditions in sections 5.4.1 and 5.4.2, respectively. According to the summary of various models available in the literature, which were presented in section 5.1.2 and the findings of the previous section on the failure of existing models to predict the current measurements at artificial sites, the empirical correlation approach is used to develop a new approach to predict the measurements at artificial sites.

5.4.1 Bubble departure diameter

It is reported in section 5.2.2 that the liquid velocity has a strong effect on bubble departure diameter, while the effects of superheat or heat flux are relatively weak within the range of investigated level of superheat. In addition, the effects of subcooling and orientation are available.

The effects of the liquid velocity, superheat, and subcooling are represented by the liquid Reynolds number Re_l (Yang et al., 2016) calculated from the hydraulic diameter of the channel, superheat Jakob number Ja_{sup}, and subcooling Jakob number Ja_{sub} respectively, according to the previous suggestions in the literature. The effect of the orientation is not represented by a special parameter due to the limited experimental data, and its effects are absorbed by the constant coefficients of the model. As suggested in section 5.1.2, the bubble departure diameter is normalized by the Laplace length (Lo). The dimensionless departure diameter was expressed by equation (5.94) as:

$$D_d^* \equiv f(Ja_{sup}, Ja_{sub}, Re_l) \tag{5.94}$$

Based on the current experimental results, the correlation of dimensionless departure diameter is acquired by using the linear regression method and the outcome is shown in equation (5.95).

$$D_d^* \equiv \frac{D_d}{Lo} = 221.9 \cdot Ja_{sup}^{-0.006293} \cdot Ja_{sub}^{0.05873} \cdot Re_l^{-0.6309} \tag{5.95}$$

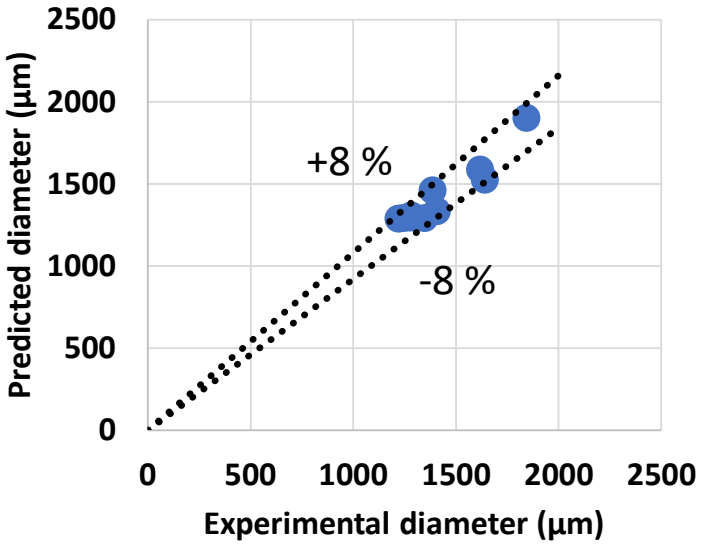


Figure 5.8 Comparisons between the bubble departure diameter predicted by the new empirical model and the measurements.

Figure 5.8 shows comparisons between data predicted by the correlation and the experimental data. All predicted data fit in the relative error of ±8 % of the measurements with a mean absolute error of 3.89 %. The dashed lines in the figure represent the thresholds of +8 % and -8 % in error, respectively.

The exponent values of Ja_{sup} and the Ja_{sub} are much smaller than that of the Re_l. This is consistent with the experimental observations. This indicates that the significance of both effects is lower than that of the liquid velocity. This coincides with the observations and the newly developed force model reported in section 5.5 for the bubble departure diameter prediction. In this force balance model, the departure diameter is mainly determined by the surface tension force and drag force, the latter being mainly determined by the liquid velocity.

The superheat Jakob number, subcooled Jakob number and the liquid Reynolds number are defined using the form of equations (5.6) and (5.29). This correlation is fitted based on the ranges of $3.19\text{E}-03 \leq Ja_{sup} \leq 2.64\text{E}-02$, $1.01\text{E}-02 \leq Ja_{sub} \leq 4.73\text{E}-02$ and $5.60\text{E}+03 \leq Re_l \leq 1.03\text{E}+04$. It is reported in Chapter 3 that the physics of flow boiling at natural and artificial cavities are quite different. Thus, the range of the proposed new correlation is not expanded using the existing database reported in the literature for natural sites.

5.4.2 Bubble departure frequency

In equation (5.4), the bubble departure frequency is determined by the growth time and the waiting time. The observed maximum ratio of the two times tw/tg is 0.013 % for all cases in Table 5.1. Therefore, in the current study, the waiting time is much shorter compared to the growth time, and thus, the frequency is determined by the growth time. Thus, in this section, the data on growth time is correlated with the current measurements.

Based on the analysis, it is found that the growth time is determined by the bubble growth profile and the departure diameter. The growth profile is affected by the heat flux and the level of subcooling, which was demonstrated in Chapter 4. The related parameters affecting the bubble departure diameter are the Reynolds number, the subcooled Jakob number, and the superheat Jakob number. The latter has negligible effect, and it is neglected in the prediction of the growth time. The effects of heat flux (N_{qG}) on the dimensionless growth period (t_g^*) are accepted based on suggestions of Prodanovic, Fraser & Salcudean (2002) and Situ et al. (2008), respectively; see equations (5.96) and (5.98). The dimensionless growth period is correlated with the dimensionless heat flux, subcooled Jakob number and Reynolds number. The predicted data by this equation (5.97) fits in the range of ± 27 % of the experimental data with the absolute mean error of 14.7 %.

$$t_g^* \equiv \frac{t_g \eta_g}{(\frac{\rho_f \eta_f^2}{\sigma})^2} = f(N_{qG}, Ja_{sub}, Re_l) \tag{5.96}$$

$$t_g^* = 10^{31.108} \cdot N_{qG}^{-1.1821} \cdot Ja_{sub}^{1.1132} \cdot Re_l^{-4.1810} \tag{5.97}$$

$$N_{qG} = \frac{q_w D_d}{\eta_f \rho_g h_{fg}} \tag{5.98}$$

The sign of the exponent coefficients is consistent with experimental observations and shows that the increase in heat flux and liquid velocity reduces the growth time. The growth time for negative wall superheats is also included. The application range of Jakob number, Reynolds number and dimensionless heat flux are $1.01E-02 \leq Ja_{sub} \leq 4.73\text{E}-02$,$5.60E+03 \leq Re_l \leq 1.03\text{E}+04$, $1.08E-02 \leq N_{qG} \leq 1.97\text{E}-01$ respectively.

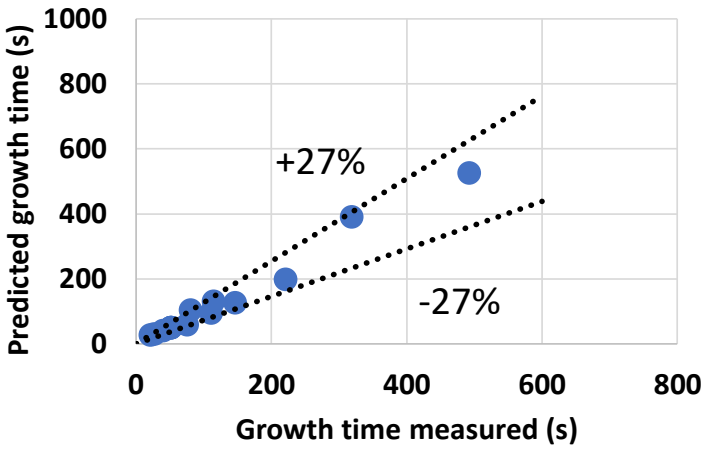


Figure 5.9 Comparison between the bubble growth time predicted by the model and the measurements. Note that the inverse of the growth time quantifies the bubble departure frequency.

5.5 Force balance modelling approaches

The bubble departure diameter from the nucleation wall is a critical parameter in models predicting the heat flux of the boiling process. Thus, the ability of models to predict the departure diameter is critical for model performance. The departure diameter prediction is widely studied in the literature for boiling at natural sites. This section considers the balance of the forces on a bubble growing at the artificial cavity during boiling and evaluates the ability of such a model to predict the bubble departure diameter.

Section 5.5.1 presents the established criterion for bubble departure from natural sites and the experimental observations of differences that may be present during bubble departure from artificial cavities, respectively. Bubbles growing at artificial cavities experience surface tension, drag and growth forces. The equation that describes the balance of these three forces is introduced in section 5.5.2, and the developed model is proposed in section 5.5.3.

5.5.1 The criterion for bubble departure

The net force experienced by a growing bubble attached at a nucleation site during boiling is considered to be zero in the direction of the flow and the direction normal to the wall (Klausner et al., 1993; Sugrue & Buongiorno, 2016). The bubble departure and lift-off are the result of a violation of the force balance in the x and y directions, respectively. Therefore, the force balance of a growing bubble is considered with directions of the flow and normal to the wall denoted as x and y, respectively.

An experimental observation of bubble behaviour at the departure time, as recorded by the experiments of Chapter 4, is shown in Figure 5.10.

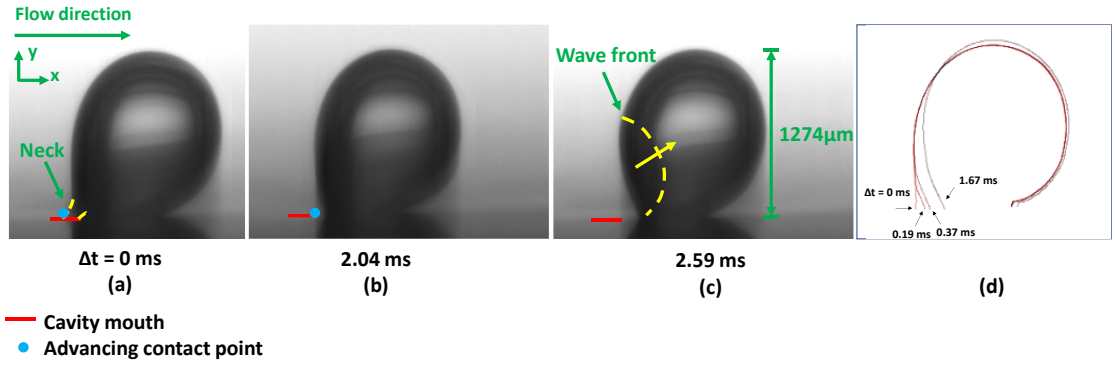


Figure 5.10 Images showing a typical bubble at the departure time from an artificial nucleation site during flow boiling. Δt=0 represents the time that the neck connecting the bubble with the cavity at the advancing contact point breaks.

The bubble size gradually increases during the growth period. Because of the drag force, the bubble slightly swings back and forth in the flow direction, as discussed in section 3.11. As the drag force increased with time, the bubble inclined towards the flow direction, and the neck (represented by the yellow lines in Figure 5.10 (a)) connecting the bubble with the cavity narrowed. As the swing amplitude increases, the advancing half-part of the neck (yellow line connected with the advancing contact point) breaks at Δt=0. The bubble is shown in Figure 5.10 (b) at time Δt=2.04 ms after neck breaking.

The breakage of the neck generates a shock propagating along the bubble surface, and the wave front is indicated by the yellow dashed line in Figure 5.10 (c). During the wave propagation, the evolution of the bubble outline after the breakage is shown in Figure 5.10 (d), where Δt is referenced to the breakage time. It is found that the advancing contact point shrinks towards the bubble while the receding contact point is fixed. As a result, the contact area is reduced, and finally, the bubble lifts off from the wall due to the reduced surface tension force, which is due to the movement of the advancing contact point after the neck breakage. Thus, the criterion for the bubble departure time from the nucleation wall during flow boiling is the breakage of the neck at the advancing contact point.

This observation suggests that the relevant force for bubble departure is the local surface tension force at the neck at the advancing contact point rather than at the whole contact area. The neck breakage occurs in the flow direction (x direction), and thus, the force balance in the x direction is violated first. Forces applied in the x direction are estimated in section 5.5.2.

5.5.2 Bubble force balance in the flow direction

As mentioned in section 5.5.1, it is believed that the bubble departure occurs when the force balance in the x direction is violated first. Thus, the contributing forces along the x flow direction on a growing bubble during flow boiling are reviewed. The surface tension force maintains the bubble on the nucleation site, while the drag force and growth force attempt to

lift the bubble off the nucleation site. The definition and estimation equation of each force is introduced below.

Surface tension force

Equation (5.99) is widely utilized in the literature to estimate the surface tension force. It is proposed by Klausner et al. (1993) and accepted in literature (Zeng et al., 1993; Zhou et al., 2020b; Yun et al., 2012), where α, β, σ and d_w refer to the advancing and receding contact angles (in radians), the surface tension and the contact diameter respectively. This equation is derived by integrating the surface tension force along the whole bubble contact line on the surface, see equation (5.100).

$$F_{sx} = -\int_0^{\pi} D_w \sigma \cos\gamma \cos\phi \, d\phi \tag{5.99}$$

$$F_{sx} = -1.25 D_w \sigma \frac{\pi(\alpha-\beta)(\sin\alpha + \sin\beta)}{\pi^2 - (\alpha-\beta)^2} \tag{5.100}$$

As mentioned in section 5.5.1, the surface tension force generated by the neck at the advancing contact point plays a key role at the threshold of the bubble departure. Thus, an estimation of the surface tension force generated by the neck is required, which is calculated by integrating the surface tension force along the contact line of the neck. To estimate the surface tension force, equation (5.99) is applied while the lower bound is set to $\pi/2$ matching observations of the breakage of the half-part of the neck in this experimentation reported in section 5.5.1. D_w is defined as the diameter of the cavity mouth because the neck diameter is assumed to be the same as the cavity mouth. Figure 5.11 helps to explain the assumption. The surface tension force generated by the half-part neck can be regarded as the surface tension generated by the bubble contact line at the angle ϕ of 90 ° to 180 °.

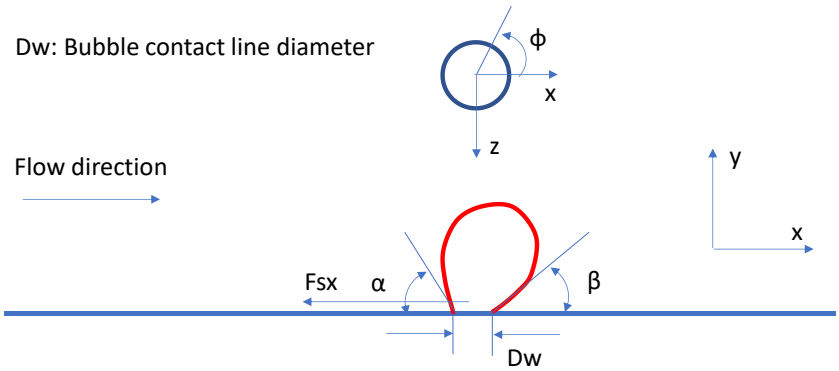


Figure 5.11 Schematic diagram of the behaviour of a growing bubble on a nucleation wall under flow boiling conditions at an artificial site.

Because of the above assumptions, the surface tension force generated by the neck in the x direction is calculated by equation (5.101):

$$F_{sx} = -1.25D_w\sigma\frac{2\pi^2 cos\left(\frac{\beta+\alpha}{2}\right) + 2\pi(\beta-\alpha)\,sin\,\alpha}{2\beta^2 - 4\alpha\beta + 2\alpha^2 - 2\pi^2} \tag{5.101}$$

The reported advancing and receding contact angles at the bubble departure time in the literature are 45 ° and 36 ° respectively (Klausner et al., 1993), 56 ° and 42 ° (Zhou et al., 2020b), 89° and 9° (Raj, Pathak & Khan, 2017), 91 ° and 8 ° (Sugrue, Buongiorno & McKrell, 2014). At the departure time, the current study measured, as shown in Chapters 3 and 4, that the advancing and receding contact angles are 135 ° and 45 °, respectively, which are different from those reported before due to boiling at an artificial site. Based on the measured values of the current study, the surface tension force generated by the neck is calculated as -6.94E-06 N by equation (5.101). The negative value of surface tension force indicates that the force acts in the opposite direction of the flow (x direction) and balances the drag force in the direction of flow, which helps to attach the bubble to the wall.

Drag force

The bubble at the artificial cavity grows at the time range of 21-493 s and interacts with the flow. Drag force is experienced by the bubble. In the literature, an estimate of the drag force for a bubble attached to the wall is not available. Therefore, for simplicity, the drag force is assumed to be that of a sphere, as utilized by Du, Zhao & Bo (2018), and the force is expressed by equation (5.102):

$$F_{drag} = 0.5C_D\rho_F\Delta U^2\pi R^2 \tag{5.102}$$

where ρ_l represents the liquid density, ΔU_c refers to the relative velocity between the bubble mass centre and the surrounding liquid and R the bubble radius. The drag coefficient C_D for steady flow around a sphere is expressed by equation (5.103).

$$C_D = \frac{24}{Re_b}\left(1 + 0.15Re_b^{0.687}\right) + 0.42/\left(1 + 4.25\times10^4 Re_b^{-1.16}\right) \tag{5.103}$$

Re_b represents the bubble Reynolds number whose range is around 3E+05, which is defined by equation (5.104):

$$Re_b = \frac{\rho_f\Delta UD}{\mu_f} \tag{5.104}$$

where the bubble is regarded as stationary, and its velocity is zero. The liquid velocity at the bubble mass centre is estimated based on a laminar flow model. The liquid velocity profile at the bubble mass centre is estimated based on the solution obtained by CFD software ANSYS 2023 R1 Fluent, based on a laminar flow model. To obtain this calculation, a 2D flow channel is used with a rectangular length and height of 110 mm and 10 mm, respectively. The 2D flow channel is meshed with rectangular grids. Figure 5.12 shows the geometry of the 2D flow channel with meshes.

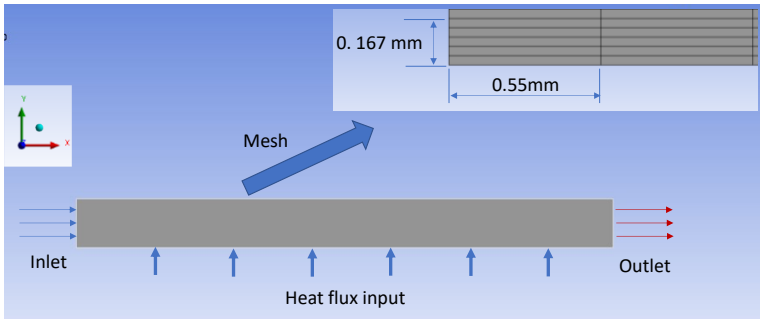


Figure 5.12 The 2D test channel geometry and the corresponding mesh of the model that was used to calculate the liquid velocity at the bubble mass centre.

The assumptions utilized in this study are steady state condition, developing region for incompressible laminar flow, and no heat loss. The inlet velocity is set to uniform, and the pressure outlet is zero-gauge pressure. For the developing water flow, the energy equation and laminar viscosity model are solved. A pressure-velocity coupled system is employed and relaxation factors are at default levels. When the residual of continuity and energy reaches 10-6, simulation is terminated.

Before the calculation, a grid independence test was performed to investigate the effect of element number on the velocity. When refining the grid, the grid height is reduced from 1 mm to 0.033 mm with a constant width of 0.55 mm so that the number of grid elements increases from 200 to 80,601. The liquid velocity for case 3 of Table 5.1 at the reference point 0.5 mm from the nucleation surface at the cavity location is calculated for the grid independence test. It is found that the velocity reduces from 0.146 m/s for the number of grid elements of 2,000 to 0.116 m/s for 10,000 elements, and this value remains unchangeable for several elements in the range of 40,000 to 80,601. Thus, it is concluded that the effect of the selected number of elements on the calculated velocity is negligible when the number is larger than 10,000, i.e., mesh grid independence has been achieved. Therefore, the calculation of the liquid velocity at the bubble mass centre was performed with a selected number of elements of 60,000. A constant heat flux was set up for the wall boundary.

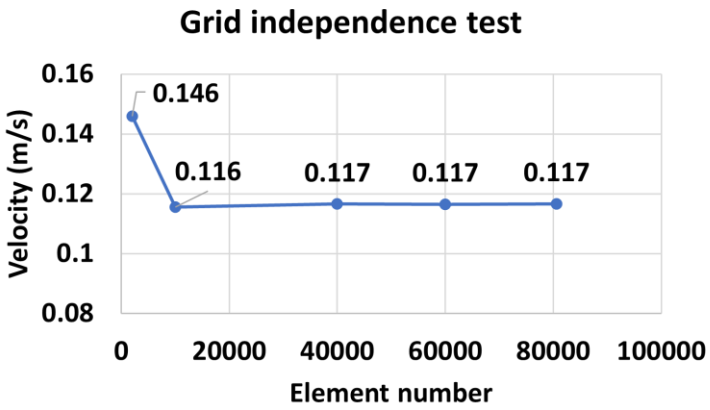


Figure 5.13 Grid independence test for the computational calculation of the liquid flow velocity at the location of the bubble mass centre.

Growth force

As the bubble size increases, the expanding interface pushes the liquid outward. Based on Newton's third law, there will be a force acting on the bubble interface by the liquid interface. This force is defined as a growth force.

The bubble growth force is resulted from the pressure difference inside and outside the bubble interface for a growing bubble, which can be expressed as Rayleigh's equation (5.105) (Klausner et al., 1993; Du et al., 2018).

$$P_v = P_\infty + \rho_f \left(R\ddot{R} + \frac{3}{2}\dot{R}^2 \right) \tag{5.105}$$

where P_v, P_∞, ρ_l, R represent pressure inside the bubble, pressure in the liquid, liquid density, and bubble radius, respectively. The $(\dot{})$ denotes differentiation with respect to time.

By integrating the pressure difference over the hemispherical surface of a bubble, the bubble growth force can be written as equation (5.106).

$$F_{du} = -\frac{\pi}{4} D_w^2 \rho_f \left(R\ddot{R} + \frac{3}{2}\dot{R}^2 \right) \tag{5.106}$$

where D_w refers to the diameter of the contact area. During the actual bubble growth process, the bubble is distorted and inclined in the flow direction. This asymmetry will induce an x-component of bubble growth force in the direction opposite to the mean flow, and thus, the final expression of the growth force is shown in equation (5.107), which is accepted in literature (Klausner et al., 1993; Yun et al., 2012; Zhou et al., 2020b).

$$F_{dux} = -\rho_f \pi R^2 \left(R\ddot{R} + \frac{3}{2}\dot{R}^2 \right) sin\theta \tag{5.107}$$

where θ refers to the inclination angle of the bubble relative to the vertical direction. The inclination angle at the bubble departure time is found as $\pi/18$ in literature (Raj, Pathak & Khan, 2017; Yun et al., 2012; Klausner et al., 1993). The measured inclination angle of the current study is around 45°.

The growth model is fitted by a power law equation based on the measurements of Chapter 4. The growth profile for case 3 in Table 4.1 is found in equation (5.108)

$$R = 0.0004892 \times t^{0.24} \tag{5.108}$$

The first and second derivatives are in the scale of 1E-06 and 1E-08 at the departure time (t=51.9 s) for this case. The calculated growth force is then 3.29758E-15 N, which is much smaller than the surface tension force. Thus, this force can be neglected.

5.5.3 Comparison between predicted departure diameter and measurements

The net forces applied on the bubble in the x direction can be expressed by equation (5.109).

$$F_{sx} + F_{dux} + F_{drag} = \rho_g V_g \frac{dU_b}{dt} = \sum F_x \tag{5.109}$$

In section 5.5.2, it was found that the growth force F_{dux} is of the order of 1E-15 N due to the slow growth rate, which is negligible. The term $\frac{dU_b}{dt}$ in equation (5.109) equals zero because the bubble is regarded as static. Thus, the force balance equation is a simplified equation (5.110).

$$F_{sx} + F_{drag} = 0 \tag{5.110}$$

The estimated surface tension F_{sx} in section 5.5.2 is a constant and equals -6.94E-06 N. Thus, by rearranging equation (5.110), the departure bubble diameter can be obtained by equation (5.111)

$$D_d = 2\left(\frac{2F_{sx}}{C_D \rho_f \Delta U^2 \pi}\right)^{1/2} \tag{5.111}$$

According to this model, the predicted bubble departure diameter is calculated, and it is plotted against the measurements of Chapter 4 for all cases of Table 4.1 in Figure 5.14. The absolute value of the mean error is 9.47 %. 92 % of the measurements are present within an error range of ±20 %. A relatively large error of -18 % and -37 % is obtained for two cases 10 and 11 of Table 4.1 (i.e., small water inlet temperature of 82 °C and 72 °C, respectively). It is

noted that the measured bubble departure diameters for negative wall superheats (cases 4 and 5 of Table 4.1) are also included in Figure 5.14, with a maximum mean error of 8 %. This indicates that the data at the negative wall superheats can also be predicted by this model. Therefore, the comparison between predicted, based on the developed model, and measured results is considered satisfactory.

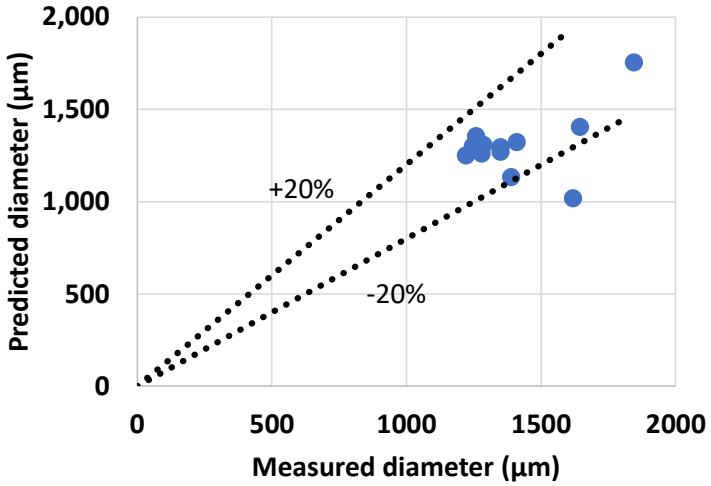


Figure 5.14 Comparison between the predicted bubble departure diameter from equation (5.111) and the measured departure diameter for all cases of Table 4.1.

5.6 Summary

The bubble departure diameter and frequency are two critical parameters in the estimation of boiling heat flux. This chapter evaluated the effects of water inlet velocity, inlet temperature, wall heat flux and orientation on the two critical parameters. The empirical and force balance approaches are the modelling strategies developed in the current chapter to predict the bubble departure diameter and frequency from flow boiling at an artificial cavity, which was required because bubble behaviour is different from natural cavities. A summary of the findings is provided below.

1. Experimental observations

   The flow velocity has an obvious effect on the bubble frequency. As the velocity reduces by 45 %, the frequency gains a reduction of 89 %, and departure diameter increases by 44 %. The wall heat flux significantly influences the bubble frequency. As the wall heat flux increases by 8 times from 3.1 kW/m^2, the frequency increases by 1365 %. However, the bubble departure diameter only slightly fluctuates between 1221 to 1350 µm. As the water subcooling increases by 3.2 times, the diameter increases by around 27 %, and the frequency is reduced by 45 %.

2. Empirical approach

   The dimensionless departure diameter was correlated with the Reynolds number, superheated Jakob number and subcooled Jakob number and a new correlation was

developed. The correlation predicted the measurements with a mean absolute error of 3.89 %. The weighting of the superheated Jakob number and subcooled Jakob number in the correlation is smaller than that of the Reynolds number. The dimensionless departure frequency was correlated with dimensionless heat flux, subcooled Jakob number and Reynolds number with an absolute mean error of 14.7 %.

3. Force balance approach

   The bubble departure diameter was also predicted by a force model by evaluating the surface tension, drag, and growth forces experienced by a growing bubble in the flow direction. The surface tension force equation proposed by Klausner et al. (1993) was modified according to the experimental observations. The drag force estimated for a bubble attached to the wall is not available, and, for simplicity, the drag force model for a sphere was utilised. An estimate of the growth force showed that it was on the scale of 1E-15 N, which is negligible compared to the surface tension and drag forces. Therefore, the estimated departure diameter was obtained by balancing the above three forces but eventually omitting the growth force due to its negligible contribution, with an average mean error of 8.47 %. However, the effect of water temperature is not represented well by this model, and more research is required to optimize it.

Based on the above findings, the correlations between bubble departure diameter, frequency, forces, and experimental conditions for flow boiling at artificial sites are summarised in Figure 5.15. The departure diameter is determined by the surface tension and drag forces. The bubble growth profile is possibly affected by evaporation, condensation and the presence of non-condensable gas. As a result, the growth time is determined by the departure diameter and the growth profile. Due to the low value of the waiting time, the bubble departure frequency is determined by the growth time.

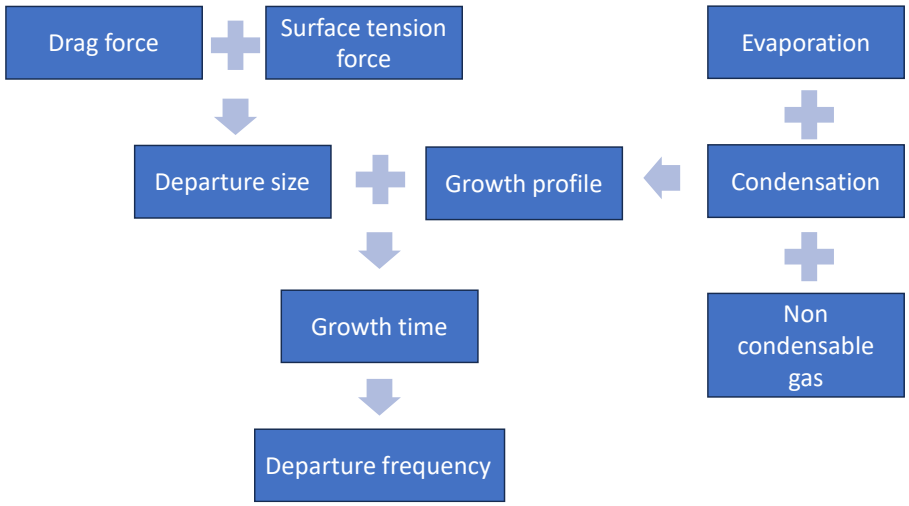


Figure 5.15 Flow chart showing the interdependency of various parameters and experimental conditions that determine the processes during flow boiling at artificial nucleation sites.

Chapter 6 Bubble dynamics at single and pair of artificial cavities and effect of cavity geometry

There are always many cavities located on a real heat transfer surface. Multiple nucleation site interactions have been found to play an important role in pool boiling heat transfer performances (Gong & Cheng, 2016) and are expected to play an important role in flow boiling as well. However, a controlled study of bubble interaction at multiple natural nucleation cavities is not possible to organise. Therefore, using artificial sites allows to vary the geometry of the cavity and the spacing between multiple sites.

There are limited studies in the literature of single artificial cavities and even fewer for multiple cavities interacting with each other during flow boiling. These have shown that the cavity diameter (Shoji & Takagi, 2001; Yu, Lu & Cheng, 2006; Gong, Cheng & Quan, 2016), cavity depth (Yu, Lu & Cheng, 2006; Hutter et al., 2010) and spacing between multiple cavities (Hutter et al., 2012; Zhang & Shoji, 2003) affect bubble characteristics. However, the details of the microscale of the physical process of bubble behaviour are not available. Thus, the effects of these three factors are investigated and presented in sections 6.1, 6.2 and 6.3.1, respectively. Section 6.4 provides a summary of the findings.

6.1 Effect of single cavity depth

Effects of the cavity depth on bubble growth, waiting time and departure diameter are introduced in section 6.1.1. The conditions for an activated cavity are also detailed in section 6.1.2.

6.1.1 Bubble growth, waiting time and departure diameter

The effect of cavity depth on bubble characteristics is investigated using the experimental facility described in Chapter 2. The considered conditions for a single cavity with a depth range of 0.2 to 0.95 mm and a cavity diameter of 0.2 mm are tabulated in Table 6.1. Note that the numbering of the cases in the table starts from number 13, extending the cases that were studied earlier and reported in Table 4.1. The bubbles of this range of depths behave in a similar way as reported in Chapter 3 and Chapter 4. The temporal evolution of the bubble growth profile, departure diameter, growth time and waiting time are presented in Figure 6.1

(a-c), respectively. Figure 6.1 (a) shows that the temporal evolution of bubble growth for all cavity depths follows the same behaviour. Similarly, Figure 6.1 (b) shows that the growth time varies from 71 to 79 s, and the departure diameter varies from 1282 to 1365 µm with small fluctuations of 6 %. Such low fluctuations of bubble departure diameter are possibly due to local flow instabilities. In Figure 6.1 (b), the growth time behaves similarly to the bubble departure diameter since the growth rates between cases are similar, and, therefore, the growth time increases with the increase of departure diameter. Figure 6.1 (c) shows that the bubble waiting time between sequential bubble events reduces from 3 ms to 1.8 ms with some fluctuations with the increase of cavity depth from 0.2 mm to 0.95 mm.

Table 6.1 Matrix of operating flow boiling conditions for artificial cavities with depth range from 0.2 to 0.95 mm and constant cavity diameter 0.2 mm.

Case number	Cavity depth (mm)	Velocity (m/s)	Heat flux (W/m^2)	Water inlet temperature (°C)	Superheat (°C)
13	0.2				
14	0.4				
15	0.6	0.214	22713±1076	93.3±1.3	6.13±0.725
16	0.8				
17	0.95				

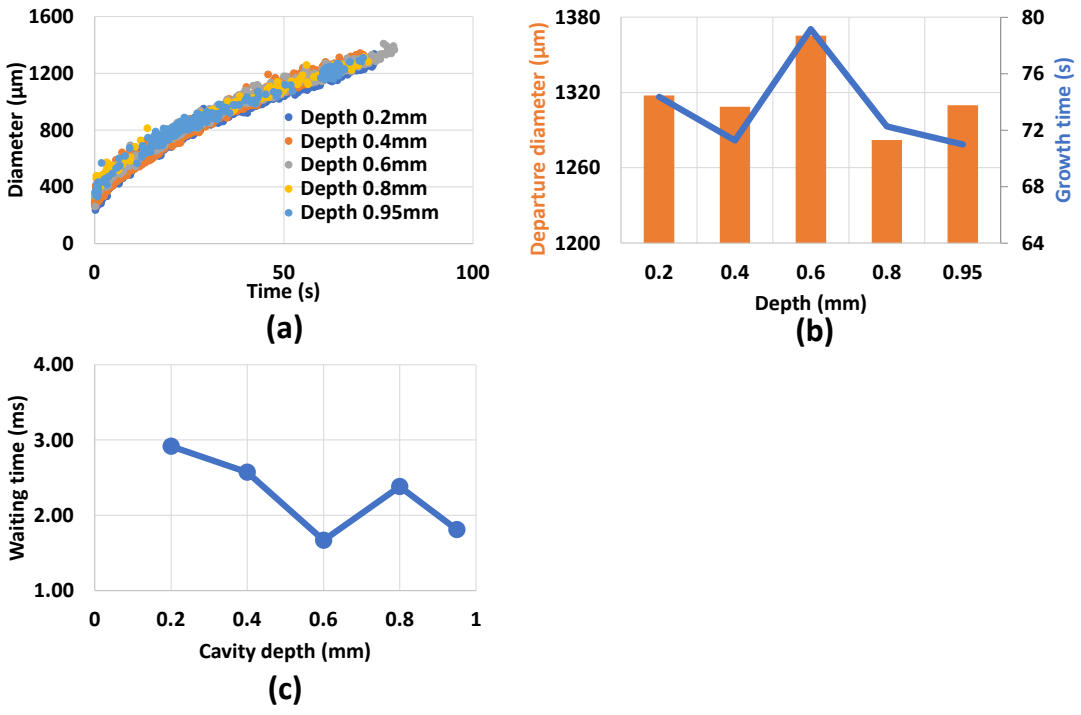


Figure 6.1 Temporal evolution of bubble growth (a), bubble departure diameter and growth time (b) and bubble waiting time (c) for artificial cavities with a depth range of 0.2-0.95 mm and diameter of 0.2 mm (cases according to Table 6.1).

The literature has shown that a rapid decline of overall heat transfer coefficients occurs for cavity depths of 0.2 and 0.11 mm (Yu, Lu & Cheng, 2006), which explains that deeper cavities delay the departure of bubbles, decreasing bubble departure frequency. However, the

current experimental results observed at a depth range of 0.2-0.95 mm do not support the proposed explanation. Hutter et al. (2010) investigated the effect of cavity depth of 40, 80 or 100 μm on bubble behaviour and found, in agreement with the current study, that there is no visible influence of cavity depth on departure diameter and waiting times. However, there is less scatter in the behaviour of the bubble frequency at a cavity with a depth of 100 μm compared to a depth of 80 μm. Singh, Mikic & Rohsenow (1976b) found that, for a given cavity mouth radius, as cavity depth decreases, comparatively less amount of vapour is trapped in the cavity, and the stability of bubble behaviour on the cavity is decreased, resulting in higher values of required superheats for boiling. The effects of the cavity depth on the growth profile and the growth period are not obvious.

The results of this experimentation, plotted in Figure 6.1 (a, b), suggest that cavity depth in the range of 0.2-0.95 mm has negligible effects on the temporal evolution of bubble growth, departure diameter, and growth period. The increase in cavity depth may lead to a reduction of bubble waiting time; see Figure 6.1 (c) due to the increased stability at a deeper cavity, which is reported by Singh, Mikic & Rohsenow (1976b).

6.1.2 Continuous boiling in cavities

During the operation of the experimental facilities with different cavity geometries, there were conditions that led to intermittent boiling, i.e. cavities generating boiling bubbles but then stopping. As a consequence, two different boiling behaviours were observed for the artificial cavities in terms of different depth ranges at cases 13-17 in Table 6.1 and cases 18-19 in Table 6.2. These are summarised below.

Type 1 Cavity Behaviour

Type 1 behaviour of an artificial cavity is related to the successful generation of boiling bubbles after switching the experimental facility off at the end of experimentation and then restarting it the next day. This occurs only for cavities with a diameter of 0.2 mm and depths ≥0.6 mm for those considered in this study. It is believed that the origin of this cavity behaviour that delivers continuous operation is due to the remaining air or gas trapped inside a cavity after stopping the experimentation.

Type 2 Cavity Behaviour

Type 2 behaviour cavities include those with a diameter of 0.2 mm and depths of 0.2 or 0.4 mm and cavities with diameters of 0.05-0.15 mm with an aspect ratio (depth/diameter) of 3. Those cavities generate boiling bubbles throughout a day of experimentation, but they stop generating boiling bubbles when the rig is restarted the following day after stopping it at the

end of the day. This behaviour persists even when the superheat of the nucleation wall is increased to 20 °C, and this condition is maintained for one hour after restarting the rig following an interruption of experimentation. It is interesting that this behaviour changes, and the cavity becomes active if the rig is fully dried at the end of the experimentation of one day. To dry the cavity, the substrate is placed in a vacuum that causes any remaining water inside the cavity to boil off. Additional investigation showed that Type 2 behaviour occurs when the wall temperature is slightly lower (1 to 2 °C) than the bulk water temperature for at least 8 mins. The green curves 1 and 2 in Figure 6.2 represent the observed temporal evolution of the liquid-vapour interface at the cavity mouth area when the temperature of the wall is lower than the liquid. It is found that the interface gradually shrinks toward the cavity interior. At late times, the interface is out of view as it becomes hidden by the cavity wall. In terms of the Type 2 behaviour of artificial cavities, a nucleation surface with several cavities, which have been fully filled with liquid in advance of operation, may delay the formation of film boiling and increase the critical heat flux.

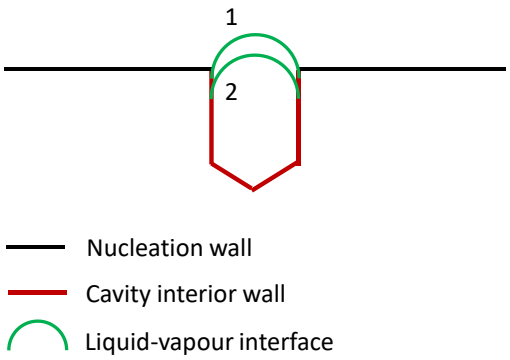


Figure 6.2 Temporal evolution of the liquid vapour interface at the artificial cavity mouth area.

In summary, the existence of Type 2 behaviour of artificial cavities is due to the cavity becoming fully filled with liquid when the wall temperature is below the water temperature. This causes the deactivation of the cavity, which is persistent even at tested conditions of high wall superheats. Therefore, a cavity of this size, geometry and experimental conditions will initiate boiling if air or vapour is trapped inside it.

Discussion

The findings of section 6.1.2 indicate that cavity depth affects the liquid filling of the cavity. For increased depths, the pressure difference between the two sides of the gas-liquid interface may be balanced, which resists the further movement of the liquid-vapour interface inside the cavity. The exact reason is not clear. As a result, some non-condensable gas remains trapped in deeper cavities, which contributes to the repeatable boiling operation of cavities even after the experimentation is stopped.

An additional suggestion is that there is an effect of the cavity aspect ratio (depth/diameter) since the cavity with aspect ratio 3-5, namely a diameter of 0.2 mm and depth of 0.6-1 mm, has type 1 behaviour and remains always active, while cavities with diameter 0.2 mm and depths from 0.2 to 0.4 mm, namely aspect ratios from 1 to 2, exhibit type 2 behaviour. The effects of the cavity aspect ratio on the intermittent operation of cavities require further investigation.

6.2 Effect of cavity diameter

In this section, the effect of cavity diameter on bubble characteristics is investigated, and the operating conditions used are shown in the experimental matrix of Table 6.2. The cavity diameter varies from 0.05 to 0.2 mm with the same aspect ratio (depth/diameter) of 3.

Table 6.2 Matrix of operating flow boiling conditions for artificial cavities with a diameter range of 0.05 to 0.2 mm for constant aspect (depth/diameter) ratio 3. The case numbers start from 17, continuing the cases considered previously in Table 4.1 and Table 6.1.

Case number	Cavity diameter (mm)	Velocity (m/s)	Heat flux range (W/m^2)	Water inlet temperature range (°C)	Superheat range(°C)
18	0.05	0.214	22581±201	94.05±0.55	6.26±0.33
19	0.1				
20	0.15				
15	0.2				

The bubble growth profiles, departure diameter, growth time and waiting time for the conditions and cavity diameters of Table 6.2 are presented in Figure 6.3 (a-c), respectively. Figure 6.3 (a) shows that the temporal evolution of the bubble growth follows the same behaviour for all cavity diameters. The bubble at this diameter range behaves the same way as that reported in Chapter 3 and Chapter 4.

Figure 6.3 (b) shows that the bubble departure diameter increases from 1079 to 1365 μm while the cavity diameter increases from 0.05 to 0.2 mm. This finding is consistent with the developed bubble departure force model of section 5.5. The model shows that a larger departure diameter occurs for a larger cavity diameter due to the larger surface tension forces. Since the temporal evolutions of the bubble growth are similar, the time required to reach a larger diameter is increased. That is why the growth time generally increases from around 60 to 79 seconds. The smaller growth time recorded for cavity diameter 0.1 mm is due to the corresponding slightly higher measured growth rate.

Figure 6.3 (c) shows that the waiting time gradually reduces from 4.8 ms to 1.8 ms with the considered increase of the cavity diameter, which agrees with the observations of Figure 6.1 (c). Since a part of the vapour remains inside the cavity after bubble departure, the waiting time refers to the time required for the bubble tip to be observed at the cavity mouth as the

bubble grows at the cavity interior due to increased interior vapour pressure and mass due to evaporation. Reduction of waiting time is observed in both Figure 6.1 (c) and Figure 6.3 (c), possibly due to the higher local temperature resulted due to increased cavity interior heat transfer area. The thermal conductivity of the vapour inside the cavity is lower than that of stainless steel. As a result, possibly, the local temperature of the cavity is higher.

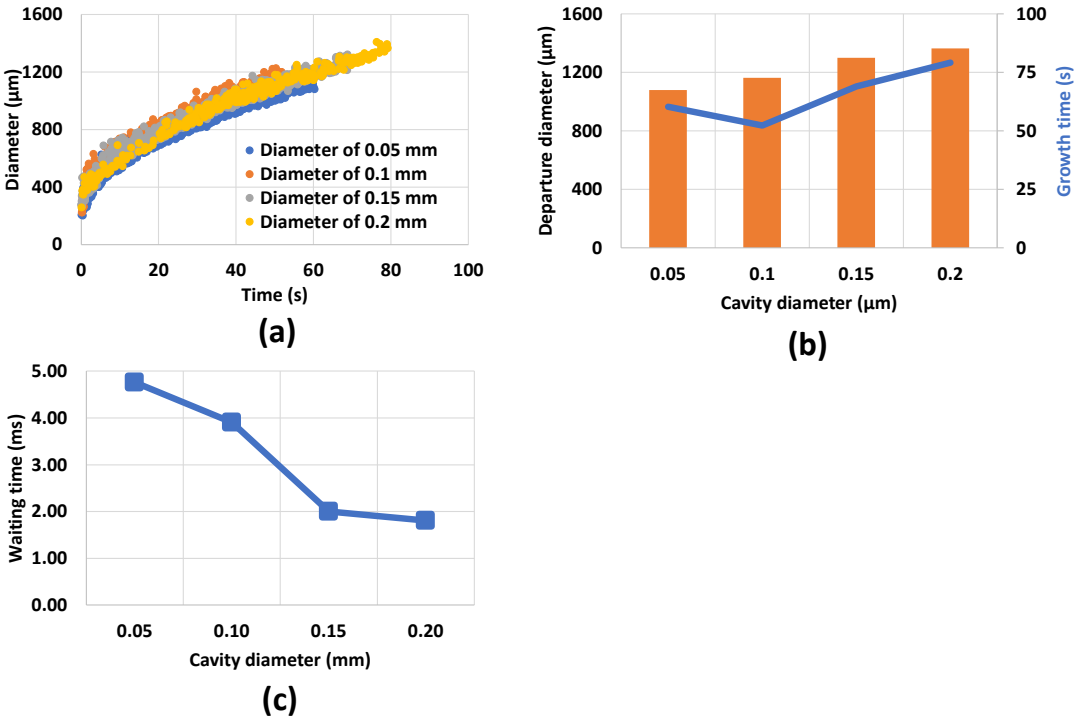


Figure 6.3 Temporal evolution of bubble growth (a), bubble departure diameter and growth time (b) and bubble waiting time (c) for artificial cavities with a diameter range of 0.05-0.2 mm at constant aspect (depth/diameter) ratio 3.

Kurul & Podowski (1990) assumed that wall heat flux consisted of three parts in subcooled flow boiling, namely latent heat of evaporation, liquid-phase convection and sensible heat due to quenching. The latent heat of evaporation is defined in equation (1.1). The product of fD^3 of this equation is studied as a parameter that assesses the heat transfer rate in the cavity.

The value of fD^3 represents the vapour volume flowrate generated at the wall and is plotted against the cavity diameter in Figure 6.4, which shows that it gradually increases from 2.08 E-11 to 3.22 E-11 m^3/s, which is an indication of the increased heat transfer rate for an increased cavity diameter from 0.05 to 0.2 mm. The results confirm the non-linear rate of increase of transferred heat inside the cavity with the cavity diameter, which supports the observed behaviour in Figure 6.4.

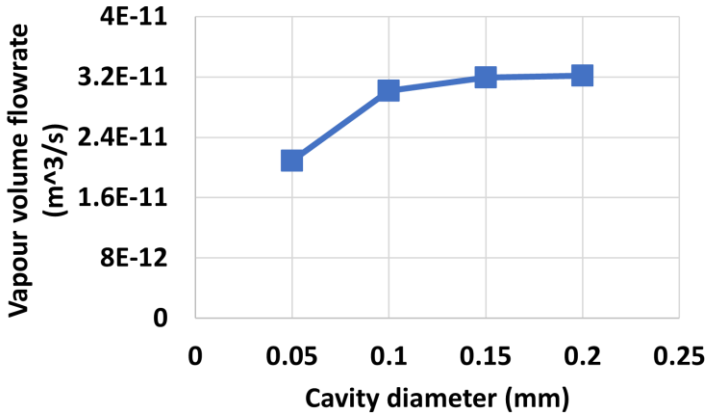


Figure 6.4 Change of vapour volume flowrate (fD^3) as a function of artificial cavity diameter.

6.3 Bubble behaviour at artificial cavity pairs during flow boiling

The effect of spacing between two artificial cavities on the bubble growth period, waiting time and growth profile are reported in section 6.3.1. The effects of experimental conditions on bubble behaviour at two cavities with fixed spacing are reported in section 6.3.2.

6.3.1 Effect of spacing between two cavities on bubble behaviour

The bubble behaviour at a single cavity was investigated in chapters 3-5 and sections 6.1 and 6.2. However, a typical nucleation wall has many nucleation sites, so bubbles are initiated at multiple cavities. Therefore, they may behave differently than bubbles at single cavities. The purpose of the current section is to provide an understanding of bubble formation that may lead to improved design of heat exchanger walls with higher heat transfer rates during boiling and possibly higher critical heat flux. Thus, an understanding of the effect of spacing between cavities on bubble characteristics is important for improved designs.This section presents bubble behaviour when initiated at two artificial cavities with spacing in a range between 0.4 mm and 1.2 mm for a constant cavity diameter of 0.2 mm and cavity aspect ratio of 5.

(a) Experimental setup

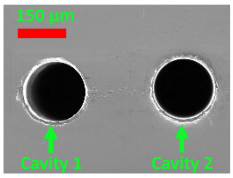
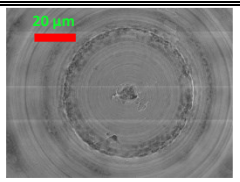
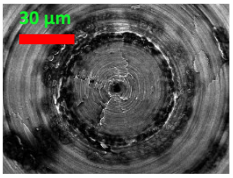
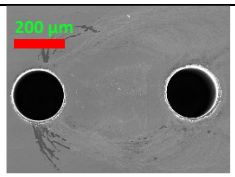
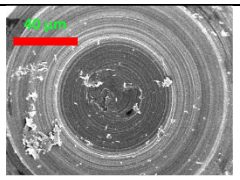
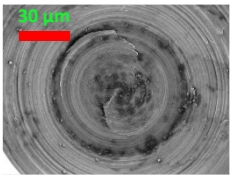
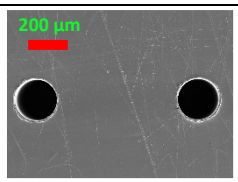
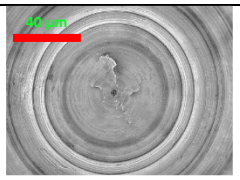
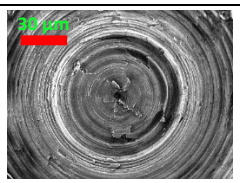
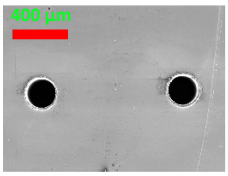
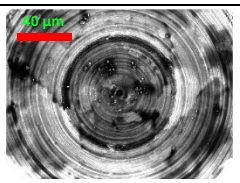
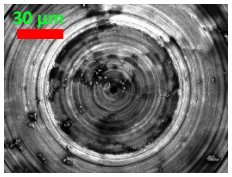
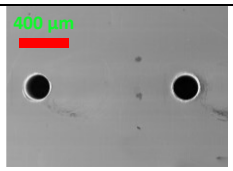
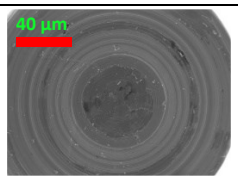
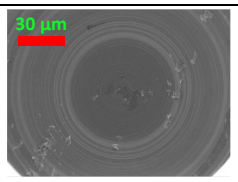
The experimental rig of Figure 2.1 was used for this study. However, the nucleation wall of the test section was replaced with another one containing two artificial cavities. Different nucleation walls were manufactured and tested parametrically for different cavity spacings. The two cavities had a constant diameter of 0.2 mm and a depth of 1 mm, so an aspect ratio of 5. Each cavity geometry remains the same as the single cavities tested in Chapter 3 to Chapter 5. The cavities are positioned behind each other in the direction of the liquid flow. The experimentation conditions are kept the same as those of Case 7 in Table 4.1.

(b) Cavity preparation

The two cavities were drilled using a lubricated micro-drill. SEM imaging showed that some lubricant oil remained inside the cavities after the drilling process concluded. A cleaning process took place to avoid the influence of the remaining oil on the boiling process. The nucleation wall with the manufactured cavities was submerged in isopropanol or a detergent and placed in an ultrasonic bath in an upward direction. The process gradually removes the air trapped inside the cavities and fills them up with the cleaning liquids that remove/dissolve the oil. After the cleaning process, SEM imaging indicated that solid nanoparticles were discovered inside the cavities as a product of the drilling process. It was found that the change of plate orientation inside the ultrasonic bath (placing this with the cavities facing downwards instead of upwards during the cleaning process) was a necessary step to remove the nanoparticles formed; this was confirmed with a final SEM imaging of the cavities.

The cleaning process sometimes takes 6 hours to fully dissolve the oil and release the remaining particles from inside the cavity. The images of the cleaned cavity top and bottom surface, captured by SEM, are shown in Table 6.3, where cavities 1 and 2 are named along the flow direction. The bubbles growing at cavities 1 and 2 are named bubbles 1 and 2, respectively.

Table 6.3 Images of the bottom and top surfaces of artificial cavities with spacings 0.4, 0.6, 0.8, 1 and 1.2 mm

Spacing (mm)	Top surface for Cavity 1 and 2	Bottom surface for Cavity 1	Bottom surface for Cavity 2
0.4			
0.6			
0.8			
1			
1.2			

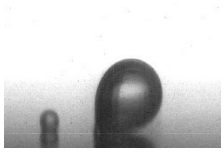
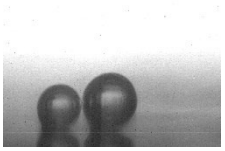
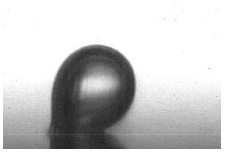
(c) Characterising bubble cycles

The captured images of the temporal evolution of the bubble pair growing at the two artificial sites showed that, at different time periods, the size of bubble 1 could be larger or smaller than bubble 2. For example, bubble 1 is merged into bubble 2, and a new bubble will be initiated at cavity 1. As a result, bubble 1 is smaller than bubble 2 at the cavity 2.

To analyse all possible bubble size evolution permutations, the bubble cycles are classified into four cases according to bubble size differences at a given observation time. Table 6.4 shows typical bubble images at the start and end times of each of the four cases. The start time refers to the moment that the criterion shown in Table 6.4 is met. When both bubbles evolve separately at the growth period, three cases are identified, namely C1, C2 and C3, referring to states where the size of bubble 1 is smaller, similar, and larger than the size of bubble 2, respectively. Case C4 is associated with bubbles 1 and 2 merging into one single larger bubble. At the end of each case, the two bubbles may merge or not. Therefore, the probability of the appearance of one case after another is presented in section 6.3.1. These

four cases will be used below to analyse the bubble behaviour when flow boiling occurs at two artificial sites.

Table 6.4 Typical bubble images at the start and end times of each of the four identified cases, which have been identified from the imaging study of bubble formation at two cavities during flow boiling.

Case Name	Criterion	Start time	End time
C 1	Bubble 1 < bubble 2		
C 2	Bubble 1 ~ bubble 2		
C 3	Bubble 1 > bubble 2		
C 4	One bubble (merging)		

(d) Temporal bubble evolution

The complete bubble cycles are classified into the four cases described in section 6.3.1 (c). Table 6.5 shows an example of the time sequence of different bubble case types. The time sequence of cases is found to change with the cavity spacings. Table 6.5 shows the different cases that occur in a temporal sequence between the start of Case C2 till the next time that case C2 re-appears.

The temporal sequences of the bubble cases for spacing between cavities of 0.4 mm are used as an example to explain the reason for the cases formation at such temporal sequence in Table 6.5. Table 6.5 shows that for cavity spacing 0.4 mm, the temporal sequence of a bubble cycle is C2, C4, C1, C3, C4, C1 and again C2 from left to right. It appears that for the small space of 0.4 mm, as the two individual bubbles grow for case C2, they touch and merge into one. As a result, case C4 is formed as the second stage after case C2. The merged bubble of case C4 keeps growing, and at a later time, the merged bubble departs from cavity 1 and is anchored to cavity 2. As this happens, a new bubble is formed at cavity 1, which initiates case C1. Then, the large bubble at cavity 2 departs, and case C3 starts, as a new bubble is initiated at cavity 2. As time evolves and the bubbles grow, they merge to initiate again a case C4 event. Later, case C1 is initiated because the merged bubble of case C4 departs from cavity 1

and is anchored to cavity 2, which allows a new bubble to form at cavity 1, initiating a new case C1 event. The early departure of the large bubble 2 of case C1 results in the formation of a new bubble at cavity 2, which is of similar size as that at cavity 1 and case C2 in re-initiated.

Table 6.5 Temporal sequences of cases of bubble pair evolution from left to right side for spacings of 0.4-1.2 mm between the two artificial cavities during flow boiling.

Spacing (mm)	Case C2	Case C4	Case C1	Case C3	Case C4	Case C1	Case C2
0.4							
0.6							
0.8							
1.0							
1.2							

(e) Temporal sequence and probability distribution of bubble cases

Table 6.5 shows that the case that may follow case C1 can be case C3 or case C2, which indicates the variation of the temporal sequence of appearance of different cases for the same cavity spacing of 0.4 mm. As the cavity spacing increases, case C4 does not often appear due to the lower probability of the two bubbles touching and merging. This section uses time sequences as examples of Table 6.5 to quantify the probability of the appearance of a bubble case after each of the four cases C1-C4 for spacings between cavities of 0.4-1.2 mm. The probability was quantified by using 6-15 events depending on the different length of time period, and the results are presented in Table 6.6.

The probability of each case was estimated according to the following method. As an example, cavity spacing of 0.8 mm shows that cases C4 and C1 appear 12 and 1 times, respectively, in a temporal sequence after case C3 during a recorded time of 13 mins. Thus, the estimated probability of appearance in the temporal sequence of case C4 after C3 is 12/13 (92.3 %) and case C1 after C3 is 1/13 (7.7 %), which are the quantities shown in Table 6.6.

Table 6.6 presents the observed bubble case in the first left column and, in the second column, the bubble case that follows the current case for each spacing between cavities. The probability of appearance of the next case is shown in parentheses in the table. Table 6.6 shows that, for cavity spacing of 0.4 mm, bubble cases C3 and C2 may appear in the temporal

sequence with a possibility of 87.5 % and 12.5 %, respectively, after case C1. The results for each bubble case are discussed below.

Table 6.6 Probability of appearance of a bubble case after each of the four cases C1-C4 in the temporal sequence for spacings of 0.4-1.2 mm between the two artificial cavities during flow boiling

	Spacing (mm)				
	0.4	0.6	0.8	1.0	1.2
First case	Next case (probability of appearance)				
C1	C3 (87.5 %) C2 (12.5 %)	C3 (100 %)	C3 (78.6 %) C2 (21.4 %)	C2 (100 %)	C 2 (100 %)
C2	C4 (100 %)	C1 (100 %)	C1 (100 %)	C1 (57.1 %) C2 (28.6 %) C3 (14.2 %)	C2 (16.8 %) C3 (83.3 %)
C3	C4 (100 %)	C4 (100 %)	C4 (92.3 %) C1 (7.7 %)	C4 (100 %)	C4 (62.5 %) C2 (25 %) C1 (12.5 %)
C4	C2 (46.7 %) C1 (53.3 %)	C2 (87.5 %) C1 (12.5 %)	C2 (100 %)	C2 (100 %)	C2 (100 %)

Classification of case C1

This part discusses the probability of the appearance of different cases after case C1 for spacings 0.4-1.2 mm. The probability of the appearance of C3 after C1 is 87.5 %, 100 % and 78.6 % for spacings 0.4, 0.6 and 0.8 mm, respectively, which indicates that this case follows C1 most of the time for spacings of 0.4-0.8 mm. However, this probability is gradually reduced and replaced by the appearance of C2 with a probability of 100 % for spacings 1 and 1.2 mm. For spacings 0.4-0.8 mm, bubble 2 tends to detach from the wall without interacting with bubble 1. At these spacings, the time of existence of case C1 is in the range of 19-41 s, which leads to an increased bubble size 2 and an increase of the corresponding drag force. Thus, bubble 2 tends to detach from the wall without interacting with bubble 1, which makes case C3 appear. However, for spacings 1 and 1.2 mm, the time of existence of case C1 is reduced to 0.02 - 0.09 s, as quantified by the average bubble time in Figure 6.5 (a). Similarly, bubble 2 departs from the wall early, and thus, bubble 1 has time to grow without interacting with bubble 2. Thus, the nucleated bubble 2 gains a similar size as that of bubble 1. This is the reason for the appearance of case C3. The image analysis shows that, for different spacings, the case period varies, which further affects the probability of the appearance of the next case. It is noted that the reason for the appearance of case C2 is different for spacing 0.4 mm than for spacings of 0.8-1.2 mm. For spacing 0.4 mm, case C2 is formed due to the departure of the merged bubble of case C4. However, for spacings 0.8-1.2 mm, case C2 is formed due to the short period of presence of case C1 and the departure of bubble 2.

Classification of case C2

This sub-section considers the cases that follow case C2 for spacings 0.4 mm to 1.2 mm. The cases that follow C2 are C4, C1 and C3 for spacings 0.4, 0.6-1.0, and 1.2 mm with a probability of 100 %, 100 % and 57.1 %. The reason is that for the small spacing of 0.4 mm, it is easier for the two bubbles to merge into one as they grow. For increased spacing of 0.6-1 mm, bubble 1 tends to merge with bubble 2 due to the influence of the liquid flow. For spacing 1.2 mm, bubble 2 tends to detach from the wall without merging due to the increased spacing.

Classification of case C3

For the leading bubble case C3, the size of bubble 1 is larger than that of bubble 2. The effect of drag force then inclines bubble 1 in the direction of the flow, bringing it closer to bubble 2 to initiate coalescence with bubble 2. As a result, the two bubbles are easily merged into one. This is proved by the probability of cases following case C3 in Table 6.6, which is higher for Case C4 following C3 with probability 100 %, 100 %, 92.3 %, 100 % and 62.5 % for spacings of 0.4, 0.6, 0.8, 1.0, and 1.2 mm respectively. This behaviour is reduced for spacing 1.2 mm because the increased spacing does not allow bubble coalescence that covers the two cavities. Alternatively, the two bubbles coalesced and immediately detached from the surface as one bubble.

Classification of case C4

For the leading bubble case C4, the probability of case C2 following case C4 increases from 46.7 % for spacing 0.4 mm to 100 % for spacings 0.8-1.2 mm. For cavity spacing 0.4 mm, there is a 53.3 % probability that the coalesced bubble departs from cavity 1 and is anchored to cavity 2. For increased spacing, bubble coalescence is eliminated. It appears that the increased cavity spacing increases the difficulty for a coalesced bubble to cover a larger area and cover both cavities.

(f) Average duration and probability of observation of bubble pair cases

In section 6.3.1, it is mentioned that the duration of each bubble case varies with cavity spacing. This section reports the average duration of presence of each case and its associated probability to be encountered at a random occurrence in time based on the duration of its existence. The reported percentage, to some extent, represents the probability of observing one case at a random instance after the initiation of the recording period. The average duration and probability of presence of cases C1-C4 for spacings 0.4-1.2 mm are presented in Figure 6.5 (a) and (b), respectively.

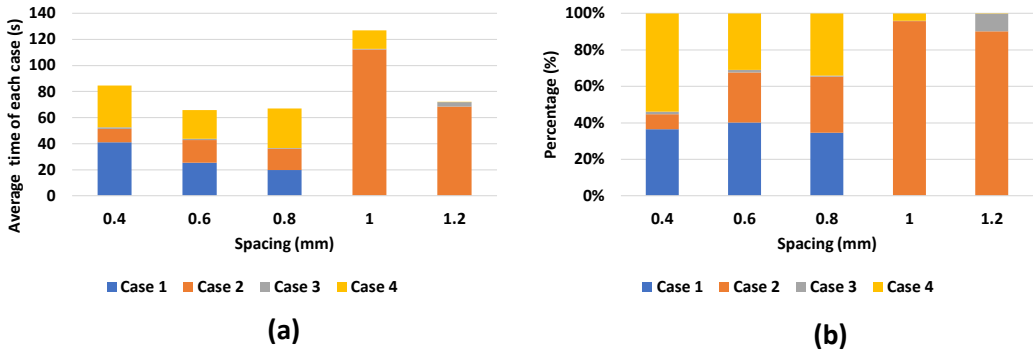


Figure 6.5 Average duration (a) and probability (b) of the presence of cases C1, C2, C3 and C4 as a function of cavity spacing during flow boiling at two artificial sites.

Classification of case C1

It is observed in Figure 6.5 (a) that as the cavity spacing increases from 0.4 to 1.2 mm, the average duration of case C1 reduces from 40.99 to 0.02 s. In Table 6.6, case C1 is initiated by cases C2, C3 and C4 due to the interaction of the two bubbles. However, the increased spacing restricts such interaction, and as a result, the duration of case C1 is shortened.

The probability of presence of C1 for cavity spacings from 0.4 mm to 0.8 mm shows a small variation between 34 and 40 %. However, a sharp reduction of around 33.9 % is observed for spacing 1 mm, while the average duration is reduced from 19.8 to 0.09 s. Thus, there is possibly a threshold between cavity spacing of 0.8 mm and 1 mm that triggers a significant presence decrease of case C1. Since the typical bubble diameter is around 1 mm, the probability of two bubbles coalescing is reduced for cavity spacing of 1 mm.

Classification of case C2

In Figure 6.5 (a), the average duration of case C2 gradually increases from 10.3 s to 112 s for an increase of cavity spacing from 0.4 to 1 mm, which means that the increase of spacing enhances the existence of case C2 since the interaction of the two bubbles is reduced. However, it is interesting to find that as the spacing increases by 0.2 mm above 1 mm, the probability of presence is reduced from 96 % to 90 % due to the percentage increase of case C3. In addition, the average duration is reduced from 112 to 68 s. This possibly indicates that there is a spacing threshold for case C2 as well. The observed reduction occurs due to the departure of bubble 2. As the spacing increases, bubble 2 tends to depart from the cavity without interaction with bubble 1, which is enhanced for cavity spacing larger than 1mm.

Classification of case C3

The maximum average duration of case C3 is around 3.33 s, which is much smaller than that of Cases C1, C2 and C4, which have maximum durations of 41 s, 112 s and 32 s in Figure 6.5 (a), respectively. This is because, for case C3, bubble 1 is larger than bubble 2, and

bubble 1 easily inclines toward bubble 2 due to flow effects and shortens the spacing between the two bubbles. As a result, bubbles 1 and 2 can easily coalesce. As Table 6.6 shows, case C4 always follows case C3 because of this reason. The average time slightly varies between 0.34 and 1.15 s for cavity spacings between 0.4 and 0.8 mm. However, it increases to 3.33 s for a spacing of 1.2 mm, since larger spacing restricts bubble coalescence.

Classification of case C4

The average duration of case C4 gradually reduces from 32 s to 0.08 s for an increase of cavity spacing from 0.4 mm to 1.2 mm in Figure 6.5 (a). The probability of presence gradually decreases from 53.94 % to 0.15 % due to the inability of bubbles to coalescence for the larger spacing.

(g) Evaluation of cavity spacing on the heat transfer rate

This section uses the measurements to evaluate the influence of the cavity spacing on the heat transfer rate. The volume flow rate of the vapour is calculated by dividing the total volume of the departed bubbles by one spacing during the recording time, which represents the net rate of transferring heat away from the wall. The number of departed bubbles, the volume of these bubbles, the recording time, and the calculated average vapour volume flowrate per cavity are shown in Table 6.7. The evolution of the parameter, average vapour volume flowrate per cavity, is presented in Figure 6.6.

Table 6.7 Estimate of vapour volume flowrate per artificial cavity at the nucleation wall during flow boiling.

Spacing (mm)	0.4	0.6	0.8	1	1.2
Number of departed bubbles	17	19	29	13	19
Vapour volume of all departed bubbles (μm^3)	2.36E+10	2.15E+10	3.37E+10	3.02E+10	1.94E+10
Recording time (s)	8.96E+02	5.70E+02	8.01E+02	7.03E+02	3.80E+02
Frequency (number/time)	1.90E-02	3.33E-02	3.62E-02	1.85E-02	5.00E-02
Vapour volume flowrate per cavity ($\mu m^3 \cdot s^{-1}$)	1.32E+07	1.88E+07	2.10E+07	2.15E+07	2.55E+07

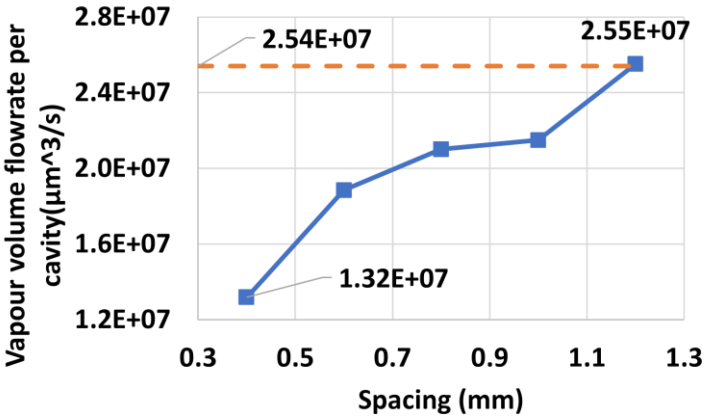


Figure 6.6 Vapour volume flowrate per cavity as a function of cavity spacing.

Figure 6.6 shows that the average vapour volume flowrate per cavity generated by the bubbles on the nucleation wall gradually increases from 1.32E+07 to 2.55 E+07 $\mu m^3/s$. This shows that the cavity spacing of 1.2 mm is desirable to remove more energy through phase change from the wall.

This finding is probably due to the contribution of the reduced duration of the presence of case C4 for increased cavity spacing in Figure 6.6 (d). For case C4, the growing bubbles at the two cavities coalesced into one and covered the two cavities, increasing the amount of vapour generation per unit time and area. To some extent, this bubble behaviour leads to a local film boiling. It is known that vapour film covering a surface reduces the heat transfer rate due to the low thermal conductivity of the vapour. Thus, the increase of cavity spacing reduces the duration of bubble events of case C4, helping to remove more heat from the wall. In summary, the results show that the boiling heat transfer rate is reduced as the cavity spacing is reduced. This has implications for the design of a nucleation wall that can deliver maximum heat transfer rate during flow boiling.

In Figure 6.6, the average volume rate per cavity for a single cavity exposed to the same condition as the two cavities is also added, which is a constant value of 2.54E07 $\mu m^3/s$. This further indicates that for cavity spacing of 1.2 mm, the average heat transfer rate per cavity is close to that of the single cavity. Therefore, the smaller cavity spacing reduced the heat transfer rate, and the recommended cavity spacing on the nucleation wall for this study is around 1.2 mm. This is in agreement with the findings of Yu, Lu & Cheng (2006), who found that smaller cavity spacing results in lower heat transfer performance due to horizontal bubble coalescence.

In the simulation work of Gong & Cheng (2016), a mutual inhibition of heat transfer rate is reported between adjacent bubble nucleation sites. This inhibition reduces as the spacing increases. A non-dimensional spacing parameter P^*, the ratio of the distance (P) of the leading edge of the two adjacent cavities divided by the Laplace length (L_h), is defined to quantify this

inhibition. Such inhibition is eliminated for $P^* \geq 2.25$. Figure 6.7 demonstrates the definition of P^*.

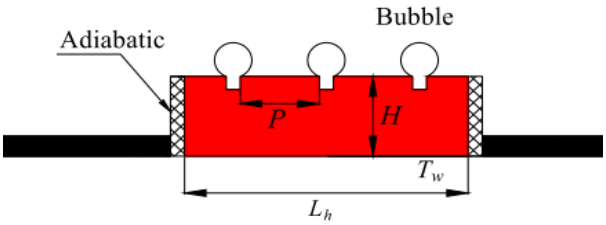


Figure 6.7 Schematic of cavity arrangements on a nucleation wall with definition of the cavity distance P (Gong & Cheng, 2016).

It is reported that bubble merging occurs for $P^* = 0.9$, and the bubbles become independent from each other for $P^* = 2.25$ and 4.5. However, in the current experiments, the two bubbles tends to be merged at $P^* = 0.08$ (spacing of 0.4 mm). The mutual inhibition of the heat transfer rate of the two cavities is eliminated at $P^* = 0.4$ (spacing of 1.2 mm) when the vapour volume generation rate is close to that at a single cavity, see Figure 6.6. Therefore, the value of P^* as an inhibition threshold differs in the current study. This is probably due to the extremely small liquid–vapour density ratio of 10 (Gong & Cheng, 2016), while the corresponding value is around 2000 in the current study. This demonstrates that the operating conditions, i.e. operating pressure, will influence the interaction between nucleation cavities. Since the size of the generated bubbles is expected to reduce at high pressure, the distance between the cavities can be reduced before bubbles start interacting. This effect must also be considered for the design of a nucleation wall with improved performance.

6.3.2 Effect of operating conditions on cavity pair ebullition behaviour

Chapter 3 and Chapter 4 presented the bubble behaviour, including the temporal evolution of the bubble growth at a single cavity during flow boiling. Section 6.3.1 examined the influence of the spacing between the two cavities. These results demonstrated that the existence of a second artificial cavity leads to interaction between the two bubbles that modifies their temporal evolution for certain cavity spacing. This section reports the effect of experimental conditions on the temporal evolution of the bubble growth generated from two cavities with fixed spacing.

The results of section 6.3.1 showed that the interaction between bubbles generated at two artificial cavities with a spacing of 0.6 mm is more repeatable than for other spacings. Therefore, a cavity spacing of 0.6 mm was selected as a reference to study the effect of operating conditions on the temporal evolution of the two bubbles.

Definition of experimental operating conditions

The experimental arrangement of Chapter 2 was used to study the behaviour of two boiling bubbles generated at two artificial cavities. The two cavities were manufactured on a nucleation wall and followed the cleaning process, explained in section 6.3.1. The images of the two cavities with a spacing 0.6 mm are shown in Table 6.3.

The operating conditions that have been considered for the study of this chapter are shown in Table 6.8. The case number continues by extending the case numbers reported in Table 6.2. The operating conditions of case 24 can be regarded as a reference. In comparison to case 24, the conditions examine lower wall superheat, lower inlet velocity and lower water inlet temperature correspond to cases 21, 22 and 23, respectively. The cases 5, 2 and 11 of Table 4.1 gain the same experimental conditions as cases 21, 22 and 23, respectively. The findings of the single cavity studies of Chapter 4 indicate that the selected operating conditions will influence the bubble growth rate and amplitude of fluctuations. In this section, the two parameters are investigated to assess the effects of the experimental conditions.

Table 6.8 Operating conditions for studies of the behaviour of the two bubbles generated at two artificial cavities during flow boiling.

Case number	Liquid Velocity (m/s)	Heat flux (W/m^2)	Water inlet temperature (°C)	Wall superheat (°C)
21	0.214	6.54E+03	93.57663	-2.73965
22	0.166	2.38E+04	93.98312	8.815339
23	0.221	5.11E+04	73.99825	6.974223
24	0.214	2.60E+04	93.69807	8.461761

Temporal evolution of the diameter of two interacting bubbles

Section 6.3 indicated that there are four cases that can occur during the temporal evolution of two bubbles. These are cases C1, C2, C3, and C4 of Table 6.4, and case C4 refers to coalesced single bubbles. For comparison with single bubbles formed at the single cavity, case C4 is selected.

For Case C4, the two bubbles coalesce and are observed growing as a single bubble attached at a location above the two artificial cavities. The temporal evolution of the coalesced bubble growth of case C4 for operating conditions of cases 21, 22, 23 and 24 of Table 6.8 is plotted in Figure 6.8. Time zero in Figure 6.8 is the time that the two bubbles coalesce and start growing together as a single bubble. The growth rate at operating conditions 21, 22, 23 and 24 is 3.5, 5.6, 5.3 and 11.7 μm/s, respectively. The maximum growth rate is obtained for operating condition 24, which has the highest heat flux and low condensation, and the lowest for condition 21, which has the lowest heat flux, in agreement with expectations from the single cavity results of Chapter 4. The growth rate for the bubble

at case 7 in Table 4.1 is 11.3 μm/s at a similar size range. Cases 7 and 24 are operated under similar conditions. This coincidence indicates that under the same operating condition, the effect of the presence of another cavity on the growth rate of a merged bubble is negligible compared to that at a single cavity.

The initial size of the coalesced bubble at the merger moment (time equals zero) are 833, 920, 877 and 871 μm for conditions 21-24, respectively, which are all very similar. The departure bubble diameter at conditions 21, 22, 23 and 24 is 1078, 1620, 1268 and 1144 μm, respectively. It can be found that the maximum departure size is obtained at the lower velocity. This is consistent with observations for the single cavity and consistent with the force balance model of section 5.5. The temporal evolution of the bubble diameter of equation (4.1) fitted for a single cavity is plotted in Figure 6.8 (d) with orange dots. The predicted size is smaller than the measured initial bubble size because the initial size of 871 μm is the result of the merge of two bubbles. After that, the growth rate of the predicted data and measured data are 13 and 11.7 μm/s, respectively. This indicates that, under similar conditions, the effects of another cavity with spacing 0.6 mm on the bubble growth rate is negligible except for the underestimation of bubble size at the initial stage compared to that at the single cavity.

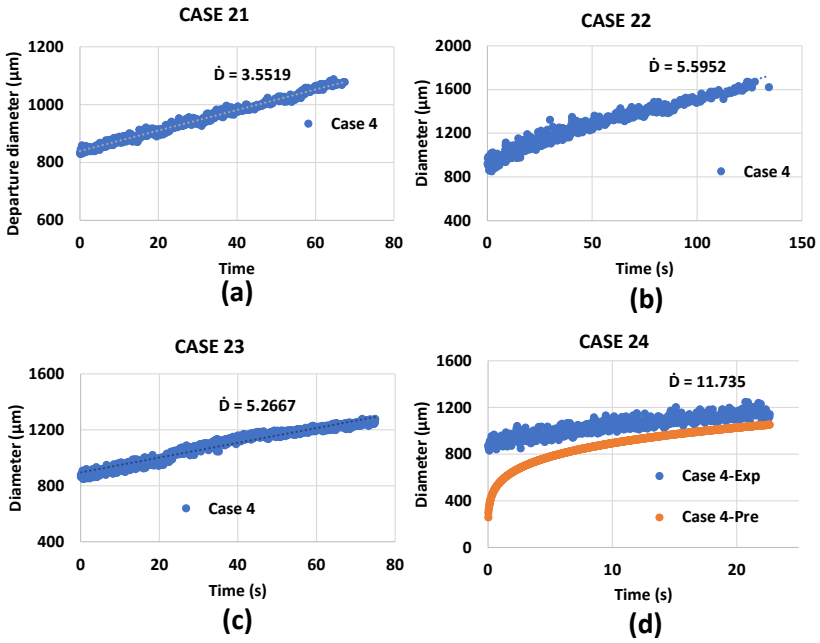


Figure 6.8 Temporal evolution of the diameter of the coalescent single diameter at two artificial sites during case C4 under flow boiling for operating condition cases 21 (a), 22 (b), 23 (c) and 24 (d) of Table 6.8.

Typical temporal sequences of the coalesced bubble images are shown in Figure 6.9. These images show that the way that the coalesced bubble grows is qualitatively similar to observations for a single cavity. By comparing the bubble images in Figure 3.9 (a) and Figure 6.9, similar bubble behaviour is observed for the single bubble and the merged bubble at the two cavities in terms of the inclination angle and the contact diameter. The inclination angle for the merged bubble slowly increases to around 20 ° from zero and jumps to 45 ° within 0.2

s. After that, the departure occurs. The inclination angle of 45° occurring at the departure moment is the same as that for the single cavity. The low inclination angle before the departure is the result of the strong surface tension force contributed by the larger contact area, which resists the bubble inclination along the flow direction. This is not observed at the single cavity. The departure of the coalesced bubble anchored to the wall occurs due to the breakage of the neck at cavity 1, and the resulting shock triggers the neck breakage at cavity 2. This is similar to the observation for the single bubble reported in section 5.5. The bubble contact diameter at the departure moment is 0.74 times the departure size on average, which is slightly smaller than that (0.76) for the single cavity in section 3.9.

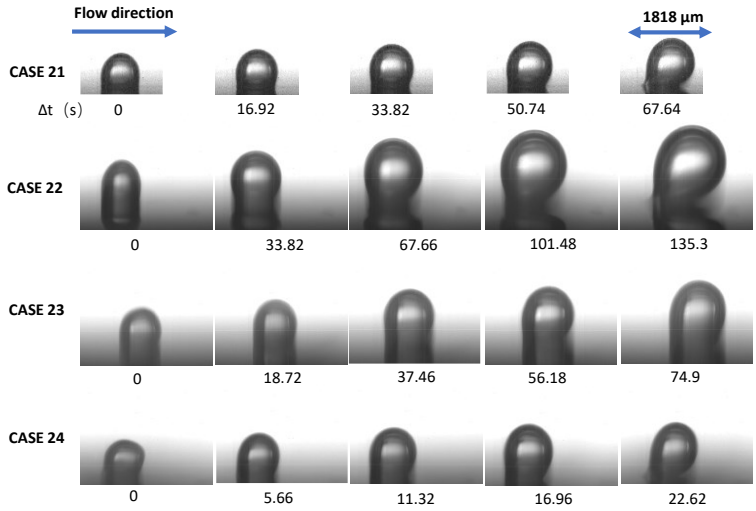


Figure 6.9 Recorded images of the coalescent bubbles growing as one at the two artificial sites during case C4 under flow boiling for operating condition cases 21, 22, 23 and 24 of Table 6.8. The scale arrow in the first row is the same for all rows.

6.4 Summary

This chapter presented the effects of cavity depth and diameter on bubble growth time, waiting time, departure diameter and frequency. In addition, the effects of cavity spacings and experimental conditions on the two cavities are investigated. The findings are summarised as follows.

1. Cavity depth at a range of 0.2 to 0.95 mm shows negligible effects on bubble growth time and growth temporal evolution. However, the waiting time generally reduces with cavity depth.
2. Two types of artificial cavities are found with characteristics affecting their bubble activation properties. Type 1 cavities can always activate bubble formation during boiling, even after re-starting the experimental rig. Type 2 cavities cannot initiate boiling evens when the wall superheat is raised to 20 °C and maintained for one hour. Type 2 cavities may increase the critical heat flux by resisting the formation of film

boiling. Type 2 cavities act in this way because their dimensions do not allow to trap gas inside, and therefore boiling cannot be initiated.

3. Negligible effects are observed on the bubble growth profile for cavities at diameter ranges of 0.05 to 0.2 mm. However, the bubble departure diameter reduces with cavity diameter. This is caused by the reduced surface tension force. The bubble waiting time shows a reduction with an increase in cavity diameter, which may happen due to the increased heat transfer area in the cavity and higher local temperature.
4. The growth of bubbles at two artificial cavities is affected by bubble interaction with each other. The complete bubble cycles are divided into four cases according to the relative size of the two bubbles at the two cavities. The average duration of the presence of each bubble case, the probability and the sequence of each case vary with cavity spacing.
5. Smaller cavity spacing results in a longer time of appearance of a merged bubble covering the two cavities. This reduces the net boiling heat transfer rate evaluated according to the parameter of average bubble volume flowrate per cavity. The rate increases with cavity spacing in a non-linear manner, and the maxima were observed at the maximum spacing of 1.2 mm, which was almost equal to the heat transfer rate of a single isolated cavity.
6. The effects of experimental conditions on bubble behaviour formed at two artificial cavities are reported based on bubble case C4. The growth profile of the coalesced bubble shows a linear increase for all tested experimental conditions, which are the same as those for a single cavity. In addition, the bubble growth rate shows values in the same size range. These findings indicate that the effect of the presence of a second cavity on the net heat flux of the coalesced bubble at the same condition is negligible.

Chapter 7 Conclusions and recommendations for future work

7.1 Conclusions

This thesis studies the bubble characteristics at artificial cavities during flow boiling and compares bubble behaviour between artificial and natural cavities. The physics of bubble formation and temporal evolution during boiling at artificial sites have not been understood, and this study provides new insights. Detailed summaries of the findings have been presented at the end of each chapter. This section provides an overview of the novel aspects of the research, starting with the boiling at natural cavities and then continuing with boiling at artificial cavities.

1. The large variability of the bubble characteristics and the stochastic behaviour of bubbles formed at natural sites has been reported in the literature and verified by this study. A novel contribution of the current research was the identification of the exact locations of active natural sites and the quantification of the associated geometry of natural cavities. The identification of the location of the natural cavities on the nucleation wall was achieved by observing the location of surface patterns formed by the increased local surface temperature below the boiling bubbles attached at natural sites. These patterns were formed by the dry surface below the bubbles, which was verified by the evaluation of material deposits on the surface at the location of the patterns that included elements that were present in the liquid. Two types of natural sites were identified. Some are indeed physical cracks, which has been the assumption in the literature. However, the location of the patterns showed that most active natural cavities are smaller than the resolution of the imaging microscope, i.e. 0.25 microns, and probably not physical cracks. This finding suggests that another boiling initiation mechanism may be present, in addition to the current understanding of bubble initiation at cavities where preexisting gas embryos are present.
2. The bubble characteristics at artificial sites are significantly different than those at natural sites, as established by current measurements at identical operating conditions. The size of artificial cavities is larger than the natural cavities, with a diameter of 0.2 mm and a depth of 0.95 mm. The results showed that at artificial cavities, the bubble growth period increased by 23,290 times, and the bubble departure diameter doubled relative to natural cavities, while the bubble characteristics were fairly repeatable at

different events. The large bubble growth time is determined by the much slower growth rate and the higher departure diameter.

3. The bubble growth mechanism at the artificial cavity is not well understood. Although the bubble growth mechanism at natural cavities is reported and explained by the contributions of evaporation of the liquid microlayer below the bubble, superheated layer, and condensation, this physical mechanism is not present at artificial cavities due to the large increase of the bubble growth period. It is suspected that the presence of a amount of non-condensable gas inside the bubble and the local high temperature at the bubble contact area play an important role at the bubble growth rate. Although there is substantial evidence that supports the above contributions, direct verification is still required. Therefore, the measured bubble growth period at artificial cavities could not be predicted from existing models developed for natural sites, and therefore, a new empirical correlation was developed that could fit well the dimensionless diameter.
4. The bubble departure diameter and frequency are two critical parameters for the estimation of boiling heat flux. The bubble frequency at artificial cavities is determined by the bubble growth period only because of the negligible value of the waiting time. The bubble departure diameter and growth period at artificial cavities are predicted by two dimensionless correlations, which consist of a group of dimensionless parameters, including the Reynolds number, dimensionless heat flux, superheat Jakob number and the subcooled Jakob number representing the effects of liquid velocity, heat flux, wall superheat, and subcooling. The two correlations predict the bubble departure diameter and frequency with a mean absolute error of 3.89 % and 14.7 %, respectively, relative to the current measurements.
5. In addition to the developed empirical correlations, the force balance approach on the growing boiling bubbles was used at artificial sites, and a model was developed to predict the bubble diameter, which considered the surface tension, drag and growth forces. The growth force was found negligible. The surface tension and drag forces, in agreement with Du, Zhao & Bo (2018), play the dominant role in the bubble departure diameter estimation. In this new model of the current study, the bubble departure size is determined by the liquid flow velocity and the surface tension force, which is also affected by the artificial cavity diameter. The model shows a good prediction of the bubble departure diameter with a mean absolute error of 8.47 %. However, a drawback remains since the relative error is increased with the reduction of the water inlet temperature, which needs additional investigation.
6. Since the artificial cavity diameter plays an important role on the bubble departure diameter, the effect of cavity geometry on the departure diameter and frequency was

considered in terms of the cavity depth and diameter. The effect of cavity depth on the bubble departure diameter and growth period was negligible. For increased artificial cavity diameter, larger bubble departure diameter and growth time were observed, which is consistent with the findings of the force balance model. Finally, the waiting time was reduced with the increase of the artificial cavity diameter and cavity depth, possibly due to the higher local temperature resulted by the increased interior heat transfer area of the cavity.

7. An important finding is that bubble boiling can occur for nucleation wall temperatures that are lower than the corresponding liquid saturation temperature, which is termed as negative superheat, by up to -3.7 °C. The experimental evidence showed that the local temperature on the nucleation wall below the bubbles could increase above the average wall temperature and transfer the required heat for the growth of the bubble. However, for negative superheat, the temporal evolution of the bubble growth followed a different behaviour than for cases with positive superheat, which indicated that the dominant mechanism associated with conditions of negative superheat was different. However, the developed empirical models and force balance models could capture this behaviour successfully.
8. Practical heat transfer surfaces under flow boiling conditions have a large number of nucleation cavities present on the surface, which may lead to interactions between growing bubbles and modify the observations for bubbles growing at single cavities. Therefore, the bubble dynamics were also investigated at various cavity spacings for two identical artificial cavities to examine the probability of interactions between the two bubbles growing at single cavities. The results showed that bubble interactions led to an increased probability of coalescence due to the influence of the liquid flow and the spacing of the cavities. The bubble merging resulted in larger or smaller bubble sizes being present on each of the cavities relative to the single cavity results. For clarity, four cases were defined according to the relative size of the two bubbles at the two cavities, which indicated that the merger becomes difficult as the bubble interactions are weakened for increased cavity spacings. The cavity spacing affected the temporal sequence of the identified four bubble pair cases and the average bubble growth time. The maximum heat transfer was found for cavity spacing of 1.2 mm when the bubble interaction became negligible, as quantified by measurements of the volume of the generated vapour, using the parameter fD^3, based on the measured bubble frequency f and bubble departure diameter D.
9. The effects of the operating flow conditions on the growth profile of two bubbles with cavity spacing of 0.6 mm were established, and more emphasis was given to the behaviour of the merged bubble that remained attached on the surface between the

cavities. A larger bubble departure diameter is obtained at conditions with lower liquid flow velocity, which is consistent with the findings of the developed force balance model. A higher growth rate was observed at conditions with higher flux and smaller condensation. In general, the growth profiles of individual bubbles above the pair of artificial cavities are similar to that at single cavities on the nucleation wall till the initiation of bubble interaction when the bubble size becomes large relative to the cavity spacing.

10. The design of heat transfer surfaces with artificial cavities in a channel flow was considered to identify approaches to deliver an optimised heat transfer rate. The study with cavity spacings of 0.4-1.2 mm showed that the spacing of 1.2 mm leads to maximum heat transfer because of the measured maximum value of the steam volume generated at this spacing.

(a) Design for higher critical heat flux

To achieve higher critical heat flux, cavities with a diameter of 0.05 mm and depth of 0.15 mm are suggested. These cavities are filled with liquid after the end of experimentation and deactivated bubble formation at a wall superheat of 20 °C. The deactivation of vapour formation is possibly an efficient way to resist the initiation of film boiling, which may increase the critical heat flux. However, the heat transfer rate before the critical heat flux point may be lower because only force convection is present. Thus, the proposed surface design for higher critical heat flux is to add an array of cavities with a diameter of 0.05 mm and depth of 0.15mm located at spacings of 1.2 mm.

(b) Design for higher heat transfer coefficient

This design is suggested to correct the drawbacks of the higher critical heat flux design. Considering the strong interaction of bubbles at a heated surface with a number of cavities, cavities with smaller diameters are proposed, for example, with a diameter of 0.05 mm, and depth of 0.2 mm or deeper. This design ensures that artificial cavities can continuously initiate boiling even after stopping and restarting operations. The small cavity diameter generates lower surface tension force, which leads to higher bubble departure frequency and increased heat transfer coefficient. The drawback is that at high wall heat flux, film boiling may be initiated. The optimum proposed design is an array of cavities with a diameter of 0.05 mm, depth of 0.2 mm or deeper and spacing between cavities of 1.2 mm.

7.2 Future work

1. The advancing contact point is observed being at the cavity mouth centre at the bubble departure time from the artificial cavity. This possibly results in a flow of

liquid towards the cavity, which can increase the bubble growth rate. This suggestion requires investigation, which requires visualisation in a transparent cavity with the help of a fluorescent dye.

2. Periodic fluctuations of the bubble size at the departure time were found, which had a period of 0.161 s for the cavity with diameter and depth of 0.2 and 0.95 mm. This is possibly induced by vortex shedding behind the bubbles as the liquid flows around them. Measurements of flow velocity close to the bubbles using the Particle Image Velocimetry technique or a flow visualisation by using a dye can reveal the influence of the bubbles on the flow profile downstream of the bubble.
3. The liquid microlayer below a bubble plays an important role in the bubble growth at natural sites. However, the liquid microlayer evolution for bubbles at the artificial cavity during flow boiling is not found. Understanding the evaporation rate of the liquid microlayer can assist the development of an energy balance model at artificial cavities, which can explain the formation of the surface patterns that are formed due to liquid evaporation at the microlayer. The surface pattern forms an efficient marker for locating the boiling sites, which may be further investigated and developed as a common way for locating the natural site. Based on the two considerations, the evolution of the microlayer and formation mechanism of the pattern deserves further investigation.
4. The proposed force balance model for the prediction of the departure diameter performs well for an inlet water temperature of 95 °C. However, the relative error is increased at lower inlet water temperatures, such as 74 and 84 °C. Improving the accuracy of the model is important because the departure diameter affects the boiling heat flux. Therefore, understanding the origin of this model behaviour requires investigation.
5. The bubble growth mechanism at positive and negative wall superheats is still not clear, and the bubble growth profile at positive wall superheats at the artificial cavity is fitted with a dimensionless equation. Possibly, the evaporation of the microlayer, superheat layer and condensation layer play a role. In addition to that, possible, the non-condensable gas and the local higher temperature at the cavity may play a role as well. Thus, measurements of the local temperature at the artificial cavity and the concentration of non-condensable gas in the bubble require additional investigation. In terms of the local temperature measurements, possibly a thermocouple embedded underneath the nucleation site is helpful or using an IR camera to measure the local temperature of the nucleation wall, which must be manufactured from a transparent sapphire substrate.

6. It is found that cavities with depth of 0.2 mm and 0.4 mm and diameter of 0.2 mm are filled with liquid after the end of experimentation. Such cavities with filled liquid failed to initiate boiling even at a wall superheat of 20 °C for around one hour, while intensive boiling is observed at the whole nucleation surface. This indicates that a cavity with filled liquid resists the formation of vapour. Thus, the deactivation of boiling may be a way to prevent the formation of film boiling and increase the critical heat flux. The maximum superheat tested in the experimentation was limited to 20 °C in this project, and it is interesting to examine if this is true to higher wall superheats. It is suggested to evaluate if a liquid-filled cavity can enhance the critical heat flux by restricting the initiation of boiling.
7. Two types of natural cavities were observed in this experiment. The type associated with physical cracks, which coincides with the description of natural sites in the literature, is not the dominant based on the current observations. The second type of natural cavity was more common in the current study, which initiates boiling despite having a size smaller than the resolution of the microscope of 0.25 mm. Boiling initiation at such types of natural cavities where physical cracks are not observed needs to be investigated.
8. This suggestion is not only related to boiling research. It is related to the surprising observation of nanoparticle formation on the wall of the artificial cavities. Uniformly distributed circular nanoparticles were found inside an artificial cavity after immersing it into a vacuum ambient. The cavity was cleaned with detergent before. This may be a way to investigate the formation of nanoparticles on surfaces. If such nanoparticle manufacturing can be delivered on demand, it, may also allow the study of the boiling heat transfer and heat transfer in general from surfaces with deposited nanoparticles.

Chapter 8 Bibliography

Abdelmessih, A.H., Hooper, F.C. & Nangia, S. (1972) Flow effects on bubble growth and collapse in surface boiling. *International Journal of Heat and Mass Transfer*. 15 (1), 115–125. doi:10.1016/0017-9310(72)90170-6.

Akiyama, M. & Tachibana, F. (1974) Motion of vapor bubbles in subcooled heated channel. *Bull JSME*. 17 (104), 241–247. doi:10.1299/jsme1958.17.241.

Amidu, M.A., Jung, S. & Kim, H. (2018) Direct experimental measurement for partitioning of wall heat flux during subcooled flow boiling: Effect of bubble areas of influence factor. *International Journal of Heat and Mass Transfer*. 127, 515–533. doi:10.1016/j.ijheatmasstransfer.2018.07.079.

Baldwin, C.S., Bhavnani, S.H. & Jaeger, R.C. (2000) Toward optimizing enhanced surfaces for passive immersion cooled heat sinks. *IEEE Transactions on Components and Packaging Technologies*. 23 (1), 70–79. doi:10.1109/6144.833044.

Bashforth, F. & Adams, J.C. (1883) *An attempt to test the theories of capillary action by comparing the theoretical and measured forms of drops of fluid*. University Press.

Basu, N. (2003) *Modeling and experiments for wall heat flux partitioning during subcooled flow boiling of water at low pressures*.

Basu, N., Warrier, G.R. & Dhir, V.K. (2005) Wall heat flux partitioning during subcooled flow boiling: Part 1 - Model development. *Journal of Heat Transfer*. 127 (2), 131–140. doi:10.1115/1.1842784.

Bon, B., Guan, C.K. & Klausner, J.F. (2011) Heterogeneous nucleation on ultra smooth surfaces. *Experimental Thermal and Fluid Science*. 35 (5), 746–752. doi:10.1016/j.expthermflusci.2010.05.003.

Bosnjaković, F. (1930) Verdampfung und Flüssigkeitsüberhitzung. *Technische Mechanik und Thermodynamik*. 1 (10), 358–362. doi:10.1007/BF02640224.

Brooks, C. (2014) *Wall nucleartion and the two-fluid model in subcooled boiling flow*.

Brooks, C.S. & Hibiki, T. (2015) Wall nucleation modeling in subcooled boiling flow. *International Journal of Heat and Mass Transfer*. 86, 183–196. doi:10.1016/j.ijheatmasstransfer.2015.03.005.

Brooks, C.S., Silin, N., Hibiki, T. & Ishii, M. (2015) Experimental investigation of wall nucleation characteristics in flow boiling. *Journal of Heat Transfer*. 137 (5). doi:10.1115/1.4029593.

Bui, T.D. & Dhir, V.K. (1985) Transition boiling heat transfer on a vertical surface. *Journal of Heat Transfer*. 107 (4), 756–763. doi:10.1115/1.3247501.

Canny, J. (1986) A computational approach to edge detection. *IEEE Transactions on Pattern Analysis and Machine Intelligence*. PAMI-8 (6), 679–698. doi:10.1109/tpami.1986.4767851.

Cao, Y., Kawara, Z., Yokomine, T. & Kunugi, T. (2016) Visualization study on bubble dynamical behavior in subcooled flow boiling under various subcooling degree and flowrates. *International Journal of Heat and Mass Transfer*. 93, 839–852. doi:10.1016/j.ijheatmasstransfer.2015.10.053.

Cattafesta, L., Bahr, C. & Mathew, J. (2010) Fundamentals of Wind-Tunnel Design. In: *Encyclopedia of Aerospace Engineering*. Wiley. p. doi:10.1002/9780470686652.eae532.

Chen, D., Pan, L.M. & Ren, S. (2012) Prediction of bubble detachment diameter in flow boiling based on force analysis. *Nuclear Engineering and Design*. 243, 263–271. doi:10.1016/j.nucengdes.2011.11.022.

Chen, D. qi, Pan Liang-ming, L.M., Yuan, D. wen & Wang, X. jun (2010) Dual model of bubble growth in vertical rectangular narrow channel. *International Communications in Heat and Mass Transfer*. 37 (8), 1004–1007.

doi:10.1016/j.icheatmasstransfer.2010.06.023.

Chen, H., Chen, G., Zou, X., Yao, Y. & Gong, M. (2017) Experimental investigations on bubble departure diameter and frequency of methane saturated nucleate pool boiling at four different pressures. *International Journal of Heat and Mass Transfer*. 112, 662–675. doi:10.1016/j.ijheatmasstransfer.2017.05.031.

Chen, J.C. (1966) Correlation for boiling heat transfer to saturated fluids in convective flow. *Industrial & engineering chemistry process design and development*. 5 (3), 322–329. doi:10.1021/i260019a023.

Chi-Yeh, H. & Griffith, P. (1965a) The mechanism of heat transfer in nucleate pool boiling-Part I. Bubble initiaton, growth and departure. *International Journal of Heat and Mass Transfer*. 8 (6), 887–904. doi:10.1016/0017-9310(65)90073-6.

Chi-Yeh, H. & Griffith, P. (1965b) The mechanism of heat transfer in nucleate pool boiling—Part I. *International Journal of Heat and Mass Transfer*. 8 (6), 887–904. doi:10.1016/0017-9310(65)90073-6.

Chu, H. & Yu, B. (2009) A new comprehensive model for nucleate pool boiling heat transfer of pure liquid at low to high heat fluxes including CHF. *International Journal of Heat and Mass Transfer*. 52 (19–20), 4203–4210. doi:10.1016/j.ijheatmasstransfer.2009.04.010.

Cole, R. (1960) A photographic study of pool boiling in the region of the critical heat flux. *AIChE Journal*. 6 (4), 533–538. doi:10.1002/aic.690060405.

Dadhich, M. & Prajapati, O.S. (2019) A brief review on factors affecting flow and pool boiling. *Renewable and Sustainable Energy Reviews*.112 pp.607–625. doi:10.1016/j.rser.2019.06.016.

Das, A.K., Das, P.K. & Saha, P. (2009) Performance of different structured surfaces in nucleate pool boiling. *Applied Thermal Engineering*. 29 (17–18), 3643–3653. doi:10.1016/j.applthermaleng.2009.06.020.

Deng, D., Wan, W., Tang, Y., Wan, Z. & Liang, D. (2015) Experimental investigations on flow boiling performance of reentrant and rectangular microchannels - A comparative study. *International Journal of Heat and Mass Transfer*. 82, 435–446. doi:10.1016/j.ijheatmasstransfer.2014.11.074.

Dhir, V.K., Abarajith, H.S. & Li, D. (2007) Bubble dynamics and heat transfer during pool and flow boiling. *Heat Transfer Engineering*. 28 (7), 608–624. doi:10.1080/01457630701266421.

Dinh, T.N., Tu, J.P., Dinh, A.T. & Theofanous, T.G. (2003) Nucleation phenomena in boiling on nanoscopically smooth surfaces. *41st Aerospace Sciences Meeting and Exhibit*. doi:10.2514/6.2003-1035.

Dong, X. & Zhang, Z. (2021) Mechanism study of bubble maximum diameter in the subcooled boiling flow for low-pressure condition. *International Journal of Heat and Mass Transfer*. 164, 120585. doi:10.1016/j.ijheatmasstransfer.2020.120585.

Du, J., Zhao, C. & Bo, H. (2018) Investigation of bubble departure diameter in horizontal and vertical subcooled flow boiling. *International Journal of Heat and Mass Transfer*. 127, 796–805. doi:10.1016/j.ijheatmasstransfer.2018.07.019.

Du, J., Zhao, C., Bo, H. & Zhou, Y. (2018) A simplified force-balance model to predict bubble departure diameter in horizontal flow boiling. *International Conference on Nuclear Engineering, Proceedings, ICONE*. 6A, 1–6. doi:10.1115/icone26-81302.

Euh, D., Ozar, B., Hibiki, T., Ishii, M. & Song, C.-H. (2010) Characteristics of Bubble Departure Frequency in a Low-Pressure Subcooled Boiling Flow. *Journal of Nuclear Science and Technology*. 47 (7), 608–617. doi:10.1080/18811248.2010.9720958.

Faghri, A., Zhang, Y. & Howell, J.R. (2010) *Advanced Heat and Mass Transfer*. Global Digital Press.

Fang, X., Wang, R., Chen, W., Zhang, H. & Ma, C. (2015) A review of flow boiling heat transfer of nanofluids. *Applied Thermal Engineering*.91 pp.1003–1017. doi:10.1016/j.applthermaleng.2015.08.100.

Farber, E.A. & Scorah, R.L. (1948) Heat transfer to water boiling under pressure. *Journal of Fluids Engineering*. 70 (4), 369–380. doi:10.1115/1.4017741.

Fritz, W. (1935) The calculation of the maximum volume of steam bladders. *Phys. Z*. 36, 379–384.

Fritz, W. & Ende, W. (1936) Über den Verdampfungsvorgang nach kinematographischen Aufnahmen an Dampfblasen. *Phys. Z*. 37, 391–401.

Gao, M., Zhang, L., Cheng, P. & Quan, X. (2013) An investigation of microlayer beneath nucleation bubble by laser interferometric method. *International Journal of Heat and Mass Transfer*. 57 (1), 183–189. doi:10.1016/j.ijheatmasstransfer.2012.10.017.

Goel, P., Nayak, A.K., Ghosh, P. & Joshi, J.B. (2018) Experimental study of bubble departure characteristics in forced convective subcooled nucleate boiling. *Experimental Heat Transfer*. 31 (3), 194–218. doi:10.1080/08916152.2017.1397821.

Golobic, I., Petkovsek, J., Baselj, M., Papez, A. & Kenning, D.B.R. (2009) Experimental determination of transient wall temperature distributions close to growing vapor bubbles. *Heat and Mass Transfer*. 45 (7), 857–866. doi:10.1007/s00231-007-0295-y.

Gong, S. & Cheng, P. (2016) Two-dimensional mesoscale simulations of saturated pool boiling from rough surfaces. Part II: Bubble interactions above multi-cavities. *International Journal of Heat and Mass Transfer*. 100, 938–948. doi:10.1016/j.ijheatmasstransfer.2016.04.082.

Gong, S., Cheng, P. & Quan, X. (2016) Two-dimensional mesoscale simulations of saturated pool boiling from rough surfaces. Part I: Bubble nucleation in a single cavity at low superheats. *International Journal of Heat and Mass Transfer*. 100, 927–937. doi:10.1016/j.ijheatmasstransfer.2016.04.085.

Griffith, P. & Wallis, J.D. (1960) The role of surface conditions in nucleate boiling. *Chem. Eng. Prog., Symp. Ser.* 56 (30), 49–63. http://libraries.mit.edu/docs.

Groß, T.F., Bauer, J., Ludwig, G., Fernandez Rivas, D. & Pelz, P.F. (2018) Bubble nucleation from micro-crevices in a shear flow: Experimental determination of nucleation rates and surface nuclei growth. *Experiments in Fluids*. 59 (1), 12. doi:10.1007/s00348-017-2459-y.

Hamzekhani, S., Shahraki, F., Mohebbi-Kalhori, D. & Fardinpour, M.R. (2022) Experimental investigation and modeling of bubble departure frequency for pool-boiling heat transfer. *Chemical Engineering & Technology*. 45 (11), 2049–2060. doi:10.1002/ceat.202100624.

Han, C.-Y. (1962) *The mechanism of heat transfer in nucleate pool boiling*. Massachusetts Institute of Technology. http://hdl.handle.net/1721.1/11434.

Hänsch, S. & Walker, S. (2019) Microlayer formation and depletion beneath growing steam bubbles. *International Journal of Multiphase Flow*. 111, 241–263. doi:10.1016/j.ijmultiphaseflow.2018.11.004.

Harada, T., Nagakura, H. & Okawa, T. (2010) Dependence of bubble behavior in subcooled boiling on surface wettability. *Nuclear Engineering and Design*. 240 (12), 3949–3955. doi:10.1016/j.nucengdes.2010.03.016.

Hatton, A.P. & Hall, I.S. (1966) Photographic study of boiling on prepared surfaces. In: *International Heat Transfer Conference Digital Library*. 1966 Begel House Inc. p.

He, Y., Hu, C., Li, H., Hu, X. & Tang, D. (2022) Reliable predictions of bubble departure frequency in subcooled flow boiling: A machine learning-based approach. *International Journal of Heat and Mass Transfer*. 195, 123217. doi:10.1016/j.ijheatmasstransfer.2022.123217.

Henry, C.D., Kim, J. & McQuillen, J. (2006) Dissolved gas effects on thermocapillary convection during boiling in reduced gravity environments. *Heat and Mass Transfer/Waerme- und Stoffuebertragung*.42 (10) pp.919–928. doi:10.1007/s00231-006-0140-8.

Hibiki, T. & Ishii, M. (2003) Active nucleation site density in boiling systems. *International Journal of Heat and Mass Transfer*. 46 (14), 2587–2601. doi:10.1016/S0017-9310(03)00031-0.

Hibiki, T. & Ishii, M. (2009) Interfacial area transport equations for gas-liquid flow. *Journal of Computational Multiphase Flows*. 1 (1), 1–22. doi:10.1260/175748209787387089.

Ho, J.Y., Wong, K.K. & Leong, K.C. (2016) Saturated pool boiling of FC-72 from enhanced

surfaces produced by Selective Laser Melting. *International Journal of Heat and Mass Transfer*. 99, 107–121. doi:10.1016/j.ijheatmasstransfer.2016.03.073.

Howell, J.R. & Siegel, R. (1966) Incipence, growth, and detechment of boiling bubbles in saturated water from artificial nucleation sites of known geometry and size. *Proc. 3rd Int. Heat Transf Conf.* IV, 12–33. doi:10.1615/ihtc3.1120.

Hsu, Y.Y. (1962) On the size range of active nucleation cavities on a heating surface. *Journal of Heat Transfer*. 84 (3), 207–213. doi:10.1115/1.3684339.

Hutter, C., Kenning, D.B.R., Sefiane, K., Karayiannis, T.G., Lin, H., Cummins, G. & Walton, A.J. (2010) Experimental pool boiling investigations of FC-72 on silicon with artificial cavities and integrated temperature microsensors. *Experimental Thermal and Fluid Science*. 34 (4), 422–433. doi:10.1016/j.expthermflusci.2009.03.010.

Hutter, C., Sefiane, K., Karayiannis, T.G., Walton, A.J., Nelson, R.A. & Kenning, D.B.R. (2012) Nucleation site interaction between artificial cavities during nucleate pool boiling on silicon with integrated micro-heater and temperature micro-sensors. *International Journal of Heat and Mass Transfer*. 55 (11–12), 2769–2778. doi:10.1016/j.ijheatmasstransfer.2012.02.014.

Ivey, H.J. (1967) Relationships between bubble frequency, departure diameter and rise velocity in nucleate boiling. *International Journal of Heat and Mass Transfer*. 10 (8), 1023–1040. doi:10.1016/0017-9310(67)90118-4.

Jakob, M. (1949) *Heat transfer*. Vol. 1.

Jakob, M. & Linke, W. (1935) Boiling heat transfer. *Phys. Z*. 36 (2), 267–273.

Jung, S. & Kim, H. (2014) An experimental method to simultaneously measure the dynamics and heat transfer associated with a single bubble during nucleate boiling on a horizontal surface. *International Journal of Heat and Mass Transfer*. 73, 365–375. doi:10.1016/j.ijheatmasstransfer.2014.02.014.

Kaiho, K., Okawa, T. & Enoki, K. (2017) Measurement of the maximum bubble size distribution in water subcooled flow boiling at low pressure. *International Journal of Heat and Mass Transfer*. 108, 2365–2380. doi:10.1016/j.ijheatmasstransfer.2017.01.027.

Kandlikar, S.G. (1999) *Handbook of Phase Change: Boiling and Condensation*.

Kandlikar, S.G. & Grande, W.J. (2003) Evolution of microchannel flow passages—thermohydraulic performance and fabrication technology. *Heat Transfer Engineering*. 24 (1), 3–17. doi:10.1080/01457630304040.

Kandlikar, S.G., Kuan, W.K., Willistein, D.A. & Borrelli, J. (2006) Stabilization of flow boiling in microchannels using pressure drop elements and fabricated nucleation sites. *Journal of Heat Transfer*. 128 (4), 389–396. doi:10.1115/1.2165208.

Kandlikar, S.G., Mizo, V.R. & Cartwright, M.D. (1995) Investigation of bubble departure mechanism in subcooled flow boiling of water using high-speed photography. In: *Proc. Convective Flow Boiling Conf*. 1995 pp. 161–166.

Kandlikar, S.G., Steinke, M.E. & Balasubramanian, P. (2002) Single-phase flow characteristics and effect of dissolved gases on heat transfer near saturation conditions in microchannels. In: *ASME International Mechanical Engineering Congress and Exposition*. 2002 pp. 197–204.

Kaneyasu, N., Yasunobu, F., Satoru, U. & Haruhiko, O. (1984) Effect of surface configuration on nucleate boiling heat transfer. *International Journal of Heat and Mass Transfer*. 27 (9), 1559–1571. doi:10.1016/0017-9310(84)90268-0.

Kang, Z. & Wang, L. (2018) Boiling heat transfer on surfaces with 3D-printing microstructures. *Experimental Thermal and Fluid Science*. 93, 165–170. doi:10.1016/j.expthermflusci.2017.12.021.

Kim, D.E., Song, J. & Kim, H. (2016) Simultaneous observation of dynamics and thermal evolution of irreversible dry spot at critical heat flux in pool boiling. *International Journal of Heat and Mass Transfer*. 99, 409–424. doi:10.1016/j.ijheatmasstransfer.2016.04.009.

Klausner, J.F., Mei, R., Bernhard, D.M. & Zeng, L.Z. (1993) Vapor bubble departure in forced convection boiling. *International Journal of Heat and Mass Transfer*. 36 (3),

651–662. doi:10.1016/0017-9310(93)80041-r.

Klausner, J.F., Mei, R. & Zeng, L.Z. (1997) Predicting stochastic features of vapor bubble detachment in flow boiling. *International Journal of Heat and Mass Transfer*. 40 (15), 3547–3552. doi:10.1016/s0017-9310(97)00012-4.

Kocamustafaogullari, G. & Ishii, M. (1983) Interfacial area and nucleation site density in boiling systems. *International Journal of Heat and Mass Transfer*. 26 (9), 1377–1387. doi:10.1016/s0017-9310(83)80069-6.

Kubo, H., Takamatsu, H. & Honda, H. (1999) Effects of size and number density of micro-reentrant cavities on boiling heat transfer from a silicon chip immersed in degassed and gas-dissolved FC-72. *Journal of Enhanced Heat Transfer*. 6 (2–4). doi:10.1615/JEnhHeatTransf.v6.i2-4.80.

Kuo, C.-J. & Peles, Y. (2007) Local measurement of flow boiling in structured surface microchannels. *International Journal of Heat and Mass Transfer*. 50 (23–24), 4513–4526. doi:10.1016/j.ijheatmasstransfer.2007.03.047.

Kuo, C.J. & Peles, Y. (2008) Flow boiling instabilities in microchannels and means for mitigation by reentrant cavities. *Journal of Heat Transfer*. 130 (7), 72402–72410. doi:10.1115/1.2908431.

Kuo, C.J. & Peles, Y. (2009) Flow boiling of coolant (HFE-7000) inside structured and plain wall microchannel. *Journal of Heat Transfer*. 131 (12), 1–9. doi:10.1115/1.3220674.

Kurul, N. & Podowski, M.Z. (1990) Multidimensional effects in forced convection subcooled boiling. In: *International Heat Transfer Conference Digital Library*. 1990 Begel House Inc. p.

Levin, A.A. & Khan, P. V. (2018) Experimental observation of the maximum bubble diameter in non-stationary temperature field of subcooled boiling water flow. *International Journal of Heat and Mass Transfer*. 124, 876–883. doi:10.1016/j.ijheatmasstransfer.2018.03.078.

Levy, S. (1967) Forced convection subcooled boiling-prediction of vapor volumetric fraction. *International Journal of Heat and Mass Transfer*. 10 (7), 951–965. doi:10.1016/0017-9310(67)90071-3.

Liaw, S.P. & Dhir, V.K. (1989) Void fraction measurements during saturated pool boiling of water on partially wetted vertical surfaces. *Journal of Heat Transfer*. 111 (3), 731–738. doi:10.1115/1.3250744.

Lie, Y.M., Ke, J.H., Chang, W.R., Cheng, T.C. & Lin, T.F. (2007) Saturated flow boiling heat transfer and associated bubble characteristics of FC-72 on a heated micro-pin-finned silicon chip. *International Journal of Heat and Mass Transfer*. 50 (19–20), 3862–3876. doi:10.1016/j.ijheatmasstransfer.2007.02.010.

Liu, Z. & Winterton, R.H.S. (1991) A general correlation for saturated and subcooled flow boiling in tubes and annuli, based on a nucleate pool boiling equation. *International Journal of Heat and Mass Transfer*. 34 (11), 2759–2766. doi:10.1016/0017-9310(91)90234-6.

Lou, S.-T., Ouyang, Z.-Q. & Zhang, Y. (2000) Nanobubbles on solid surface imaged by atomic force microscopy. *The Journal of Chemical Physics*. 18, 14706. doi:10.1116/1.1289925.

Malenkov, I.G. (1971) Detachment frequency as a function of size for vapor bubbles. *Journal of Engineering Physics*. 20 (6), 704–708. doi:10.1007/bf01122590.

Martínez-Cuenca, R., Brooks, C.S., Juliá, J.E., Hibiki, T. & Ishii, M. (2015) Stochastic nature of wall nucleation and its impact on the time average boundary condition. *Journal of Heat Transfer*. 137 (2). doi:10.1115/1.4028975.

Marto, P.J., Moulson, J.A. & Maynard, M.D. (1968) Nucleate pool boiling of nitrogen with different surface conditions. *Journal of Heat Transfer*. 90 (4), 437–444. doi:10.1115/1.3597539.

Mehta, R.D. & Bradshaw, P. (1979) Design rules for small low speed wind tunnels. *The Aeronautical Journal*. 83 (827), 443–453. doi:10.1017/s0001924000031985.

Merte Jr, H. (1988) Nucleate pool boiling: High gravity to reduced gravity; liquid metals to cryogens. In: *New Mexico Univ., Transactions of the Fifth Symposium on Space*

Nuclear Power Systems. 1988 pp. 437–442.

Mikic, B.B., Rohsenow, W.M. & Griffith, P. (1970) On bubble growth rates. *International Journal of Heat and Mass Transfer*. 13 (4), 657–666. doi:10.1016/0017-9310(70)90040-2.

Moffat, R.J. (1988) Describing the uncertainties in experimental results. *Experimental Thermal and Fluid Science*. 1 (1), 3–17. doi:10.1016/0894-1777(88)90043-x.

Mohanty, R.L. & Das, M.K. (2017) A critical review on bubble dynamics parameters influencing boiling heat transfer. *Renewable and Sustainable Energy Reviews*. 78, 466–494. doi:10.1016/j.rser.2017.04.092.

Morel, T. (1975) Comprehensive design of axisymmetric wind tunnel contractions. *Journal of Fluids Engineering, Transactions of the ASME*. 97 (2), 225–233. doi:10.1115/1.3447255.

Mu, Y.T., Chen, L., He, Y.L., Kang, Q.J. & Tao, W.Q. (2017) Nucleate boiling performance evaluation of cavities at mesoscale level. *International Journal of Heat and Mass Transfer*. 106, 708–719. doi:10.1016/j.ijheatmasstransfer.2016.09.058.

Mukherjee, A., Basu, D.N. & Mondal, P.K. (2022) Mesoscopic characterization of bubble dynamics in subcooled flow boiling following a pseudopotential-based approach. *International Journal of Multiphase Flow*. 148, 103923. doi:10.1016/j.ijmultiphaseflow.2021.103923.

Mukherjee, A. & Dhir, V.K. (2004) Study of lateral merger of vapor bubbles during nucleate pool boiling. *Journal of Heat Transfer*. 126 (6), 1023–1039. doi:10.1115/1.1834614.

Nam, Y. & Ju, Y.S. (2008) Bubble nucleation on hydrophobic islands provides evidence to anomalously high contact angles of nanobubbles. *Applied Physics Letters*. 93 (10), 103115. doi:10.1063/1.2981572.

Narayan, S., Singh, T. & Srivastava, A. (2020) Experiments on pool boiling regimes and bubble departure characteristics of single vapor bubble under subcooled bulk conditions. *Experimental Thermal and Fluid Science*. 111. doi:10.1016/j.expthermflusci.2019.109943.

Nukiyama, S. (1934) The maximum and minimum values of the heat Q transmitted from metal to boiling water under atmospheric pressure. *International Journal of Heat and Mass Transfer*. 9 (12), 1419–1433. doi:10.1016/0017-9310(66)90138-4.

O'connor, J.P., You, S.M. & Chang, J.Y. (1996) Gas-Saturated Pool Boiling Heat Transfer From Smooth and Microporous Surfaces in FC-72. *Journal of Heat Transfer*. 118 (3), 662–667. doi:10.1115/1.2822683.

Ooi, Z.J., Kumar, V., Bottini, J.L. & Brooks, C.S. (2018) Experimental investigation of variability in bubble departure characteristics between nucleation sites in subcooled boiling flow. *International Journal of Heat and Mass Transfer*. 118, 327–339. doi:10.1016/j.ijheatmasstransfer.2017.10.116.

Owoeye, E.J. & Schubring, D.W. (2016) CFD analysis of bubble microlayer and growth in subcooled flow boiling. *Nuclear Engineering and Design*. 304. doi:10.1016/j.nucengdes.2016.04.027.

Podowski, R.M., Drew, D.A., Lahey Jr, R.T. & Podowski, M.Z. (1997) A mechanistic model of the ebullition cycle in forced convection subcooled boiling. In: *Eighth international topical meeting on nuclear reactor thermal-hydraulics*. 1997 pp. 1535–1542.

Prodanovic, V., Fraser, D. & Salcudean, M. (2002) Bubble behavior in subcooled flow boiling of water at low pressures and low flow rates. *International Journal of Multiphase Flow*. 28 (1), 1–19. doi:10.1016/S0301-9322(01)00058-1.

Qi, Y. & Klausner, J.F. (2005) Heterogeneous nucleation with artificial cavities. *Journal of Heat Transfer*. 127 (11), 1189–1196. doi:10.1115/1.2039111.

Rainey, K.N., You, S.M. & Lee, S. (2003) Effect of pressure, subcooling, and dissolved gas on pool boiling heat transfer from microporous, square pin-finned surfaces in FC-72. *International Journal of Heat and Mass Transfer*. 46 (1), 23–35. doi:10.1016/S0017-9310(02)00257-0.

Raj, S., Pathak, M. & Khan, M.K. (2017) An analytical model for predicting growth rate and

departure diameter of a bubble in subcooled flow boiling. *International Journal of Heat and Mass Transfer*. 109, 470–481. doi:10.1016/j.ijheatmasstransfer.2017.02.026.

Ranz, W. E. and Marshall, W.R. (1952) Evaporation from drops. *Chemical Engineering Progress*. 48, 141–146.

Richenderfer, A., Kossolapov, A., Seong, J.H., Saccone, G., Demarly, E., Kommajosyula, R., Baglietto, E., Buongiorno, J. & Bucci, M. (2018) Investigation of subcooled flow boiling and CHF using high-resolution diagnostics. *Experimental Thermal and Fluid Science*. 99, 35–58. doi:10.1016/j.expthermflusci.2018.07.017.

Rohsenow, W.M. (1952) A method of correlating heat-transfer data for surface boiling of liquids. *Journal of Fluids Engineering*. http://hdl.handle.net/1721.1/61431.

Ross, T.K. (1967) Corrosion and heat transfer — a review. *British Corrosion Journal*. 2 (4), 131–142. doi:10.1179/000705967798326821.

Roy, R.P., Velidandla, V., Kalra, S.P. & Peturaud, P. (1994) Local measurements in the two-phase region of turbulent subcooled boiling flow. *Journal of Heat Transfer*. 116 (3), 660–669. doi:10.1115/1.2910920.

Saitoh, S., Daiguji, H. & Hihara, E. (2005) Effect of tube diameter on boiling heat transfer of R-134a in horizontal small-diameter tubes. *International Journal of Heat and Mass Transfer*. 48 (23–24), 4973–4984. doi:10.1016/j.ijheatmasstransfer.2005.03.035.

Sakurai, A. & Shiotsu, M. (1977a) Transient pool boiling heat transfer: Part 1: Incipient boiling superheat. *Journal of Heat Transfer*. 99 (4), 547–553. doi:10.1115/1.3450740.

Sakurai, A. & Shiotsu, M. (1977b) Transient pool boiling heat transfer: Part 2: Boiling heat transfer and burnout. *Journal of Heat Transfer*. 99 (4), 554–560. doi:10.1115/1.3450741.

Sarker, D., Franz, R., Ding, W. & Hampel, U. (2017) Single bubble dynamics during subcooled nucleate boiling on a vertical heater surface: An experimental analysis of the effects of surface characteristics. *International Journal of Heat and Mass Transfer*. 109, 907–921. doi:10.1016/j.ijheatmasstransfer.2017.02.017.

Sato, Y. & Niceno, B. (2015) A depletable micro-layer model for nucleate pool boiling. *Journal of Computational Physics*. 300, 20–52. doi:10.1016/j.jcp.2015.07.046.

Shen, B., Suroto, B.J., Hirabayashi, S., Yamada, M., Hidaka, S., Kohno, M., Takahashi, K. & Takata, Y. (2015) Bubble activation from a hydrophobic spot at “negative” surface superheats in subcooled boiling. *Applied Thermal Engineering*. 88, 230–236. doi:10.1016/j.applthermaleng.2014.10.054.

Shoji, M., Mosdorf, R., Zhang, L., Takagi, Y., Yasui, K. & Yokota, M. (2002) Features of boiling on an artificial surface - Bubble formation, wall temperature fluctuation and nucleation site interaction. *Journal of Thermal Science*. 11 (3), 226–234. doi:10.1007/s11630-002-0059-4.

Shoji, M. & Takagi, Y. (2001) Bubbling features from a single artificial cavity. *International Journal of Heat and Mass Transfer*. 44 (14), 2763–2776. doi:10.1016/S0017-9310(00)00300-8.

Siedel, S., Cioulachtjian, S. & Bonjour, J. (2008) Experimental analysis of bubble growth, departure and interactions during pool boiling on artificial nucleation sites. *Experimental Thermal and Fluid Science*. 32 (8), 1504–1511. doi:10.1016/j.expthermflusci.2008.04.004.

Singh, A., Mikic, B.B. & Rohsenow, W.M. (1976) Active sites in boiling. *Journal of Heat Transfer*. 98 (3), 401–406. doi:10.1115/1.3450567.

Sinha, G.K., Mahimkar, S. & Srivastava, A. (2019) Schlieren-based simultaneous mapping of bubble dynamics and temperature gradients in nucleate flow boiling regime: Effect of flow rates and degree of subcooling. *Experimental Thermal and Fluid Science*. 104, 238–257. doi:10.1016/j.expthermflusci.2019.02.018.

Situ, R., Hibiki, T., Ishii, M. & Mori, M. (2005) Bubble lift-off size in forced convective subcooled boiling flow. *International Journal of Heat and Mass Transfer*. 48 (25–26), 5536–5548. doi:10.1016/j.ijheatmasstransfer.2005.06.031.

Situ, R., Ishii, M., Hibiki, T., Tu, J.Y., Yeoh, G.H. & Mori, M. (2008) Bubble departure

frequency in forced convective subcooled boiling flow. *International Journal of Heat and Mass Transfer*. 51 (25–26), 6268–6282. doi:10.1016/j.ijheatmasstransfer.2008.04.028.

Sommers, A.D. & Yerkes, K.L. (2013) Using micro-structural surface features to enhance the convective flow boiling heat transfer of R-134a on aluminum. *International Journal of Heat and Mass Transfer*. 64, 1053–1063. doi:10.1016/j.ijheatmasstransfer.2013.05.053.

Song, Y., Gong, S., Vaartstra, G. & Wang, E.N. (2021) Microtube surfaces for the simultaneous enhancement of efficiency and critical heat flux during pool boiling. *ACS Applied Materials & Interfaces*. 13 (10), 12629–12635. doi:10.1021/acsami.1c00750.

Sriraman, S.R. (2008) *Pool boiling on nano-finned surfaces*. Texas A & M University.

Sugrue, R. & Buongiorno, J. (2016) A modified force-balance model for prediction of bubble departure diameter in subcooled flow boiling. *Nuclear Engineering and Design*. 305. doi:10.1016/j.nucengdes.2016.04.017.

Sugrue, R., Buongiorno, J. & McKrell, T. (2014) An experimental study of bubble departure diameter in subcooled flow boiling including the effects of orientation angle, subcooling, mass flux, heat flux, and pressure. *Nuclear Engineering and Design*. 279, 182–188. doi:10.1016/j.nucengdes.2014.08.009.

Sun, T., Gui, N., Yang, X., Tu, J. & Jiang, S. (2018) Effect of contact angle on flow boiling in vertical ducts: A pseudo-potential MRT-thermal LB coupled study. *International Journal of Heat and Mass Transfer*. 121, 1229–1233. doi:10.1016/j.ijheatmasstransfer.2018.01.088.

Takata, Y., Hidaka, S. & Uraguchi, T. (2006) Boiling feature on a super water-repellent surface. *Heat Transfer Engineering*. 27 (8), 25–30. doi:10.1080/01457630600793962.

Theofanous, T.G., Tu, J.P., Dinh, A.T. & Dinh, T.N. (2002) The boiling crisis phenomenon part I: Nucleation and nucleate boiling heat transfer. *Experimental Thermal and Fluid Science*. 26 (6–7), 775–792. doi:10.1016/S0894-1777(02)00192-9.

Thorncroft, G.E., Klausner, J.F. & Mei, R. (1998) An experimental investigation of bubble growth and detachment in vertical upflow and downflow boiling. *International Journal of Heat and Mass Transfer*. 41 (23), 3857–3871. doi:10.1016/s0017-9310(98)00092-1.

Tong, L.S. (2018) *Boiling heat transfer and two-phase flow*. Routledge.

Tyrrell, J.W.G. & Attard, P. (2001) Images of nanobubbles on hydrophobic surfaces and their interactions. *Physical Review Letters*. 87 (17). doi:10.1103/PhysRevLett.87.176104.

Unal (1976) Maximum bubble diameter , maximum rate during the subcooled nucleate flow boiling. *Int. J. Heat Mars Transfer.* 19, 643–649. doi:10.1016/0017-9310(76)90047-8.

Ünal, H.C. (1976) Maximum bubble diameter, maximum bubble-growth time and bubble-growth rate during the subcooled nucleate flow boiling of water up to 17.7 MN/m2. *International Journal of Heat and Mass Transfer*. 19 (6), 643–649. doi:10.1016/0017-9310(76)90047-8.

Vlachou, M.C. & Karapantsios, T.D. (2018) Effect of channel inclination on heat transfer and bubble dynamics during subcooled flow boiling. *International Journal of Thermal Sciences*. 124, 484–495. doi:10.1016/j.ijthermalsci.2017.10.041.

Vlachou, M.C., Lioumbas, J.S., David, K., Chasapis, D. & Karapantsios, T.D. (2017) Effect of channel height and mass flux on highly subcooled horizontal flow boiling. *Experimental Thermal and Fluid Science*. 83, 157–168. doi:10.1016/j.expthermflusci.2017.01.001.

Wei, J.J. & Honda, H. (2003) Effects of fin geometry on boiling heat transfer from silicon chips with micro-pin-fins immersed in FC-72. *International Journal of Heat and Mass Transfer*. 46 (21), 4059–4070. doi:10.1016/S0017-9310(03)00226-6.

Yang, G., Zhang, W., Binama, M., Sun, J. & Cai, W. (2022) Review on bubble dynamic of subcooled flow boiling-part a: Research methodologies. *International Journal of Thermal Sciences*. 108019. doi:10.1016/j.ijthermalsci.2022.108019.

Yang, L.X., Guo, A. & Liu, D. (2016) Experimental investigation of subcooled vertical upward flow boiling in a narrow rectangular channel. *Experimental Heat Transfer*. 29 (2), 221–243. doi:10.1080/08916152.2014.973978.

Yin, C.P., Yan, Y.Y., Lin, T.F. & Yang, B.C. (2000) Subcooled flow boiling heat transfer of R-134a and bubble characteristics in a horizontal annular duct. *International Journal of Heat and Mass Transfer*. 43 (11), 1885–1896. doi:10.1016/s0017-9310(99)00278-1.

Yoo, J., Estrada-Perez, C.E. & Hassan, Y.A. (2014) A proper observation and characterization of wall nucleation phenomena in a forced convective boiling system. *International Journal of Heat and Mass Transfer*. 76, 568–584. doi:10.1016/j.ijheatmasstransfer.2014.04.063.

Yoo, J., Estrada-Perez, C.E. & Hassan, Y.A. (2018) Area of bubble influence due to sliding bubbles in subcooled boiling flow. *International Journal of Heat and Mass Transfer*. 125, 43–52. doi:10.1016/j.ijheatmasstransfer.2018.04.058.

Yoo, J., Estrada-Perez, C.E. & Hassan, Y.A. (2016a) Experimental study on bubble dynamics and wall heat transfer arising from a single nucleation site at subcooled flow boiling conditions – Part 1: Experimental methods and data quality verification. *International Journal of Multiphase Flow*. 84, 315–324. doi:10.1016/j.ijmultiphaseflow.2016.04.018.

Yoo, J., Estrada-Perez, C.E. & Hassan, Y.A. (2016b) Experimental study on bubble dynamics and wall heat transfer arising from a single nucleation site at subcooled flow boiling conditions – Part 2: Data analysis on sliding bubble characteristics and associated wall heat transfer. *International Journal of Multiphase Flow*. 84, 292–314. doi:10.1016/j.ijmultiphaseflow.2016.04.019.

Yu, C.K., Lu, D.C. & Cheng, T.C. (2006) Pool boiling heat transfer on artificial micro-cavity surfaces in dielectric fluid FC-72. *Journal of Micromechanics and Microengineering*. 16 (10), 2092–2099. doi:10.1088/0960-1317/16/10/024.

Yuan, D., Chen, D., Yan, X., Xu, J., Lu, Q. & Huang, Y. (2018) Bubble behavior and its contribution to heat transfer of subcooled flow boiling in a vertical rectangular channel. *Annals of Nuclear Energy*. 119, 191–202. doi:10.1016/j.anucene.2018.05.010.

Yuan, D.W., Pan, L.M., Chen, D., Zhang, H., Wei, J.H. & Huang, Y.P. (2011) Bubble behavior of high subcooling flow boiling at different system pressure in vertical narrow channel. *Applied Thermal Engineering*. 31 (16), 3512–3520. doi:10.1016/j.applthermaleng.2011.07.004.

Yun, B.J., Splawski, A., Lo, S. & Song, C.H. (2012) Prediction of a subcooled boiling flow with advanced two-phase flow models. *Nuclear Engineering and Design*. 253, 351–359. doi:10.1016/j.nucengdes.2011.08.067.

Zeitonu, O. & Shoukri, M. (1996) Bubble behavior and mean diameter in subcooled flow boiling. *Journal of Heat Transfer*. 118 (1), 110–116. doi:10.1115/1.2824023.

Zeng, L.Z., Klausner, J.F., Bernhard, D.M. & Mei, R. (1993) A unified model for the prediction of bubble detachment diameters in boiling systems-II. Flow boiling. *International Journal of Heat and Mass Transfer*. 36 (9), 2271–2279. doi:10.1016/s0017-9310(05)80112-7.

Zhang, C., Zhang, L. & Xu, H. (2018) The influence of surface orientation on the onset of nucleate boiling from microporous surfaces. *International Journal of Heat and Fluid Flow*. 73, 163–173. doi:10.1016/j.ijheatfluidflow.2018.05.010.

Zhang, L., Gong, S., Lu, Z., Cheng, P. & Wang, E.N. (2021) A unified relationship between bubble departure frequency and diameter during saturated nucleate pool boiling. *International Journal of Heat and Mass Transfer*. 165, 120640. doi:10.1016/j.ijheatmasstransfer.2020.120640.

Zhang, L. & Shoji, M. (2003) Nucleation site interaction in pool boiling on the artificial surface. *International Journal of Heat and Mass Transfer*. 46 (3), 513–522. doi:10.1016/S0017-9310(02)00291-0.

Zhang, Y., Liu, B., Zhao, J., Deng, Y. & Wei, J. (2018a) Experimental study of subcooled

flow boiling heat transfer on a smooth surface in short-term microgravity. *Microgravity Science and Technology*. 30 (6), 793–805. doi:10.1007/s12217-018-9629-2.

Zhang, Y., Liu, B., Zhao, J., Deng, Y. & Wei, J. (2018b) Experimental study of subcooled flow boiling heat transfer on micro-pin-finned surfaces in short-term microgravity. *Experimental Thermal and Fluid Science*. 97, 417–430. doi:10.1016/j.expthermflusci.2018.05.003.

Zhou, P., Huang, R., Huang, S., Zhang, Y. & Rao, X. (2020a) Experimental investigation on active nucleation site density and bubble departure frequency in subcooled flow boiling by using bubble tracking algorithm. *International Journal of Heat and Mass Transfer*. 148, 119081. doi:10.1016/j.ijheatmasstransfer.2019.119081.

Zhou, P., Huang, R., Huang, S., Zhang, Y. & Rao, X. (2020b) Experimental investigation on bubble contact diameter and bubble departure diameter in horizontal subcooled flow boiling. *International Journal of Heat and Mass Transfer*. 149, 119105. doi:10.1016/j.ijheatmasstransfer.2019.119105.

Zuber, N. (1963) Nucleate boiling. The region of isolated bubbles and the similarity with natural convection. *International Journal of Heat and Mass Transfer*. 6 (1), 53–78. doi:10.1016/0017-9310(63)90029-2.

Zuber, N. (1961) The dynamics of vapor bubbles in nonuniform temperature fields. *International Journal of Heat and Mass Transfer*. 2 (1), 83–98. doi:10.1016/0017-9310(61)90016-3.